TECHNISCHE UNIVERSITÄT WIEN
Vienna University of Technology

DISSERTATION

Surface and Bulk Characterization of Transition Metal Oxides: A Density Functional Theory Study of ZrO_2 and VO_2

Ausgeführt zum Zwecke der Erlangung des akademischen Grades eines Doktors der technischen Wissenschaften unter der Leitung von

Ao.Univ.Prof. Dr.techn. Josef Redinger

und

Privatdoz. Dr.techn. Florian Mittendorfer

Institut für Angewandte Physik E134

Center for computational materials science

eingereicht an der Technischen Universität Wien
Fakultät für Physik

von

Ing. Jakub Planer

e01529549

Wien, am 24. August 2021

Kurzfassung

Die vorliegende Dissertation befasst sich mit der Charakterisierung der strukturellen und elektronischen Eigenschaften von zwei Übergangsmetalloxiden, Vanadiumdioxid (VO_2) und Zirkoniumdioxid (ZrO_2), mit Hilfe von Dichtefunktionaltheorie (DFT) Rechnungen.

Neue Experimente haben gezeigt, dass auf einem Metallsubstrat gewachsene dünne $VO_2(110)$ Schichten als auch die (110) Oberfläche von VO2 Einkristallen mit Rutilstruktur (2×2) artige Rekonstruktionen aufweisen. Da VO_2 als stark korreliertes Material angesehen werden kann, wurde zuerst die Genauigkeit und Verlässlichkeit einer Beschreibung mittels üblichen DFT Funktionalen untersucht. Dies schließt eine Anwendung folgender Funktionale mit nichtmagnetischer (NM), antiferromagnetischer (AFM) und ferromagnetischer (FM) Spinanordnung ein: PBE, PBE+U (U = 2 eV), sowie die kürzlich entwickelten meta-GGA Funktionale SCAN und SCAN+rVV. Die vorliegende Arbeit zeigt, dass das SCAN Funktional generell eine bessere Beschreibung der Volumeneigenschaften als PBE und PBE+U Funktionale liefert. Betreffend die Stabilität von Rutil VO_2 Oberflächen mit verschiedenen niedrig indizierten Orientierungen hängt diese in den meisten Fällen nicht von der angenommenen Spinanordnung ab, jedoch wurden einige Abweichungen festgestellt. Zum einem zeigen (NM) Rechnungen für die (001) Oberfläche eine Absenkung der oberflächennahen V-t_{2g} Zustände, was von einer Verminderung Oberflächenenergie begleitet wird, zum anderen wurde ein ähnlicher Effekt für alle untersuchten Oberflächenorientierungen beobachtet, wenn das PBE+U Funktional zum Einsatz kommt, welches in der Rutil Volumenphase bei magnetischen Spinanordnungen eine ungewünschte elektronische Bandlücke öffnet. Anschließend wurden stöchiometrische und nichtstöchiometrische (2×1) und (2×2) Rekonstruktionen auf der (110) Rutiloberfläche mit Hilfe von fortgeschrittenen Techniken zur Strukturoptimierung, wie etwa Simulated Annealing oder der Optimierung von Zufallsstrukturen einschließlich einer modifizierten $V_2O_5(001)$ Monolage, untersucht. Die Berechnungen sagen voraus, dass ringartige polyedrische Terminierungen, die elektronisch und strukturell mit einer $V_2O_5(001)$ Monolage verwandt sind, äußerst stabil sind. Diese neuartigen Strukturen weisen eine höhere Stabilität auf der (110) Rutiloberfläche auf als Adsorptionsphasen von Sauerstoff. Obwohl die Stabilität der vorhergesagten neuen Strukturen zum Teil vom gewählten Funktional abhängt, gibt das SCAN Funktional in FM Spinanordnung den besten Kompromiss, da es sowohl eine vernünftige Beschreibung der strukturellen und elektronischen Eigenschaften der Rutil VO_2 Volumenphase als auch der Reaktionsenthalpie für höhere Vanadium Oxidationsstufen liefert. Die neuen vorhergesagten Oberflächenstrukturmodelle stimmen auch deutlich besser mit experimentellen STM Messungen überein als einfache Sauerstoffstrukturen auf der (110) Rutiloberfläche.

Im Falle des zweiten in dieser Arbeit behandelten Oxids, Zirkoniumdioxid, wurde im ersten Schritt wieder die Genauigkeit verschiedener DFT Funktionale evaluiert. Experimentell beobachtete und theoretisch vorhergesagte Zirkoniumdioxid Polymorphe wurden untersucht und die strukturellen und elektronischen Eigenschaften mit Viel- Elektronen

Benchmark-Rechnungen, die über die DFT Ebene hinausgehen, verglichen. Dabei liefert das SCAN+rVV Funktional die beste Übereinstimmung mit den Benchmark-Rechnungen, besser als PBE, PBE+U, und auch Hybrid-funktionale, die sowohl die energetischen Unterschiede zwischen den stabilen Polymorphen als auch die Stabilität vorhergesagter metastabiler Phasen überbewerten. Eine abschließende Untersuchung von Sauerstoffdefekten zeigt, dass die Bildungsenergie einer neutralen Sauerstofffehlstelle über 5.5 eV liegt. Abhängig von Kristallstruktur und verwendetem DFT Funktional kann diese bis auf 6.9 eV ansteigen. Für positiv geladene Defekte wird die Defektenergie unter der Annahme, dass sich das Fermi Niveau in der Mitte der Bandlücke befindet, um 2 eV abgesenkt.

Sauerstoffdefekte rufen auch eine rund um den Defekt lokalisierte elektronische Ladungsdichte hervor, was sich im Auftreten von Defektzustände in der elektronischen Bandlücke über der Mitte näher beim Leitungsbandminimum äußert. Dies stimmt recht gut überein mit aktuellen experimentellen Studien an Sauerstoffdefekten in auf Rh(111) gewachsenen tetragonalen ZrO_2 Filmen.

Abstract

This thesis is focused on a characterization of structural and electronic properties of two transition metal oxides, vanadium dioxide (VO_2) and zirconium dioxide (ZrO_2, zirconia), with the help of Density Functional Theory (DFT) calculations.

Recent experimental findings have revealed that the rutile $VO_2(110)$ surface of supported thin films and single crystals undergo a (2×2) surface reconstruction. Since the vanadium dioxide is classified as a strongly correlated material, the performance and reliability of standard DFT functionals has been tested including the PBE, PBE+U (U = 2 eV), as well as the recently developed meta-GGA SCAN and SCAN+rVV functionals, all with nonmagnetic (NM), antiferromagnetic (AFM) and ferromagnetic (FM) spin ordering. The present work shows that the SCAN functional generally improves the bulk properties over PBE and PBE+U and also shows that the calculated stability of low-index VO_2 surface orientations, is in most cases independent of the chosen spin configuration, with several identified exceptions. First, the nonmagnetic (NM) calculations on the (001) surface show a lowering of surface-decomposed V-t_{2g} states, accompanied by a lowered surface energy. Second, a similar effect has been observed for all surface orientations when using the PBE+U functional, which opens an electronic band gap in the rutile phase when performing the spin-polarized calculations. Finally, the stoichiometric and off-stoichiometric (2×1) and (2×2) surface reconstructions have been characterized with the help of simulated annealing, an optimization of random structures and the adaption of a $V_2O_5(001)$-like monolayer. Polyhedral 'ring'-like terminations, electronically and structurally related to a $V_2O_5(001)$-like monolayer are predicted. These proposed novel surface structures are more stable than pure oxygen adsorption phases on the rutile $VO_2(110)$ surface. Unfortunately, the stability of the predicted phases depends to some extent on the chosen functional, in which the spin-polarized SCAN functional offers the best compromise, as it gives both a reasonable description of the structural and electronic properties of the rutile VO_2 bulk phase and the enthalpy of reaction for higher vanadium oxidation states. Furthermore, the predicted surface oxide models agree much better with experimental STM data than oxygen only adsorption models for the rutile $VO_2(110)$ surface.

As concerns the insulator zirconia, the performance and accuracy of different DFT functionals was assessed in a first step. Both experimentally observed and theoretically predicted polymorphs have been treated comparing both structural and electronic properties to beyond-DFT benchmark calculations. For zirconia, the SCAN+rVV functional agrees best with the benchmark calculations, better than other (GGA, GGA+U and hybrid) functionals, which overestimate both energetic differences between the common phases and the stability of the predicted meta-stable phases. A subsequent investigation concerning oxygen vacancies in zirconia polymorphs revealed that the cost of forming a neutral oxygen vacancy is above $5.5\,\mathrm{eV}$, depending on the bulk phase and functional used, which may raise this value up to $6.9\,\mathrm{eV}$. However, the oxygen vacancy formation energy is lowered by

2 eV for positively charged defects considering a Fermi level situated in the middle of the band gap. The oxygen vacancies also leave behind a localized electronic charge density in vicinity of a defect, which induces electronic states within the electronic band gap found above mid-gap closer to the conduction band minimum (CBM). This is in agreement with recent experimental studies of defects in thin tetragonal films grown on Rh(111) substrate.

List of Acronyms

CI Configuration interaction

DFT Density Functional Theory

DMFT Dynamical Mean-Field Theory

GGA Generalized Gradient Approximation

HEG Homogeneous Electron Gas

HEMT High Electron Mobility Transistors

L[S]DA Local [Spin] Density Approximation

LEED Low-Energy Electron Diffraction

ML Machine Learning

MOSFET Metal Oxide Semiconductor Field Effect Transistors

PVD Physical Vapour Deposition

RPA Random Phase Approximation

SOFC Solid Oxide Fuel Cells

STM Scanning Tunnelling Microscopy

TDDFT Time-Dependent Density Functional Theory

TMO Transition Metal Oxide

VBM Valence Band Maximum

Contents

vi

vii

Chapter 1

Introduction

Transition Metal Oxides (TMOs) represent a large and fascinating group of compounds which exhibit a huge variety of technologically important physical properties. For example, the nature of interatomic bonding ranges from purely ionic (CuO, AgO)[1] to covalent (OsO_4, RuO_4)[2] and purely or partially metallic (TiO, Ag_2O)[3, 4]. Therefore, they cover the whole range of electrical conductivity starting from good insulators such as ZrO_2[5] semiconductors (TiO_2, Cu_2O)[6], conductors (ReO_3, crystalline IrO_2)[7, 8] and high-temperature superconductors (cuprates such as $YBa_2Cu_3O_7$ or $La_{2-x}Ba_xCuO_4$)[9]. Considering the magnetic properties, examples include diamagnetic materials: V_2O_5[10], paramagnetic: Ti_2O_3[11], antiferromagnetic: NiO[12], ferrimagnetic: Fe_3O_4[13] or ferromagnetic: CrO_2[14]. Several TMOs can also form compounds with different stoichiometries. For example, experimentally observed vanadium oxides exist in many stoichiometries including VO, V_2O_3, VO_2 and V_2O_5 bulk phases, Wadsley phases V_nO_{2n+1} ($n = 1 - 6$) and Magnéli phases V_nO_{2n-1} ($n = 4 - 9$)[15]. Different stoichiometries lead to changes both in crystal structure and in electronic properties.For these reasons they are applied in many fields of state-of-the-art technology such as lithium-ion batteries[16], supercapacitors[17], gas sensors[18], solid oxide fuel cells[19] or superconductors[20]. They also play an important role as catalysts in preparation of organic and inorganic compounds[21, 22] and hence tremendous efforts have been taken in experimental and theoretical investigations of these important materials.

Recent developments of novel technologies involving transition metal oxides rely on an understanding of the origin behind their physical properties. J. B. Goodenough[23] already discussed the main general concepts of several mechanisms, which significantly influence the behaviour of TMOs, as illustrated in following lines. Transition metals are elements that form groups 3 (IIIb) to 12 (IIb) of the periodic table. Unlike in other elements, the valence electrons of transition metals interacting with an environment are localized in two shells, namely s and d. This interaction depends on the overlap with valence electrons of a transition metal with neighbouring atoms. However, valence electrons from s and p shells are itinerant so they form chemical bonds easily, f electrons remain localized and they can therefore hardly interact. The transition-metal d electrons represent a compromise between itinerant and localized states and thus may exhibit both an itinerant and localized behaviour, depending on the specific transition element and its environment.

As Goodenough pointed out[23], two effects play a significant role in the type of bonding. Transition metal oxides form primarily ionic bonds induced by a charge transfer between the metal and the surrounding oxygen atoms. This process costs a certain energy which is counterbalanced by the electrostatic Madelung energy between the oxygen anions and
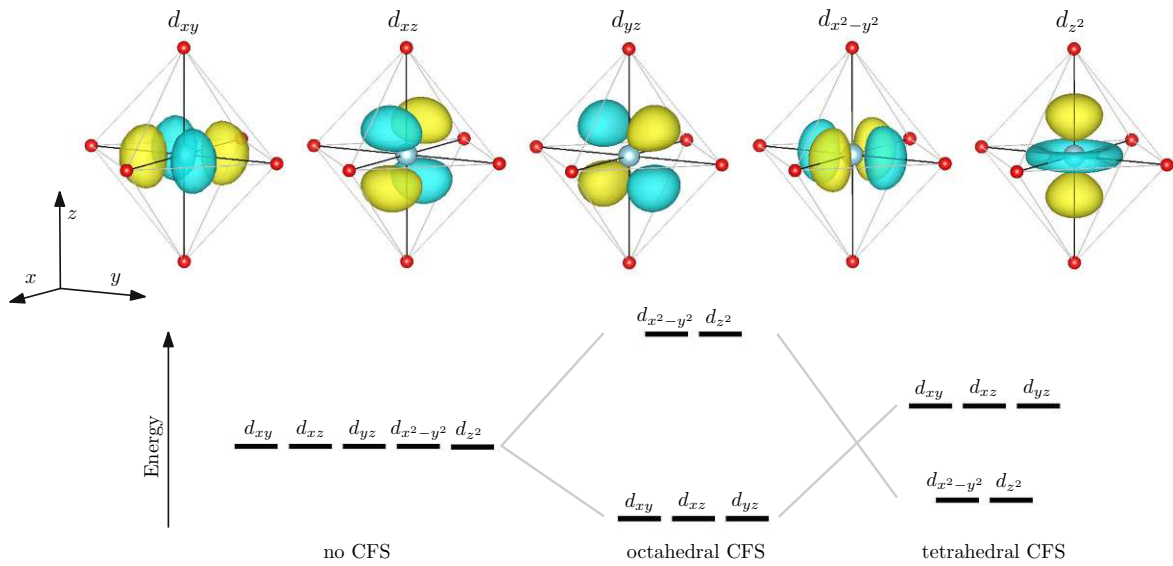
Fig. 1.1: Effect of the Crystal Field Splitting (CFS) on energy levels of transition metal d orbitals evoked by octahedral and tetrahedral coordination geometry.

metal cations in the crystal lattice. The created internal electrostatic field stabilizes the oxygen $2p$-states shifting them down in energy and raising the metal d-states above the oxygen states close to the Fermi energy E_F. Since the oxygen $2p$ and metal d-states are not too distant in energy, covalent bonding is also present causing a split between the occupied energetically lowered bonding orbitals stabilizing the system, and the unoccupied antibonding orbitals which are pushed upwards by the same amount of energy. The covalent bonding process reduces the ionic bonding by transferring electrons back to the metal ion and the prevailing effect depends on the specific compound. Experimental and theoretical evidence[24, 25] shows that an increasing oxidation state of a metal transforms ionic bonding to covalent.

In an atomic model, the d-shell is composed of five energetically degenerate atomic orbitals: d_{xy}, d_{yz}, d_{xz}, $d_{x^2-y^2}$, d_{z^2}. However, when the metal atom is placed into the crystal structure, a static electric field produced by surrounding negatively-charged oxygen atoms leads to a splitting of the atomic-like energy levels as the atomic d orbitals interact with the surrounding charge differently. Hence, the way how the degeneracy is broken depends on the coordination geometry of a metal atom. This process, also called Crystal Field Splitting (CFS), is depicted together with the atomic d orbitals in an octahedral coordination geometry in Figure 1.1 where the metal atom is surrounded by six ligands situated at the x, y, and z axes. The CFS raises the two σ- orbitals with e-symmetry ($d_{x^2-y^2}$, d_{z^2}) above the three π- orbitals with t symmetry (d_{xy}, d_{yz}, d_{xz}). Conversely, in a tetrahedral geometry the order of the t_{2g} and e_g orbitals is reversed and the size of the splitting is 4/9 lower[26]. The CFS als impacts the electronic properties of transition metal oxides: For example, when the d orbital is occupied by more than one electron, the exchange energy that stabilizes high-spin states (more unpaired electrons occupying different d orbitals) competes with the crystal field splitting. Since the CFS is lower in a tetrahedral coordination, these

2

compounds prefer high-spin state, but for an octahedral coordination, the CFS is usually too large to be counterbalanced by the exchange interaction and therefore low spin states are observed.

In 1937, Jahn and Teller[27] postulated the theorem that "*all non-linear nuclear configurations are unstable for an orbitally degenerate electronic state*". This statement also holds for crystal structures of transition metal oxides that have degenerated ground states. This degeneracy leads to geometrical distortions, reducing the symmetry and lowering the total energy of a system. Another instability that occurs in transition metal oxides was described by Mott[28], who described metal-to-insulator transitions as the result of charge screening if the electron density is large. Furthermore, Peierls[29] stated that a one-dimensional, equally spaced linear chain with one electron per ion will undergo a distortion which doubles the periodicity of a crystal in the direction of the distortion and opens the electronic gap. This distortion leads to fluctuations of electron density and the formation of charge density waves. A Peierls distortion also occurs in 3D systems, including transition metal oxides, when the electronic conductivity relies on linear chains in one dimension.

This incomplete list of physical processes already sheds some light on the physical origins behind the many interesting properties of transition metal oxides. However, due to the complexity of these systems both an experimental and theoretical characterization of these materials remains a very challenging task.

1.1 The scope of the thesis

This thesis presents a Density Functional Theory (DFT) study of two transition metal oxides. The first, vanadium dioxide, has been investigated from two perspectives: First, the present work covers a procedure that provides structural models for recently discovered rutile $VO_2(110)$ (2×2) surface reconstructions identified on both supported thin films[30, 31] and single crystals[32]. Investigations of the single crystal surface provided a deeper insight into the detailed surface structure and allowed for a comparison with recent experimental findings. Second, vanadium dioxide is known to be a strongly correlated material and there is a certain lack of knowledge on the performance of DFT for VO_2 surface systems. Hence, a particular focus of this thesis is also the comparison of developed structural models with STM experiments and a description of the performance that offer standard (GGA, GGA+U) and recently developed (meta-GGA) DFT functionals on rutile VO_2 surfaces.

The second oxide is zirconium dioxide also known as zirconia (ZrO_2), where the present thesis deals with an ab-initio characterization of bulk phases and the formation of oxygen vacancies with different charge state. Zirconia has many technologically important applications including catalysts, gas sensors and solid oxide fuel cells, where both processes at the surface and bulk defects play an important role. Recent experiments[33–36] have shown that properties of thin zirconia films are influenced both by the formation of oxygen vacancies as well as by the Rh(111) substrate. The performance of DFT functionals in bulk systems has been assessed by a comparison with benchmark post-DFT many-electron approaches. Two new meta-stable phases predicted by DFT are characterized and then

the main emphasis is directed towards the formation of oxygen vacancies in the bulk, as well as in supported and unsupported thin films.

The outline of the thesis is following: In Chapter 2 the computational methods relevant for this thesis are introduced. Chapter 3 sums up the results of the vanadium dioxide studies. After a brief introduction, the motivating interesting new experiments on VO_2 surfaces are presented. A performance study of various DFT functionals for VO_2 bulk systems follows, which provides useful insights for the subsequent characterization of unreconstructed low-index rutile VO_2 surfaces. The main part of this chapter deals with the three methods employed in the characterization of the rutile VO_2 (2×2) surface reconstructions, namely simulated annealing, an explicit modification of a V_2O_5 monolayer, and an optimization of random structures. The structural models obtained in these ways are subsequently used both in a detailed comparison with recent experimental data[32] and also in a discussion of the performance of different DFT functionals applied to the complex VO_2 surface systems. The final Chapter 4 focuses on highly precise calculations on the phase stability of zirconia polymorphs and is concluded by results concerning the formation of oxygen vacancies in the bulk, in supported and unsupported zirconia films.

Chapter 2

Theoretical background

One of the elemental problems of computational materials science is a correct description of basic properties of many-electron systems, including structural parameters, electronic and magnetic properties, excitation energies, vibrational spectra and many others. Recently, the rapid development of computing technology and theoretical concepts has allowed the treatment of more and more complex structures such as multi-layered structures, surface reconstructions, point defects, dislocations and quasi-crystals, all of them in the large interest of the frontier technology. A theoretical description of these systems is therefore extremely useful for a correct understanding of physical processes related to these materials. Furthermore, experimental investigations at an atomistic level are very intricate and often the direct observation of a property of interest is not possible. In this context, computational materials science offers a way to complement the experimental observations.

The success of the computational methods relies on the correct description of basic properties of atomistic systems which comprise electrons and nuclei. The first fundamental property is the electronic structure which describes the state of electronic motion in the electrostatic field of nuclei. The distribution of electrons in space determines chemical bonding between atoms and is therefore directly related to the stability of a system which manifests itself as atomistic, binding or cohesive energy. Furthermore, the electronic structure also determines other important properties of a system such as electrical conductivity or magnetic ordering. Furthermore, the electronic structure can also influence the geometry of the system. The basic property concerning the nuclei is their position in space which determines the geometry of the system, including bond lengths, bond angles and symmetries. One of the approaches which offers an access to the theoretical investigation of these properties is to find out the electronic ground state, which is determined by the Hamiltonian of the atomistic system. These methods are called *ab-initio* or *from first principles* because they are based on fundamental laws of physics without the need to use system-dependent empirical parameters. In this chapter the main scope of first-principles methods as used in this thesis will be introduced and discussed.

2.1 Introduction

The discussion of basic concepts of the *ab-initio* methods starts with the non-relativistic Schrödinger equation which determines the state of a quantum-mechanical system by an object called the wave function. The equation was postulated in 1925 by the Austrian physicist Erwin Schrödinger and its time-dependent form can be written in the following way:

$$\hat{H}\Psi(\mathbf{x}_1, \mathbf{x}_2, \ldots, \mathbf{x}_N, t) = i\hbar \frac{\partial \Psi(\mathbf{x}_1, \mathbf{x}_2, \ldots, \mathbf{x}_N, t)}{\partial t}. \tag{2.1}$$

This equation comprises the two fundamental objects describing a quantum-mechanical system. The first of them is called the Hamiltonian operator $\hat{H}$ and its eigenvalue corresponds to the total energy of the system. Hence, the operator contains terms related to the kinetic energy of all particles in a system, as well as interactions inside the system and interactions with external fields. The latter object is the wave function $\Psi(\mathbf{x}_1, \mathbf{x}_2, \ldots, \mathbf{x}_N, t)$, which describes the state of the system composed of N particles in time t. The coordinates $\mathbf{x}_i$ contain both the position and the spin component, which emerges directly from a relativistic generalization. Furthermore, other relativistic effects such as the finite speed of light must be included in case of heavy elements like gold or mercury to ensure the correct treatment of core electrons. Apart from this, the quantum-mechanical methods used in the present work suppose that Coulomb interactions are predominant while other forces are neglected. In contrary to classical mechanics, the state of a system in quantum mechanics is described by a complex multi-dimensional function Ψ instead of position and momentum vectors per each particle which are fundamental objects in classical mechanics. The Hamiltonian operator in a particular system depends on the distribution of particles which interact with each other constituting usually a many-body problem. Consequently, the analytic solution of the Schrödinger equation is only known for elemental systems like the hydrogen or He$^+$ atom, a particle in an (in)finite well or the quantum harmonic oscillator. Even if more complex quantum mechanical systems become intractable analytically and several approximations are necessary for solving the many-body problem, the aforementioned examples and their solutions are crucial for building the subsequent approximations which help to understand the properties of larger quantum systems.

The first approximation, that most of quantum-mechanical methods start with in atomistic systems, rests on the fact that protons are approximately $1800\times$ heavier than electrons. Hence, the motion of nuclei is much slower than the motion of electrons. One can therefore safely assume most of the time, that the electrons in a system adapt immediately to a change in the nucleic positions and that the motion of nuclei is governed by the effective electric field due to the electrons. In mathematical terms, the many-body wave function Ψ describing the system of i electrons and j nuclei is decomposed into the electronic wave function ψ and the wave function of nuclei χ. Omitting the spin components and the time dimension one can write this as:

$$\Psi(\mathbf{r}_1, \mathbf{r}_2, \ldots, \mathbf{r}_i, \mathbf{R}_1, \mathbf{R}_2, \ldots, \mathbf{R}_j) = \psi_{\{\mathbf{R}_1, \mathbf{R}_2, \ldots, \mathbf{R}_j\}}(\mathbf{r}_1, \mathbf{r}_2, \ldots, \mathbf{r}_i) \times \chi(\mathbf{R}_1, \mathbf{R}_2, \ldots, \mathbf{R}_j), \tag{2.2}$$

where $\mathbf{r}_i$ and $\mathbf{R}_j$ are position vectors for electrons and nuclei, respectively. $\{\mathbf{R}_k\}$ marks the set of nucleic positions that are considered to be fixed. This separation enables a

decomposition of the Hamiltonian into two decoupled systems by neglecting cross terms between electronic and nucleic motion. Many practical examples consider "frozen-in" nuclei, where the total energy of the system is determined by an electronic Hamiltonian with an external electric field emanating from a fixed distribution of positively charged nuclei. This is called the *adiabatic* or Born-Oppenheimer approximation. In practice, this approximation is used to find electronic ground states and vibrational modes, but cannot be used when non-adiabatic effects play a role. This might happen when movements of nuclei are fast or movements of electrons are slow. Typical examples when the Born-Oppenheimer approximation breaks down represent transition states in chemical reactions[37], phonon modes of graphene[38] and electron-lattice coupling effects – essential for the standard theory of superconductivity or Jahn-Teller distortions[39].

Within the adiabatic approximation, the electronic Hamiltonian $\hat{H}_e$ of an atomistic system is composed of N electrons and M nuclei at positions $\{\mathbf{R}_j\}$ with charges Z_j has the form:

$$\hat{H}_e = \underbrace{-\frac{1}{2}\sum_{i=1}^{N}\nabla_i^2}_{\hat{T}_e} + \underbrace{\sum_{i}^{N}\sum_{j>i}^{N}\frac{1}{|\mathbf{r}_i - \mathbf{r}_j|}}_{\hat{V}_{ee}} + \underbrace{\sum_{i}^{N}\sum_{j=1}^{M}\frac{Z_j}{|\mathbf{r}_i - \mathbf{R}_j|}}_{\hat{V}_{en}} \tag{2.3}$$

This equation shows that the electronic Hamiltonian includes the kinetic energy operator $\hat{T}_e$ describing the movements of electrons and two potential energy operators – $\hat{V}_{ee}$ and $\hat{V}_{en}$ standing for electron-electron and electron-nuclei interactions. Note that this equation does not contain any further physical constants such as $\hbar$ or ϵ_0, which are no longer present when switching to the use of atomic units.

In the present work the arrangement of nuclei in a system will often change in order to obtain the energetically most favorable configuration. This is possible in the framework of the Born-Oppenheimer approximation by the calculation of the electronic system separately for each nucleic arrangement. In order to compare the total energies of different arrangements, on must also add the nuclear repulsion to the total energy of the electronic system, that is described by operator $\hat{V}_{nn}$:

$$\hat{V}_{nn} = \sum_{i}^{M}\sum_{j>i}^{M}\frac{Z_i Z_j}{|\mathbf{R}_i - \mathbf{R}_j|}$$

Using the Born-Oppenheimer approximation, the Schrödinger equation is also analytically solvable for the simplest molecular system H_2^+. Despite the simplification that the Born-Oppenheimer approximation offers, more complex systems are still intractable analytically because of the electron-electron interaction $\hat{V}_{ee}$ that couples the motion (positions) of the electrons. Further approximations used in this thesis decouple the electronic system into a set of independent one-particle systems interacting via and moving in an variationally optimized average potential. The Hamiltonian for an electron that is moving in an average potential $V_{\text{avg.}}$ of an atomistic system has the following form:

$$\hat{H}_{IP} = \frac{\nabla_i^2}{2} + V_{\text{avg.}}\big(\mathbf{r}_i, \{\mathbf{R}_j\}\big). \tag{2.4}$$

The two following sections describe methods to approximate the electronic Hamiltonian containing the full electron-electron interactions by an independent-particle Hamiltonian, where each electron is treated separately and moves in an average potential as described by equation 2.4.

2.2 Hartree and Hartree-Fock equations

Both methods that are discussed in this section can be considered as variational approaches where the electronic wave function of the many-electron system $\psi(\mathbf{r}_1, \mathbf{r}_2, \ldots, \mathbf{r}_i)$ is approximated by products of one-electron wave functions. These approximations lead directly to a simplification of the full-interacting Hamiltonian (eq. 2.3) to the effective-field single-particle Hamiltonian (eq. 2.4) when neglecting correlation effects and interactions with other electrons in the system.

The Hartree method starts with an *ansatz* where the all-electron wave function is written as a product of one-electron wave functions:

$$\psi(\mathbf{r}_1, \mathbf{r}_2, \ldots, \mathbf{r}_i) = \phi_1(\mathbf{r}_1) \cdot \phi_2(\mathbf{r}_2) \cdot \ldots \ldots \cdot \phi_i(\mathbf{r}_i). \tag{2.5}$$

Consequently, the electrons are independent of each other and interact only via an average mean-field potential to be determined.

The simple treatment of the many-electron wave function has certain drawbacks that limit the usability of the Hartree method for real systems. First of all, the probability density $\rho(\mathbf{r}_1, \mathbf{r}_2, \ldots, \mathbf{r}_i)$ is just a product of one-electron densities:

$$\rho(\mathbf{r}_1, \mathbf{r}_2, \ldots, \mathbf{r}_i) = \rho_1(\mathbf{r}_1) \cdot \rho_2(\mathbf{r}_2) \cdot \ldots \ldots \cdot \rho_i(\mathbf{r}_i), \tag{2.6}$$

which means that the probability of finding an electron at a position $\mathbf{r}_i$ is independent of the probability of finding another electron at a position $\mathbf{r}_j$. However, in real systems electrons are correlated. The second problem arises from the fact that the simple Hartree product in eq. 2.5 assumes that electrons are assigned to specific orbitals. Hence, it is possible to distinguish them by an orbital they are assigned to. However, all fermions require antisymmetric wave function with respect to particle exchange for their correct description which also includes the condition that particles are indistinguishable.

To overcome these problems, the Hartree-Fock method can be employed, which correctly takes into account that N-electron wave functions ψ of N must be antisymmetric with respect to an exchange of two electrons which leaves the wave function unchanged except except for a minus sign:

$$\psi(\mathbf{r}_1, \mathbf{r}_2, \ldots, \mathbf{r}_x, \ldots, \mathbf{r}_y, \ldots, \mathbf{r}_N) = -\psi(\mathbf{r}_1, \mathbf{r}_2, \ldots, \mathbf{r}_y, \ldots, \mathbf{r}_x, \ldots, \mathbf{r}_N) \tag{2.7}$$

A straightforward way to generate an antisymmetric wave function was proposed and applied to atoms by Fock[40] in 1930. A wave function that is antisymmetric with respect to any exchange can be written in the form of a Slater determinant:

$$\psi_{\mathrm{AS}}(\mathbf{x}_1, \mathbf{x}_2, \dots) = \frac{1}{\sqrt{N!}} \begin{vmatrix} \psi_1(\mathbf{x}_1) & \psi_2(\mathbf{x}_1) & \dots & \psi_N(\mathbf{x}_1) \\ \psi_1(\mathbf{x}_2) & \psi_2(\mathbf{x}_2) & \dots & \psi_N(\mathbf{x}_2) \\ \vdots & \vdots & \ddots & \vdots \\ \psi_1(\mathbf{x}_N) & \psi_2(\mathbf{x}_N) & \dots & \psi_N(\mathbf{x}_N) \end{vmatrix} \tag{2.8}$$

Using this expression for the wave function, one can derive the Hartree-Fock equations using a variational procedure for the solution of the Schrödinger equation. Using the Dirac's bra-ket notation the total energy of the electronic system can be written as:

$$E = \frac{\langle \psi_{\mathrm{AS}} | \hat{H}_e | \psi_{\mathrm{AS}} \rangle}{\langle \psi_{\mathrm{AS}} | \psi_{\mathrm{AS}} \rangle} \tag{2.9}$$

The denominator normalizes the wave function and if all one-electron wave functions are already normalized, $\langle \psi_{\mathrm{AS}} | \psi_{\mathrm{AS}} \rangle$ becomes 1 due to the pre-factor $\sqrt{N!}$ in the Slater determinant (eq. 2.8). One also assumes that one-electron wave functions, also denoted as spin orbitals, are orthogonal and the electronic Hamiltonian $\hat{H}_e$ has the same form as in equation 2.3. By plugging the expression of the wave function 2.8 into equation 2.9, many terms cancel out due to orthogonality of the spin orbitals and one arrives at the following expression for total energy:

$$E = \langle \psi_i | \hat{H}_e | \psi_i \rangle = \underbrace{\sum_i^N \langle \psi_i | - \frac{1}{2} \nabla_i^2 | \psi_i \rangle}_{T} + \underbrace{\sum_i^N \langle \psi_i | \sum_{j=1}^M \frac{Z_j}{|\mathbf{r}_i - \mathbf{R}_j|} | \psi_i \rangle}_{V_{en}} \\ + \underbrace{\sum_{i=1}^N \sum_{j>i}^N \langle \psi_i \psi_j | \frac{1}{|\mathbf{r}_i - \mathbf{r}_j|} | \psi_i \psi_j \rangle + \sum_{i=1}^N \sum_{j>i}^N \langle \psi_i \psi_j | \frac{1}{|\mathbf{r}_i - \mathbf{r}_j|} | \psi_j \psi_i \rangle}_{V_{ee}} \tag{2.10}$$

The total energy is composed of the expectation values of the kinetic energy T, the electron-nuclei interaction V_{en} and the electron-electron Coulomb and Exchange interactions omitting correlation effects as denoted by V_{ee}. Two-electron integrals are introduced which have the form

$$\langle \psi_i \psi_j | \frac{1}{|\mathbf{r}_1 - \mathbf{r}_2|} | \psi_k \psi_l \rangle = \delta(\sigma_i, \sigma_k) \int d\mathbf{r}_1 d\mathbf{r}_2 \psi_i^*(\mathbf{r}_1) \psi_j^*(\mathbf{r}_2) \frac{1}{|\mathbf{r}_1 - \mathbf{r}_2|} \psi_k(\mathbf{r}_1) \psi_l(\mathbf{r}_2).$$

Here, $\delta(\sigma_i, \sigma_k)$ stands for the *delta* function which gives 0 if spin-orbitals ψ_i and ψ_k have opposite spins, and 1 otherwise. Equation 2.10 can also be considered as the energy functional for a wave function in the form of the Slater determinant. Hence, one may apply a variational principle to this expression and define the resulting solution as the set of one-electron wave functions $\langle \psi_k \rangle$ which yield the minimum energy value, and satisfy

the orthogonality condition on the orbitals. The problem can be solved by using Lagrange multipliers, which expresses the constraints for the desired solution as

$$\delta E - \sum_{kl} \epsilon_{kl}(\langle \delta\psi_k|\psi_l\rangle - \langle\psi_k|\delta\psi_l\rangle) = 0. \tag{2.11}$$

Using equations 2.10 and 2.11 we arrive to the expression for the Hartree-Fock equations:

$$-\frac{1}{2}\nabla_i^2\psi_i(\mathbf{r}_i) - \sum_{j=1}^{M}\frac{Z_j}{|\mathbf{r}_i - \mathbf{R}_j|}\psi_i(\mathbf{r}_i) + \sum_{j}^{N}\left[\int \frac{|\psi_j(\mathbf{r}_j)|^2}{|\mathbf{r}_i - \mathbf{r}_j|}\mathrm{d}\mathbf{r}_j\psi_i(\mathbf{r}_i) - \right.$$
$$\left. - \delta(\sigma_i,\sigma_j)\int\frac{\psi_j^*(\mathbf{r}_j)\psi_i(\mathbf{r}_j)}{|\mathbf{r}_i - \mathbf{r}_j|}\mathrm{d}\mathbf{r}_j\psi_j(\mathbf{r}_i)\right] = \epsilon_i\psi_i(\mathbf{r}_i). \tag{2.12}$$

The first three terms stand for the kinetic energy, the electron-nuclei interaction and the static Coulomb interaction, which also determine the Hartree equations. The fourth term is the same as the third, except for an exchange of the labels i,j of the one-electron wave functions ψ and a minus sign and is known as the 'exchange' interaction. Unlike the static Coulomb interaction, the exchange term is purely non-local, because the evaluation of its value at a position $\mathbf{r}_i$ depends on the values of ψ_i at all possible values of $\mathbf{r}_j$. There is no analogue in classical mechanics to the exchange interaction. Nevertheless, one can understand this term first as an electronic interaction which decreases the Coulomb interactions (repulsion) between electrons with parallel spins, and second as an interaction which creates an 'exchange hole' in the vicinity of an electron. This means that the probability of finding another electron with the same spin close to the considered one is suppressed. This is in accordance with Pauli's exclusion principle, which also originates in the antisymmetry of the wave function.

Equation 2.12 can be classified as a non-linear equation because the one-electron wave functions ψ_i are coupled via Coulomb and Exchange interactions. In practice, the one-electron wave functions are expressed in basis functions that are suitably chosen according to the considered system. Once the basis set is fixed, the solution of the Hartree-Fock equations is transformed into a matrix eigenvalue problem that is solved via a self-consistent iterative procedure. This is described in more detail in the next section.

The main advantage of the Hartree-Fock method over the Hartree approximation is the exact cancellation of the self-interaction by the exchange term in eq. 2.12. This can be illustrated by considering $\psi_j = \psi_i$, and consequently $\sigma_j = \sigma_i$. Then, the coulomb and exchange terms yield:

$$\int\frac{|\psi_i(\mathbf{r}_j)|^2}{|\mathbf{r}_i - \mathbf{r}_j|}\mathrm{d}\mathbf{r}_j\psi_i(\mathbf{r}_i) - \overbrace{\delta(\sigma_i,\sigma_i)}^{1}\int\frac{\overbrace{\psi_i^*(\mathbf{r}_j)\psi_i(\mathbf{r}_j)}^{|\psi_i(\mathbf{r}_j)|^2}}{|\mathbf{r}_i - \mathbf{r}_j|}\mathrm{d}\mathbf{r}_j\psi_i(\mathbf{r}_i) = 0 \tag{2.13}$$

While the Hartree method without a proper consideration of the self-interaction error is practically useless the Hartree-Fock method, despite the neglect of correlation effects for electrons of unlike spins yields realistic results and is commonly used in chemistry for calculations of molecular energies and geometries.

For systems where the Hartree-Fock theory yields an insufficient accuracy due the neglect of electronic correlations there are several ways how to improve the solutions. One method is based on perturbation theory which treats correlations as a small perturbation to the electronic Hamiltonian. The wave function is then expressed as a power series in artificial coefficients up to the nth order, where n is usually chosen between 2 and 4. This is called second, third and fourth order Møller–Plesset perturbation theory. The second approach is based on the expression of the many-electron wave function in terms of linear combination of Slater determinants whre each additional Slater determinant includes excited state orbitals. Since this method works with (many) different electronic configurations, it is called a Configuration interaction (CI). However, the practical use of these methods is limited by the size of the studied system due to the unfavourable computational scaling and immense computational cost for larger systems. In the next section a different way for treating the exchange and correlation effects is introduced, that requires much less computational resources.

2.3 Density Functional Theory (DFT)

DFT has become one of the most successful methods used in condensed matter physics and quantum chemistry. Due to its good performance in predicting various physical properties and aiding the interpretation of experimental results, it has evolved into a major tool in computational materials science over the last fourty years. It is frequently used nowadays in investigations of many physical properties including structural stabilities and the electronic structure of molecules and solids, atomic and molecular adsorption, molecular dynamics, STM and AFM simulations and vibrational spectra. It also serves as a basis for more advanced methods such as the Dynamical Mean-Field Theory (DMFT) for a determination of electronic structure of strongly correlated materials, the Random Phase Approximation (RPA) for an improved description of electron-electron interactions by a screened Coulomb potential, the Time-Dependent Density Functional Theory (TDDFT) which opens the door for a concise theoretical description of light-matter interactions, or the Machine Learning (ML) for studying complex datasets. In 2015, Robert O. Jones published a review on the history, development and prominence of Density Functional Theory, showing the dramatic increase of published papers related to this topic from ∼600 in 1991 to ∼16000 in 2015[41]. In 2014, twelve out of hundred most ever cited papers were related to the Density Functional Theory[42]. At the 7th and 8th place two technical papers introducing two approximate functionals – LYP[43] and B3LYP[44] are found. The two publications written by P. Hohenberg, W. Kohn and L. J. Sham[45, 46] who laid the foundation stone of the DFT ranked at the 34th and 39th place.

The success of the DFT lies in its ability to treat quantum mechanical systems quite accurately with a reasonable computational cost. For example, the scaling behaviour of DFT for a system treated by a basis set of the size M is, without any further simplifications, M^3. The Hartree-Fock method scales M^4 and post-HF methods scale up to M^7[47]. Considering its accuracy, DFT more often yields results superior to the Hartree-Fock method and is therefore widely used not only for solid but also for molecular systems.

The starting point of DFT is the aforementioned work of Hohenberg and Kohn[46] who postulated the theorem which forms the cornerstone of this method. They have shown

that the electronic ground state ψ_0 is fully determined by the electronic density ρ_0 which is defined as

$$\rho(\mathbf{r}) = \int d\mathbf{r}_2 d\mathbf{r}_3 \ldots d\mathbf{r}_N \psi^*(\mathbf{r}, \mathbf{r}_2, \ldots, \mathbf{r}_N) \psi(\mathbf{r}, \mathbf{r}_2, \ldots, \mathbf{r}_N) \tag{2.14}$$

To prove this, Hohenberg and Kohn considered the Schrödinger equation in the form

$$[\underbrace{\hat{T} + \hat{V}_{ee} + \hat{v}_{ext}}_{\hat{H}}]\psi = E\psi, \tag{2.15}$$

where the Hamiltonian $\hat{H}$ comprise the kinetic energy $\hat{T}$, electron-electron interaction $\hat{V}_{ee}$ and external potential $\hat{v}_{ext}$, which usually embraces the Coulomb repulsion between nuclei and the attraction between electrons and nuclei.

The first statement of the Hohenberg-Kohn theorem establishes a one-to-one correspondence between the external potential $\hat{v}_{ext}$ and the ground state wave function ψ_0 in the case of non-degenerate ground states. The same mapping is valid for ψ_0 and ground state density ρ_0, except for degenerate ground states. Both statements can be proved by *reductio ad absurdum*, as shown here for the second one.

Assume that ρ_0 can be generated by two different ground state wave functions ψ_0 and ϕ_0 which correspond to external potentials v_{ext} and w_{ext}, respectively. Then the Ritz principle yields two inequations for the ground state energies that correspond to wave functions ψ_0 and ϕ_0:

$$E_0 = \langle \psi_0 | \hat{T} + \hat{V}_{ee} + \hat{v}_{ext} | \psi_0 \rangle < \langle \phi_0 | \hat{T} + \hat{V}_{ee} + \hat{v}_{ext} | \phi_0 \rangle, \tag{2.16}$$

$$E_0' = \langle \phi_0 | \hat{T} + \hat{V}_{ee} + \hat{w}_{ext} | \phi_0 \rangle < \langle \psi_0 | \hat{T} + \hat{V}_{ee} + \hat{w}_{ext} | \psi_0 \rangle. \tag{2.17}$$

By addition and subtraction of $\hat{w}_{ext}$ and $\hat{v}_{ext}$ the inequations 2.16 and 2.17 read as:

$$E_0 < \underbrace{\langle \phi_0 | \hat{T} + \hat{V}_{ee} + \hat{w}_{ext} | \phi_0 \rangle}_{E_0'} - \langle \phi_0 | \hat{w}_{ext} - \hat{v}_{ext} | \phi_0 \rangle, \tag{2.18}$$

$$E_0' < \underbrace{\langle \psi_0 | \hat{T} + \hat{V}_{ee} + \hat{v}_{ext} | \psi_0 \rangle}_{E_0} - \langle \psi_0 | \hat{v}_{ext} - \hat{w}_{ext} | \psi_0 \rangle. \tag{2.19}$$

Now, considering the multiplicative character of $\hat{v}_{ext}$ and $\hat{w}_{ext}$ and the presumption that the ground state wave functions ψ_0 and ϕ_0 yield the same ground state density ρ_0, one can rewrite both inequations in an integral form:

$$E_0 < E_0' - \int d\mathbf{r} \left[w_{ext}(\mathbf{r}) - v_{ext}(\mathbf{r}) \right] \underbrace{\int d\mathbf{r}_2 \ldots d\mathbf{r}_N \phi_0^*(\mathbf{r}, \mathbf{r}_2, \ldots, \mathbf{r}_N) \phi_0(\mathbf{r}, \mathbf{r}_2, \ldots, \mathbf{r}_N)}_{\rho_0(\mathbf{r})}, \tag{2.20}$$

$$E_0' < E_0 - \int d\mathbf{r} \left[v_{ext}(\mathbf{r}) - w_{ext}(\mathbf{r}) \right] \underbrace{\int d\mathbf{r}_2 \ldots d\mathbf{r}_N \psi_0^*(\mathbf{r}, \mathbf{r}_2, \ldots, \mathbf{r}_N) \psi_0(\mathbf{r}, \mathbf{r}_2, \ldots, \mathbf{r}_N)}_{\rho_0(\mathbf{r})}. \tag{2.21}$$

Finally, adding inequations 2.20 and 2.21 yields

$$E_0 + E_0' < E_0' + E_0, \tag{2.22}$$

which is a contradiction. Therefore, the one-to-one correspondence between the ground state density ρ_0 and ground state wave function ψ_0 has been proven. This implicates that the external potential, the ground state wave function and the ground state density uniquely determine each other. As a consequence, if one can assume that the ground state wave function is a unique functional of the ground state density, then the same is true for any observable of the ground state. An especially important quantity of Density Functional Theory (DFT) is the total energy E which can be written as a functional of ρ:

$$
\begin{aligned}
E[\rho] &= \langle \psi[\rho] | \hat{H} | \psi[\rho] \rangle = F[\rho] + \int \mathrm{d}\mathbf{r} \rho(\mathbf{r}) v_{ext}(\mathbf{r}), \\
F[\rho] &= \langle \psi[\rho] | \hat{T} + \hat{V}_{ee} | \psi[\rho] \rangle
\end{aligned}
\tag{2.23}
$$

Another consequence of the aforementioned mapping between the ground state wave function and ground state density is the possibility to apply the Ritz variational principle to the total energy functional of the electron density. In other words the ground state energy is the minimum value of all possible energies that originate from permissible electronic densities ρ. Consequentially, the electronic density that yields the minimum energy is the ground state density. In practice, the ground state density is fully determined by the functional $F[\rho]$ in eq. 2.23 which does not depend on the external potential v_{ext} and thus is universal.

Similar to the Hartree-Fock method the DFT ground state density and the ground state energy is determined variationally. In DFT the constraint to the ground state density is the number of electrons contained in the ground state density. Using again Lagrange multipliers, a variation of the energy functional under the constraint of keeping the number N of electrons fixed yields

$$
\frac{\delta}{\delta \rho(\mathbf{r})} \left\{ E[\rho(\mathbf{r})] - \mu \left(\int \mathrm{d}\mathbf{r} \rho(\mathbf{r}) - N \right) \right\} = 0.
\tag{2.24}
$$

As mentioned above, the proof of the Hohenberg-Kohn theorem is only valid for non degenerate ground states. For degenerate ground states one can prove the existence of a mapping between an external potential v_{ext}, and a class of ground state wave functions respectively a class of ground state densities, which are disjoint for different v_{ext}. The variational principle is therefore still valid, only with a difference that more solutions exist for the electronic density $\rho(\mathbf{r})$ from equation 2.24.

The Hohenberg-Kohn theorem proves the existence of a density functional for the total energy, but it does not show the way how to derive its specific expression. Hence, exact expression for the functional of $E[\rho(\mathbf{r})]$ is unknown and for practical applications must be approximated by physical reasoning.

2.3.1 Kohn-Sham Scheme

In 1965, Kohn and Sham[45] suggested the mapping of the many-body system defined by the wave function ψ_e, or – according to the HK theorem, by the ground state density ρ_0, onto an independent-particle system described by a non-interacting one-electron Hamitonian like in eq. 2.4, which yields the same ground state density ρ_0. According to the HK-theorem, the system is fully determined by the electronic ground state density and

therefore both approaches are equal. Thus, the Kohn-Sham scheme replaces the intractable many-body system by an auxiliary non-interacting one-electron system with the kinetic energy operator $\hat{T}$ and a local effective potential $V_{\text{eff}}(\mathbf{r})$. The construction of the effective potential is done by comparing to the interactions in the full interacting system in the following way. The many-body ground state energy reads:

$$E_{\text{MB}}[\rho] = T[\rho] + E_{en}[\rho] + E_{ee}[\rho]. \tag{2.25}$$

The contribution from the electron-nuclei interactions $E_{en}[\rho]$ can be expressed exactly in terms of one-electron densities. The kinetic energy term is decomposed into the kinetic energy of non-interacting particles $T_n[n]$ and a residue due to correlation effects $T_c[n]$:

$$T[\rho] = T_n[\rho] + T_c[\rho]. \tag{2.26}$$

Subsequently, the electron-electron interaction $E_{ee}[\rho]$ is decomposed into the static Coulomb or Hartree-term and a residue that contains exchange and correlation effects:

$$E_{ee}[\rho] = E_H[\rho] + E_{xc}[\rho]. \tag{2.27}$$

By putting both parts together one gets

$$E_{\text{MB}}[\rho] = T_n[\rho] + E_{en}[\rho] + E_H[\rho] + \underbrace{E_{xc}[\rho]}_{E_{xc}[\rho]+T_c[\rho]}. \tag{2.28}$$

Here an exchange-correlation functional $E_{xc}[\rho]$ is introduced, which contains all the non-local exchange and correlation effects. Considering the kinetic energy of the non-interacting electrons $T_n[\rho]$, an expression in terms of the electron density is still unknown. In the Kohn-Sham scheme it is therefore evaluated in terms of the auxiliary one-electron wave functions. Note that this step is not mandatory and there exist several attempts to construct an orbital-free DFT [48, 49] where the kinetic part is calculated directly from the electron density. In the Kohn-Sham scheme, $T_n[\rho]$ has the form

$$T_n[\rho] = \sum_i^N \left\langle \psi_i[\rho] \left| -\frac{\nabla^2}{2} \right| \psi_i[\rho] \right\rangle. \tag{2.29}$$

After this step, the mapping onto the non-interacting auxiliary system is complete, because all terms of the many-body energy functional are expressed by non-interacting wave functions and the electronic density. Putting equations 2.28 and 2.29 into 2.24 yields the so-called Kohn-Sham equations:

$$\left\{ -\frac{1}{2}\nabla^2 + \sum_j^M \frac{Z_j}{|\mathbf{R}_j - \mathbf{r}|} + \int d\mathbf{r}' \frac{\rho(\mathbf{r}')}{|\mathbf{r} - \mathbf{r}'|} + \frac{\delta E_{xc}}{\delta \rho(\mathbf{r})} \right\} \psi_i = \epsilon_i \psi_i. \tag{2.30}$$

Here, the electron density $\rho(\mathbf{r})$ is written as the sum of the one-electron densities as determined from the auxiliary Kohn-Sham one-electron wave functions:

$$\rho(\mathbf{r}) = \sum_i^N |\psi_i(\mathbf{r})|^2 \tag{2.31}$$

The first three terms in equation 2.30 on the left side correspond to the kinetic energy, the electron-nuclear atttraction and the static electron-electron interaction, just as in the Hartree approximation. The last term contains all the exchange and correlation interactions which involve not only the electronic exchange and correlation contributions, but also the correlation contribution to the kinetic energy.

The Kohn-Sham equations are coupled together via the electron density ρ. In order to solve them, one-electron wave functions are expressed in a finite basis set, which transforms the problem of solving the set of coupled differential equations into finding matrix eigenvalues. The following self-consistent iterative procedure is used:

Figure 2.1 displays the procedure of the self-consistent iterative method for solving the Kohn-Sham equations. As mentioned in the previous section, a similar approach is used to solve the Hartree-Fock equations. Comparing both methods, the Hartree-Fock approximation searches for the ground state of a many-body wave function in terms of Slater determinants, whereas the Kohn-Sham scheme uses one-electron wave functions to represent the electronic ground state density and subsequently the ground state energy and other properties of the system. Unlike the Kohn-Sham scheme, the Hartree-Fock equations are non-local due to the exchange term.

In order to solve the Kohn-Sham equations 2.30 one needs a specific representation of the exchange-correlation functional $E_{xc}[\rho]$. The exact form of this term is unknown, but there have been huge efforts to find proper approximate functionals that would be transferable between many different atomistic systems. Thus, discussing the main outline of the history and recent development of the exchange-correlation functionals is appropriate.

2.3.2 Exchange and correlation functionals

The exchange-correlation functional encompasses the differences between the kinetic energies of non-interacting electrons and fully interacting system, and the difference between the exact dynamic Coulomb and the static Hartree interaction. The basic idea behind a construction of the exchange-correlation term is to find an expression only in terms of the electron density, including the correlation contribution to be added to the kinetic energy calculated from the Kohn-Sham orbitals. Such a procedure is feasible via the *adiabatic connection* as briefly discussed in the following.

The Kohn-Sham picture can be connected to the exact Schrödinger equation via a tunable electron-electron interaction with an interaction strength λ:

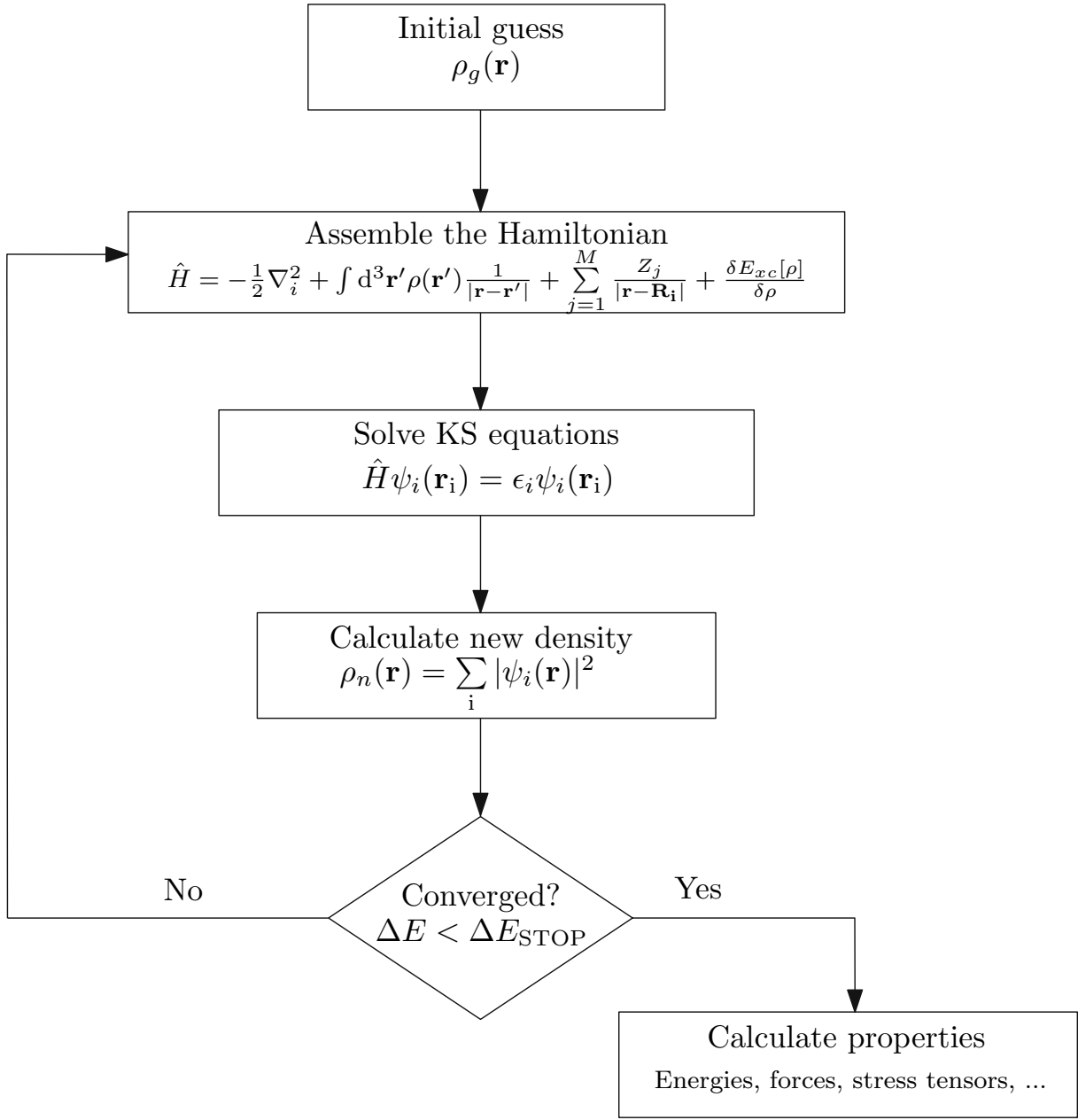$$V_{ee,\lambda} = \sum_{i=1}^N \sum_{j>i}^N \frac{\lambda}{|\mathbf{r}_i - \mathbf{r}_j|} \tag{2.32}$$

Fig. 2.1: A scheme of the self-consistent DFT cycle. At the beginning a trial electronic density ρ_g is assumed to build the Hamiltonian. The Kohn-Sham equations are subsequently solved and another electronic density ρ_n is evaluated from resulting one-electron wave functions. The convergence criterion is usually defined as the total energy difference between the last two cycles. When it is fulfilled, the one-electron wave functions are used to calculate ground state properties of the system.

For $\lambda = 0$, this term vanishes, whereas $\lambda = 1$ represents the standard Coulomb interaction. Now one can define the exchange-correlation functional with help of $V_{ee,\lambda}$:

$$E_{xc}[\rho] = \underbrace{(E_{ee}[\rho] + T[\rho])}_{F_{\lambda=1}[\rho]} - \underbrace{T_n[\rho]}_{F_{\lambda=0}[\rho]} - E_H[\rho], \tag{2.33}$$

where $F_\lambda[\rho]$ are functionals containing the kinetic energy and the tunable electron-electron interaction at a fixed density ρ. Now one can express the F functional of the full-interacting system with help of the non-interacting system using the Hellmann-Feynman theorem[50]:

$$F_{\lambda=1} = F_{\lambda=0} + \int_0^1 \frac{\mathrm{d}F_\lambda}{\mathrm{d}\lambda}\mathrm{d}\lambda = T_n[\rho] + \int_0^1 \langle\psi_\lambda|V_{ee}|\psi_\lambda\rangle \tag{2.34}$$

The derivative of F_λ with respect to the tuning parameter λ nullifies the kinetic energy term does not dependend on λ. Plugging equation 2.34 into 2.33 leads to a cancellation of the kinetic energy terms and one gets the following expression for the exchange-correlation energy:

$$E_{xc} = \int_0^1 \mathrm{d}\lambda \, \langle\psi_\lambda|V_{ee}|\psi_\lambda\rangle - E_H[\rho]. \tag{2.35}$$

The price to be paid for the removal of the kinetic energy terms is the evaluation of the integral for all values of the interaction parameter λ between 0 and 1. However, a big advantage of the *adiabatic connection* is a certain insight into the properties of the exchange-correlation functional. Because the kinetic energy term has been replaced, equation 2.35 can be rewritten in terms of the *exchange-correlation hole* density ρ_{xc}, which can be defined as a deviation from the average electron density at $\mathbf{r}$ due to the presence of another electron at $\mathbf{r}'$. The exchange-correlation term is then expressed in the following way:

$$E_{xc} = \int \mathrm{d}\mathbf{r}\mathrm{d}\mathbf{r}'\frac{\rho(\mathbf{r})\rho_{xc}(\mathbf{r},\mathbf{r}')}{|\mathbf{r}-\mathbf{r}'|}. \tag{2.36}$$

This expression allows to formulate several constraints to E_{xc} and ρ_{xc}, which an exact expression fulfils and which have to be considered in a construction of approximated forms. One of the constraints is the summation rule of the exchange-correlation hole density that can be expressed as

$$\int \mathrm{d}\mathbf{r}'\rho_{xc}(\mathbf{r},\mathbf{r}') = -1. \tag{2.37}$$

This constraint arises from the electron-electron repulsion, which reduces the probability of finding an electron in the vicinity of another one. Thus, the *exchange-correlation hole* is a region of space near an electron where other electrons can be hardly found. In the following paragraphs the most successful ways providing widely used approximations for the exchange-energy functional will be given.

Local [Spin] Density Approximation (L[S]DA)

The most simple, but still very successful approximation of the exchange-correlation functional originates in the Homogeneous Electron Gas (HEG) model, for which an exact analytic expression of the exchange term is known. In this approximation, the exchange-correlation interaction is expressed in terms of a local exchange-correlation energy density that is integrated over the whole space. The L[S]DA approximation leads to an exchange-correlation term that is only a function of the electron density, by evaluating the local exchange-correlation energy density from the expressions for the HEG at the local density

at each point in space. For open-shell systems, the spin-up and spin-down densities are treated separately as given by the expression of the exchange-correlation energy as

$$E_{xc}^{\text{LSDA}} = \int d\mathbf{r}\epsilon_{xc}[\rho_\uparrow(\mathbf{r}), \rho_\downarrow(\mathbf{r})]\rho(\mathbf{r}) \tag{2.38}$$

The expression for the exchange-correlation energy is split into an exchange and a correlation part. This allows to use an analytic expression for the exchange as obtained from the HEG[51]:

$$E_x^{\text{LSDA}} = -\frac{3}{2}\left(\frac{3}{4\pi}\right)^{\frac{1}{3}} \int d\mathbf{r}\left[\rho_\uparrow^{\frac{4}{3}}(\mathbf{r}) + \rho_\downarrow^{\frac{4}{3}}(\mathbf{r})\right] \tag{2.39}$$

This expression shows that the exchange interaction is, as expected from the Hartree-Fock theory, counting only interactions between parallel spin pairs, as there is no coupling between the electronic spin-up and spin-down densities. The correlation term that includes the remaining electron-electron interactions is not known analytically and thus approximations based on accurate quantum Monte Carlo simulations[52] of the HEG at several values of the electronic density have been proposed. The most common parametrizations derived from these data are known as VWN[53], PZ81[54] and PW92[55] LSDA functionals.

L[S]DA was the first successful application of DFT and the Kohn-Sham scheme for the characterization of electronic and structural properties of many different solid systems. The accuracy of the L[S]DA functionals depends on the system in consideration. Since they originate in the expressions of the exchange-correlation energies for the HEG, one can generally say that the more the electron density approaches a uniform distribution over all space, the more accurate LDA is. Surprisingly, LDA also works well for many inhomogeneous systems. This is due on the one hand to the accurate quantum Monte Carlo results ensuring that the sum rules for the exchange-correlation hole are satisfied to a large degree, and on the other to a well known cancellation of errors between the exchange and correlation energy contributions[47]. But LDA also suffers from shortcomings such as an overestimation of binding energies and an underestimation of bond lengths and electronic band gaps[56]. Thus, many inhomogeneous systems require corrections to the local approximations for exchange and correlation energy. A systematic improvement including such corrections consists considers gradients of the electron density in the expression of the exchange-correlation functional.

Generalized Gradient Approximation (GGA)

To overcome the shortcomings of the LDA, the expression for the exchange-correlation energy is augmented by gradients of the electron density leading to the Generalized Gradient Approximation (GGA) in the following way:

$$E_{xc}^{\text{GGA}} = \int d\mathbf{r}\epsilon_{xc}[\rho_\uparrow(\mathbf{r}), \rho_\downarrow(\mathbf{r}), \nabla\rho_\uparrow(\mathbf{r}), \nabla\rho_\downarrow(\mathbf{r})]\rho(\mathbf{r}) \tag{2.40}$$

Since the LDA method has been established, many generalized gradient functionals satisfying the normalization condition (sum rule) for the exchange-correlation hole have been developed. Some of the best-known examples of GGA functionals were developed by Perdew and Wang – PW86 [57, 58] and PW91 [59]; Lee, Yand and Paar – LYP [43];

Perdew, Burke, Ernzerhof – PBE[60] and its revised versions[61, 62], including PBEsol [63] for an improved description of bulk systems.

The inclusion of electronic gradients in the exchange-correlation functional generally leads to an improved description of properties that are also reasonably well captured by LDA. A considerable improvement has been found for atomization energies [56, 64–66], binding energies and structural properties such as bond lengths and angles [51]. The success of the GGA functionals lies also in a better description of exchange and correlation energies. Even though the GGA total exchange-correlation energy is not generally superior to the LDA due to cancellation of errors, GGA functionals offer a more realistic behaviour of the individual parts. Due to its overall improvements the GGA functionals have become a very popular and widely used choice, but do not always yield better results than LDA due to a non-systematic error cancellation in exchange and correlation energy which is sometimes more effective in LDA.

Generally, the GGA functionals still suffer from a poor description of ionization energies which is related to an insufficient compensation of the self-interaction contained in the Hartree energy. As a consequence, electronic properties of unoccupied states, including the size of the HOMO-LUMO gap might not be sufficiently well described and more advanced methods are necessary for these purposes.

Meta-generalized gradient approximation

A reasonable extension of the gradient corrections is a consideration of second-order derivatives of the electronic density. Such functionals are classified as meta-GGA functionals. In this work the recently developed Strongly Constrained and Appropriately Normed (SCAN) functional [67] developed by Sun, Ruszinsky and Perdew will be considered which is the first functional that respects all 17 known constraints for proper meta-GGA functionals. This functional introduces the kinetic energy density τ as an additional parameter

$$\tau_{\{\uparrow,\downarrow\}} = \frac{1}{2} \sum_{i}^{\text{occ.}} |\nabla \psi_{i,\{\uparrow,\downarrow\}}(\mathbf{r})|^2, \tag{2.41}$$

in the expression of the exchange-correlation energy (eq. 2.40). The arrows $(\uparrow, \downarrow)$ tag the spin-up and spin-down kinetic energy densities, calculated from the one-electron Kohn-Sham orbitals $\psi_i(\mathbf{r})$. Considering the performance of the SCAN functional, it generally further improves properties that are not treated sufficiently well in GGA, such as electronic band gaps, lattice constants and bulk moduli[68]. The SCAN functional also improves the energetics in a certain sense: unlike LDA and GGA, it does not overbind the O_2 molecule and describes the O_2 bond dissociation energy[69] well. On the other hand, a careful assessment is necessary as, for example, the SCAN functional tends to overestimate formation enthalpies of binary TMOs[69] and excessively favours localized spin-polarized states, which leads to an incorrect prediction of the symmetry-broken ground state of 2D graphene [70] or a wrong description of the stability of Fe phases[71].

Hybrid functionals

As already mentioned before, the Hartree-Fock method delivers an exact exchange contribution, but correlation effects are completely neglected. The idea behind the construction of the so-called hybrid functionals is to calculate the exchange contribution with the help of the Hartree-Fock method. Note, that it is also possible to incorporate the Hartree-Fock exchange into the Kohn-Sham picture by using auxiliary one-electron wave functions via the so called optimized potential method [72, 73] and once the energy evaluated, its value is combined with a DFT functional. Since in a hybrid functional the DFT exchange is replaced by the Hartree-Fock exchange, the basic formula proposed by Becke [74] for the total energy reads:

$$E_{xc}^{\text{hyb.}} = E_{xc}^{\text{DFT}} + a_0(E_x^{\text{HF}} - E_x^{\text{DFT}}), \tag{2.42}$$

where the parameter a_0 was adjusted to fit atomization energies. Another way for determining this parameter was proposed by Perdew, Burke and Ernzerhof[75] who suggested to rewrite the expression for the total energy to depend on a coupling constant in an adiabatic connection fashion (eq. 2.35):

$$E_{xc,\lambda}^{\text{hyb.}}(n) = E_{xc,\lambda}^{\text{DFT}} + (E_x^{\text{HF}} - E_x^{\text{DFT}})(1 - \lambda)^{n-1}, \tag{2.43}$$

where n is a parameter to be determined. The form of this expression becomes clear when plugged into the adiabatic connection formula

$$E_{xc}^{\text{hyb.}} = \int_0^1 \mathrm{d}\lambda E_{xc,\lambda}^{\text{hyb.}}(n) = E_{xc}^{\text{DFT}} + \frac{1}{n}(E_x^{\text{HF}} - E_x^{\text{DFT}}), \tag{2.44}$$

which reproduces the previous expression (eq. 2.42) proposed by Becke. Now the n parameter can be determined with the help of perturbation theory in such a way that $E_{xc,\lambda}^{\text{hyb.}}$ matches $E_{xc,\lambda}^{\text{DFT}}$ in value, slope and the second derivative at $\lambda = 1$[75], which happens for $n = 4$ and $a_0 = 0.25$. This parameter is used for the PBE0 functional, which mixes the Hartree-Fock contribution with the PBE GGA functional. The main drawback of the hybrid functionals is the computational cost due to evaluation of two-electron integrals. This was improved by Heyd, Scuseria and Ernzerhof [76] who split the Coulomb interaction into long-range (LR) and short-range (SR) components

$$\frac{1}{r} = \underbrace{\frac{1 - erf(\omega r)}{r}}_{\text{SR}} + \underbrace{\frac{erf(\omega r)}{r}}_{\text{LR}} \tag{2.45}$$

and showed that the long-range contributions for the exchange energy are rather small and tend to cancel out with the corresponding exchange contribution from the PBE functional. In equation 2.45, $erf(x)$ is the gaussian error function and ω represents a tuneable screening parameter. The resulting HSE03 functional reads

$$E_{xc}^{\text{HSE}} = 0.25E_x^{\text{HF,SR}}(\omega) + 0.75E_x^{\text{PBE,SR}}(\omega) + E_x^{\text{PBE,LR}}(\omega) + E_c^{\text{PBE}}. \tag{2.46}$$

The original value of ω was subsequently revised by Krukau et al.[77], leading to the HSE06 functional with $\omega = 0.11a_0^{-1}$ that has also been used in this work.

The big success of the hybrid functionals lies in a better description of the band gap values for semiconducting materials as well as other ground state properties such as lattice constants[78]. It also offers a reasonable treatment of small molecules.

Van der Waals functionals

The standard Density Functional Theory fails to correctly describe long-range, non-local interactions such as van der Waals (vdW) forces. This is due to the local or semi-local character of the exchange-correlation functionals which tend to underestimate the strength of weakly bound systems. However, some layered materials, where van der Waals interactions play an important role – such as graphene, hexagonal boro-nitride or transition metal dichalcogenides – are of profound scientific interest due to their potential technical applications in novel technologies[79–82]. Furthermore, van der Waals contributions were also found to be important in adsorption studies of both organic and inorganic molecules for catalysis[83, 84].

Van der Waals corrections may be incorporated in DFT as a non-local term in several ways. Grimme et al.[85] introduced so called DFT–D3 dispersion corrections added to the Kohn-Sham energy. In this method the correction terms for the energies and forces are both obtained from system-dependent informations, such as cartesian coordinates and atomic numbers, and from ab-initio pre-calculated atomic dispersion coefficients and cutoff radii. The great advantage of this method is its applicability not only within the DFT framework, but also in semi-empirical and force-field methods.

Another approach proposed by Dion et al.[86] considered the van der Waals corrections as an additional non-local term to the correlation energy E_c^{nl} which enters the Kohn-Sham self-consistent cycle:

$$E_{xc} = E_{xc}^{\mathrm{DFT}} + E_c^{nl}. \tag{2.47}$$

Vydrov and Van Voorhis[87] came up with an expression for the additional term that was subsequently revised by Sabatini et al. for an efficient evaluation in a plane wave framework[88]. The expression can be written as

$$E_c^{nl} = \int \mathrm{d}\mathbf{r}\rho \left[\frac{\hbar}{2} \int \mathrm{d}\mathbf{r}'\rho' \Phi\big(\mathbf{r}, \mathbf{r}', \rho, \rho', |\nabla\rho|, |\nabla\rho'|\big) + \beta \right]. \tag{2.48}$$

In this expression $\rho(\mathbf{r})$ is the electron density, $\Phi(\mathbf{r}, \mathbf{r}')$ denotes the kernel which describes the density-density interactions and β is a parameter that ensures a zero value for the resulting E_c^{nl} term for the uniform electron gas. The van der Waals kernel contains two parameters that are defined empirically. The first one, denoted as C, is related to the correct long-range interactions between molecules to resemble a $-C_6/R^6$ behavior, resulting in a value of $C = 0.0093$. The second one, tagged as b is related to the damping of the E_c^{nl} term for small $|\mathbf{r} - \mathbf{r}'|$ values. This parameter was determined as $b = 15.7$ in the work of Peng et al.[89] for the meta-GGA SCAN functional. As a side note, the damping factor is noticeably larger than for the original rVV10 functional that started from PW86 exchange and (GGA) PBE functionals, where $b = 6.3$. This indicates that the SCAN functional, which takes the kinetic energy density as an additional input, can also partially

capture intermediate-range van der Waals interactions. In this thesis the SCAN functional with van der Waals corrections proposed by Sabatini et al. is marked as SCAN+rVV.

2.3.3 DFT+U

In real materials, DFT often faces the challenging problem to properly describe at the same time highly delocalized electrons whose electron density is similar to uniform electron gas, and strongly localized electrons, such as *d-* or *f-* states, that rather keep their atomic-like character and might therefore strongly influence each other due to electron-electron repulsion. Hence, standard DFT functionals may fail to describe systems where valence electrons are localized in these shells. This is primarily caused by two effects. First, according to the *aufbau principle*, *d-* and *f-* electrons are not screened by *s-* or *p-* orbitals from higher shells and therefore are pulled towards the core by the attractive Coulomb interaction. Second, the effect of localization effect is strong for *3d* and *4f* orbitals because the radial parts of these wave functions are nodeless. Thus, a major part of the electron density is localized in the vicinity of nuclei. As a result, standard DFT theory often predicts[90] a metallic character for such materials that are experimentally found to be insulators, as is the for compounds such as Transition Metal Oxides with partially filled *d*-shells.

The different behaviour of localized and delocalized states suggests to treat them differently. The DFT+U approach is one of the simplest models that tries to capture the physics of the localized states by considering orbital-dependent Coulomb interactions. The starting point for the description of such interactions is the Hubbard model[91]:

$$H = t \sum_{<i,j>,\sigma} (c_{i,\sigma}^{\dagger} c_{j,\sigma} + h.c.) + U \sum_i n_{i,\downarrow} n_{i,\uparrow}. \tag{2.49}$$

t denotes a term that describes the hopping amplitude of particles between neighbouring sites $<i,j>$ and also represents the single-particle contribution to the total energy, $c_{i,\sigma}^{\dagger}$ and $c_{j,\sigma}$ are creation and annihilation operators which create (annihilate) a particle with a spin σ on site i (j). The $n_{i,\sigma}$ stands for a number operator which counts the number of particles with spin σ on site i. As outlined above, the Hubbard model is composed of two terms, where first one describes the hopping between neighbouring sites and the second one denotes a Coulomb interaction with strength U between electrons that occupy the same site. This follows the assumption that electrons are localized and the repulsive interaction between electrons occupying different sites is negligible. In this picture, two limiting cases can occur: first, if $t >> U$, the electrons can freely move between the sites and usually this case is well captured within the standard DFT theory and second, if $U >> t$, the electrons do not have enough energy to overcome the repulsive on-site interaction and the system becomes insulating even when the *d-* shell is half-filled.

Now, DFT+U treats the localized electrons within the Hubbard model while the remaining electrons are treated by the chosen DFT functional. Hence, the total energy in the DFT+U method can be written as

$$E^{\mathrm{DFT+U}}[\rho(\mathbf{r}), \{n_{i,\sigma}\}] = E^{\mathrm{DFT}}[\rho(\mathbf{r})] + E^{\mathrm{U}}[\{n_{i,\sigma}\}] - E^{\mathrm{DC}}[\{n_{i,\sigma}\}], \tag{2.50}$$

where $\{n_{i,\sigma}\}$ represents occupations of local sites expressed in a localized basis, E^{U} is the energy due to the Hubbard Hamiltonian and E^{DC} marks a correction term to avoid a double counting of the energy that is already taken into account by the DFT functional. This double-counting term, however, is not uniquely defined and several expressions have been developed.

In this work Dudarev's implementation[92] will be used, that is invariant with respect to the rotation of the atomic orbital basis set. The final expression for the DFT+U energy in Dudarev's approach reads:

$$E^{\mathrm{DFT+U}} = E^{\mathrm{DFT}} + \frac{U-J}{2} \sum_\sigma \left[\left(\sum_m \hat{n}^\sigma_{m,m} \right) - \left(\sum_m \sum_{m'} \hat{n}^\sigma_{m,m'} \hat{n}^\sigma_{m',m} \right) \right], \qquad (2.51)$$

where an on-site occupancy matrix $\hat{n}^\sigma_{m,m'}$ has been introduced. The J parameter stands for the exchange interaction and proceeds from the double-counting correction but only the difference $U-J$ is considered in practice. The second term in equation 2.51 can be considered as an energy penalty to the DFT energy since the term $U-J$ is positive in practice. This penalty is lowest when $\hat{n}^\sigma = \hat{n}^\sigma \hat{n}^\sigma$, which is the case for either fully occupied or completely unoccupied energy levels. Hence, unlike standard DFT functionals and in agreement with the Hubbard model, DFT+U tends to localize electrons on specific sites and thus facilitates the formation of an electronic gap between occupied and unoccupied states.

2.4 *Ab-initio* Thermodynamics

Density Functional Theory as a ground-state theory is a zero-temperature concept while many real applications such as heterogeneous catalysis and related physical processes like adsorption, diffusion or dissociation take place at finite temperatures and pressures both of which need to be considered to describe the experimental evidence. Therefore, finite temperature and pressure effects must be included in a comparison of DFT results with real experiments. In this section, the work of Reuter and Scheffler [93, 94] will be followed who employed an *ab-initio*, atomistic thermodynamic model to construct a phase diagram of surface structures of RuO_2 as function of temperature and pressure. However, this procedure is rather universal and their approach can be used not only for different surface systems, but also for a propere description of the formation of defects such as oxygen vacancies.

The relevant property to be evaluated in a theoretical description of physical processes performed at a finite pressure is the Gibbs free energy $G(T, p, \{N\})$ of the respective reaction. Considering one topic of this thesis, an evaluation of the stability of vanadium dioxide surface reconstructions, the most stable surface shows the lowest surface free energy γ at a given temperature and pressure. The free energy γ is defined as:

$$\gamma = \frac{1}{S} \left[G(T, p, N_V, N_O) - N_V \cdot \mu_V(T, p) - N_O \cdot \mu_O(T, p) \right] \qquad (2.52)$$

Usually, bulk vanadium dioxide acts as a reservoir instead of metallic vanadium which creates a constraint between the chemical potentials of V and O:

$$\mu_V(T,p) + 2\mu_O(T,p) = g_{VO_2}(T,p), \tag{2.53}$$

where $g_{VO_2}(T,p)$ is the Gibbs free energy per VO$_2$ unit. The oxygen chemical potential is usually constrained via molecular oxygen as used in experiments. Thus, the formula for the evaluation of the surface free energy reads

$$\gamma = \frac{1}{S}\Big[G(T,p,N_V,N_O) - N_V \cdot g_{VO_2}(T,p) + (2N_V - N_O)\frac{1}{2}\mu_{O_2}(T,p)\Big]. \tag{2.54}$$

The values of the oxygen chemical potential are limited by reduction and oxidation processes of the bulk. This sets the boundary limits to the oxygen chemical potential which is relevant for comparison with experiments.

Since DFT calculations are performed for a certain volume V of the unit cell, the calculated total energies correspond to the Helmholtz free energy $F(T,p,N_V,N_O)$ at zero temperature completely neglecting the vibrational energy. To link the desired Gibbs free energy to the value obtained from the DFT calculations one writes

$$G(T,p,N_V,N_O) = \underbrace{E^{\mathrm{DFT}} + F^{\mathrm{vib}}(T,p,N_V,N_O)}_{F(T,p,N_V,N_O)} + pV(T,p,N_V,N_O), \tag{2.55}$$

where $F^{\mathrm{vib}}(T,p,N_V,N_O)$ includes the vibrational and entropy contributions to the Helmholtz free energy. The influence of this term on the resulting Gibbs free energy depends on the temperature and hence on the experimental conditions. At room temperature the size of its contribution is comparable to the errors introduced by DFT itself. Even though an approximate value of the vibrational contribution can be extracted with the help of a frequency analysis, this contribution is supposed to be rather small and will be therefore neglected in this work. The last term in equation 2.55 is significant only at high pressures[94] and is omitted as well. Using these approximations, the resulting expression for the surface free energy yields

$$\gamma = \frac{1}{S}\Big[E_{\mathrm{Slab}}^{\mathrm{DFT}} - N_V \cdot E_{\mathrm{Bulk,\ VO_2}}^{\mathrm{DFT}} + (2N_V - N_O)\frac{1}{2}\mu_{O_2}(T,p)\Big], \tag{2.56}$$

where N_V and N_O denote the number of vanadium and oxygen atoms that comprise the considered system. The temperature dependence of the oxygen chemical potential can be extracted from thermochemical tables while the dependence on pressure is derived from the ideal gas equation of state.

2.5 Wannier functions

The one-electron wave functions that enter the Kohn-Shan self-consistent cycle (Figure 2.1) are in practice expressed in a certain basis set that is chosen according to the considered atomistic system. For periodic systems Bloch's theorem is usually applied[95], which states that the solution of the Schrödinger equation in a periodic system takes the form of a

function that is periodic over the crystal lattice, modulated by a plane wave. This can be mathematically written as

$$\psi_{n,\mathbf{k}}(\mathbf{r}) = e^{i\mathbf{k}\cdot\mathbf{r}} \cdot u_{n,\mathbf{k}}(\mathbf{r}), \tag{2.57}$$

where the function $u(\mathbf{r})$ is unchanged when the position vector $\mathbf{r}$ is translated by a lattice vector $\mathbf{R}$:

$$u_{n,\mathbf{k}}(\mathbf{r}) = u_{n,\mathbf{k}}(\mathbf{r} + \mathbf{R}). \tag{2.58}$$

However, such basis is not convenient for an exploration of physical processes such as chemical bonding, on-site interactions and polarization due to its delocalized character. As pointed out by Wannier[96], there is an alternative representation of the one-electron functions that is orthogonal, periodic over the unit cell and spatially localized – Wannier functions. A Wannier function $w_{n,\mathbf{R}}(\mathbf{r})$ that is localized in space and centered on lattice site $\mathbf{R}$ can be obtained from the Bloch states in the following way[97]:

$$w_{n,\mathbf{R}} = \frac{V}{2\pi^3} \int\limits_{BZ} d\mathbf{k} \left[\sum_m \mathbf{U}_{mn}^{(\mathbf{k})} \psi_{m,\mathbf{k}}(\mathbf{r}) \right] e^{-i\mathbf{k}\cdot\mathbf{R}}. \tag{2.59}$$

This equation has the form of an inverse Fourier transform which keeps both the lattice periodicity of the Wannier functions and their mutual orthogonality. In contrast to the delocalized Bloch wave functions, Wannier functions are more localized spatially, depending on the chosen unitary matrix $\mathbf{U}_{mn}^{(\mathbf{k})}$ that mixes the Bloch states at each $\mathbf{k}$. There is certain freedom in choosing this matrix and therefore one usually seeks for a transformation that yields maximally-localized Wannier functions.

In this thesis the method of Marzari and Vanderbilt[98] will be used for obtaining maximally-localized Wannier functions by minimizing the gauge-dependent spread with respect to the set of $\mathbf{U}_{mn}^{(\mathbf{k})}$, as implemented in the WANNIER90 code[97].

Chapter 3

Vanadium dioxide (VO$_2$)

3.1 Introduction

Vanadium dioxide is considered to be a strongly correlated material. It undergoes a metal-to-insulator transition (MIT) at 65 °C from the high-temperature metallic rutile (R) phase (space group P4$_2$/mnm, Fig. 3.1a) to the low-temperature semiconducting monoclinic (M) phase (space group P2$_1$/c, Fig. 3.1b), which is accompanied by the formation of paired vanadium chains. The drastic change in resistivity goes with changes in optical, thermal and magnetic properties. Furthermore, the transition temperature can be modulated by doping either to lower temperatures when using *e.g.* W^{6+}, Nb^{5+}, Mo^{6+}, Tb^{3+}, Al^{3+} [99–104], or to elevated temperatures when doped by Cr^{3+} or Ge^{4+}[105, 106]. The transition process is categorized as ultrafast, taking only $26 - 500$ fs. [107–109]. These changes that are related to the MIT can be potentially used in many applications such as optoelectronic switches[110], gas sensors[111], Mott-field effect transistors[112], memristive devices[113] and smart window coatings[114, 115].

Owing to the numerous potential applications of VO$_2$, the bulk properties have been studied applying a vast number of theoretical approaches[116]. It has been shown that standard methods within the DFT framework fail to completely recover the electronic, structural and magnetic properties of the rutile and monoclinic VO$_2$ phase. For example, both the local density approximation (LDA) and the generalized gradient approximation (GGA) fail to open an 0.6 eV band gap in the monoclinic (M1) phase[117, 118]. This shortcoming might be eliminated either by using the DFT+U variant [119], or meta-GGA and hybrid functionals, as analyzed by Stahl and Bredow [120, 121]. According to their findings, DFT+U leads to strong structural distortions of the monoclinic phase and a wrong energetic ordering of the VO$_2$ phases. Furthermore, conventional hybrid functionals such as HSE06 or PBE0 lead to a splitting of the conduction band in the metallic rutile phase and thus the Fock mixing parameter needs to be adjusted to correctly describe the electronic structure of the rutile and monoclinic phases[121, 122]. Stahl and Bredow also concluded[120] that the meta-GGA SCAN functional offers a good compromise between accuracy and computational cost.

The driving mechanism behind the MIT was recently investigated by Brito et al.[123] by performing combined DFT and embedded dynamical mean-field theory (DMFT) calculations. Such a combination constitutes a powerful approach to evaluate the many-body electronic structure of strongly correlated materials[124] and in particular to describe the MIT between a metal and a Mott insulator, as is the case for the present system, where the electronic transition can be described as a Mott transition in the presence of
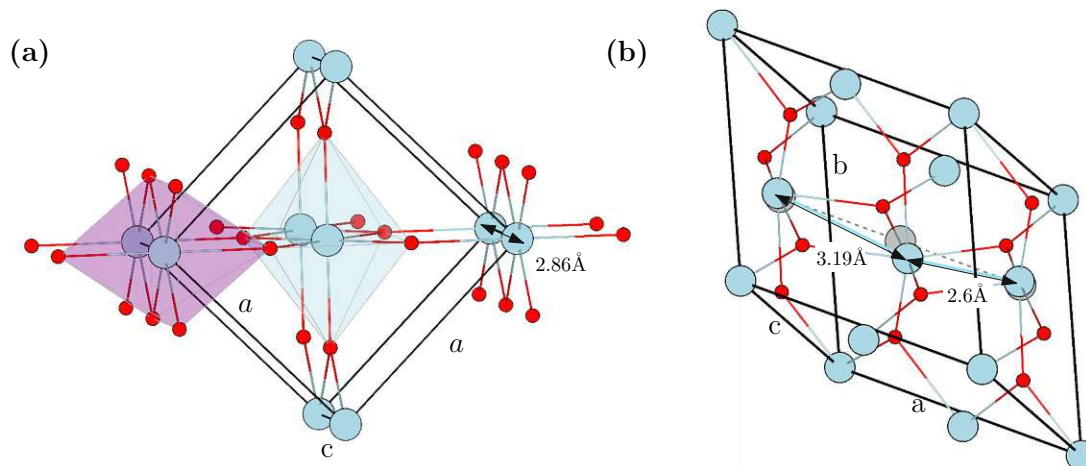
Fig. 3.1: Bulk structures of the (a) Rutile (R) and (b) Monoclinic (M) VO_2 phases. Gray spheres denote the positions of the vanadium atoms in the rutile phase.

strong intersite exchange. This is in agreement with the finding of Zhu et al.[116] who used the modified Becke-Johnson exchange together with LDA correlation potentials for both rutile and monoclinic VO_2 phases, to show that the MIT can be characterized as a correlation driven transition.

In contrast to the vanadium dioxide bulk systems, VO_2 surfaces and VO_2 thin films have been studied to a much lesser degree. The surface free energy of the bare and oxygen-covered low-index facets was investigated by Mellan et al.[125] employing the non-magnetic PBE functional. PBE+U calculations performed by Wahila et al.[30] indicate that the surface free energy of corresponding surfaces is lower for the rutile than for the monoclinic phase. Furthermore, they find it necessary to include spin-polarization in order to avoid negative values for the surface free energies of oxygen-rich reconstructions. In a very recent study[126], the rutile and monoclinic VO_2 surfaces were studied with the hybrid sc-PBE0 functional with an adjusted Fock mixing parameter. Despite its good performance on both bulk phases, the hybrid sc-PBE0 functional surprisingly fails to describe the surface energies of rutile VO_2 which do not converge upon increasing the thickness of the slab and even yield negative values for thicker slabs. On the experimental side, recent studies show the presence of a (2×2) reconstruction on the VO_2 (110) surface, accompanied by a change in the surface oxygen content of single crystals[32] and thin films [30, 31].

The aforementioned DFT studies using the PBE(+U) approach on the rutile VO_2 (110) surfaces under oxygen-rich conditions [30, 125] were done only for regular oxygen adsorption phases. However, a very recent study by Wagner et al. [32] indicates the presence of (2×2) surface reconstructions with tetrahedrally coordinated V atoms. In order to shed some more light on these findings, a detailed study of various oxygen adsorption phases and surface reconstructions on rutile VO_2 surfaces is presented, and the performance of common DFT functionals, including GGA, GGA+U, meta-GGA and meta-GGA+U is evaluated. In agreement with the experimental findings of Wagner et al. [32], we show that the simple regular oxygen adsorption phases considered in the previous calculations[30, 125] are less stable than surface terminations with tetrahedral V coordination polyhedra that are structurally and electronically related to a V_2O_5(001) monolayer. This findings

impose another important constraint to the DFT functional used for the description of off-stoichiometric VO_2 surface terminations, namely a correct description of the stability of the insulating V_2O_5 phase with respect to VO_2. This chapter starts with an investigation of the bulk properties of both rutile and monoclinic phases where experimental values pertaining to structural and electronic properties are compared to those obtained by applying different DFT functionals. These results are used to calculate the stability of low-index facets of rutile VO_2. In the last section the building process of atomistic models for the experimentally observed $VO_2(110)$ (2×2) surface reconstructions is presented and its results are compared to experimental data. The Appendix A contains several notes on the computational setup used in calculations to obtain the results presented in this chapter.

3.2 Motivation: Experimental results

The recent experimental results[32] call for a detailed knowledge of the atomic-scale structure of VO_2 surfaces. Here the most important experimental findings as presented in a combined experimental and theoretical work[32] are summarized, which motivated the extensive computational studies of VO_2 systems in this thesis.

The (2×2) surface reconstruction was achieved after annealing at temperatures higher than $600\,°C$ which resulted into larger terraces than after annealing at $560\,°C$. Annealing was performed at oxygen pressures 5×10^{-11} mbar and the surface did not change when the pressure was increased to 2×10^{-6} mbar. These values correspond to an oxygen chemical potential between $-2.1\,eV$ and $-1.7\,eV$ where the (2×2) surface reconstruction is thermodynamically stable.

The XPS measurements of the vanadium and oxygen core levels were acquired with normal and grazing (surface sensitive) emission as the function of the annealing temperature, ranging from $350\,°C$ to $700\,°C$. The normal and grazing emission data have shown distinctly different peak shapes which indicates that the surface contains an increased concentration of V^{5+} and hence, more oxygen as compared to the bulk.

Finally, the atomically-resolved STM experiments have shown, in agreement with measured LEED patterns, that the most prominent reconstruction is an adlayer with (2×2) symmetry, which was observed in most preparations covering the larger part of the surface. On the other hand, the rutile (1×1) $VO_2(110)$ surface was only observed at step edges or in small holes of the adlayer. The thickness of the reconstructed adlayer was measured with STM to be $\sim 1.6\,Å$. The captured STM patterns are shown in Figure 3.2 with four different contrasts that were tip-related. The superstructure consists of rectangular double rows made of spots parallel to the [001] direction. Furthermore, the narrow ('n') and wide ('w') spacing between these rows was revealed, see white vertical lines in Figure 3.2. This rectangular pattern is decorated with contrast-independent additional features. The first of them is a single protrusion sitting in the 'wide' row with a similar apparent height as the spots that form the rectangular pattern. As shown in panels 3.2a-c (white ellipses), these features often occupy every other site along the rows, leading to the flower-like pattern. The second feature marked with white arrows is located on the same site, but with a fuzzy appearance. Both features were stable during the STM measurements and do not diffuse at $80\,°C$. The qualitatively different pattern is visible in

Figure 3.2d which shows the structure containing the domain boundaries. The inset shows that these domain boundaries feature a zigzag (Z) arrangement of protrusions along the rows, instead of the expected rectangular (R) pattern. Note that the two rows framing the wide spacing are always aligned in the [$1\bar{1}0$] direction. This is indicated by connected dots in the inset in Figure 3.2d and the zigzag pattern is always visible within the double row.

The STM images also reveal that the (2×2) double rows are always aligned with respect to the bright rows of the rutile VO_2(110) (1×1) surface layer beneath, as shown in Figure 3.3. The presence of the (2×2) surface reconstruction is displayed together with a small hole exhibiting the unreconstructed (1×1) surface. The alignment marks the yellow line that points along the [001] direction, showing that the dark rows of the (2×2) surface superstructure are centered on bright rows of the VO_2(110) (1×1) layer beneath. Similarly, the surface superstructure is also aligned in the [$1\bar{1}0$] direction in the following way: The dark rows of the rectangular (2×2) pattern are placed on top of the dark rows of the unreconstructed (110) (1×1) surface. This is marked in the right panel with the light blue lines. In addition, bright spots that form the rectangular pattern of the (2×2) superstructure are also centered on the dark rows of the unreconstructed surface. As it will be shown, the (1×1) surface is composed of bright rows separated by 6.43 Å and agrees with simulated STM images of the bare (110) surface. Considering the (2×2) reconstruction, the light blue and yellow lines determine the (2×2) surface supercell which contains two mirror planes depicted in light green and violet color. Bright spots that form the (2×2) superstructure show the double row structure with the wide ('w') and narrow ('n') spacing, see the blue lines.
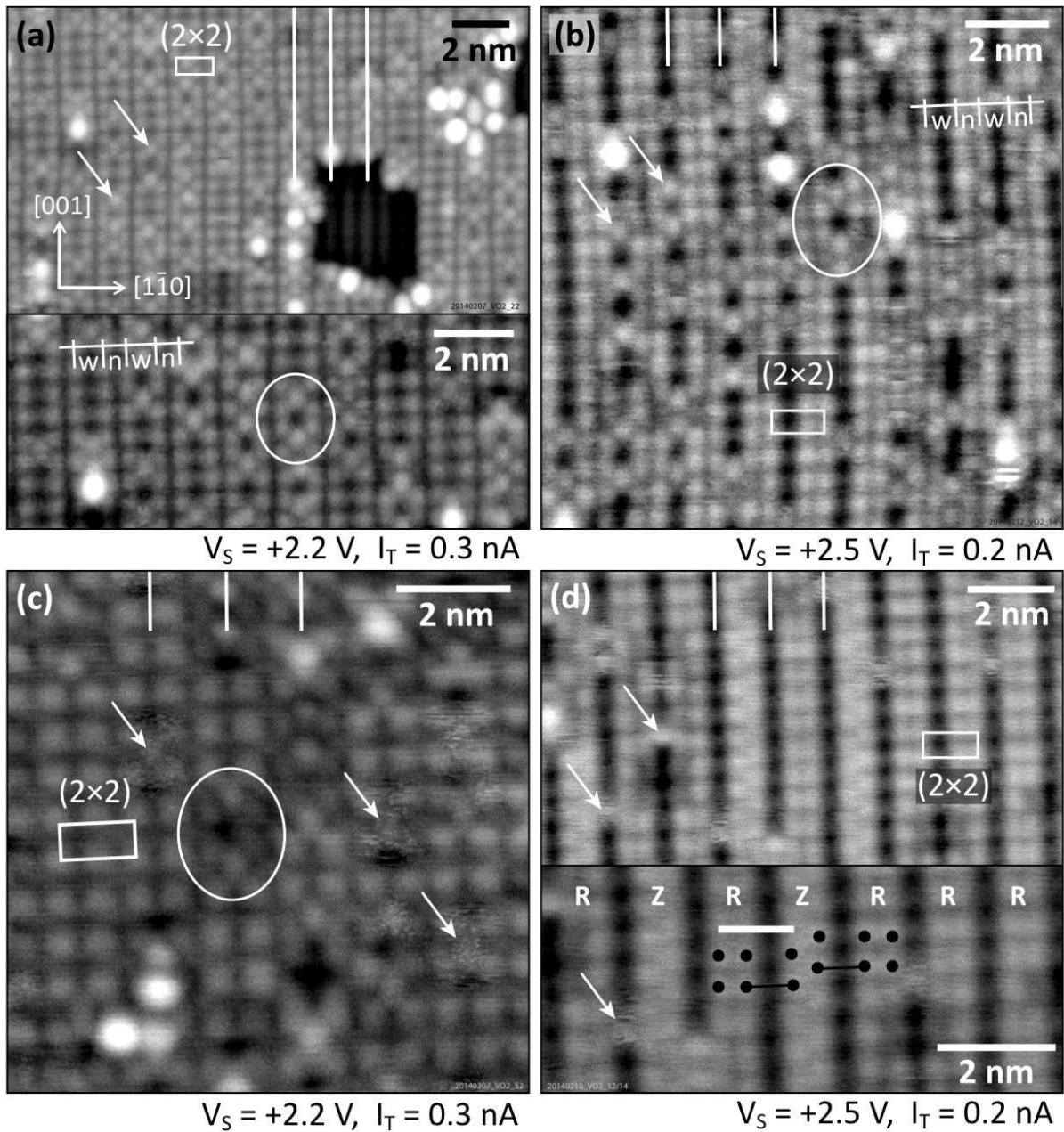
Fig. 3.2: STM images and details of the (2×2) row structure. White markers in the top part of each panel indicate the positions of the wide spacing between the double rows. Comparison of (a) and (b) shows that contrast does not always emphasize the wide spacing as the main depression. Additional features in the wide sites are marked by white arrows. (a, b) Most common appearances showing double rows. The alignment of the wide spacing with respect to the bright rows of the VO_2 surface visible inside the holes is indicated in (a). (c) Square appearance, *i.e.*, equal spacings in $[1\bar{1}0]$ are observed. (d) Distinct double row structure with domain boundaries (displacements within the double row along $[100]$), resulting in lines with zigzag (Z) structure, in contrast to the usual rectangular (R) arrangement. Image taken from [32].

30
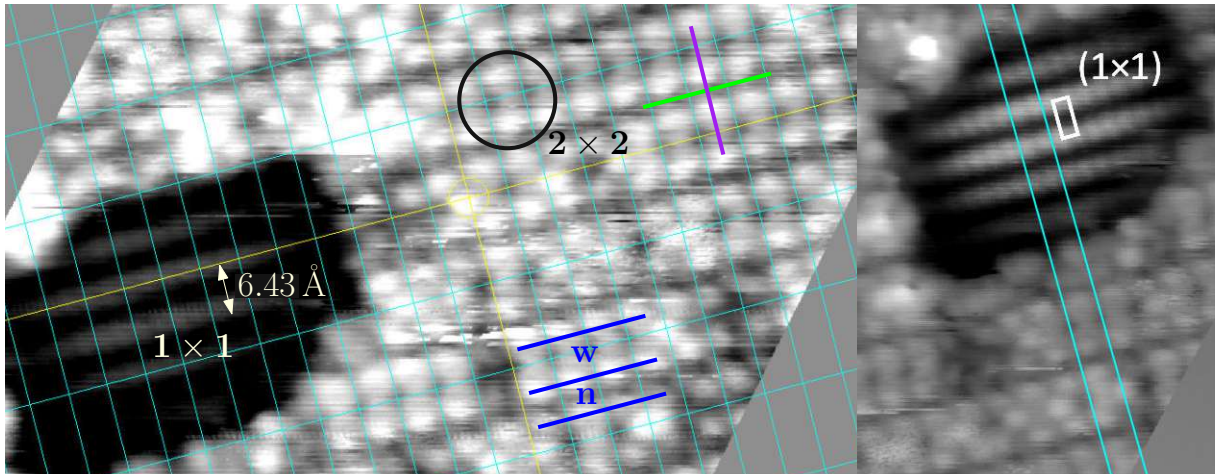
Fig. 3.3: STM contrasts and details of the (2×2) row structure. Left panel: dark blue lines indicate the positions of the wide ('w') and narrow ('n') spacing between the double rows. The alignment of the (2×2) reconstruction with respect to the unreconstructed $VO_2(110)$ (1×1) surface visible inside the hole is indicated by the yellow line, showing that the dark rows of the (2×2) reconstruction are centered on the bright rows of the (1×1) unreconstructed surface. The resulting pattern of the (2×2) reconstruction shows two mirror planes, namely (001) and $(1\bar{1}0)$ that are represented by violet and green lines, respectively. Right panel shows the alignment of the (2×2) reconstruction with respect to the unreconstructed (110) surface below in $[1\bar{1}0]$ direction (light blue lines), showing that also in this case the dark rows in both area are centered on each other. Image adjusted from [32].

3.3 Bulk properties of rutile (R) and monoclinic (M) VO₂ phases

Before starting an investigation of the bulk properties of both metallic (R) and insulating (M) VO$_2$ phases, it is illustrative to recall several experimental findings. The structure of the high-temperature rutile phase is depicted in Figure 3.1a. The rutile phase exhibits a tetragonal unit cell with lattice vectors $a = 4.55\,\text{Å}$ and $c = 2.85\,\text{Å}$ [127]. Vanadium atoms are surrounded by six oxygen atoms in the form of edge-sharing octahedra with oxygen-vanadium distances equal to 1.9 Å. The z axes of the octahedra point either along the [110] or [1$\bar{1}$0] direction – always perpendicular to the direction of the [001] lattice vector, making octahedra either straightened (colored in blue) or laid (colored in violet), see Figure 3.1a. These octahedra are equally separated by the length of the [001] lattice vector, namely 2.85 Å.

The low-temperature monoclinic phase undergoes a transition that is described by the transformation matrix[128] shown in Eq. 3.1, where M and R indices denote the M and R phase, respectively. Therefore, the rutile R[001] axis is parallel to the monoclinic M[100] direction after the transformation. The same relation also holds for any crystallographic plane characterized by indices (hkl).

$$
\begin{pmatrix} a \\ b \\ c \end{pmatrix}_M = \begin{pmatrix} 0 & 0 & -2 \\ -1 & 0 & 0 \\ 0 & 1 & 1 \end{pmatrix} \cdot \begin{pmatrix} a \\ b \\ c \end{pmatrix}_R \tag{3.1}
$$

Apart from the transformation of the unit cell vectors, the most prominent feature of the monoclinic phase is the occurence of paired vanadium atoms along the rutile [001] (monoclinic M[100]) direction, which changes the equal V-V distances from 2.85 Å to 2.6 Å for the shorter distance and to 3.2 Å for the longer distance. Consequently, the octahedra are distorted and the central vanadium atoms move away from the center of octahedra, as depicted in Figure 3.1b. The gray spheres represent positions of vanadium atoms in the symmetric rutile R phase. On a side note, other phases were also indentified in experiments applying tensile stress along the c direction. Figure 3.4 depicts the stress-temperature phase diagram for vanadium dioxide, showing the presence of an insulating high-pressure monoclinic (M2) phase and intermediate trigonal (T) phase. Furthermore, Arcangeletti et al. detected [129] a metallization of the monoclinic M phase under a large pressure, leading to the metallic monoclinic (mM) phase.

Changes in the electronic structures induced by the metal-to-insulator transition are described in detail in the work of Eyert[131]. In the rutile phase, the crystal field splits the vanadium $3d$ band in antibonding π^* orbitals (d_{xy}, d_{yz}, d_{xz}) marked as Vt_{2g} at lower energies and in antibonding σ^* orbitals (d_{z^2}, $d_{x^2-y^2}$) denoted noted as Ve_g above, see Figure 3.7. The structural changes present in the monoclinic (M) phase are accompanied by a further split of the Vt_{2g} manifold in a single a_{1g} orbital, aligned along the rutile c-axis (corresponding to the d_{xy} orbital), and in two degenerate d_{xz}, d_{yz} orbitals. In case of the rutile phase, Vt_{2g} as well as e_g orbitals overlap with neighboring d-orbitals which causes a metallic character. However, the V-V pairing in the monoclinic phase yields a split of the a_{1g} states into bonding and antibonding states. Furthermore, the hybridization with O$2p$
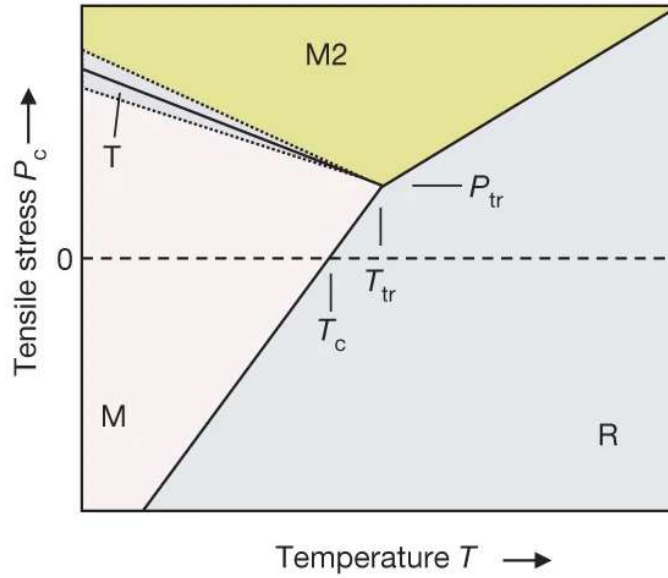
Fig. 3.4: Stress-temperature phase diagram of the vanadium dioxide. T_c denotes the transition temperature $65.0\,°C$ at the zero tensile stress along the c direction. Image reprinted from [130].

states is stronger due to distortion of octahedra and the e_g^π states are pushed to higher energies. Both effects contribute to the opening of the $\sim 0.6\,eV$ band gap as it is illustrated in Figure 3.5.

3.3.1 Results: VO₂ phases

The performance of the DFT functionals was first assessed for the structural and electronic properties of the rutile (R) and monoclinic (M) VO$_2$ phases, using ferromagnetic, antiferromagnetic and non-magnetic spin configurations. One antiferromagnetic configuration has been considered for each phase. For the rutile phase antiferromagnetic ordering is considered along the [111] direction so that vanadium atoms in violet octahedra in Figure 3.1a have different spin configuration than vanadium atoms in blue octahedra. In the monoclinic phase the antiferromagnetic ordering is considered along the monoclinic a direction where the vanadium-vanadium pairing occurs. Table 3.1 shows the respective performance for the rutile VO$_2$ phase and all spin configurations. The PBE, SCAN and SCAN+rVV DFT functionals with ferromagnetic spin treatment show a good agreement with experiment regarding the lattice parameters and volumes of the unit cells, resulting into maximal errors of about $1\,\%$ and $2\,\%$ respectively. However, the spin-polarized PBE+U functional calculates a strong distortion of the unit cell, squeezing and expanding the a and c lattice parameters respectively, which leads to an overestimation of the c/a ratio by $6.3\,\%$. Furthermore, (FM) PBE+U calculations show an $0.42\,eV$ electronic gap after the structural optimization. The magnetization energy E_{mag} defined as a difference between the (FM) and (NM) or (AFM) and (NM) spin configurations shows that all functionals find the ferromagnetic ordering among all the other considered orderings to be most favourable
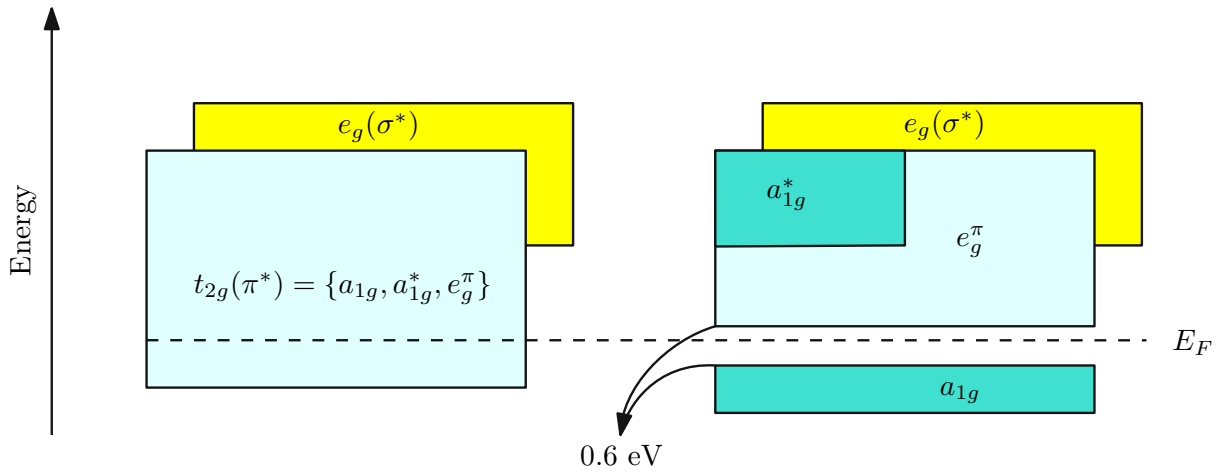
Fig. 3.5: A sketch of the structure of the V $3d$ band in the R and M VO$_2$ phases. Respective band widths and their approximate positions on the energy axis are taken from [123].

which is in agreement with a previous report [120]. The antiferromagnetic spin ordering leads to a minor extension (compression) of the a (c) lattice parameters, which leads to a larger deviation of the c/a ratio as compared to the ferromagnetic ordering. Considering the energetic stability of the calculated antiferromagnetic spin ordering this configuration is 20 meV to 213 meV per formula unit less preferred than the favoured ferromagnetic order. Non spin-polarized calculations show a similar trend for the calculated unit cell parameters as the (AFM) calculations. The a lattice vector is extended and c is compressed, resulting in a worse c/a ratio when compared to the (FM) spin ordering. This effect is even more pronounced in respect to the (AFM) calculations. Furthermore, (NM) calculations yield the lowest volumes of the unit cell among the studied spin configurations. All functionals except the PBE show that the (NM) spin configuration in the rutile VO$_2$ phase is the least stable. The PBE functional predicts the same stability for the (AFM) and (NM) spin ordering. All functionals show that the non-magnetic configuration is $79 - 321$ meV/f.u. less stable with respect to the (FM) spin ordering. According to the experimental observations[132], the rutile VO$_2$ phase is paramagnetic which is difficult to capture with DFT calculations for two reasons. First, the paramagnetism in VO$_2$ is induced by temperature, but DFT calculations describe the ground state at 0 K. Second, a calculation of disordered magnetic moments in paramagnetic materials requires the consideration of large supercells and a subsequent searching for a correct spin ordering in a large configuration space of all magnetic moments. This work assumes that surface properties and experimentally observed reconstructions are not strongly influenced by the paramagnetic spin (dis)order of the rutile phase and therefore a ferromagnetic spin ordering which appears to be the most stable in the DFT calculations is used in the following.

Structural parameters of the monoclinic VO$_2$ phase are shown in Table 3.2. The ferromagnetic calculations give generally the best results when compared to experimental data. For all other spin configurations the [100] lattice vector is underestimated by 2 % to 3 % with respect to the experiment while the (FM) unit cells reduce the error to 0 % to 2 %. Note that the [100] lattice vector in the monoclinic phase is parallel to the rutile

		a	c	c/a	V	E_g	E_{mag}
(FM)	PBE	4.59	2.84	0.62	29.9	0	
(FM)	PBE+U	4.50	3.02	0.67	30.6	0.42	
(FM)	SCAN	4.54	2.83	0.62	29.1	0	
(FM)	SCAN+rVV	4.53	2.83	0.62	29.0	0	
(AFM)	PBE	4.62	2.78	0.60	29.7	0	79
(AFM)	PBE+U	4.50	3.02	0.67	30.6	0.69	20
(AFM)	SCAN	4.56	2.77	0.61	28.8	0	213
(AFM)	SCAN+rVV	4.54	2.81	0.62	28.9	0	160
(NM)	PBE	4.62	2.78	0.60	29.6	0	79
(NM)	PBE+U	4.63	2.79	0.60	30.0	0	321
(NM)	SCAN	4.56	2.77	0.61	28.8	0	215
(NM)	SCAN+rVV	4.55	2.76	0.61	28.6	0	212
(PM)	Exp.[133]	4.55	2.86	0.63	29.6	0	

Tab. 3.1: Calculated parameters of rutile VO_2 phase with various functionals and spin orderings: the lengths of the c, a lattice vectors [Å], volume of the unit cell V [Å^3/f.u.], electronic band gap E_g [eV] and magnetization energy E_{mag} [meV/f.u.].

[001] axis along which the vanadium pairing occurs. The resulting size of the monoclinic [001] lattice vector doesn't depend on the spin configuration and all functionals and spin configurations are in a good agreement with the experimental value, yielding a maximal relative error of about 1 %. On the other hand, the SCAN and the SCAN+rVV functionals improve the value of the [010] lattice vector in comparison with the PBE and PBE+U functionals, independent of the spin configuration. The most prominent structural change in the monoclinic VO_2 phase is the occurence of vanadium pairs along the monoclinic [100] direction as depicted in Figure 3.5b. However, there is no computational setup that exactly reproduces the experimental values. All ferromagnetic calculations underestimate the size of the buckling – the shorter d_{V-V} distance is 5 % to 6 % larger, but the longer pairing distance d_{V-V*} is calculated to be 6 % to 8 % smaller. The antiferromagnetic spin configuration except for the PBE+U functional slightly improves the shorter pairing distance d_{V-V}, but the d_{V-V*} is still strongly underestimated as for the (FM) calculations. Considering the (AFM) PBE+U functional, the pairing almost disappears and also the monoclinic lattice vectors are almost identical to the rutile unit cell. Both findings indicate that the monoclinic phase was transformed to the rutile phase during the optimization. The same effect was also observed for the ferromagnetic spin configuration where the calculation started from the insulating wave function, in which case the monoclinic phase was also transformed to the rutile phase. The underestimation of the longer pairing distances (d_{V-V*}) is improved by non spin-polarized calculations, which is either in a perfect agreement with the experiment (PBE+U, SCAN, SCAN+rVV), or in better agreement than the (FM) monoclinic VO_2 (PBE). However, using the PBE+U, SCAN and SCAN+rVV functionals lead to the underestimation of the shorter pairing distance. Hence, all functionals can describe well only one of the pairing distances. The PBE functional gives an identical value for the shorter distance, but the longer distance is still 5 % underestimated. On the other side, the remaining SCAN, PBE+U and SCAN+rVV functionals underestimate the

shorter pairing distance by 4 % to 5 % while the latter one is in an excellent agreement with experiment, yielding a relative error up to ∼1 %. Considering the electronic band gap, the PBE, SCAN and SCAN+rVV functionals in spin-polarized calculations always give a metallic character for the monoclinic phase. Although the PBE+U functional opens the electronic band gap, it simultaneously transforms the monoclinic phase to the rutile phase. On the other hand, the non spin-polarized calculations except the PBE functional open the 0.3 eV to 0.4 eV electronic band gap which is in a reasonable agreement with the experimental value of 0.6 eV[134]. Finally, Table 3.2 shows the energy differences between the rutile and the monoclinic phase with the same spin ordering. Note that the experimental value 44 meV per formula unit is obtained from calorimetric measurements[135]. The ferromagnetic spin configuration leads to the wrong order of stability, showing that the rutile phase is more stable. Even for the monoclinic phase the most stable spin configuration obtained in this work is the ferromagnetic ordering, except the aforementioned PBE+U functional which exhibits the bulk instability. The correct ordering of phase stabilities can be obtained with non-spin polarized PBE+U, SCAN and SCAN+rVV functionals which also provide a good agreement with the experimental value, resulting into a 48 meV to 67 meV/f.u. extra stability for the monoclinic phase. Only the non-magnetic PBE functional shows a different trend: the rutile phase is preferred by 14 meV.

Since the bulk properties of the VO$_2$ phases are described rather inconsistently by the considered DFT functionals, its electronic structure was looked into in more detail with the help of Wannier projections on atomic-like vanadium d orbitals. Figures 3.7 and 3.8 show the total density of states (black dashed line) and projections to vanadium atomic orbitals calculated with the above set of functionals and spin configurations. Due to the crystal field the vanadium d bands which are found in the range of $-1.6 - 6$ eV are split into lower energetic t_{2g} states (d_{xy}, d_{xz}, d_{yz}) and higher e_g states ($d_{x^2-y^2}$, d_{z^2}) of the V$3d$ band. Around -2 eV the upper edge of the O$2p$ band is shown. For each functional and each phase the projections are calculated for ferromagnetic and nonmagnetic spin ordering using both relaxed and experimental structures. Regarding the results for the rutile phase that are depicted in Figure 3.7, the spin-polarized PBE, SCAN and SCAN+rVV functionals yield qualitatively the same projections, independent of the choice of the experimental or relaxed structure. This is expected since the calculated structural parameters by these functionals and (FM) spin configurations are very close to those obtained experimentally, see Table 3.1. Spin-polarized calculations result in a splitting of the spin-up ($\uparrow$) and spin-down ($\downarrow$) channels, shifting the V$t_{2g\downarrow}$ states above the Fermi level. As a consequence, all electrons of the vanadium $3d$ band are located in the V$t_{2g\uparrow}$ states. The spin-polarized DFT+U functional shows a subsequent splitting of the V$t_{2g\downarrow}$ states, pushing the d_{xy} orbital apart from the d_{xz} and d_{xy} orbitals, and creating the 0.42 eV energy gap. In this case, all electrons from the V$3d$ band are located in the d_{xy} orbital which coincides with the edge of the O$2p$ band. These results can be directly compared with the dynamical mean-field theory benchmark calculations[123], see Figure 3.6. A comparison with the DMFT results clearly shows that the spin-polarized PBE+U functional describes the orbital occupancies improperly, which causes the formation of a monoclinic-like d_{xy} sub-band separated by 0.42 eV from the d_{xz} and d_{yz} orbitals. This behavior is only observed while using larger values of U (U $\geq$ 2 eV) and when the electronic structure is calculated at optimized

	a	b	c	c/a_R	β	V	$d_{\text{V-V}}$	$d_{\text{V-V*}}$	E_g	ΔE_R	E_{mag}
(FM) PBE	5.70	4.59	5.39	0.62	122.0	29.96	2.72	2.99	0	5	
(FM) PBE+U	5.76	4.60	5.41	0.63	120.1	30.40	2.76	3.01	0	74	
(FM) SCAN	5.67	4.54	5.35	0.63	122.1	29.13	2.72	2.96	0	3	
(FM) SCAN+rVV	5.66	4.53	5.34	0.63	122.1	28.98	2.74	2.93	0	2	
(AFM) PBE	5.65	4.60	5.39	0.61	121.7	29.80	2.69	2.97	0	-2	72
(AFM) PBE+U	6.05	4.50	5.42	0.67	123.7	30.59	3.01	3.05	0.65	1	-53
(AFM) SCAN	5.64	4.54	5.35	0.62	122.0	29.04	2.70	2.95	0	-77	133
(AFM) SCAN+rVV	5.63	4.54	5.33	0.62	121.9	28.88	2.70	2.94	0	-26	132
(NM) PBE	5.60	4.63	5.39	0.61	121.4	29.83	2.60	3.03	0	14	89
(NM) PBE+U	5.64	4.62	5.44	0.61	119.6	30.11	2.50	3.18	0.4	-67	181
(NM) SCAN	5.59	4.55	5.37	0.61	122.0	28.99	2.46	3.17	0.4	-48	165
(NM) SCAN+rVV	5.58	4.53	5.35	0.62	122.0	28.72	2.47	3.14	0.3	-53	157
(NM) Exp.	5.75[a]	4.53[a]	5.38[a]	0.63[a]	122.6[a]	29.36[a]	2.60[a]	3.19[a]	0.6[b]	-44[c]	

[a] ref. [133]
[b] ref. [134]
[c] ref. [135]

Tab. 3.2: Structural and electronic parameters of the optimized monoclinic VO_2 phase, calculated with several DFT functionals and ferromagnetic (FM) and non-magnetic (NM) spin configurations. c/a_R marks the ratio of the rutile-like c and a lattice constants, equal to $a/(2b)$ in case of the monoclinic phase. E_g denotes the band gap width (in eV), V-V and V-V* mark the size of the pairing [Å]. Considering the stability of the monoclinic phase, ΔE_R is the energy difference [meV/f.u.] between the rutile and monoclinic phase with the same magnetic ordering and E_{mag} denotes the magnetization energy [meV/f.u.] defined as energy difference between the magnetic and nonmagnetic configuration.

lattice geometries, which means geometries extended along the c direction. Therefore, the description given by PBE, SCAN and SCAN+rVV functionals is more consistent with the benchmark data. Considering the non-magnetic calculations, all functionals show similar projections, also regardless whether the relaxed or the experimental structure is taken. As shown, non-spin polarized calculations yield a $\sim$0.3 eV larger band gap between the O$2p$ and V$3d$ band, but the occupied V$3d$ bandwidth is reduced from $\sim$0.9 eV to $\sim$0.6 eV when compared to the spin-polarized calculations.

The electronic structure of the V$3d$ band in the monoclinic VO_2 phase, calculated with the same computational setup as for the rutile phase, is shown in Figure 3.8. The electronic structure of: (i) different spin configurations, (ii) calculated and experimental unit cells, and (iii) the monoclinic and the rutile phase, is compared. First, the Wannier projections calculated for the experimental structures show that the a_{1g} sub-band composed of the d_{xy} projections is singled out from the V$3d$ band and pulled below the Fermi level. This effect is generally weaker in case of the PBE functional which exhibits a certain overlap of the a_{1g} band with the remaining projections. Again, the (FM) PBE+U functional shows qualitative differences with respect to the remaining (PBE, SCAN, SCAN+rVV)
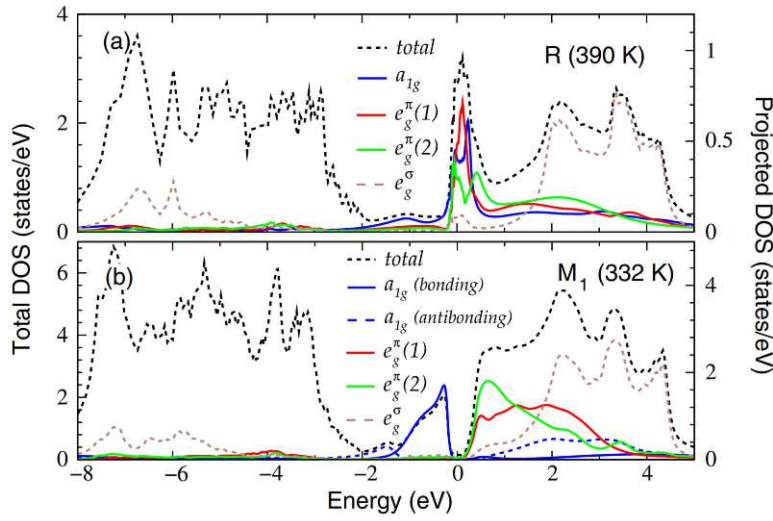
Fig. 3.6: DFT+DMFT-based total (black dashed line) and projected DOS of (a) Rutile and (b) Monoclinic phase of VO_2. The projections to a_{1g}, $e_g^\pi(1)$, $e_g^\pi(2)$, and e_g^σ states are shown in blue, red, green, and brown lines, respectively. In the notation used in this thesis, d_{xy} corresponds to the a_{1g} line, d_{xz} and d_{yz} orbitals are marked as $e_g^\pi(1)$ and $e_g^\pi(2)$ respectively, and the remaining orbitals are denoted as e_g^σ. Image reprinted from [123].

functionals, namely the splitting of the d_{xy} states into two particular sub-bands that are both shifted below the Fermi level, which is not in agreement with DMFT benchmark calculations. The relaxed structures also show more significant changes in the electronic structure than in the rutile phase. This can be expected since the structural changes are also more prominent as it was discussed before. As shown, the (NM) PBE+U, SCAN and SCAN+rVV functionals open the electronic band gap in the relaxed monoclinic structure, 0.1 eV larger than in the experimental structure. This correlates with the resulting ~0.1 Å shorter vanadium pairing distance d_{V-V}. Although the (NM) PBE functional shows the larger pairing distance that is in better agreement with experiment, it does not open an electronic band gap. Considering the electronic structure of the relaxed structures with spin-polarized functionals, the separation of the d_{xy} projection from the remaining Vt_{2g} states vanishes when the shorter pairing distance increases. As a result, the occupancies of the d_{xz} and d_{yz} projections are non-zero which is not in agreement with benchmark DMFT calculations. However, the d_{xy} projections in the monoclinic phase differ from the rutile phase in the occupation in close vicinity of the Fermi level: The rutile phase results in partial occupations of all Vt_{2g} states, but the monoclinic phase shows a clear splitting of the d_{xy} states into the occupied a_{1g} band and unoccupied a_{1g}^* band.

The structural relaxations also lead to a smaller separation of the O$2p$ and V$3d$ bands, except for the (FM) PBE+U, SCAN and SCAN+rVV functionals, which show larger changes in the electronic structure but the resulting band separations are approximately the same.

Considering the bulk calculations, a structural instability of the rutile phase was identified that was also reported by Kim et al[136]. The PBE functional shows a phonon softening instability of the R phase at Γ, leading to a collinear displacement of oxygen atoms
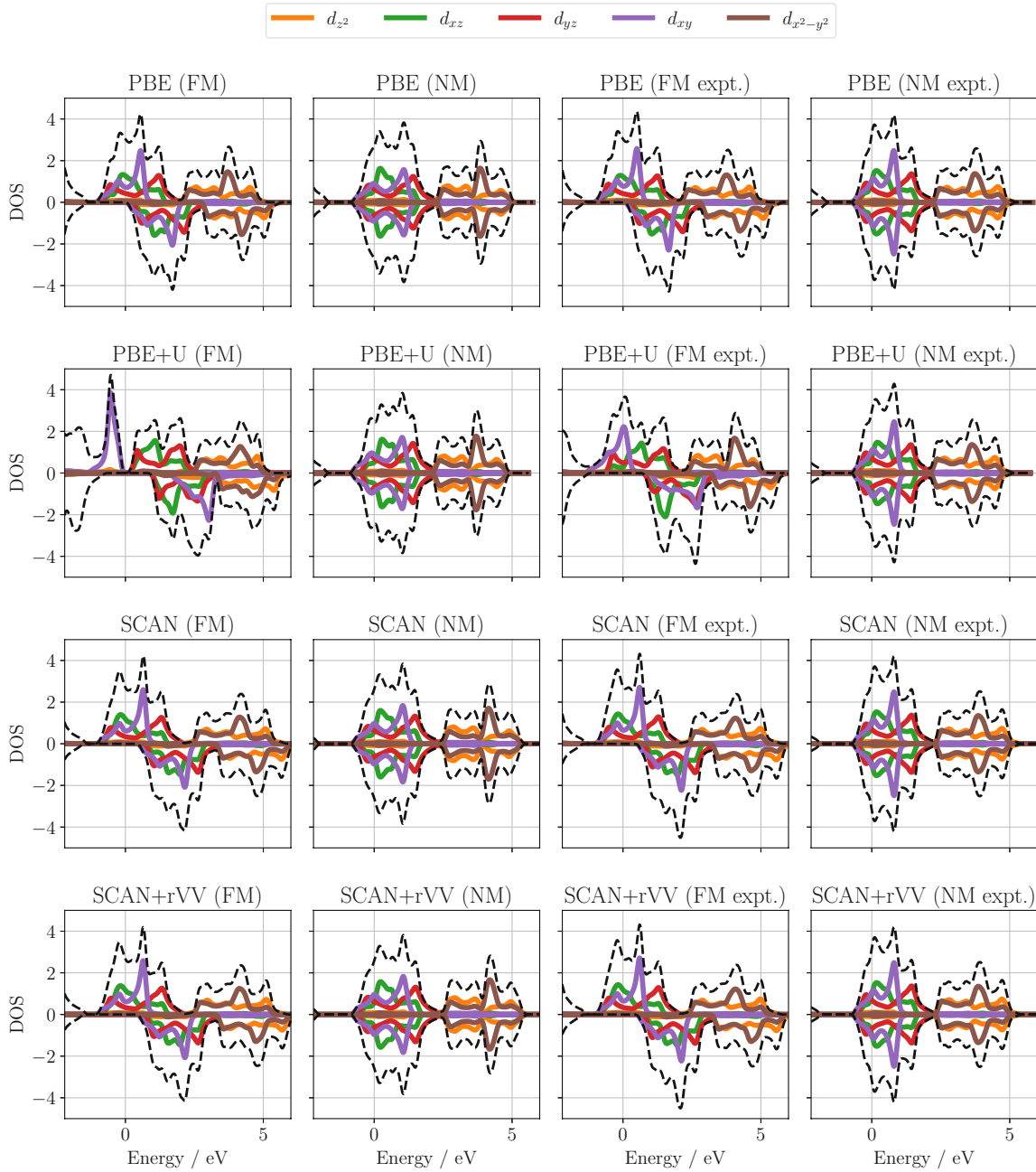
Fig. 3.7: Projected density of states onto Wannier orbitals localized at vanadium atoms in the rutile (R) phase, calculated with several DFT functionals using relaxed (two left columns) and experimental structures (two right columns). 0 marks the Fermi energy, Vt_{2g} states are formed by d_{xz}, d_{yz} and d_{xy} orbitals, d_{z^2} and $d?x^2 - y^2$ form the e_g states. Only the upper edge of the O$2p$ band (at $\sim -2\,\text{eV}$) and the whole V$3d$ band is shown.
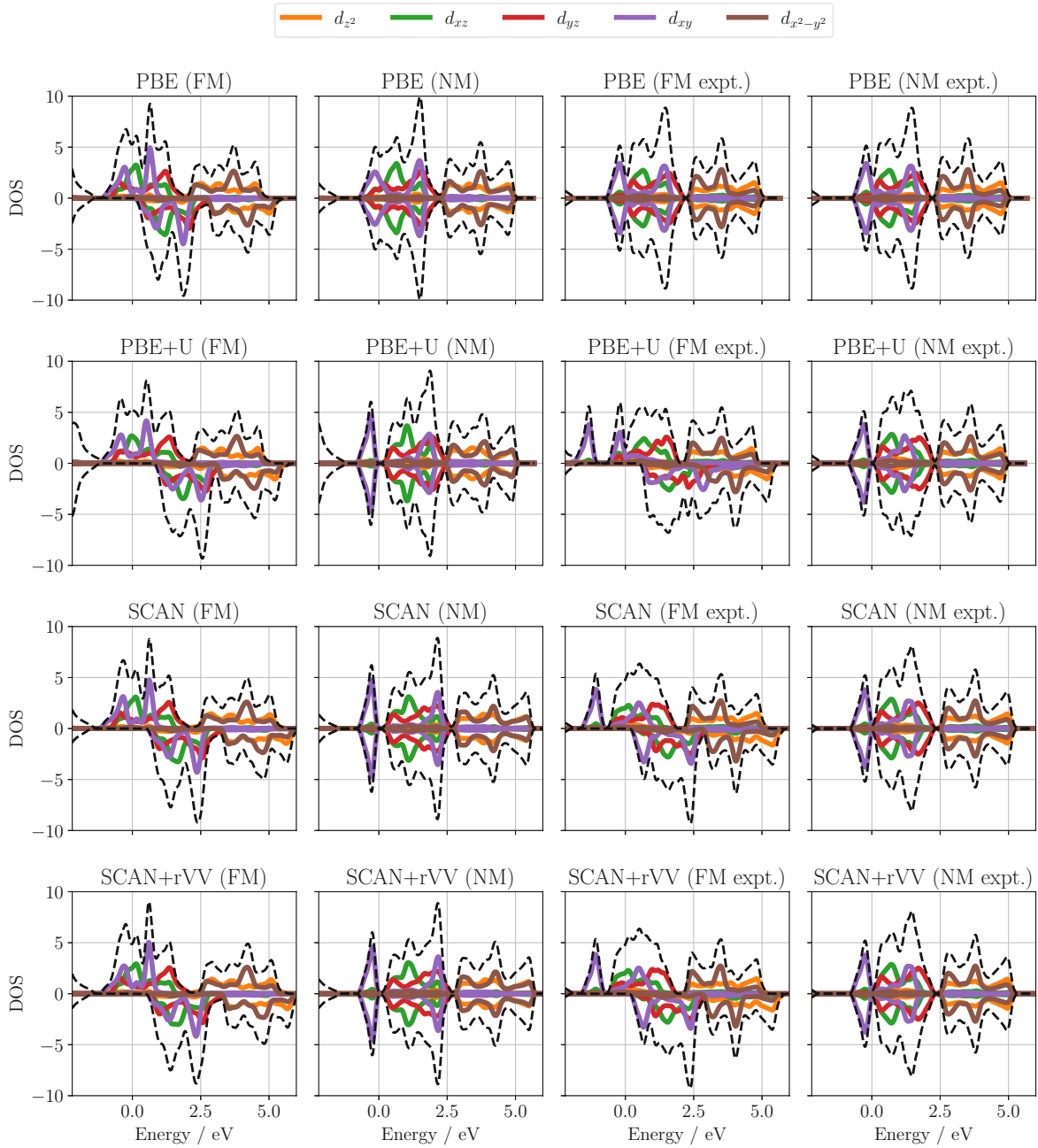
Fig. 3.8: Projected density of states onto Wannier orbitals localized at vanadium atoms in the monoclinic (M) phase, calculated with several DFT functionals using relaxed (two left columns) and experimental structures (two right columns). 0 marks the Fermi energy, Vt_{2g} states are formed by d_{xz}, d_{yz} and d_{xy} orbitals, d_{z^2} and $d_{x^2-y^2}$ form the Ve_g states. Only the upper edge of the O$2p$ band (at $\sim -2\,\text{eV}$) and the whole V$3d$ band is shown.

		FM				NM		
	PBE	PBE+U	SCAN	SCAN+rVV	PBE	PBE+U	SCAN	SCAN+rVV
ΔE	12	2	10	10	10	0	11	10

Tab. 3.3: Additional stabilization (in meV/f.u.) of the modified rutile phase. The modification is a displacement of the oxygen atoms along the rutile-*c* axis.
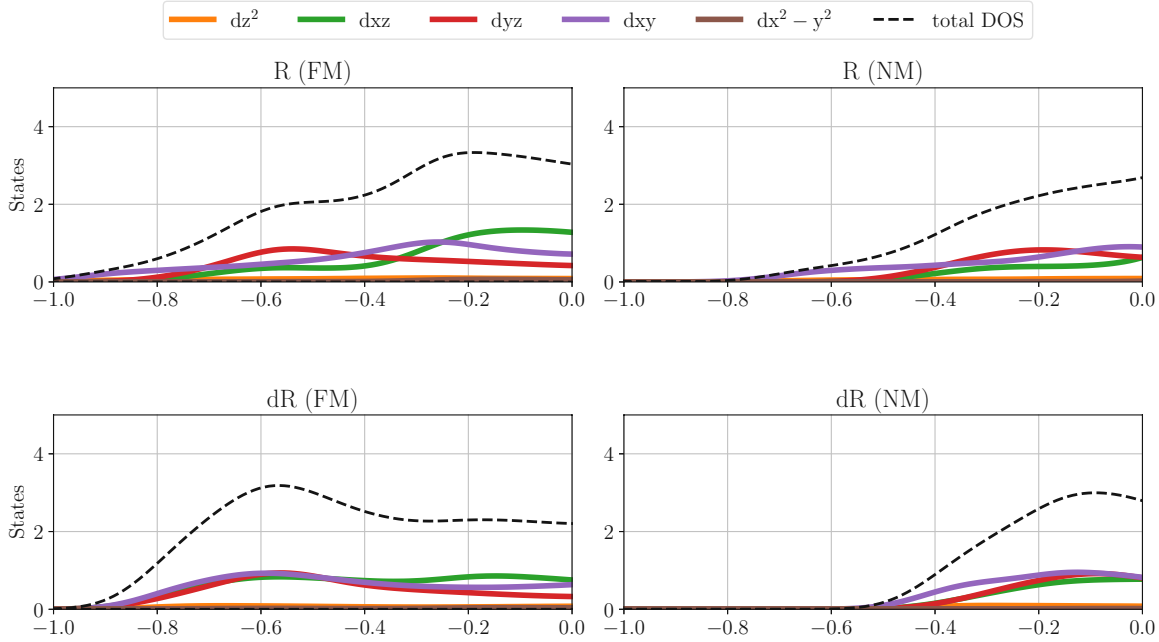
Fig. 3.9: Comparison of the total and projected density of states of the V *3d* band for the rutile (R) and displaced rutile (dR) phases, using spin-polarized (FM) and non spin-polarized (NM) PBE calculations.

along the [001] direction. Since this bulk instability might directly influence the surface calculations, the properties of the displaced oxygen R phase is briefly discussed. Table 3.3 shows that the displacement stabilizes the VO$_2$ system by 10 meV to 12 meV per VO$_2$ unit for all bare DFT functionals and spin configurations. The DFT+U method suppresses this additional stability for both spin-polarized and non-spin polarized calculations in agreement with Kim's work[136] which reported that the phonon softening instability at Γ disappears in this case. Figure 3.9 shows the effect of the displaced oxygen atoms on the total and projected density of states. Considering the (FM) spin configuration, total DOS of the rutile phase consists of the lower and higher peaks located at -0.55 eV and -0.20 eV, respectively. The displacement of the oxygen atoms leads to an exchange of these peaks and is accompanied by a shift of the d_{xy} and d_{xz} projections to lower values. Since the displacement direction is perpendicular to the d_{yz} orbital, its projection is almost unchanged. Non spin-polarized calculations show slightly different projections in the V *3d* band. The displaced rutile phase shows one peak with a maximum at -0.1 eV while the rutile DOS is continuously increasing.
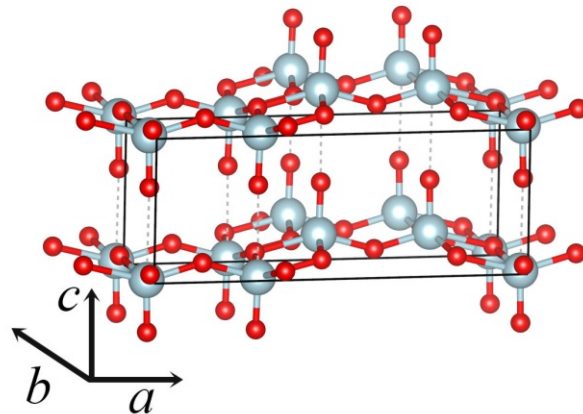
Fig. 3.10: Structure of the V_2O_5 phase. Dashed lines mark van der Waals attractive interactions between interlayer vanadium and oxygen atoms along the c directions.

3.3.2 Supporting calculations: V_2O_5 phase

Since the second part of this chapter focuses on the properties of off-stoichiometric surface terminations, a short overview of the V_2O_5 phase is given in the following paragraph. The V_2O_5 phase has an orthorhombic structure (space group P_{mmn}, a=11.51 Å, b=3.56 Å, c=4.37 Å)[137] that is formed by layers perpendicular to the [001] direction bonded with van der Waals interactions. Note that there is a certain ambiguity in notation of lattice vectors and in some literature b and c lattice vectors are interchanged. In this work the V_2O_5 layers are parallel to the (001) plane. The second significant difference between the V_2O_5 and VO_2 phases is the coordination geometry of the surrounding oxygen atoms. The rutile and monoclinic VO_2 phases are composed of distorted octahedra, whereas the V_2O_5 phase shows distorted pyramids. The structure of the V_2O_5 phase is depicted in Figure 3.10.

In contrast to the vanadium dioxide, the V_2O_5 phase was only considered in closed-shell calculations because no unpaired electrons are present in the V $3d$ band. The structural and electronic properties were analyzed with all aforementioned DFT functionals. The results are summarized in Table 3.4. As can be seen the a and b lattice parameters of the vanadium pentoxide phase are in a perfect agreement with experiment, showing relative errors below 1 %. However, the c lattice vector perpendicular to the layer planes is either too large (PBE and PBE+U by 6 %), or too small (SCAN, SCAN+rVV by 4 % and 8 % respectively). A similar overestimation of the b lattice constant with the PBE functional has already been reported in previous work [138, 139]. The strong underestimation of the SCAN+rVV functional is caused by taking into account attractive van der Waals interactions between the V_2O_5 layers which even more reduce the unit cell in this direction, when compared to the bare SCAN functional. The volume of the unit cell taken per $VO_{2.5}$ unit is significantly larger than for the VO_2 phases. This is firstly caused by rather 'open' structure of the vanadium pentoxide phase, as well as by an increased concentration of oxygen. Additional oxidation and transformation to the layered structure of the vanadium pentoxide phase leads to the large increase of the volume per formula unit, namely 60 %

	PBE	PBE+U	SCAN	SCAN+rVV	Exp.
a	11.57	11.56	11.59	11.66	11.51[a]
b	3.57	3.60	3.55	3.54	3.56[a]
c	4.65	4.66	4.20	4.04	4.37[a]
V	48.0	48.5	43.1	41.7	44.7[a]
E_g	2.0	2.2	2.0	1.9	2.2-2.4[b]
(NM) $H_f^{V_2O_5}$	-2.05	-2.00	-1.90	-1.80	-1.28
(FM) $H_f^{V_2O_5}$	-1.89	-1.35	-1.47	-1.38	

[a]Ref. [141]
[b]Ref. [140, 142–144]

Tab. 3.4: Structural and electronic parameters of the vanadium pentoxide phase, calculated with several DFT functionals and non-magnetic (NM) spin configurations. E_g is the band gap width (in eV) and $H_f^{V_2O_5}$ marks the calculated oxidation enthalpy of the vanadium pentoxide phase from the rutile VO_2. The reference energy of the rutile VO_2 phase was taken from both ferromagnetic (FM) and non-magnetic (NM) calculations.

(PBE, PBE+U), 50 % (SCAN) and 40 % (SCAN+rVV). The electronic band gap is, unlike the VO_2 phases, very well captured with all DFT functionals which yield a similar value than those obtained from the experiment that is about 2.3 eV[140] . The performance of all DFT functionals is comparable, showing that the resulting electronic band gap is 0.1 eV to 0.4 eV underestimated with respect to the experimental reference.

A relevant property for the following discussion is the oxidation enthalpy of the vanadium pentoxide phase with respect to the vanadium dioxide $H_f^{V_2O_5}$, described by the following reaction: $2VO_2 + 1/2O_2 \rightarrow V_2O_5$. As shown in the Table 3.1, this quantity is closer to the experimental value when using spin-polarized calculations as reference values for the rutile VO_2 total energies. The non-magnetic calculations overestimate the experimental value by 0.72 eV to 0.87 eV due to an energy penalty that comes from the suppression of local magnetic moments. However, spin-polarized calculations reduce this error significantly as expected, namely by $0.16-0.65$ eV. In case of the PBE+U, SCAN and SCAN+rVV functionals the calculated oxidation enthalpy is in a good agreement with experimental value of 1.28 eV, showing an error in the range of 70 meV to 190 meV per V_2O_5 unit. The PBE functional overestimates the oxidation enthalpy even when the ferromagnetic spin treatment is used, which is a consequence of two facts. First, the oxidation enthalpy is the lowest among the used functionals while performing nonmagnetic spin calculations. Second, the magnetization energy calculated with the PBE functional is significantly lower as compared to the PBE+U and SCAN functionals.

3.3.3 Summary

The performance of the Density Functional Theory was studied in several VO_x systems: rutile and monoclinic VO_2 phases, the displaced rutile VO_2 phase and V_2O_5 phase. The structural, electronic and energetic properties of these systems are presented as calculated with PBE, PBE+U, SCAN and SCAN+rVV functionals. According to the findings in

the present work there is no computational setup that describes the considered properties of all these VO_x systems at the same time in agreement with experiment. However, several computational setups have been found that can reasonably well treat the rutile and monoclinic VO_2 phases separately. For example, spin-polarized PBE, SCAN and SCAN+rVV functionals yield correct values for structural parameters as well as for electronic properties of the rutile VO_2 phase. However, the pairing distances, parameters of the unit cells, electronic band gaps and stability of the monoclinic VO_2 phase was captured well with the non-magnetic SCAN and SCAN+rVV functionals. Shown as well is the fact that the bare functionals reveal a phonon softening instability of the rutile phase at Γ, which is suppressed by the PBE+U functional. However, the on-site corrections lead to strong distortions of the rutile VO_2 phase and open an electronic band gap, which leads to changes of occupation numbers of respective Vt_{2g} orbitals. Moreover, the spin-polarized PBE+U functional predicts the wrong energetic order of the ground-state phases and shows an instability of the monoclinic phase which was transformed to the rutile phase during the structural relaxation.

In the last section the performance of the DFT functionals for the V_2O_5 phase was evaluated, showing that all functionals give a reasonable agreement with experimental data concerning the structural and electronic properties. However, a large difference between the spin-polarized and non spin-polarized calculations was identified when calculating the oxidation enthalpy of the V_2O_5 phase. In this case the total energy differences between the non-magnetic and ferromagnetic calculations change the reaction enthalpies by $0.2-0.65\,\text{eV}$ per VO_2 unit. Generally, the spin-polarized calculations yield values closer to the experiment.

3.4 Stoichiometric rutile VO$_2$ surfaces

3.4.1 (1×1) surface orientations

To investigate the surface properties of vanadium dioxide the stoichiometric low-index (011), (110), (001), (100) and (111) surface orientations as depicted in panels 3.11a-e were considered first for calculations using the PBE, PBE+U, SCAN and SCAN+rVV functionals with ferromagnetic and nonmagnetic spin configurations. As seen, the different cutting planes yield different coordination geometries of the surface vanadium atoms. The whole (011) surface is composed of corner-sharing square pyramids with surface lattice vectors equal to a and $\sqrt{a^2 + c^2}$. The topmost oxygen atoms exhibit parallel zig-zag chains along the $[01\bar{1}]$ direction, separated by the length of the a lattice vector, namely $4.55\,\text{Å}$. The (110) surface is composed of alternating chains of edge-sharing octahedra, which include the topmost row of oxygen atoms along the [001] direction, and edge-sharing square pyramids that are interconnected with octahedra by a single oxygen-vanadium bond. The lengths of the surface lattice vectors are c and $\sqrt{2}a$, which results in a $\sim 25\,\%$ smaller surface area compared to the (011) surface. The separation of rows is equal to the latter surface vector, namely $6.43\,\text{Å}$. As on the (011) surface, the topmost oxygen atoms are coordinated two-fold. Considering the (001) surface, its atomic composition is made of chains of alternating octahedra and tetrahedra, parallel to the $[1\bar{1}0]$ direction and separated by $1/2\sqrt{2}a = 3.22\,\text{Å}$. However, the vanadium atom is not placed in the

		PBE		PBE+U		SCAN	SCAN+rVV
FM	(110)	26		44		36	48
	(011)	51		66		71	82
	(100)	28		51		47	60
	(001)	74		76		97	108
	(111)	84		83		114	127
NM	(110)	24	18[a]	25	22[b]	40	53
	(011)	51	46[a]	56	30[b]	76	85
	(100)	27	26[a]	30	29[b]	50	64
	(001)	59	60[a]	60	59[b]	76	88
	(111)	86	78[a]	87		110	123

[a] ref. [125]
[b] ref. [30]

Tab. 3.5: Calculated surface free energies in meV/Å^2 for the rutile VO$_2$ low index facets.

center of tetrahedra, but close to the edge, as shown in panel 3.11c. Here the surface area, $a \cdot a$ is only ∼12 % larger than for the (110) surface. A (100) termination exhibits the smallest surface area equal to $a \cdot c$ which is ∼30 % smaller than for the (110) termination. The (100) surface is composed of the parallel rows made of edge-sharing square pyramids, separated by the a lattice vector, namely 4.55 Å as in case of the (011) surface termination. The (111) surface exhibits the most complicated surface termination, composed of the parallel chains of vanadium tetrahedra with displaced central atoms as in case of the (001) termination, linked with square pyramids in edge-sharing fashion. The separation of these rows is equal to 4.30 Å. The surface lattice vectors have the length $\sqrt{a^2 + c^2}$ and $\sqrt{2}a$, the angle between them is equal to 53.2°, resulting into the overall surface area very close to the (001) termination, 12 % higher than the area of the (110) surface unit cell.

The calculated surface energies for these surface terminations, using various DFT functionals and spin configurations are shown in Table 3.5, referenced to already reported values for the non-magnetic PBE and PBE+U functionals[30, 125]. In agreement with previous reports, all present calculations show that the (110) surface termination shows the highest stability among other low-index facets. Compared to other functionals, PBE generally yields low surface energies. Especially for the (110) surface the resulting value 24 meV/Å^2 is ∼50 % lower than for the TiO$_2$(110) surface, which is calculated to be 46 meV/Å^2[145]. This is improved with the SCAN functional or spin-polarized PBE+U functional. Furthermore, the van der Waals corrections generally increase the surface energies by 11 to 14 meV/Å^2. On the other side, the (111) surface is the least stable, independent of the chosen functional and spin configuration. In case of the (NM) PBE functional, the present values differ from the Mellan's report[125] by up to 25 % for the (110) termination, the (011) and (111) facets agree within 10 % tolerance and calculated surface energies for (100) and (001) surfaces are in a perfect accordance. The reason for the mismatch in these particular cases is a different thickness of slabs used to calculate the surface free energy. Table 3.5 shows that the spin-polarized and non-spin polarized calculations yield similar surface energies, that differ significantly (by more than 10 %) only in some special cases. The first exception is the (001) surface which yields ∼20 % decrease

(a) 011

(b) 110

(c) 001

(d) 100

(e) 111
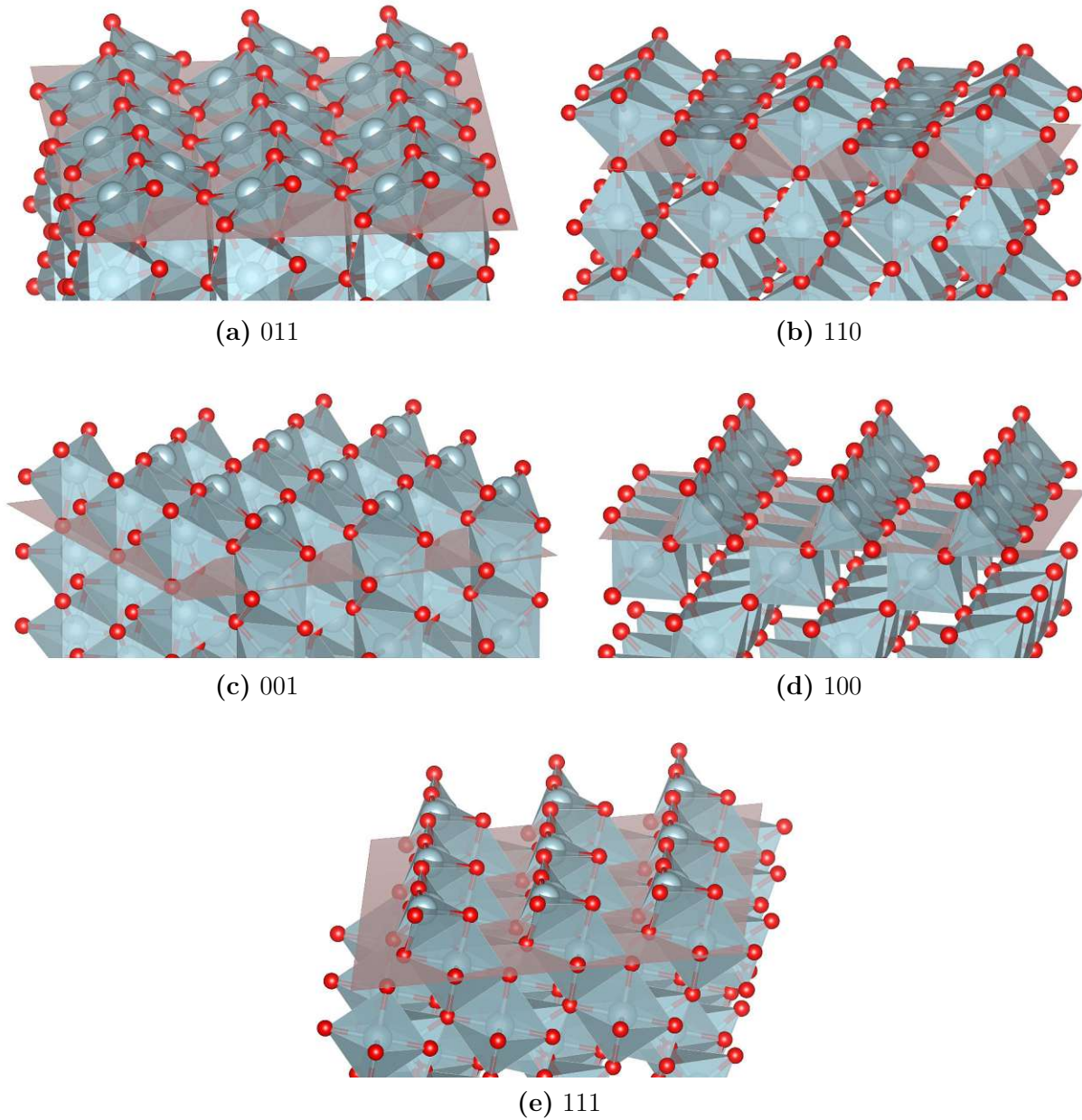
Fig. 3.11: Surface structures of considered terminations.

for the surface energy when using non-magnetic calculations. The resulting values that yields the (NM) PBE+U functional are in a perfect agreement with the values reported by Wahila[30], except for the (011) surface where the present value is, surprisingly, larger by 90 %. The decrease in the surface energy obtained from (NM) calculations with respect to (FM) calculations is also visible within all surface orientations except the (111) surface, when using the PBE+U functional. The (NM) surface energies are in this case lowered by $15 - 43\%$.

To investigate the effect that lowers the surface energies for these cases when using non spin-polarized calculations, the surface-resolved projected density of states onto atomic-like vanadium d orbitals is drawn. Projections for some particular structures are shown in

(a) (110), (NM) PBE

(b) (110), (FM) PBE

(c) (001), (NM) PBE

(d) (011), (NM) PBE+U, U=2 eV (left panel), U=3.25 eV (right panel)
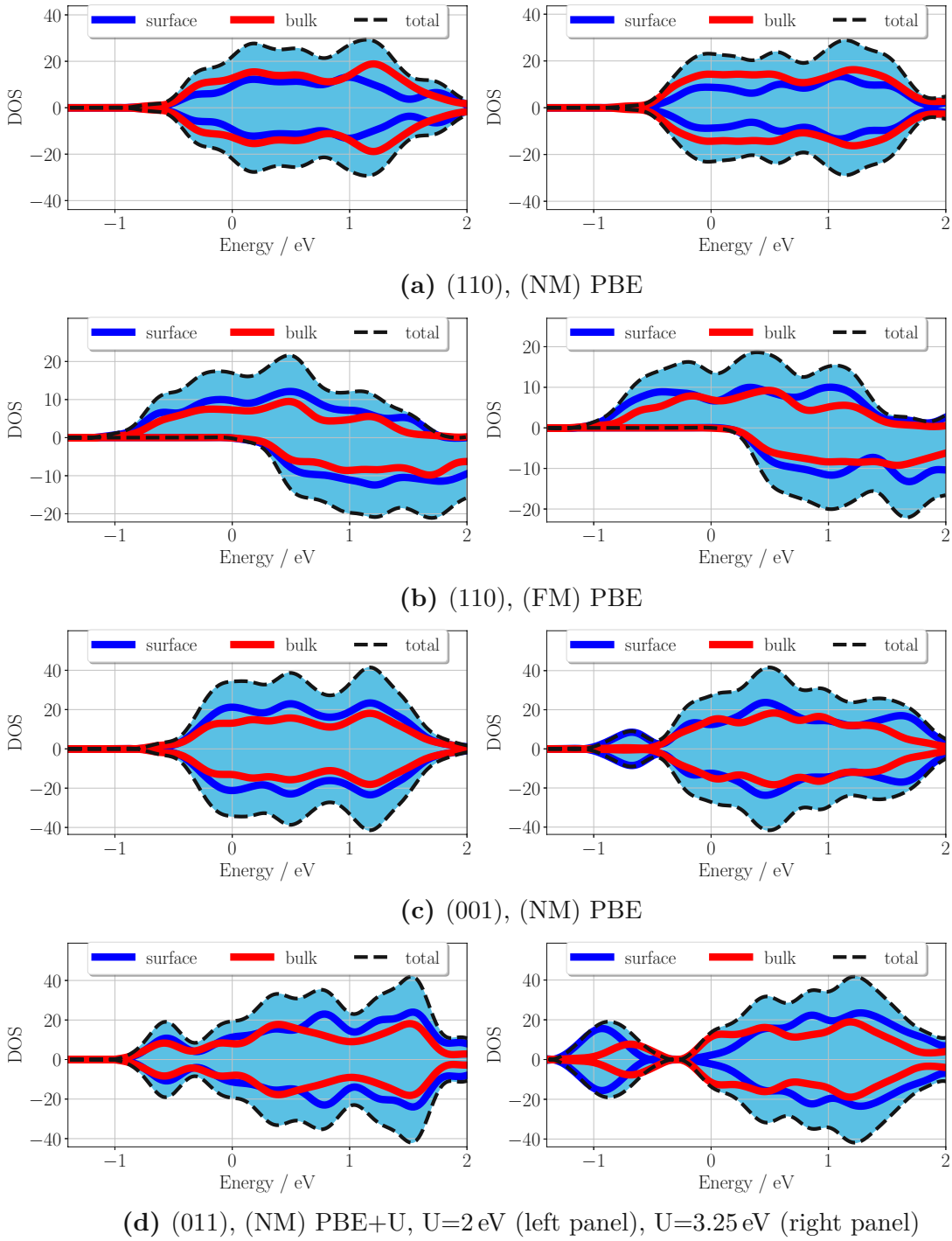
Fig. 3.12: Projected density of states near the Fermi level onto atomic-like d orbitals of the surface and bulk vanadium atoms. Left panels in (a-c) represent the unrelaxed slabs and the right panels in (a-c) show the projections after the structural relaxation. The respective surface terminations, used DFT functional and spin configuration are given in sub-captions. Panel (d) shows a comparison of V d projections with the (NM) PBE+U functional in the relaxed (011) slab while changing U from 2 eV to 3.25 eV. The latter value for U was used in the reference work[30].

Figure 3.12. Here only projections that are energetically close to the Fermi level are shown, namely the projections in the vanadium *3d* band, calculated from seven-layered slabs. In the present notation, the surface projections are considered to originate from the surface and subsurface layers which gives four layers out of seven in total. The projections from the three middle-layers are marked as the bulk states. Panels 3.12a and 3.12b display these projections in (110) slabs, calculated with the (NM) PBE and (FM) PBE functional, respectively. The left panels show projections of the unrelaxed slabs and the right ones display projections after the relaxation of atomic positions in the slab. Independent of the spin configuration, the bulk projections and surface projections show a similar trend and also the resulting surface energies from the spin-polarized and non-spin polarized calculations differ only by $2 \, \mathrm{meV/\mathring{A}^2}$. However, the qualitative results differ for the (001) slabs which also yield different results for surface free energies while using (NM) and (FM) spin configurations. This is shown in panel 3.12c with projections for the unrelaxed and relaxed slabs on the left and on the right, respectively, calculated with the non-spin polarized PBE functional. While the unrelaxed slabs result into similar projections with respect to the (110) surface (panel 3.12a, left side), the relaxed (001) slabs yield an additional peak around $-0.7 \, \mathrm{eV}$ below the Fermi level that is fully composed of surface states. Note that this additional peak is not observed in the relaxed (110) slabs (panel 3.12a, right side). On the other hand, the $\mathrm{V} t_{2g}$ projections on the bulk and surface vanadium atoms calculated with spin-polarized DFT functionals do not differ significantly from each other. These results suggest that the decrease of the surface energy in the non-magnetic calculations is caused by changes in the complex electronic structure that are imposed by the surface vanadium states. To further support this presumption, the surface free energy of the unrelaxed slabs was calculated which yield similar projections onto the surface and bulk vanadium atoms. Indeed, the surface energy of unrelaxed slabs has changed only slightly from 125 to $129 \, \mathrm{meV/\mathring{A}^2}$ between the spin-polarized and non spin-polarized calculations.

The dependence of the surface free energy on the spin configuration for the PBE+U functional is due to a split of the $\mathrm{V} t_{2g}$ band in the spin-polarized calculations, which also changes the occupation numbers of respective V3*d* orbitals, see the (NM) and (FM) density of states in Figure 3.7. Since the splitting of the $\mathrm{V} t_{2g}$ band appears in the bulk, one can expect that (FM) and (NM) calculations yield different values for the surface energy also in the unrelaxed slabs. In that case one finds out that the non spin-polarized calculations give $\sim13 \, \%$ lower surface energies. This finding indicates that the origin of the higher surface energies for all considered terminations, except the (111) surface, is related to the electronic transition in the bulk when calculated with the spin-polarized PBE+U functional.

The last difference shown in Table 3.5 is between the (NM) PBE+U (011) surface free energy, when U was set to $2 \, \mathrm{eV}$ and $3.25 \, \mathrm{eV}$. The latter value was used in the previous study [30]. The comparison of projections in relaxed (011) slabs is shown in Figure 3.12d. The most significant difference while using higher value for U, is a separation of both bulk and surface projections from the V*3d* band, showing separated peaks at $-0.7 \, \mathrm{eV}$ and $-0.9 \, \mathrm{eV}$ for bulk and surface projections, respectively. This instability is again surface dependent and has not been observed on (110) terminations.

(a) (FM) PBE   **(b)** (NM) PBE   **(c)** (NM) PBE (ref)

(d) (FM) PBE+U   **(e)** (NM) PBE+U   **(f)** (NM) PBE+U (ref)

(g) (FM) SCAN   **(h)** (NM) SCAN

(110)
(011)
(100)
(001)

(i) (FM) SCAN+rVV   **(j)** (NM) SCAN+rVV
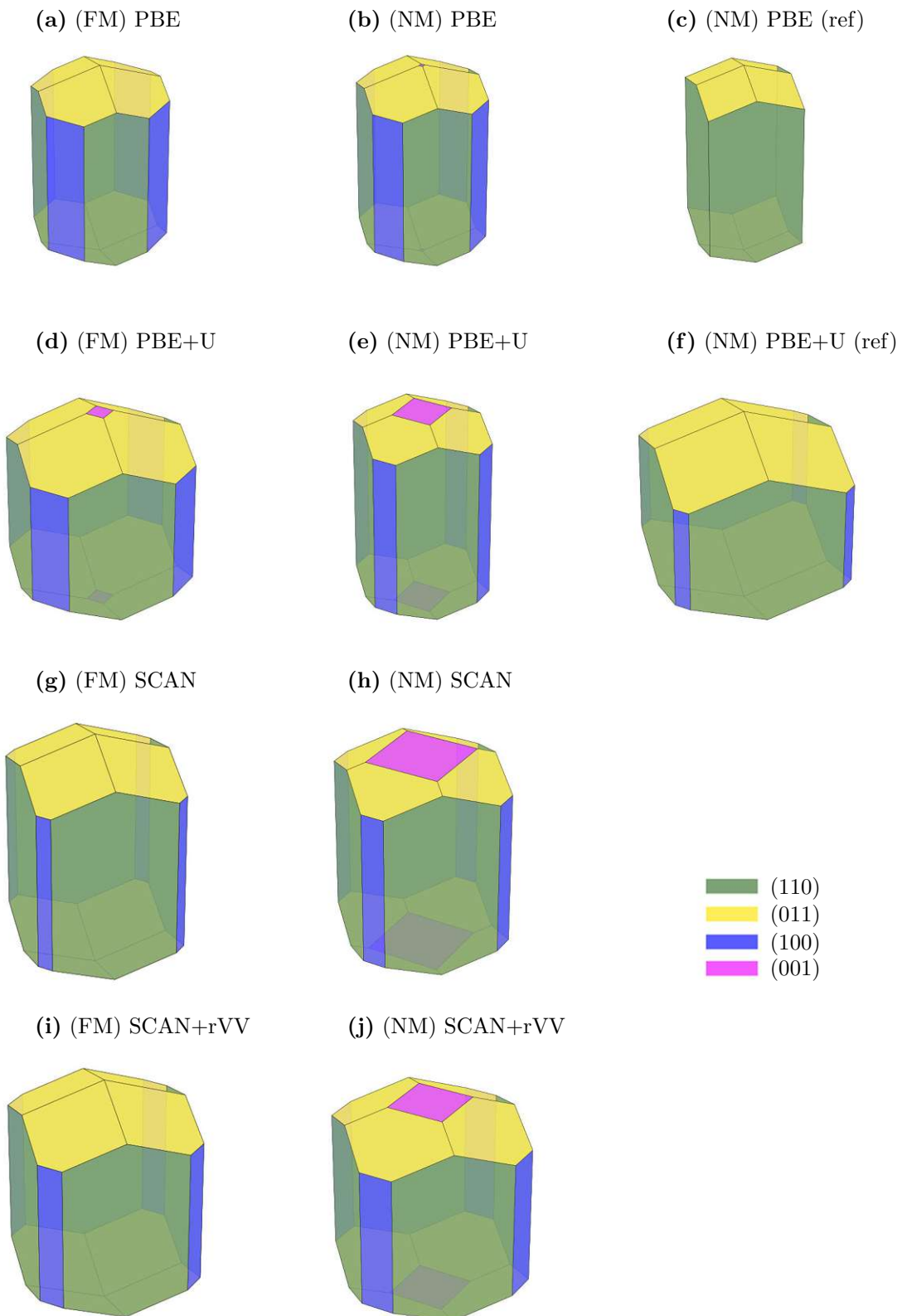
Fig. 3.13: Wulff's construction for the equilibrium rutile VO_2 particles, calculated with different DFT functionals and spin configurations. The reference values of the surface free energy for the (NM) PBE and (NM) PBE+U Wulff's constructions shown in panels (c) and (f) are taken from [125] and [30], respectively.

49

In the next step the shapes of equilibrium rutile VO_2 particles are drawn using the Wulff construction as implemented in WulffPack[146], for all functionals and nonmagnetic and ferromagnetic spin configurations. The present results are also compared to reference data obtained from reported works[30, 125] where the PBE and PBE+U functionals have been used. The resulting crystal shapes are displayed in Figure 3.13. In all cases, the (110) termination dominates in the crystal, accompanied by the (011) surface. In all present calculations, a minor contributions of the (100) surface is also visible, which is not the case in the reference (NM) PBE calculations [125]. The most prominent difference is the presence of the (001) surface in Wulff constructions resulting from non-magnetic PBE+U, SCAN and SCAN+rVV calculations, compared to the spin-polarized calculations. A comparison of the reference Wulff shapes with the present results shows significant deviations, due to the different values of the surface energy resulting from either a different computational setup (PBE), or from a larger U parameter in the PBE+U calculations.

The LEED measurement for a well-defined VO_2 single crystal orientation[32] shows a rectangular pattern above the transition temperature after annealing single crystals at $600\,°C$. LEED images allow to extract the ratio of surface lattice constants $a_S/b_S = \sim 2.3$. This value would either fit to the $VO_2(110)$ surface which yields the ratio $a_S/b_S = \sqrt{2}a_R/c_R = 2.26$, or the $VO_2(011)$ (1×2) surface that yields a ratio of the surface vectors $2\sqrt{a_R^2 + c_R^2}/a_R = 2.36$. Thus, one cannot clearly state which surface termination is observed in the experiment.

To distinguish between the (110) and (011) surfaces STM images have been computed using the Tersoff-Hamann approximation [147] and compared to experiment data. As shown in Figure 3.14, the calculated STM images of the $VO_2(110)$ terminated surface are composed of straight, bright chains with a distance of $6.45\,Å$ (for the non spin-polarized SCAN functional) which are formed by the two-fold coordinated oxygen atoms. This appearance is different from that of the semiconducting $TiO_2(110)$ surface, where the bridging oxygen rows appear dark [148], but the same as that of $RuO_2(110)$, which is also metallic [149]. Both, the appearance of rows and their separation is in agreement with experimental STM images of a rutile $VO_2(110)$ (1×1) termination, as shown in Figure 3.18. On the other side, bright features on the $VO_2(011)$ termination shown in Figure 3.14d are formed by both vanadium and oxygen atoms, resulting in zig-zag chains. Therefore, the experimental LEED patterns have been assigned to the rutile $VO_2(110)$ termination.
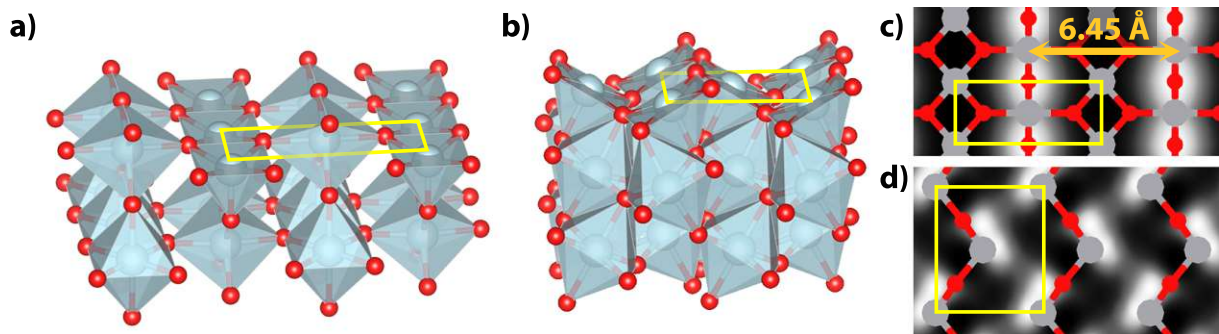
Fig. 3.14: Side views and simulated STM images (empty states) with the non-spin polarized SCAN functional of (a,c) the rutile VO$_2$(110) and (b,d) the rutile VO$_2$(011) bulk terminations using the Tersoff-Hamann approximation[147] with the bias voltage of 2 V. Image reprinted from [32].

3.4.2 Rutile VO$_2$(110) (2×1) surface reconstructions

As shown in the previous section, the rutile VO$_2$(110) surface orientation has the lowest surface energy, independent of the considered DFT functional and spin configuration, and simulated STM images agree with those obtained from the experiment. Therefore, a closer look into this particular surface termination is taken.

A simple relaxation of the VO$_2$(110) (2×2) surfaces does not result in a broken symmetry. Therefore, a simulated annealing of the bulk-terminated VO$_2$(110) (2×2) surface was performed to sample the configuration space and the resulting structure was subsequently relaxed with the PBE, PBE+U, SCAN and SCAN+rVV functionals. The non spin-polarized calculations show that even for the bare (110) surface the calculated ground state has a lower symmetry, resulting in the (2×1) superstructure shown in the left panel in Figure 3.15a. The surface displays a buckling in the topmost layer, which is formed by an unpaired zigzag line as in case of the monoclinic M2 phase[117]. The relative height difference in this buckled row depends on the respective functional and ranges from 0.20 Å to 0.43 Å. A tendency towards buckling can already be observed for the bulk phases of VO$_2$: On the one hand, a monoclinic pairing is present in the [100] direction of the monoclinic ground state, on the other hand, an imaginary DFT phonon mode of the rutile structure, also present at the PBE level[136], indicates an instability by shifting the oxygen atoms along the [001] direction with respect to the vanadium atoms. Therefore, the stability of the buckled surface was confirmed by two different models. First, fully relaxed five-layered slabs were considered. Second, five-layered slabs have been used where the bottom layer was fixed to its bulk structure and the rest of the atoms was clamped in the [001] and [1-10] direction to separate the surface from the bulk contributions so that the phonon softening instability at Γ is restricted. Even in case of the partially fixed slabs, the buckled surface shows a similar behavior: the buckling stabilizes the surface by 40 meV, 15 meV, 9 meV and 11 meV per the (2×1) slab using the (NM) PBE, PBE+U, SCAN and SCAN+rVV functionals, respectively. These results reinforce the above assumption that this buckling is indeed a surface effect and not driven by instabilities in the bulk phase. Fully relaxing the slabs increases the stability induced by the buckling by 72 meV, 39 meV, 45 meV and 59 meV per the (2×1) slab, respectively, for the functionals above. In this case the additional energy gain by the buckling is naturally increased due to an additional possible relaxation in the surface plane, which was restricted in the fixed slabs.

The buckling is accompanied by a change in the projected density of states onto *3d* orbitals of upper vanadium atoms that are situated in the buckled row. The occupation number of the vanadium *3d* band is decreased by $\sim$0.2$-$0.6 e$^-$ with respect to the unbuckled surface, depending on the functional used. However, spin-polarized calculations with ferromagnetic spin ordering show a different trend. The PBE, SCAN and SCAN+rVV functionals suppress the stability of the buckled surface and transform it into the pure (110) termination. Thus, the buckling is only present at the PBE+U level, giving 26 meV extra more stability in case of the fully relaxed slabs. Changes of the electronic structure driven by the surface buckling were further investigated with help of Wannier projections onto V *3d* orbitals on the buckled and unbuckled surface vanadium atoms, see Fig. 3.15c-e. In the present notation, the x axis of the local coordination system is set parallel to the [001] lattice vector, y axis is set perpendicular to the surface plane *i.e.* along the [110] direction and the z axis points along the [1$\bar{1}$0] direction. Panels 3.15c-e show projections
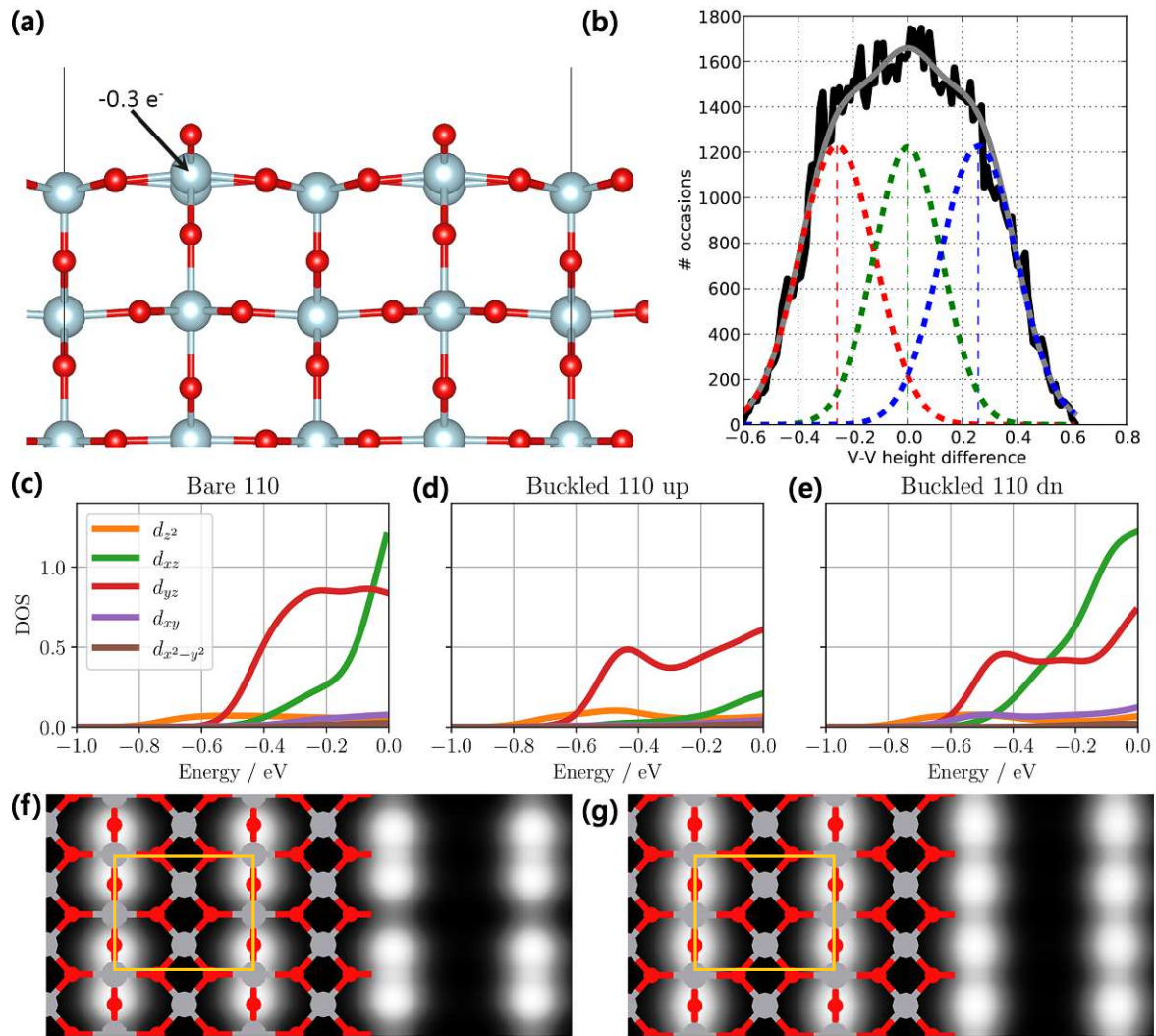
Fig. 3.15: Panel (a), buckled (2×1) reconstruction obtained from the simulated annealing and subsequent optimization. The buckling is accompanied by a change in the occupation number of the V $3d$ band of the upper vanadium atom (see the black arrow), that is decreased by 0.3 electrons as calculated with the (NM) PBE functional. The graph in panel (b) shows the distribution of the height difference between the V-V pairs during the molecular dynamics simulation (black line), fit with three Gaussian functions (red, blue and green lines) which correspond to the up-down, non-buckled and down-up configurations respectively. Gray line is the sum of all fit functions. Panels (c-d) display calculated STM images with the (NM) SCAN functional of the buckled and unbuckled surface, respectively. Yellow rectangles mark the (2×1) surface unit cells. Panels (e-f): comparison of projected density of states onto Wannier functions localized at vanadium atoms between the bare (110) and the buckled surface, calculated with the non-spin polarized SCAN functional. Only the Vanadium $3d$ band is shown.

onto the unbuckled, buckled-up and buckled-down surface vanadium sites, respectively. A comparison of those projections reveals that the d_{yz} orbital in the buckled system is less occupied with respect to the unbuckled surface and the occupation of the d_{xz} orbital is dependent on the position of the buckled vanadium atom. Wannier projections also show a difference between the surface buckling and the monoclinic buckling: while the monoclinic buckling enhances the occupation of the d_{xy} orbital[117], the d_{xy} occupation in the surface layer is reduced almost to zero.

The effect of buckling on calculated STM images is shown in bottom panels of Figure 3.15f-g. The most prominent change in calculated STM image of the buckled surface is the presence of paired bright features that proceed from the topmost two-fold oxygen atoms.

Since the small energy gain due to the buckling might render an experimental verification difficult, a molecular dynamics (MD) simulation at experimental temperatures was used to evaluate the thermal stability of the buckling. The simulation for 100 ps was performed employing the non-magnetic PBE functional, which shows the largest energy difference between the buckled and the bare (110) surface, a temperature of 350 K and a time step of 1 fs. The most prominent feature of the buckled surface, namely possible switches in the z-positions (i.e. along the surface normal) of the V-V pairs was monitored. In order to decrease the computational cost the thickness of the slabs was reduced to four layers where the bottom layer atomic positions were frozen and the k-points grid was reduced to $2 \times 2 \times 1$ points. The results of the MD simulations are shown in Figure 3.15b as the number of switches at the y axis and the buckling size at the x axis. The plot also shows a fit of the MD data (black line) with three Gaussian functions, related to the buckled (red line), non-buckled (green line) and flipped buckled (blue line) configurations. The sum of the three Gaussian fits (gray line) shows that the buckled configuration is thermally smeared since there are no maxima at the positions of the Gaussian functions related to the buckled configurations. Furthermore, the average flipping time from the up-down to down-up configurations was calculated to be 260 fs. Thus, one may conclude that the time dependent stability of the buckling is much shorter than the resolution limit of atomically resolved STM experiments, as imposed by the typical scanning rate.

Since the occupation of the V-3d states is quite sensitive to buckling, it is advisable to determine to what extent a varying oxygen coverage influences the size of the buckling, by comparing bare (clean), 50 % and 100 % covered VO_2 surfaces as depicted in Figures 3.16a-c. Figure 3.17 clearly shows that all non-magnetic functionals predict a stable buckled surface and that its stability increases with oxygen coverage. The energy gain due to the buckling ranges from 39 meV (PBE+U) to 72 meV (PBE) for the bare surface, as already discussed above, and increase with oxygen coverage, adding further stability which ranges from 61 meV (PBE+U, SCAN) to 83 meV (SCAN+rVV) per the (2×1) slab for a fully-covered surface. Quite evidently van der Waals interactions included in the SCAN+rVV functional have only a negligible impact on the stability of the surface buckling.

Since all spin-polarized functionals except PBE+U predict an unbuckled surface, these (negative) values are omitted in Figure 3.17, and only the (FM) PBE+U value of 26 meV is included. However, the trend changes with increasing the oxygen coverage to 50 %, which compared to non-magnetic runs yields a further 20 % (PBE), 60 % (PBE+U), 70 % (SCAN), and 40 % (SCAN+rVV) stabilization of the surface buckling, which ranges from
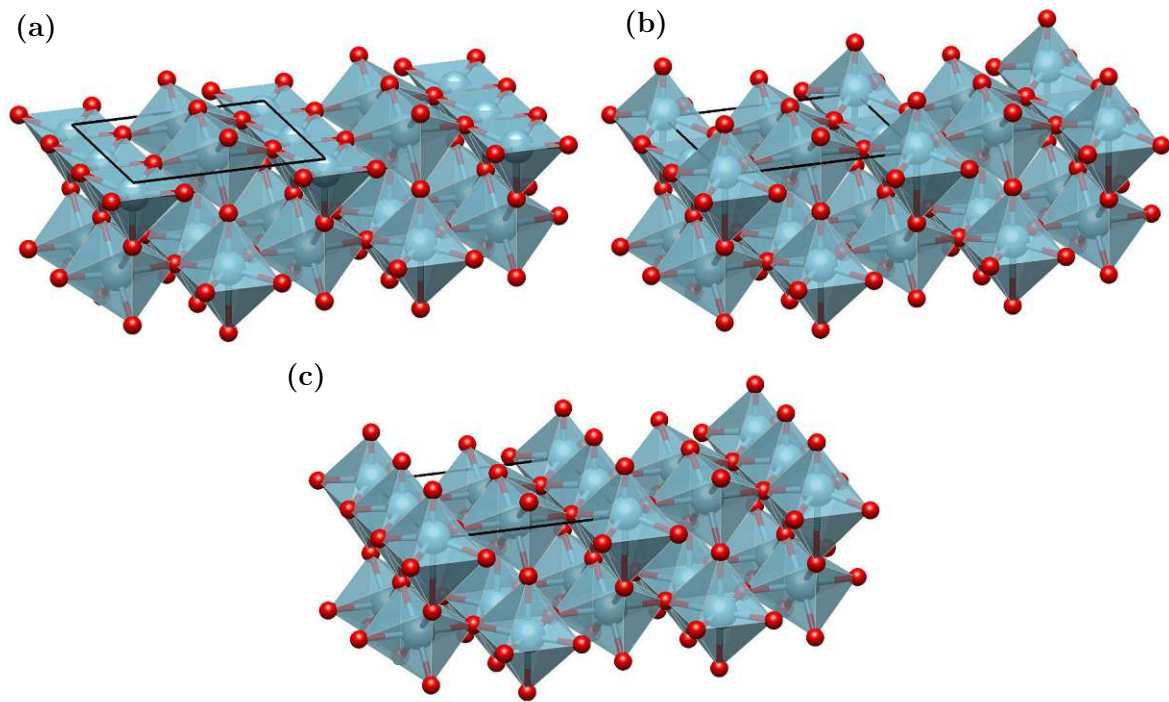
Fig. 3.16: Perspective views of (2×1) supercells showing (a) the bare 110 surface, (b) 50 % covered and (c) 100 % covered rutile $VO_2(110)$ surface. The black lines show the surface are of the (110) (2×1) supercell

100 meV to 140 meV per the (2×1) slab on an absolute scale. Increasing the oxygen coverage to the fully-covered limit, the buckled surface is most preferred for the (FM) PBE+U functional which adds a 510 meV extra stability per the (2×1) slab. The other functionals, PBE, SCAN and SCAN+rVV also prefer a buckled surface by 104 meV to 137 meV per the (2×1) slab without any significant difference between the non-magnetic and ferromagnetic spin configurations. The comparably large energy gain for the (FM) PBE+U functional is attributed to the opening of the gap in the bulk and hence to a reduced screening of the induced charge imbalances upon oxygen adsorption. Thus, this buckling might play a non-negligible role for the stabilization of oxygen-rich surface reconstructions proposed in recent experimental studies[30, 31] and even more on surfaces of the insulating M phase of VO_2.

3.4.3 Summary

The performance of the density functional theory for various rutile VO_2 surface orientations has been evaluated. A surface instability has been found on the (110) surface, which breaks the 1×1 symmetry and leads to a (2×1) superstructure. Among all studied surfaces, the (110) termination exhibits the lowest surface energy independent of the DFT functional and spin configuration and also matches best with LEED and STM experiments. The (111) surface is calculated to be the least stable and is not present in calculated shapes of the equilibrium rutile VO_2 particles.

55
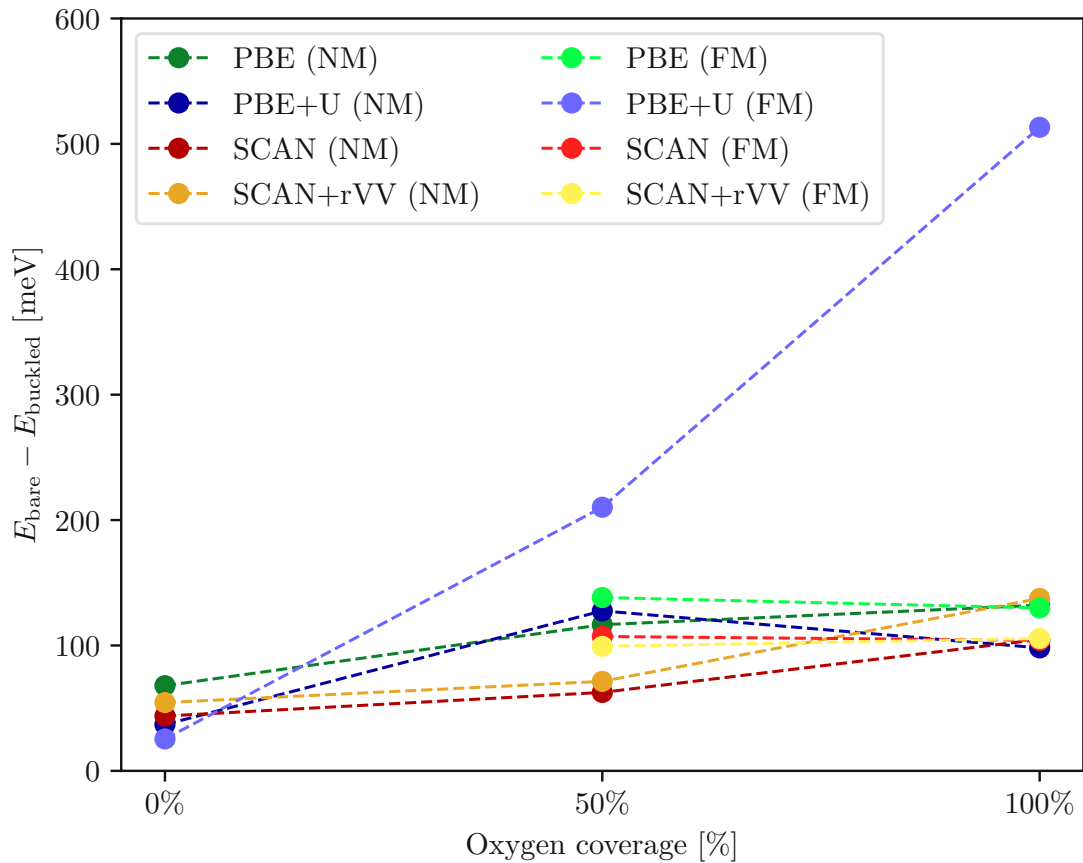
Fig. 3.17: Additional stabilization (in meV per the (2×1) slab) induced by buckling in a $VO_2(110)$ surface, determined with several DFT functionals for non-magnetic (NM) and ferro-magnetic (FM) spin configurations. (FM) PBE, (FM) SCAN and (FM) SCAN+rVV predict no buckling for bare $VO_2(110)$ and therefore these points are not included.

A comparison of the performance of different DFT functionals and spin configurations has also revealed that the resulting surface free energies for low index facets can be influenced in some particular cases by surface states or by the splitting of the V*3d* band in the bulk. The (001) termination calculated with the non-spin polarized DFT functionals show a $15-21\,\mathrm{meV/\AA^2}$ decrease compared to the spin-polarized calculations, which induces a presence of the (001) termination in the Wulff shapes. However, LEED measurements on single crystals[150] revealed that the $VO_2(001)$ surface shows faceting, which indicates that this surface termination is rather unstable. The spin-polarized PBE+U calculations, which open the band gap in the bulk rutile phase, yield higher surface energies compared to the non-spin polarized calculations. Finally, the influence of the size of the on-site Coulomb repulsion has been investigated and a dependence of the surface energies for the (011) surface orientation on the chosen value for U has been found. For this reason the present Wulff shape for the (NM) PBE+U functional differs significantly from the reported PBE+U results [30]. Since the Wulff shape obtained from the (NM) PBE+U calculations contains the unstable (001) surface, one may assume that increasing U to higher values leads to a better description of surface energies of VO_2 surface orientations.

Wannier projections onto surface vanadium atoms that form the buckled chains have revealed that the V-d_{xy} orbitals are unoccupied, in contrast to the bulk rutile and monoclinic VO_2 phases. This finding indicates that the surface buckling effect is not related to the bulk transitions. The additional stability of the buckled surface has also been investigated as the function of oxygen coverage, showing a continuous increase with higher concentration of oxygen adatoms. The highest stability of the buckled surface is obtained for the (FM) PBE+U functional which increases the adsorption energy by $0.33\,\mathrm{eV}$ compared to the unbuckled surface. Thus, this effect might also influence the stability of more complex surface reconstructions.

3.5 Oxygen-rich rutile VO$_2$(110) (2×2) surface reconstructions

The previously discussed rutile $VO_2(110)$ (2×1) reconstructions for the bare surface cannot explain the experimentally observed (2×2) reconstructions. Therefore, the aim of this section is the identification of stable off-stoichiometric surface models which can provide a deeper insight into the structural and electronic properties of surface reconstructions observed in experiments[30, 32].

The first attempt to find the structural model for this surface reconstruction is the extension of the previously discussed (2×1) adsorption phases to (2×2) surface terminations while taking into account that the most preferred adsorption sites on the rutile $VO_2(110)$ surface are square pyramids where the adsorbed oxygen forms a vanadyl bond with the surface vanadium atom [125]. Since the rutile $VO_2(110)$ (2×2) slab contains in total four adsorption sites, there are two ways how to build the surface reconstruction with no translational symmetry inside the (2×2) slab that would result into more simple surface reconstruction: adsorption of a single oxygen adatom, or three adatoms. Here, one additional oxygen atom adsorbed on the buckled surface in the (2×2) slab is considered. Its structure in perspective and top views are shown in Figure 3.18 together with calculated

STM image using the (NM) SCAN functional. As it is depicted, the additional oxygen atom causes two bright spots inside the dark row in the calculated STM image. Considering the experimentally observed symmetries, the calculated STM simulation shows a mirror symmetry along the rutile [001] axis, but the second symmetry axis parallel to the [$1\bar{1}0$] direction hasn't been reproduced. The hole in the adlayer with the unreconstructed (110) (1×1) surface that is observed in experimental STM images can be explained by removal of a surface layer and therefore the layer below is observed. However, this structural model reproduces neither the wide and narrow spacing nor the additional bright features in the center of bright rows. Thus, a direct modification of this surface model that would reproduce these experimental findings is unclear. Note that this problem also holds for other (2×2) surface reconstructions obtained from oxygen adsorption on the rutile VO_2(110) surface.

In conclusion, these findings indicate that adsorption phases are not appropriate structural models that match the experimental findings. Therefore, a more involved way was chosen to find the stable structural model that can recover the experimental STM images as discussed in the next sections.
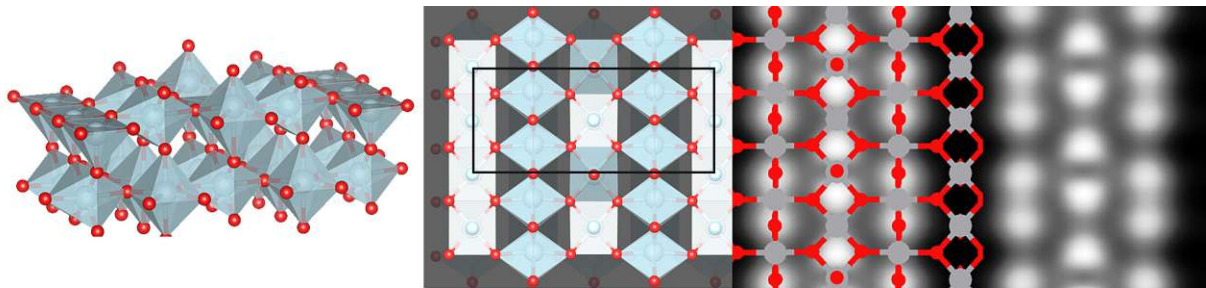
Fig. 3.18: Perspective view, top view and simulated STM image (with the SCAN functional) of the VO_2(110) buckled surface. The black rectangle marks the (2×2) surface unit cell.

3.5.1 Simulated annealing: tetrahedral terminations

In a first step simulated annealing has been used. The whole process consisted of $\sim 10^4$ ionic steps with the time step $1\,ps$ with the initial temperature $2500\,K$, cooled down to $0\,K$ using the Nosé-Hoover thermostat[151, 152] to regulate the temperature fluctuations. In the simulated annealing procedures the spin-polarized PBE functional was used for four-layered slabs where all layers except the surface layer were frozen to prevent structural changes in the bulk part. Once the simulated annealing was finished, the final structure was taken, the thickness of the slab increased by two additional layers and the structure relaxed. During the final relaxation process atoms in two additional layers were kept fixed at their bulk positions. The SCAN functional was excluded from the simulated annealing process due to too large computational costs. Simulated annealing was also done with non-magnetic PBE and PBE+U functionals which gave qualitatively similar structures to the spin-polarized PBE functional results and therefore these structures are not presented here.

In the simulated annealing calculations several surface stoichiometries have been considered, defined as the number of oxygen and vanadium atoms that comprise the surface layer. Here, the two most-stable superstructures are discussed which represent well the general properties of the structures obtained by this approach. The first structure is derived from the fully-covered (110) surface depicted in Figure 3.16. The second structure was created by a removal of two vanadium atoms and two oxygen atoms from the bare VO_2(110) surface layer. Considering the (2×2) slab, one O-V-O trilayer has an overall stoichiometry V_8O_{16}. Hence, the first structure has the surface stoichiometry equal to V_8O_{20} and the latter V_6O_{14}.

The resulting structures obtained from the simulated annealing procedure are shown in top and side views, together with simulated STM images in Figure 3.19. Both final surface structures are composed of corner-sharing tetrahedra with a drastically inflated thickness of the surface layer from 3.2 Å that corresponds to the thickness of the bulk trilayer to 7.2 Å and 4.9 Å for the V_8O_{20} and V_6O_{14} surface stoichiometries, respectively. The larger thickness of the surface layer is also visible from the perspective views, showing that the tetrahedral terminations are rather open. In contrast to the bulk part, empty channels are formed in the subsurface layer. The V_6O_{14} structure shows an empty row in the subsurface layer made of square pyramids, which can be used for adsorption of additional oxygen atoms. Also one oxygen atom occupying every second vanadium site was added, which leads to an overall surface stoichiometry of V_6O_{15}. This structure was also subsequently relaxed. Thereafter, its stability was compared to other tetrahedral terminations. Regarding the simulated STM images, both structures yield bright features located at the topmost oxygen atoms, which is consistent with the calculated STM images of the rutile VO_2(110) surface where oxygen rows also appeared as bright spots.

To compare the stability of all aforementioned tetrahedral terminations, the calculated surface free energy is drawn against the oxygen chemical potential which is depicted in Figure 3.20. In the evaluation of the surface free energy the stability of the initial structures before the simulated annealing procedure was also considered, see the dashed lines. The total energy for the relaxed systems with surface stoichiometries V_8O_{20} and V_6O_{14} after annealing are 1.5 eV and 0.5 eV per the (2×2) slab lower than the respective initial structures. As a result, the effective adsorption energies of excess oxygen atoms that are incorporated in these superstructures are lowered by 0.38 eV and 0.25 eV respectively, as shown in the graph 3.20. Among all studied surface reconstructions with the simulated annealing technique, the most stable structure is the tetrahedral V_8O_{20} reconstruction that would be preferred up to a chemical potential of $\mu = -1.91$ eV. This value for the oxygen chemical potential is close to the ultra high vacuum conditions at 900 K; $\mu_{exp.} = -2.07$ eV at which the single crystals were annealed in the experiment[32]. In even more reducing conditions related to the chemical potentials lower than -1.91 eV, the unreconstructed (1×1) surface is thermodynamically most stable.

Even though the tetrahedral terminations are more stable than the adsorption phases, they still do not match the experimental STM images. A comparison of calculated STM images (Figure 3.19) with the experiment (Figure 3.3) reveals several differences. First, the tetrahedral terminations do not reproduce the double row pattern observed in experiments. Second, the simulated STM patterns do not show a symmetry axes along the [001] and [1$\bar{1}$0] directions and therefore the match with experimental results is rather poor. Another
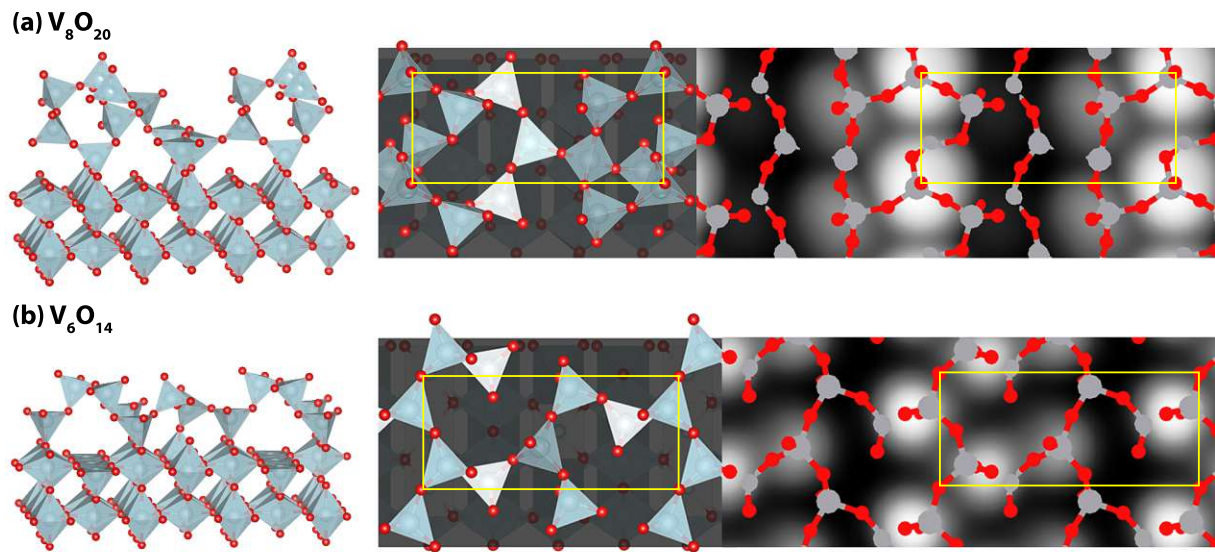
(a) V$_8$O$_{20}$

(b) V$_6$O$_{14}$

Fig. 3.19: Perspective views, top views and calculated STM images of the relaxed structures with the overall surface stoichiometries V$_8$O$_{20}$ (top panel) and V$_6$O$_{14}$ (bottom panel) obtained from the subsequent relaxation of the structures after a simulated annealing procedure. Yellow rectangles mark the rutile VO$_2$ (110) (2 × 2) surface unit cell. Both structures show surface reconstructions composed of corner-sharing tetrahedra. In the STM simulations the bright features originate from the topmost oxygen atoms.

peculiarity of the tetrahedral terminations was identified while employing other DFT functionals with ferromagnetic spin ordering. The stability of the tetrahedral terminations was investigated in more detail by relaxing the tetrahedral termination with the surface stoichiometry V$_6$O$_{14}$ (Figure 3.19b) using spin-polarized PBE+U, SCAN and SCAN+rVV functionals. From the relaxed structures one can extract again surface free energies as a function of oxygen chemical potential. In these supporting calculations the supercells were adapted to the parameters of the rutile bulk obtained from the respective functionals. The performance of the additional functionals for the tetrahedral termination is depicted in Figure 3.21. Here, only the crossing points between the surface free energies obtained from the V$_6$O$_{14}$ tetrahedral termination with the unreconstructed (110) surface (horizontal line) are shown. Note that these crossing points represent the effective adsorption energies of excess oxygen atoms incorporated in the tetrahedral termination.

The results that are depicted in Figure 3.21 show a strong dependence of the calculated crossing points and consequently on the stability of the tetrahedral terminations on the used functional. The PBE, SCAN, SCAN+rVV and PBE+U functionals yield values for the effective adsorption energies equal to -1.88 eV, 1.07 eV, -0.56 eV, and 0.07 eV, respectively. Hence, these tetrahedral terminations are stable only at the PBE level which was also used for the simulated annealing procedure.
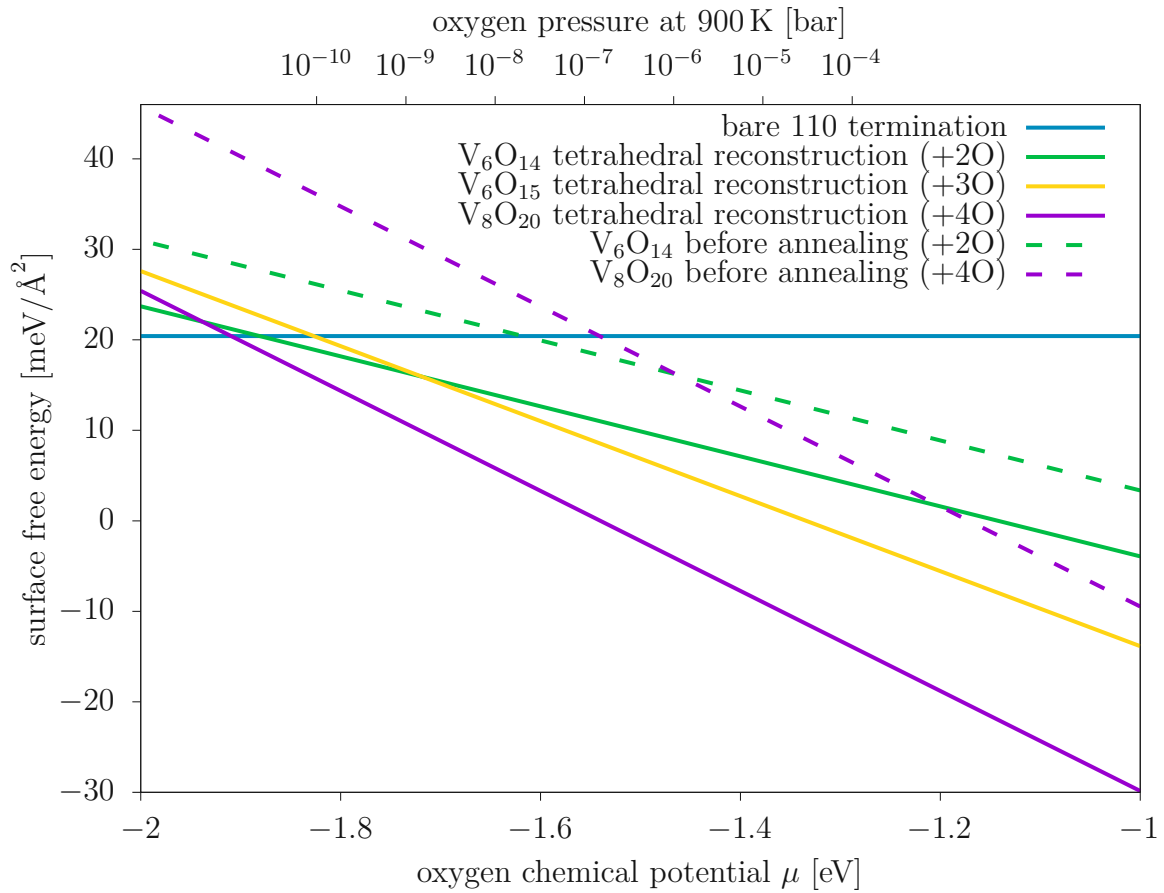
Fig. 3.20: Calculated surface free energy for the tetrahedral terminations as the function of chemical potential, using the spin-polarized PBE functional. The dashed lines represent the calculated surface free energies of the initial structures before the annealing procedure. The yellow line represents the surface free energy of the oxidized V_6O_{15} tetrahedral termination (Fig 3.19, bottom panel), where the additional oxygen atom was subsequently placed into the subsurface layer above the vanadium atom with the square-pyramidal coordination geometry.
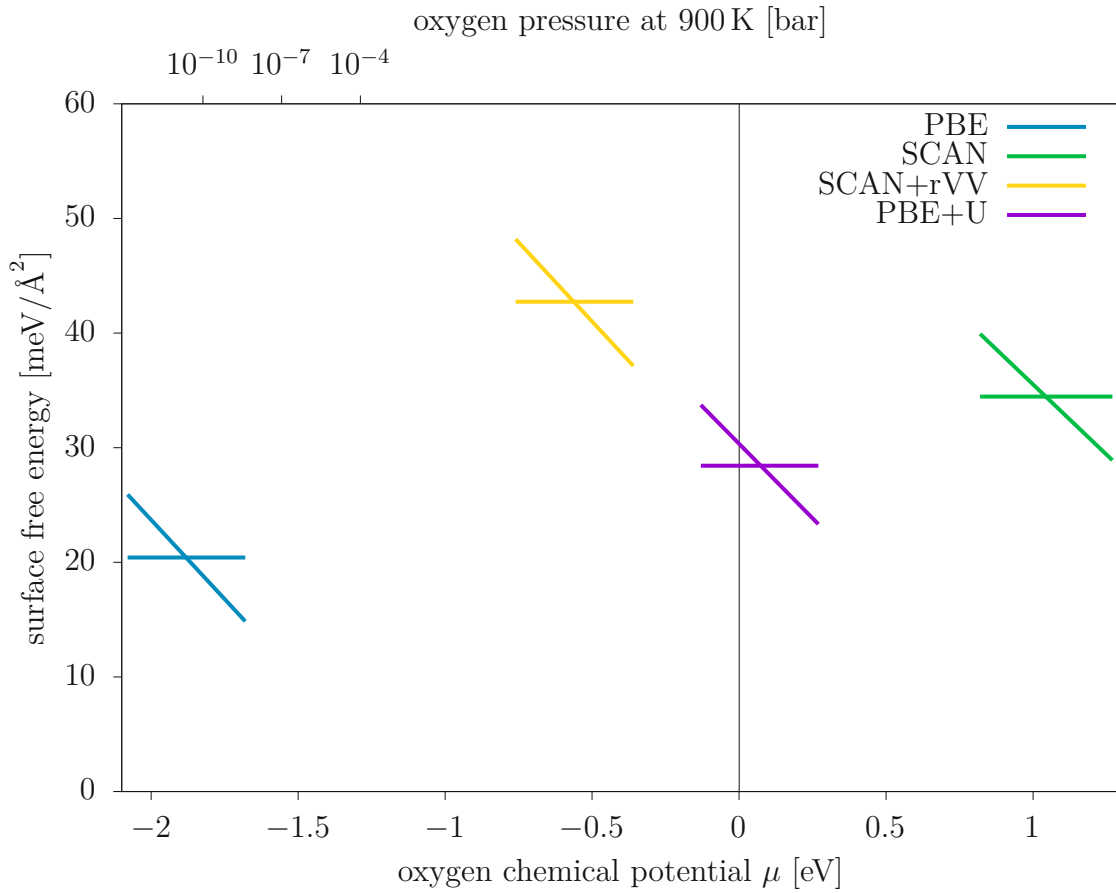
Fig. 3.21: Calculated crossing points (effective adsorption energies) of the surface free energies between the bare rutile VO_2 (110) surface and the tetrahedral termination with the V_6O_{14} surface stoichiometry (Fig 3.19, bottom panel), using the spin-polarized PBE, PBE+U, SCAN and SCAN+rVV functionals. The surface unit cells were adapted according to the relaxed bulk rutile phase with the respective DFT functional.

3.5.1.1 Summary

Performing the simulated annealing procedure with the PBE functional leads to the formation of tetrahedral reconstructions that are more stable than the adsorption phases of the VO_2 (110) surface. These structures have an open structure which causes an enhanced thickness of the surface layer. The large energy gain (1.5 eV) from the formation of the tetrahedral structures indicates that also other arrangements using same building blocks could be more stable than the adsorption phases. However, using simulated annealing for the prediction of the surface structure of $VO_2(110)$ (2×2) reconstructions has several shortcomings. First, simulated annealing is computationally expensive due to the necessity of using high initial temperatures and a proper sampling of time which results into a large number of ionic steps. These consequences exclude performing the simulated annealing with more advanced functionals such as SCAN or SCAN+rVV. Second, stabilities of structures yielded by the simulated annealing strongly depend on the chosen functional, differing up to 3 eV in calculated crossing points. Also the mismatch between the calculated and experimental STM images indicates that these tetrahedral terminations are either a PBE artefact, or the simulated annealing has not been successful in finding the most stable surface termination at the given surface stoichometry.

However, these findings concerning the properties of tetrahedral terminations can be used to find another ways to describe these complex surface terminations.

3.5.2 Educated guess: V₂O₅-like monolayer

Another hint guiding towards an appropriate atomic model for (2×2) superstructure can be derived from experimental findings: XPS measurements indicate an increased concentration of oxygen on the surface and the presence of V^{5+} cations[32]. In addition, the experimental STM images of the (2×2) superstructure (see Fig. 3.2) resemble patterns found on the V_2O_5 (001) surface as characterized by Blum et al. [153], suggesting that a vanadium pentoxide monolayer might be a good starting point for the development of an atomic model.

One takes the orientation of the V_2O_5 lattice such that the cleavage plane is (001), *i.e.*, the V=O vanadyl bonds are roughly parallel to [001]. To fit to the VO_2(110) substrate in a (2×2) configuration, the unit cell of the V_2O_5(001) monolayer needs to be expanded in [100] direction from 11.50 Å to 12.86 Å (i.e., by 12 %), breaking up the structure along the dashed symmetry plane, and in [010] direction from 3.56 Å to 5.70 Å (*i.e.*, by 60 %), see Figure 3.22a. This strong distortion leads to the rearrangement of the V_2O_5 building blocks, namely a change from edge-sharing pyramids to corner-sharing tetrahedra. The dark vanadium polyhedra pointing away from the surface (towards the vacuum) shift along the [010] direction, and the inverted (bright) polyhedra are pulled towards each other in [100] direction. This is marked by yellow arrows in Figure 3.22a. The result is a hexagonal ring of vanadium tetrahedra as shown in Figure 3.22b. A similar structure consisting of corner-sharing up- and down-pointing VO_4 tetrahedra has already been confirmed for vanadium oxide on a Pd(111) surface [154]. For the unsupported model layer (Figure 3.22b), the lateral distance between the oxygen atoms at the top of the tetrahedra along $[1\bar{1}0]$ is 3.8 Å. When this layer is supported by the rutile (110) surface as shown in Figure 3.22c and 3.22d, the distance is slightly decreased to 3.7 Å and 3.6 Å, respectively. In both cases, the surface has an overall stoichiometry of V_4O_{13}. Figures 3.22c and 3.22d show two different configurations indicating how the structure could be placed on the VO_2 substrate underneath. In the first case, panel (c), the ring termination is bound in a corner-sharing fashion, *i.e.*, with just with one oxygen bond, forming a purely tetrahedral termination, and leaving half of the undercoordinated O atoms of the substrate unterminated. These atoms, colored in orange, can be also partly or fully removed, which leads to V_4O_{12} and V_4O_{11} surface stoichiometries. In Figure 3.22d, the ring termination is shifted by a half of the (1×1) rutile [001] lattice vector as marked with the yellow arrow. The additional bond to the undercoordinated O atoms of the substrate layer converts the lower tetrahedra to square pyramids, see black circles in panels 3.22c-d. This shift stabilizes the surface termination by 0.24 eV per (2×2) supercell. Figure 3.22e shows a simulated STM image of the ring structure from the Figure 3.22d. The image consists of pairs of spots with a separation of 3.6 Å, in agreement with the experimental data for the narrow distances of the bright features from panel 3.3. Furthermore, the simulated STM image shows a proper symmetry, namely the mirror axes parallel to the [001] and $[1\bar{1}0]$ direction. Furthermore, the rectangular rows are centered on the oxygen row from the VO_2 trilayer beneath, which is in agreement with the experimentally observed alignment of the (2×2) surface termination, see the yellow line in Figure 3.3. Hence, the ring termination results into the simulated STM patterns that are in a much closer agreement with experiment when compared to the tetrahedral ring terminations obtained from the simulated annealing. As well as the ring terminations obtained from the simulated annealing, both ring structures
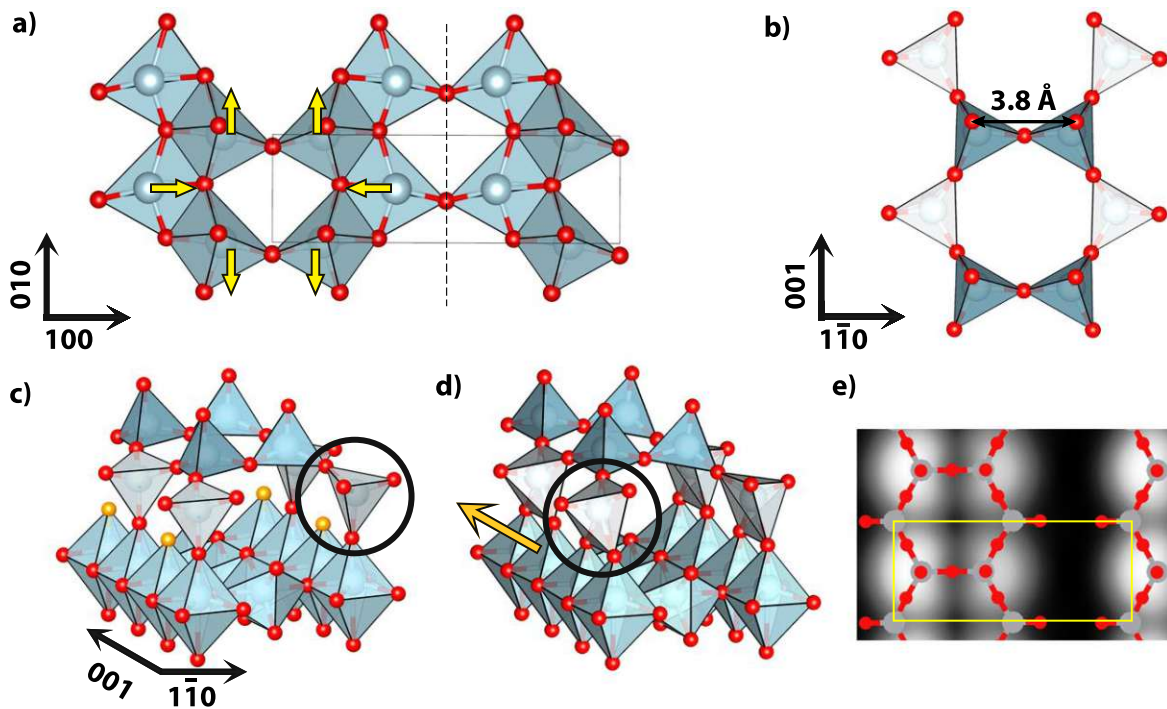
Fig. 3.22: Conceptual steps towards the rutile $VO_2(110)$ ring terminations. (a) A vanadium pentoxide (001) monolayer. The yellow arrows mark the displacement direction of the vanadium atoms, which causes the transformation to the tetrahedral 'ring superstructure' that fits the $VO_2(110)$-(2×2) supercell, shown in (b). Panels (c, d) show side views of two possibilities how this ring structure could connect to the underlying $VO_2(110)$ lattice, resulting in an overall stoichiometry of V_4O_{13}. The purely tetrahedral ring termination (panel c) contains in the subsurface layer V=O vanadyl bonds that can be subsequently removed, see oxygen atoms colored in orange. The difference between these structures is a shift along the [001] direction as it is pointed with the yellow arrow in panel (d), changing the coordination geometry of marked vanadium atoms from tetrahedra to square pyramids. The configuration in (d) is lower in energy. Figure (e) shows a calculated STM image of the ring structure in (d). Image reprinted from [32].

depicted in Figs. 3.22c-d, are thicker (5.5 Å, 5.4 Å, respectively) than a $VO_2(110)$ rutile layer with thickness of 3.2 Å.

The ring termination with the surface stoichiometry V_4O_{13} can also be modified. The most promising candidates were created by adding another vanadium tetrahedron between the rows of the original ring structure with the surface stoichiometry V_4O_{13} as it is shown in Figures 3.23a-b, forming V_5O_{14} and V_5O_{15} rings. The structure in panel (a) with the surface stoichiometry V_5O_{14} connects the rings with another vanadium tetrahedron that is bound to the subsurface layer. The vanadium rings are connected in this case by a single V-O bond to the subsurface layer, as the ring termination in the Figure 3.22c. The V_5O_{14} configuration is therefore structurally similar to the $SrTiO_3(110)$ termination that is shown as the (3×1) surface structure in ref. [155], but with two major differences. The

a) V$_5$O$_{14}$ ring

b) V$_5$O$_{15}$ ring
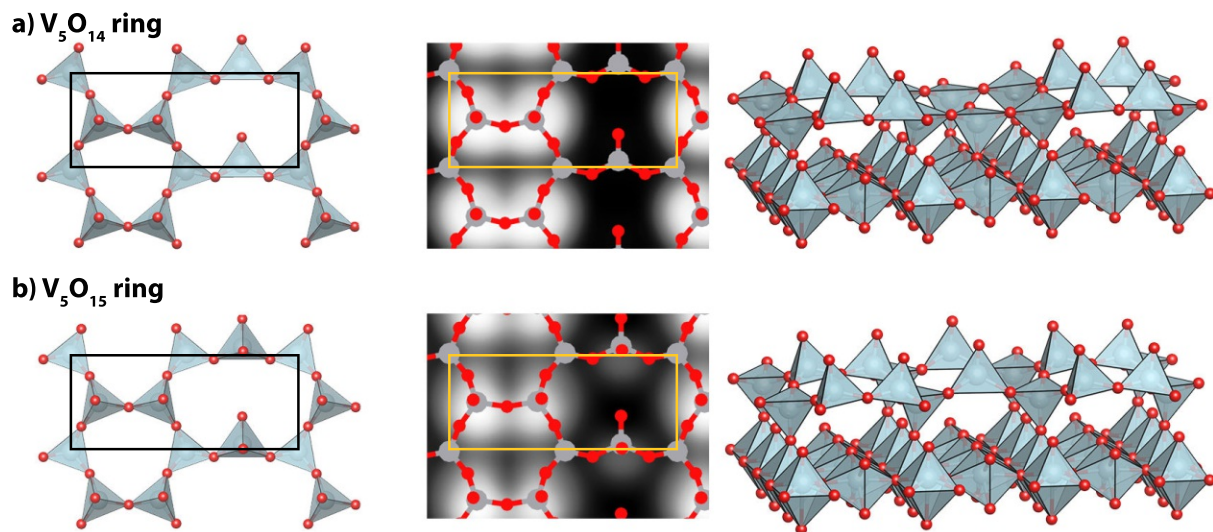
Fig. 3.23: Top views, calculated STM images and perspective views of the relaxed modifications of two ring terminations. In panel (a) the V$_4$O$_{13}$ rings are connected via an additional tetrahedron that is bound to the substrate, leading to an overall V$_5$O$_{14}$ surface stoichiometry. In panel (b) one connecting tetrahedron per (2×2) cell is flipped, resulting in adsorption of an additional oxygen. Image reprinted from [32].

first difference is related to the bonding of the superstructure to the bulk termination. In the case of VO$_2$, vanadium tetrahedra are bound only with a single V-O bond to the VO$_2$ bulk, i.e., this superstructure is more open compared to the titanium tetrahedra that terminate the SrTiO$_3$(110) surface. Secondly, some vanadium tetrahedra are additionally oxidized with another oxygen atom, which results into a disconnection from the (110) surface and the formation of vanadyl bonds on top, as it can be seen by comparing the side views of the structures in the Figure 3.23.

Simulated STM images also show patterns that are close to the experimental findings. The shorter distance between the topmost oxygen atoms of the ring structure on the left side is reduced from 3.6 Å to 3.3 Å which causes a small overlap between the bright spots. The additional oxygen atom in the structure in panel 3.23b forms a weak protrusion that sits between the double rows.

To assess the stability of various surface terminations, symmetric five-layered slabs were built with all aforementioned ring superstructures and adsorption phases, relaxed with the (NM) SCAN functional and the resulting surface free energy evaluated as a function of the oxygen chemical potential. The resulting lines representing the surface free energy as the function of oxygen chemical potential are shown in Figure 3.24. The black, horizontal line represents the stoichiometric buckled VO$_2$(110) surface. Green lines denote (2×2) supercells of this buckled surface with 1, 2 or 4 additional O atoms adsorbed as shown previously in Figures 3.18 and 3.16. For the latter two cases the present preferred structures agree with the models of an earlier DFT study by Mellan et al. [125]. Decreasing the coverage from 1/2 to 1/4 ML (1 adsorbed oxygen atom) every second oxygen atom is removed from the remaining oxygen row. Blue, orange, pink and red lines mark the oxygen-rich ring-superstructures, including V$_4$O$_{13}$, V$_5$O$_{14}$ and V$_5$O$_{15}$ stoichiometries,
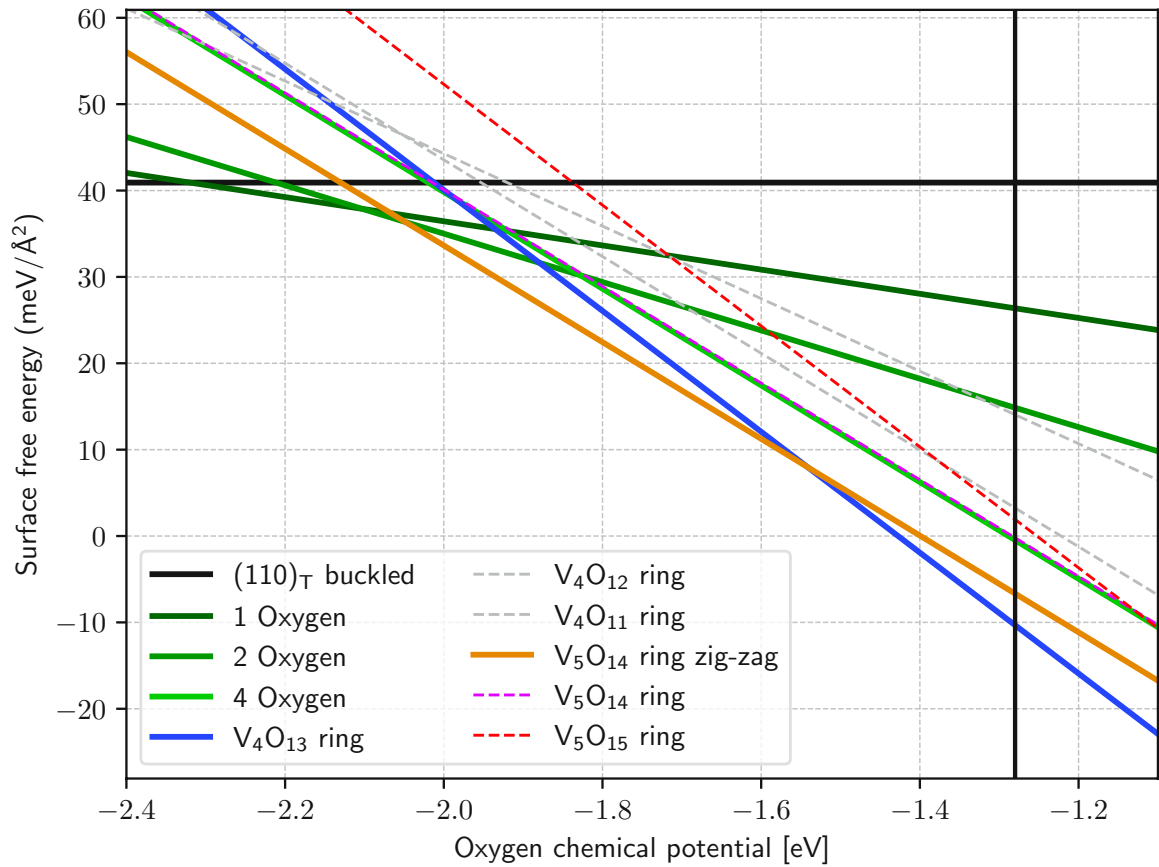
Fig. 3.24: Calculated surface free energies with the non-magnetic SCAN functional of the rutile $VO_2(110)$ surface as a function of the oxygen chemical potential. Shown are the buckled $VO_2(110)$ termination (from Fig. 3.15, black line), oxygen adsorption on the buckled (110) surface (green lines), and the ring terminations from Figures 3.22d (blue line) and 3.23a-b (dashed lines). Gray dashed lines represent the reduced V_4O_{13} ring termination from Figure 3.23c obtained by a subsequent removal of oxygen atoms (colored in orange) from the subsurface layer that create V=O vanadyl bonds, leading to the V_4O_{12} and V_4O_{11} surface stoichiometry. The solid black vertical line represents the experimental heat of formation of the vanadium pentoxide phase. Image reprinted from [32].
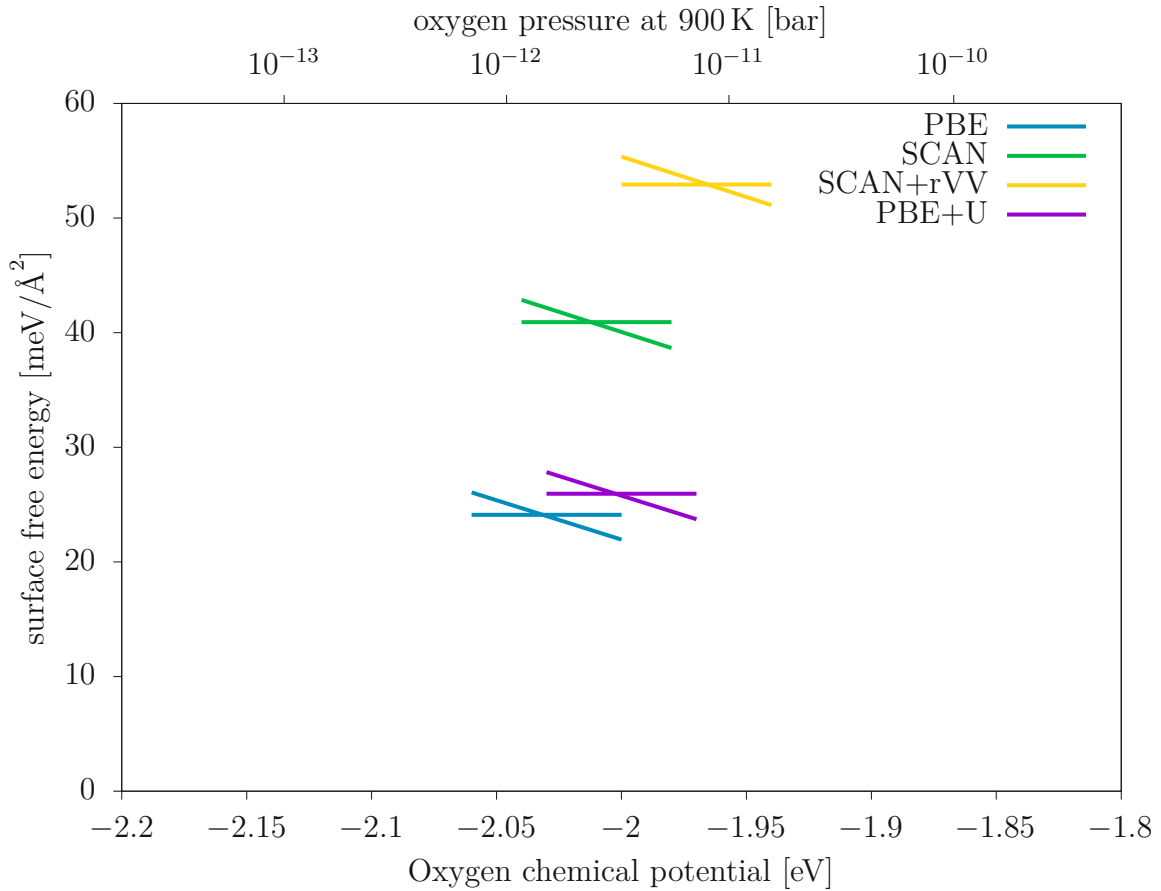
Fig. 3.25: Calculated crossing points (effective adsorption energies) of the surface free energies between the bare rutile VO$_2$ (110) surface and the V$_4$O$_{13}$ ring termination shown in Figure 3.22d, using the non-spin polarized PBE, PBE+U, SCAN and SCAN+rVV functionals. The surface unit cells were adjusted to the relaxed bulk rutile phase with the respective DFT functional.

depicted in Figures 3.22d, 3.23a-b respectively. Furthermore, gray dashed lines represent the reduced V$_4$O$_{13}$ ring structure depicted in Figure 3.22c, where the undercoordinated oxygen atoms in the subsurface layer (colored in orange) were subsequently removed from both rows, leading to the V$_4$O$_{12}$ and V$_4$O$_{11}$ surface stoichiometry. The plot also shows the stability limit of the VO$_2$ phase with respect to the vanadium pentoxide as vertical black solid line defined as the enthalpy of the following reaction: $2VO_2 + 1/2O_2 \rightarrow V_2O_5$. For calculating this phase boundary, the experimental heats of formation of the VO$_2$ and V$_2$O$_5$ phases with respect to vanadium metal [140, 156] were used.

Over a wide range of chemical potentials, the ring structures with V$_4$O$_{13}$ and V$_5$O$_{14}$ surface stoichiometry are the most stable configurations. An unreconstructed, buckled VO$_2$(110) surface, partially covered with O atoms, is only stable under strongly reducing conditions (oxygen chemical potential less than -2.05 eV).

To test whether stabilities of these ring structures are functional dependent as found for the tetrahedral terminations obtained from simulated annealing, the crossing points between the lines that correspond to the bare VO$_2$(110) surface and the V$_4$O$_{13}$ ring

termination were calculated, using non-spin polarized PBE, PBE+U and SCAN+rVV functionals. The resulting dependencies on these functionals are shown in Figure 3.25. Unlike for the tetrahedral terminations obtained from simulated annealing, the calculated stability of the V_4O_{13} ring termination is not functional-dependent and all functionals yield values for the crossing points at oxygen chemical potentials corresponding to the UHV region, yielding almost constant values for the effective adsorption energies, namely $-2.03\,\text{eV}$ $-2.01\,\text{eV}$ $-2.00\,\text{eV}$ and $-1.97\,\text{eV}$ while using (NM) PBE, PBE+U, SCAN and SCAN+rVV functionals, respectively.

3.5.2.1 Summary

It turned out that the energetic ground state of the VO_2 surface over a wide range of oxygen chemical potentials is a reconstruction, distinctly different from a bulk-terminated surface. In contrast to the tetrahedral terminations, the ring model that was built by a modification of the vanadium pentoxide monolayer can explain the main features of the STM images. The non-magnetic SCAN calculations show that the aligned, bright spots are related to the ring structure, which is the most stable surface termination at an oxygen chemical potential of $-1.87\,\text{eV}$ and higher. The V_4O_{13} ring model assigns the experimental double rows in Figure 3.3 to oxygen atoms, which are connected to vanadium tetrahedra. Another hint that points to the conclusion that the ring model is better than the tetrahedral terminations acquired from the simulated annealing is the functional-independent value for the effective adsorption energy of excess electrons incorporated in the structure. Considering that a simple adsorption phase cannot explain the atomically resolved STM measurements either, the following conclusion is appropriate: The ring terminations are central building blocks for an atomistic understanding to the rutile $VO_2(110)$ surface termination.

However, not all experimental features are captured in the present model. First, experimental STM images show the presence of additional bright spots between the double rows that are not explained by the V_4O_{13} ring termination (yellow circle in Fig. 3.3). Second, the double rows in the experiment are always aligned with respect to the neighboring row like in Fig. 3.3), but the present model also allows the hexagonal rings that form the double row pattern to be shifted by half of the rutile bulk unit cell in [001] direction, which is not observed in experiment. The effect that would restrict the observed structure just to the aligned pattern is not evident from the DFT model; probably the alignment is caused by the entities forming the additional bright spots.

The basic V_4O_{13} ring termination was obtained intuitively, but it was also shown that its subsequent intuitive modifications that were presented in Figures 3.23 are not stable. Therefore, the next section introduces yet another approach used for finding the proper surface reconstructions.

3.5.3 Optimization of random structures: Ring terminations

Before starting a discussion of the results obtained from an optimization of randomly generated structures used to obtain further structural models to explain the experimental STM pattern, several conclusions from the previous methods should be stressed, that are worth to be taken into consideration.

- The simulated annealing calculations revealed the presence of a large number of tetrahedral terminations whose stability is dependent on the chosen functional. Therefore, one needs to use also other functionals in the creation process.

- Apart from the functional-dependent tetrahedral terminations, the ring structure that was created from the vanadium pentoxide monolayer is stable on the $VO_2(110)$ substrate independent of the chosen functional. Therefore, one should look mainly for the structures whose stability does not strongly depend on the specific computational setup, as has been observed for the structures obtained from simulated annealing.

- Experimental XPS measurements revealed an increased oxidation states of vanadium atoms at the $VO_2(110)$ surface. However, the exact surface stoichiometry of the experimental $VO_2(110)$ (2×2) superstructure has not been resolved yet. Thus, one proceeds from the obtained V_4O_{13} ring model, which is energetically stable and also provides a good match with the experimental STM images. Modified surface stoichiometries are also investigated in further calculations.

Taking these conclusions into account, the stability of a large set of surface reconstructions was examined (with the size of $\sim$10000 structures) by a direct structural relaxation. Different surface stoichiometries similar to V_4O_{13} were also studied, namely V_nO_{2n+2} to V_nO_{2n+5} for n ranging from 4 to 8 which corresponds to more than a half of an additional VO_2 trilayer. Nevertheless, in case of surface terminations with $n \geq 6$, one observes the formation of the second surface layer which turned out to be unstable with respect to the oxygen adatoms on the bare $VO_2(110)$ surface. Therefore, the focus will be laid particularly on the results concerning the following surface stoichiometries: V_4O_{11}, V_4O_{13}, V_5O_{12}, V_5O_{13}, V_5O_{14}, and V_5O_{15}. Atoms that form the surface layer in the ring structure with the V_4O_{13} surface stoichiometry, are depicted in Figures 3.26a-d, colored in gray and violet. In total, the unit cells contain four vanadium atoms and thirteen oxygen atoms. The whole optimization procedure is composed of the following steps:

- At the beginning random structures are generated at a given surface stoichiometry with the USPEX package[157–159]. 1000 initial structures have been generated separately for the PBE, PBE+U and the SCAN functional. The samples consisted of the surface layer fixed to the bulk positions and one bottom layer, see Figure 3.26a.

- The initial structures were pre-optimized within 170 ionic steps with the electronic loop converged to the 10^{-3} eV, using strictly non-spin polarized calculations. The energy cut-off was set to 400 eV and the k-point grid was downgraded just to the Γ point. PBE, PBE+U and SCAN functionals were used in the optimization steps.

- One choses the 100 most stable structures from the previous step, which were relaxed using the accurate settings: 450 eV energy cut-off, $2 \times 1 \times 1$ k-points grid, electronic

(a) **(b)**

(c) **(d)**
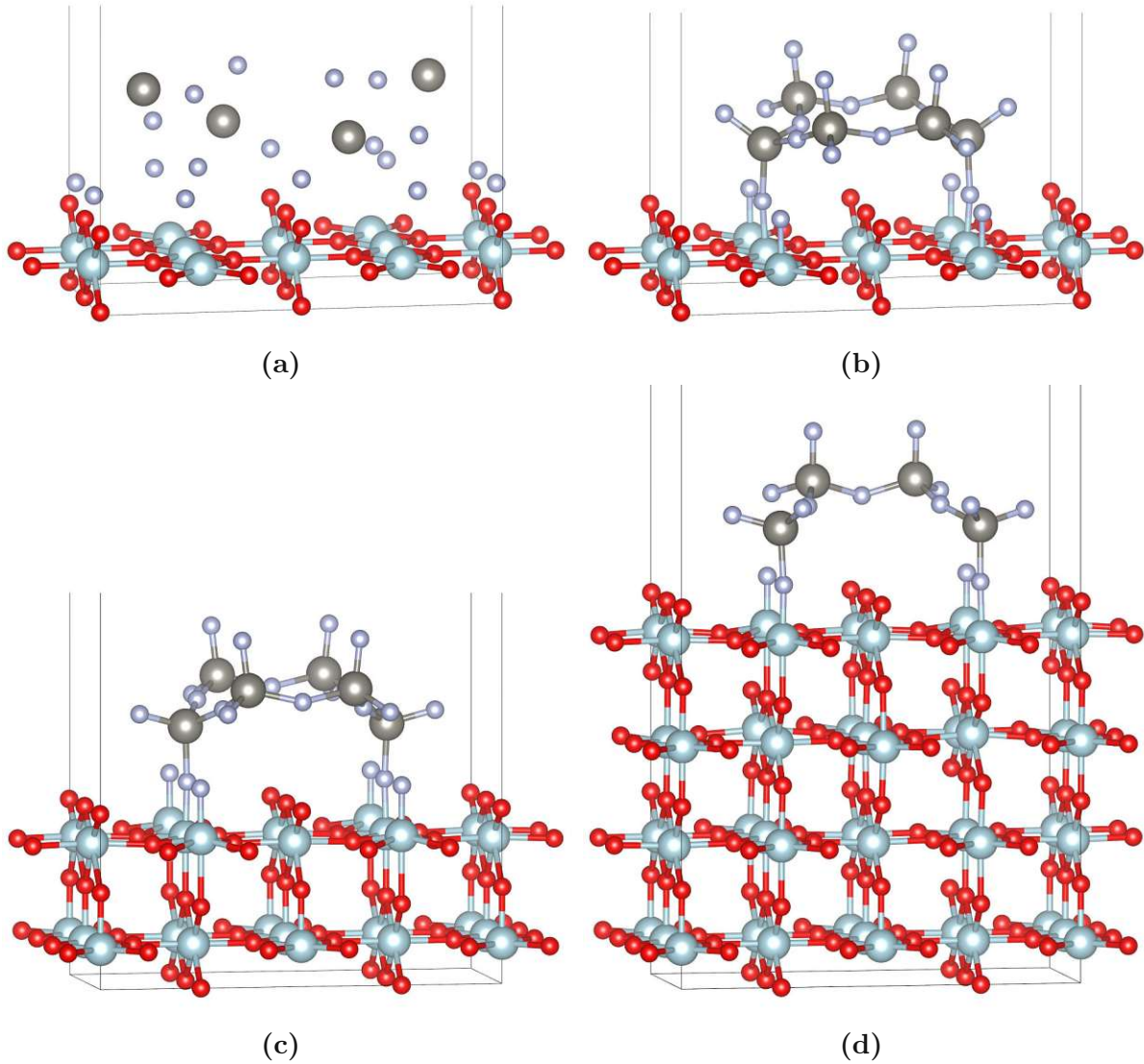
Fig. 3.26: Optimizaton process of the random structures. At the beginning, a set of 1000 random structures was generated with the USPEX[157] package as shown in panel (a). After that, all of them were pre-optimized, and the 10 % most stable ones fully relaxed, which led to a set of 100 structures, similar to the one from panel (b). At the next step, an additional substrate layer was added as shown in panel (c). Since two substrate layers were too thin according to performed convergence studies, the last step consisted of adding two more substrate layers, as shown in panel (d). Concluding, a full and accurate relaxation with all functionals using both spin-polarized (FM) and non-spin polarized (NM) electronic configurations was performed.

loop converged to 10^{-5} eV. Ionic optimization was stopped when all residual forces were smaller than 10^{-2} meV/Å. The representative structure obtained from this step is shown in Figure 4.8b

- The 30 most stable structures were selected from the previous step and improved by an additional substrate layer as depicted in Figure 3.26c. In these calculations, only the first layer was fixed to its bulk positions, surface and sub-surface layer were allowed to relax.

- Since different functionals resulted in different structures, the 10 most stable structures obtained from all respective functionals were chosen. These structures were subsequently optimized with the remaining functionals and compared with the acquired structures in the previous step. Hence, the stability of 40 structures has been compared in total for all functionals.

- The 10 most stable structures for all functionals were selected and their slab thickness increased by additional 2 layers where the bottom layer was fixed to the bulk positions as shown in Figure 3.26d. The lattice vectors were adjusted to the bulk proportions obtained by the respective functional, the k-points grid was set to $4 \times 2 \times 1$ and energy cut-off was increased to 500 eV. At this point also spin-polarized calculations have been performed for a ferromagnetic spin ordering and also the SCAN+rVV functional with a ferromagnetic and nonmagnetic spin ordering has been employed.

- In a final step, symmetric five-layered slabs were built to overcome errors induced by the presence of dipole moments induced by asymmetric slabs. Here, the same computational settings as in the previous step were used.

The splitting of the whole optimization procedure into several steps allows for an exclusion of those structures that are obviously unstable. This saves computational time, which is especially important for the SCAN functional, because it can now be used with a reasonable time cost. An advantage of this process compared to the simulated annealing is that one can massively parallelize the procedure since the relaxation of random structures is independent of each other. Naturally, the described procedure of optimization of random structures has also some limitations and shortcomings. A closer look into the functionality of the chosen settings is provided in section A.4. On a side note, there is a certain similarity between the optimization of random structures and simulated annealing: the first one can be understood as a simulated 'explosion' of the surface layer with a neglect of temperature effects. Generally, these methods can be combined together, *e.g*, by starting the simulated annealing from the 'exploded' surface structure which has not been considered in this work.

3.5.3.1 Results

Independent of the chosen functional and spin configuration, the five most stable terminations which resulted from optimizing the preselected random structures are depicted in Figures 3.27b-e. All of them are based on a general pattern shown in Figure 3.27a which displays a V_5O_{12} surface stoichiometry and is structurally similar to the (3×1) surface reconstruction of $SrTiO_3(110)$[155]. This reconstructed surface superstructure

consists of alternating octagonal and hexagonal rings made of VO_{2+x} polyhedra as most easily visible in the top view of panel 3.27a. However, the surface free energy that results from this termination is too high so that a further oxidation is required to stabilize this superstructure by adding oxygen atoms in between the octahedral rows of the subsurface layer (see the blue circle). The first stable (2×2) ring superstructure that has been obtained by the optimization of random structures with the V_4O_{13} surface stoichiometry is shown in Figure 3.27b. Note that this structure is identical to the ring termination presented in the previous section (Figure 3.22c). The modification proceeds in two steps: First, the bridging vanadium tetrahedra (see the green circles) are removed and second, two additional oxygen atoms are adsorbed on the ring pattern, which pushes the vanadium tetrahedra towards the vacuum as indicated by the the blue arrow. These modifications lead to the formation of a stable, disconnected ring structure with a V_4O_{13} surface stoichiometry and showing only VO_x tetrahedra. This ring termination is quite flexible and can be easily shifted by a quarter of the c-bulk lattice vector as indicated by the black arrow in Figure 3.27c. As a result, the lower VO_x tetrahedra are additionally bound to a second oxygen ad-atom which changes their coordination geometries to square pyramids. This change is most easily visible by comparing the features within the black circles in Figures 3.27b and c. The relative stability of these ring structures depends on the choice of the functional and will be discussed further below. Proceeding with the ring structures, another variant is shown in Figure 3.27d, which descends from the general pattern in the following way: First, the ring structure is shifted by a quarter of the $[1\bar{1}0]$ bulk lattice vector (see the red arrow in the top view) so that the bridging tetrahedra are aligned with upright octahedra of the subsurface layer as marked by the orange circle. Second, this shift of the ring termination relative to the subsurface layer is accompanied by the oxidation of different vanadium tetrahedra. All together this leads to a termination with an overall V_5O_{15} surface stoichiometry displaying a zig-zag STM pattern (see Figure 3.31). The next stable superstructure shown in Figure 3.27e is generated by shifting the previous structure by an additional quarter of the $[001]$ bulk lattice vector (see orange arrow), which again causes the bridging tetrahedra to bind to two subsurface octahedra, as easily seen by comparing the features inside the orange circles in Figures 3.27d,e. However, here, one oxygen atom is removed changing the overall surface stoichiometry to V_5O_{14} and causing the tetrahedral coordination geometry not to switch to a square pyramid as has been the case for the V_4O_{13} ring structures.

Since the ring terminations are supported on a bare surface, also oxygen atoms might be missing in the connecting subsurface layer which changes the local coordination of the affected vanadium atoms from octahedra to square pyramids. This is shown in Figure 3.27f where one considers a ring structure similar to the shifted V_4O_{13} ring (see Figure 3.27c) where the hexagonal rings are connected by bridging tetrahedra. The side view shows the stepwise removal of subsurface oxygen atoms surrounding two vanadium sites (see the green and violet circles in Figure 3.27f, which leads to a V_5O_{13} and a V_5O_{12} surface stoichiometry, respectively.

The present results reveal that the relative stability of the two V_4O_{13} surface terminations shown in Figures 3.27b,c dependends on the chosen functional. The energetic differences shown in Table 3.6 clearly indicate that the (FM) spin-polarized PBE and PBE+U functionals prefer the purely tetrahedral ring structure 3.27b by 114 and 385 meV per

	PBE	PBE+U	SCAN	SCAN+rVV
FM	-114	-385	97	137
NM	4	108	230	324

Tab. 3.6: Total energy differences (in meV per the (2×2) supercell) of the disconnected ring terminations, depicted in panels 3.27b-c. Negative number means that the stability of the purely tetrahedral ring structure (panel 3.27b) is preferred with the respective calculation setup.

(2×2) supercell while all the other functionals find the shifted modification 3.27c as more stable by $4 \,\mathrm{meV}$ to $324 \,\mathrm{meV}$.

Ring superstructures obtained by a subsequent modification, namely by the removal of undercoordinated oxygen atoms from the subsurface layer are also taken care of. This modification changes the local coordination of vanadium atoms from octahedra to square pyramids, as shown in Figure 3.27f: the green and violet circles mark two vanadium sites (panel 3.27f) from which an oxygen atom was stepwise removed, changing the surface stoichiometry to V_5O_{13} and V_5O_{12}, respectively. The stability of these superstructures is functional-dependent.

In order to compare the stability of the superstructures with different surface stoichiometries, the surface free energy of the most stable terminations is drawn in Figures 3.28 and 3.29 for ferromagnetic (FM) and nonmagnetic (NM) calculations, respectively. Furthermore, the ring terminations with a bare (110) surface (black line) and simple oxygen ad-atom (110) surface models shown in Figure 3.16 are compared. The green '1O', '2O', '4O' lines indicate the number of oxygen ad-atoms in the (2×2) supercell, namely one oxygen (Figure 3.18), two oxygen (Figure 3.16b) and four oxygen atoms (Figure 3.16c), respectively. Orange vertical lines mark the calculated and experimental oxidation enthalpy to V_2O_5 below which the bulk VO_2 is thermodynamically stable.

Oxygen adsorption on a rutile (110) surface has been already studied by Mellan et al.[125] performing non spin-polarized PBE calculations. In their work, the $\Gamma = +1$ and $\Gamma = +2$ surfaces are identical to the present $50 \,\%$ and fully covered VO_2 (110) terminations depicted in Figures 3.16b,c. However, the present calculated adsorption energies for both coverages are $\sim 0.46 \,\mathrm{eV}$ larger than the corresponding (i.e. the uncorrected) values for the $\Gamma = +1$ and $\Gamma = +2$ surfaces (see Figure 8 in ref.[125]). This rather large discrepancy in adsorption energy is caused again mainly by a different computational setup. The use of differing PAW potentials causes a $0.26 \,\mathrm{eV}$ difference and the different slab thickness increasing this value by another $0.07 \,\mathrm{eV}$. Furthermore, the models in the present work are additionally stabilized by the surface buckling, which has been neglected in the work of Mellan et al.[125] which increases the difference by $\sim 0.06 \,\mathrm{eV}$ for both coverages. The remaining small discrepancy is attributed to other effects emerging from the different computational setup.

Figures 3.28 and 3.29 show the calculated surface free energies of the bare $VO_2(110)$ surface (black lines), the oxygen ad-atom phases with different oxygen coverage (green lines) and the ring terminations depicted in Figures 3.27b-f for varying oxygen chemical potential. Concerning the V_4O_{13} ring structure only the surface free energy of the most stable variant is included. Independent of the chosen spin configuration all graphs show
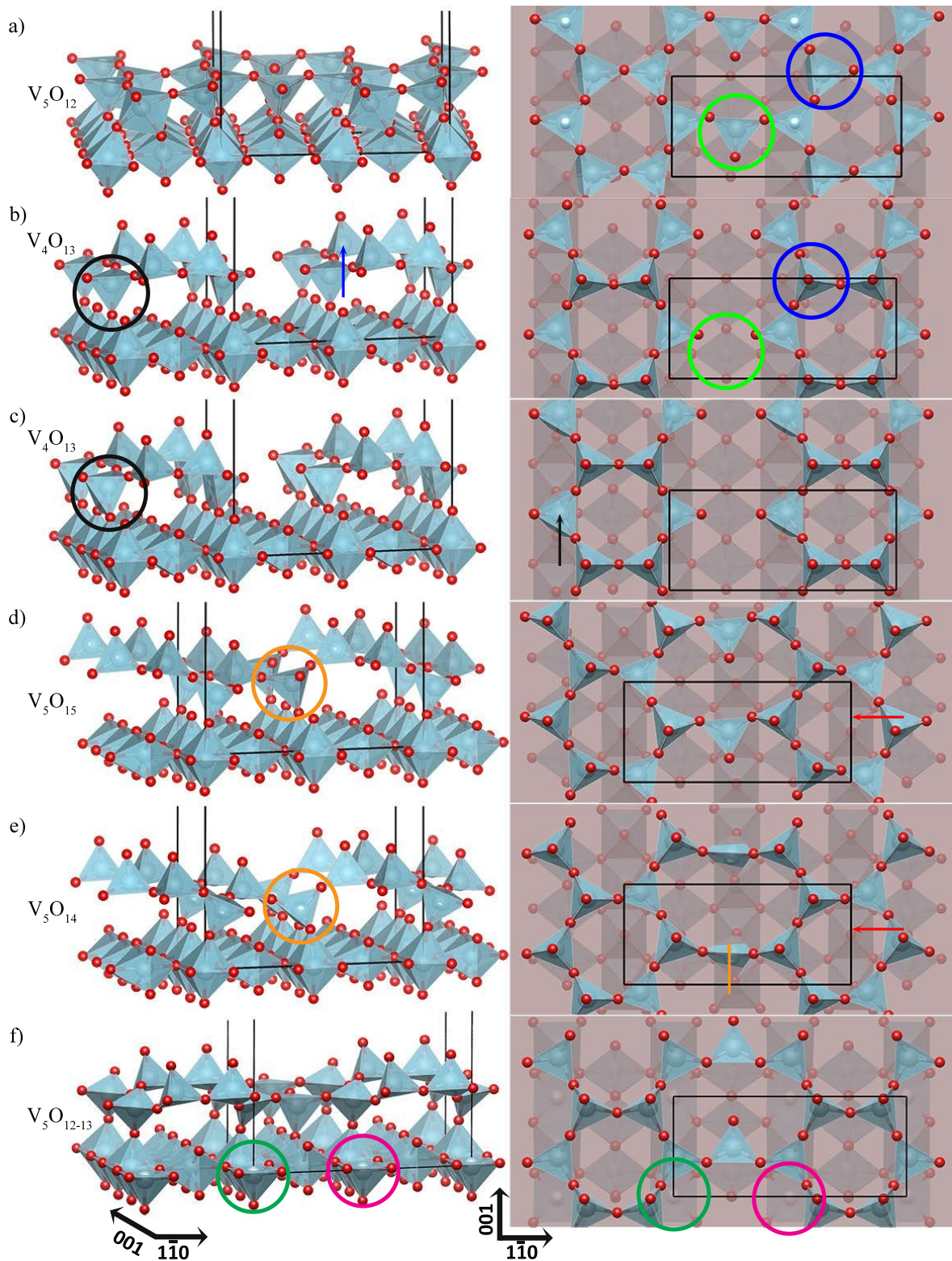
Fig. 3.27: Perspective and top views of the resulting (2×2) superstructures obtained from an optimization of random structures with different surface stoichiometries. The structures descend from an underlying pattern shown in panel (a) which is structurally similar to the (3×1) reconstruction of the $SrTiO_3(110)$ surface [155].
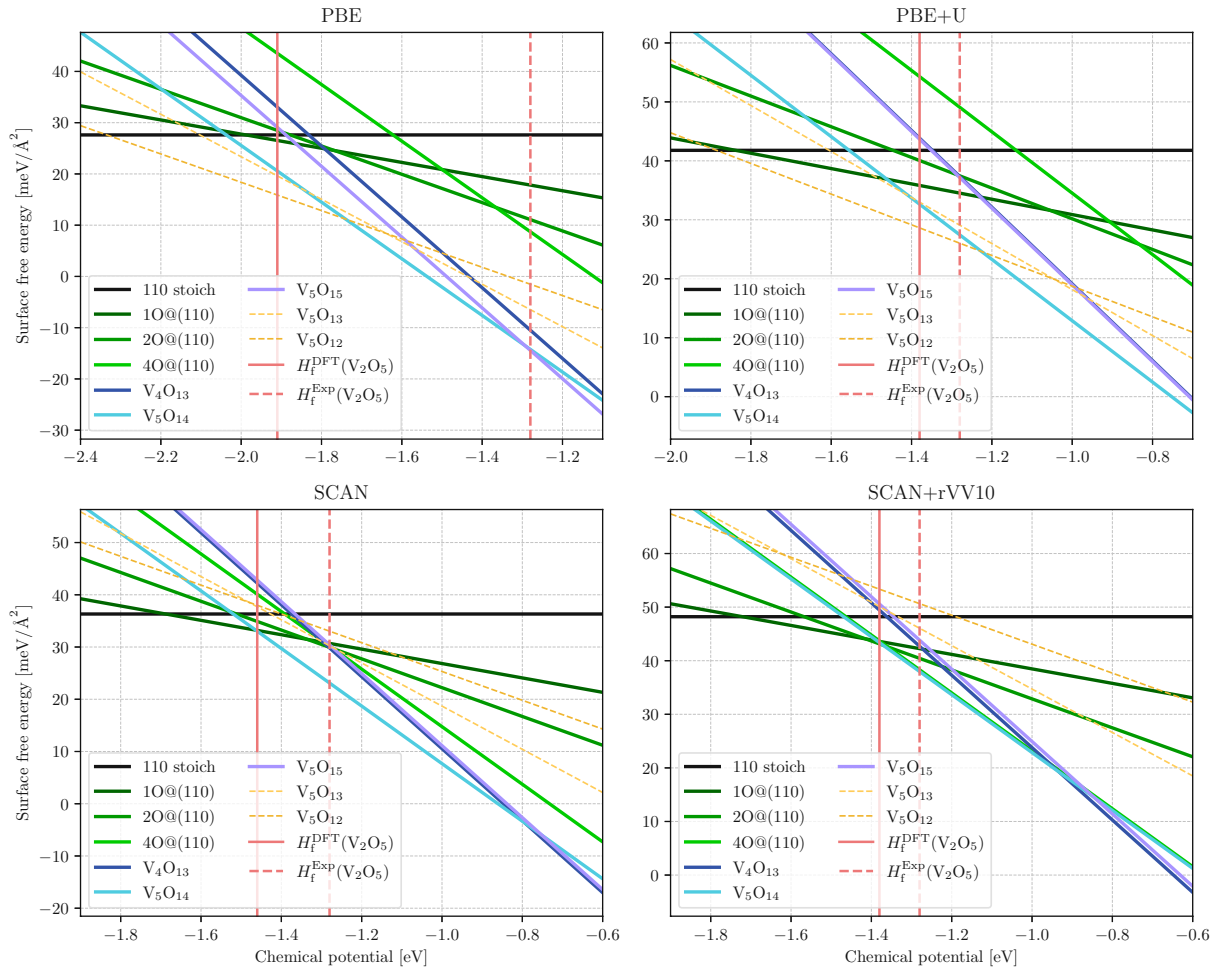
Fig. 3.28: Calculated surface free energies as a function of the oxygen chemical potential for various (2×2) $VO_2(110)$ surface terminations and a FM spin configuration.
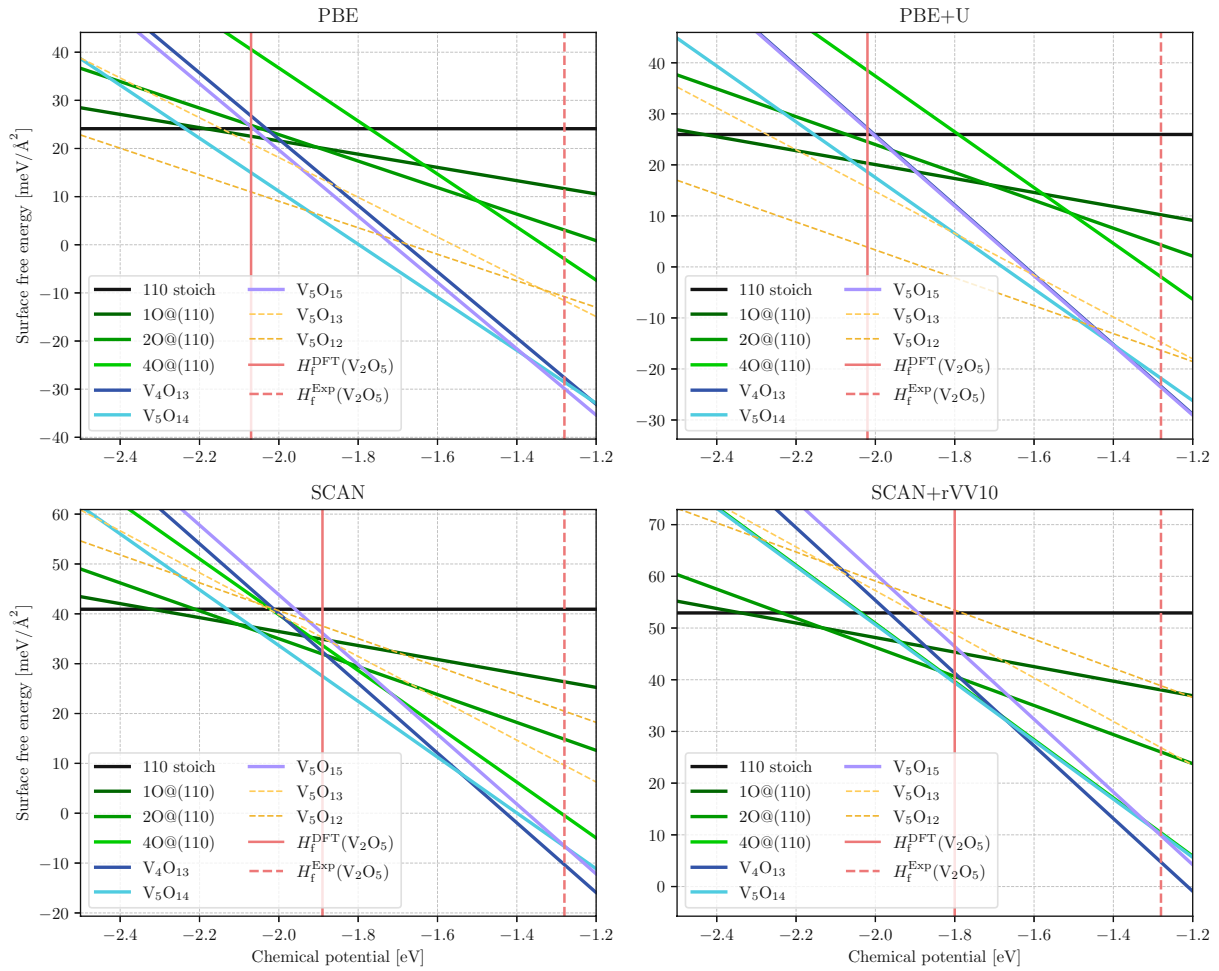
Fig. 3.29: Calculated surface free energies as a function of the oxygen chemical potential for various (2×2) $VO_2(110)$ surface terminations and a NM spin configuration.

that all the functionals considered determine the ring terminations to be more stable than (PBE, PBE+U, SCAN) or at least similarly stable (SCAN+rVV) as the oxygen ad-atom phases over the wide range of chemical potentials. However, the relative stability of the ring terminations with respect to the oxygen ad-atom phases is functional dependent. To quantify this dependency one may look at the difference between the crossing points of both the fully covered oxygen ad-atom (110) surface (light green line) and the V_5O_{14} ring phase (cyan line) with the bare stoichiometric (110) surface, which determine the effective adsorption energy of the additional oxygen atoms that are incorporated in the superstructure. Independent of the spin treatment, the PBE and PBE+U functionals places this difference between $0.4\,\mathrm{eV}$ to $0.5\,\mathrm{eV}$, SCAN prefers the V_5O_{14} ring by $0.1\,\mathrm{eV}$ and the SCAN+rVV functional renders the difference in crossing points to below $0.01\,\mathrm{eV}$. The graphs also show that the (FM) PBE, (NM) PBE and (NM) PBE+U functionals prefer the ring structures over the whole range of the oxygen chemical potentials while the other functionals and spin configurations yield an energy window in the low oxygen chemical potential region where the oxygen ad-atom phases would be preferred. On the other hand, the (FM) SCAN, (FM) SCAN+rVV and (NM) SCAN+rVV functionals show a preference for the ring terminations only in regions where the VO_2 bulk phase is calculated to be thermodynamically unstable. The strong stabilization of the ring structures for the PBE and PBE+U functionals also hints towards an existence of additional polyhedral surface terminations that are more stable than the ad-atom phases. Regarding the V_4O_{13} and V_5O_{15} rings, most of the functionals do not exhibit a significantly different stability values except for the (NM) SCAN, SCAN+rVV and (FM) PBE. While the V_5O_{15} ring is more stable by $50\,\mathrm{meV}$ (SCAN) and $80\,\mathrm{meV}$ (SCAN+rVV) than the disconnected ring, the (FM) PBE functional prefers the connected V_5O_{15} ring by $50\,\mathrm{meV}$.

For the ring structure on the reduced oxygen missing subsurface layer (panel 3.27f again a strong dependency on the chosen functional is evident. The graphs 3.28 and 3.29 find no additional stability at the SCAN or SCAN+rVV level, while these structures are preferred at the PBE and PBE+U level under strongly reducing conditions, see yellow dashed lines. Particularly the (NM) PBE+U functional prefers this structure for oxygen chemical potentials in the range of $-1.5\,\mathrm{eV}$ to $-2.8\,\mathrm{eV}$. An enhanced stability is also found at the (NM) and (FM) PBE level, showing that a doubly reduced subsurface layer would be stable for an oxygen chemical potential below $-1.9\,\mathrm{eV}$ and $-1.8\,\mathrm{eV}$ respectively. A stability window ranging from $-1.23\,\mathrm{eV}$ to $-1.89\,\mathrm{eV}$ is also found for (FM) PBE+U setups. The qualitative agreement between the PBE and PBE+U functionals can be understood by considering the existence of an electronic gap for states connected with the surface layer which will be discussed in the following section. The other functionals determine these reduced subsurface layer structures to be unstable with respect to both the other ring structures and ad-atom phases. Comparing the reduced V_5O_{13} and V_5O_{12} ring terminations reveal yet another functional dependent property. Considering their crossing points with the bare (110) surface line, the PBE and PBE+U functionals show crossing to occur at a lower oxygen chemical potential for the more reduced ring termination with a V_5O_{12} surface stoichiometry. However, these crossing points are found either roughly at the same oxygen chemical potential (SCAN) or they are even reversed (SCAN+rVV), revealing a counter-intuitive opposite trend with respect to the ad-atom phases, see green
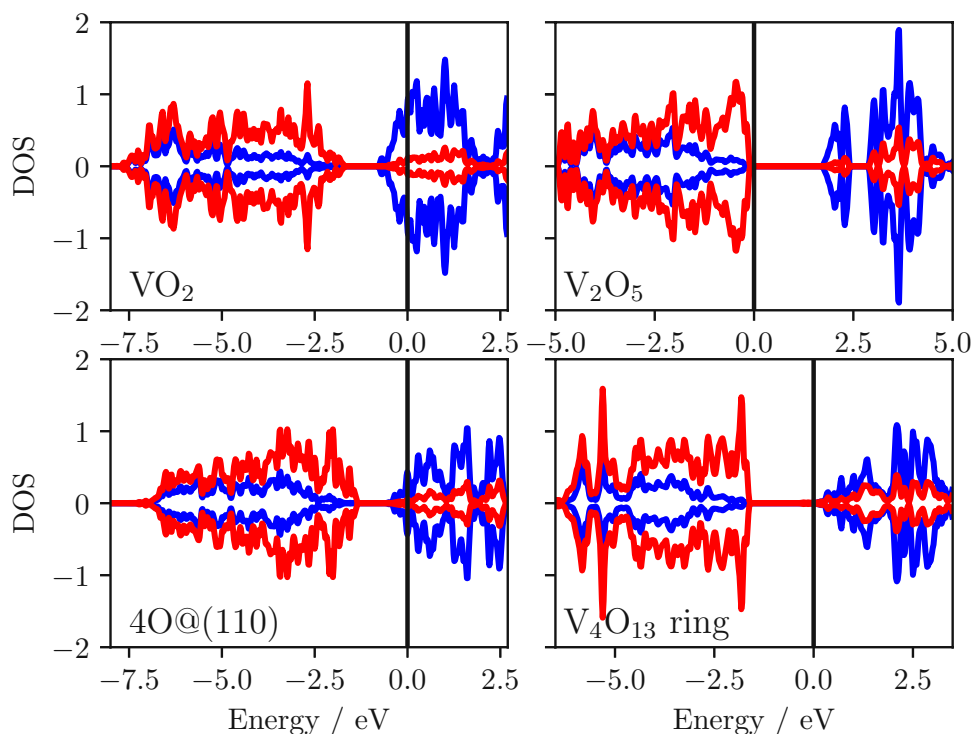
Fig. 3.30: Vanadium and oxygen projected DOS of the VO$_2$, V$_2$O$_5$ phases, and projections to surface atoms of a VO$_2$(110) surface fully covered with oxygen ad-atoms and of the V$_4$O$_{13}$ ring termination. The projected DOS was calculated with the non-magnetic PBE functional and is both normalized to a single atom and aligned at the upper edge of the O-2p band.

lines in Figures 3.28 and 3.29. Vacancies at PBE and PBE+U level stabilize the surface which is not the case for the SCAN functional.

One of the most striking differences between the spin-polarized and non spin-polarized calculations for the surface free energies concerns the absolute values of the effective adsorption energies. This difference can be illustrated best for the ring termination with a V$_5$O$_{14}$ surface stoichiometry (Figure 3.27e). While the non-magnetic calculations yield effective adsorption energies, depending on the chosen functional, between -1.88 eV to -2.06 eV, (FM) spin-polarized calculations shift the resulting values by 0.20 eV, 0.60 eV, 0.61 eV and 0.57 eV to the right (less negative values) using PBE, PBE+U, SCAN or SCAN+rVV. Note that similar shifts (± 0.1 eV) are also observed for the ad-atom phases (green lines in Figures 3.28 and 3.29). This energy shift can be attributed to higher energies for bulk rutile VO$_2$ when performing non-spin polarized calculations which are due to the neglect of local magnetic moments, see Table 3.1.

Considering a possible opening of a gap in the surface DOS of the oxygen rich ring terminations it is tempting to inspect the relation between the V$_2$O$_5$ bulk phase and the ring terminations more closely. In Figure 3.30 the projected density of states of the bulk VO$_2$ and V$_2$O$_5$ phases are compared to the oxygen ad-atom phase at full coverage (Fig. 3.16c) and the V$_4$O$_{13}$ ring. The major difference between the electronic structure of VO$_2$ and V$_2$O$_5$ bulk phases is found for the occupation of the V-3d states. While the Fermi

level cuts the V-3d bands in the VO$_2$ phase, the V$_2$O$_5$ phase shows an electronic band gap of about 2.0 eV between the O-2p and V-3d states. As can been seen in Figure 3.30, the projected surface DOS of the ring structure resembles rather closely the DOS of the V$_2$O$_5$ bulk phase, revealing an unoccupied V-3d band and hence this surface termination cannot form local magnetic moments. Figure 3.30 also shows that the terminating ring layer is insulating with a 1.9 eV band gap, which is in a good agreement with the 2.3 eV obtained for the V$_2$O$_5$ bulk (see Table 3.1). It should also be noted that the surface free energies of the ring terminations correlate with the calculated oxidation enthalpy of bulk VO$_2$. As visible from the surface free energy graphs above, the difference between the effective adsorption energy of the V$_5$O$_{15}$ ring phase and the reaction enthalpy for a V$_2$O$_5$ formation by oxidizing VO$_2$ is below 0.1 eV in all cases, while the absolute errors in calculated oxidation enthalpies range from 0.1 eV to 0.79 eV. These facts indicate, that the ring terminations are related to a monolayer of V$_2$O$_5$(001) in agreement with the previous work [32]. This finding also implies that a correct evaluation of the stability for both phases is important to properly describe the energetics of the oxygen rich surface terminations, a criterion which seems to be matched best by spin-polarized PBE+U, SCAN and SCAN+rVV calculations. However, the application of the (FM) PBE+U functional yields wrong orbital occupations and strongly overestimates the c/a ratio of the bulk rutile VO$_2$ phase. From this perspective the spin-polarized SCAN and SCAN+rVV functionals seem to be a better choice for performing calculations on VO$_2$ surfaces.

3.5.3.2 Experimental and Calculated STM images

The experimental STM images of the (2 × 2) surface reconstruction were introduced at the beginning of this Chapter in Section 3.2. In the following the validity of the present models are tested by a comparison to experiment. The calculated STM images of the superstructures obtained from the optimization of random structures (Figures 3.27b-f) exhibit two distinct patterns that are displayed in Figure 3.31. The rectangular pattern has also been presented in the previous section (Figure 3.31, left panel) and it is resembled from structures 3.27b,c,f. The second pattern, zig-zag rows, is recovered from structures 3.27d,e, which was also revealed in experiments at the domain boundaries, see 3.31 (right panel). The rectangular pattern that was more common in experiments is aligned with respect to the surface layer beneath in both [001] and [1$\bar{1}$0] directions and the rectangular STM pattern has also mirror axes in these directions (see Figure 3.3). All rectangular patterns fullfill these particularities, except the alignment in the [1$\bar{1}$0] direction that is discussed further.

As pointed out in Fig. 3.3, the dark rows that shows the experimental (2 × 2) reconstruction in STM images along the [1$\bar{1}$0] direction (the light blue line in Figure 3.31) are centered on the dark rows present in the unreconstructed VO$_2$(110) surface. The respective alignment of the structures that show the rectangular STM pattern is shown in Figure 3.32. The light blue and the green lines denote positions of the dark rows in the reconstructed surface layer and in the unreconstructed surface layer beneath, respectively. They show that the best match between the simulated and experimental STM images provides the shifted V$_4$O$_{13}$ ring superstructure. On the other hand, the remaining surface terminations mismatch the alignment by a half of the lattice vector in [001] direction.

The geometrical thickness of the reconstructed double layer ranges from $5.4\,\text{Å}$ to $5.8\,\text{Å}$, which is with respect to the experimental apparent height in STM ($1.6\,\text{Å}$) $3\times$ higher. However, this large mismatch can be explained by the insulating nature of the V_4O_{13} double layer.

However, not all experimental features are captured in the present models. First, the experimental STM images show the presence of additional bright spots between the double rows that are not explained by the V_4O_{13} ring termination (see Section 3.2). Second, the double rows in the experiment are always aligned with respect to the neighboring row as in Figures 3.3a-b, but the present model also allows the hexagonal rings that form the double-row pattern to be shifted by half of the unit cell in [001] direction, which is not observed in the experiment. The effect that would restrict the observed structure just to the aligned pattern is not evident from the DFT model; probably the alignment is caused by the entities forming the additional bright spots. Furthermore, the experimental zig-zag row always neighbors a rectangular row (see Fig. 3.31), which is not captured by the present model because of the limited periodicity of the considered (2×2) supercell.

Regarding the stability of ring terminations at the chemical potential $-2.07\,\text{eV}$ that represents annealing conditions, namely the annealing temperature and pressure, the interpretations of the surface free energy diagrams 3.28 and 3.29 are rather inconsistent. The spin-polarized SCAN and SCAN+rVV calculations predict a pristine (110) surface which is clearly observed neither in XPS spectra nor with STM measurements. Another peculiarity of the (FM) SCAN and SCAN+rVV calculations is the comparison of the calculated phase boundary of the VO_2 (red solid vertical lines) with the stability of the V_5O_{14} ring termination (cyan line) that evinces the zig-zag STM pattern, showing that this ring superstructure is stable at the values of oxygen chemical potential beyond the phase boundary, *i.e*, where the VO_2 phase is thermodynamically unstable. The same interpretation also holds for the (NM) SCAN+rVV functional although the effective adsorption energies are shifted to the lower values. The interpretation of the (NM) SCAN functional is slightly different, but still in a disagreement with the experiment: the V_5O_{14} ring termination is also stable below the phase boundary at values of oxygen chemical potential close to the experimental value $-2.07\,\text{eV}$. Therefore, one could expect the predominance of the zig-zag pattern with respect to the rectangular pattern in experiment which is not observed. With this regard the PBE and PBE+U functionals yield different results: the reduced ring termination with the V_5O_{12} surface stoichiometry (yellow dashed line) is stable at values of oxygen chemical potential of $-2.07\,\text{eV}$ regardless of the spin configuration. Therefore, these functionals predict the presence of rectangular STM pattern, in agreement with the experiment. Nevertheless, the ring structures with the V_4O_{13} and V_5O_{14} surface stoichiometries can be seen as a structural basis that explains the most prominent features of the experimentally observed surface reconstruction.

3.5.3.3 Reliability of the DFT results

The qualitatively different results obtained for different functionals raise the question on their reliability concerning the stability of the ring termination. Several aspects important for this question will be discussed in the following.

The surface free energies are calculated according to equation A.4. As shown, three different atomic systems are part of the calculations: a slab, VO_2 bulk and the oxygen
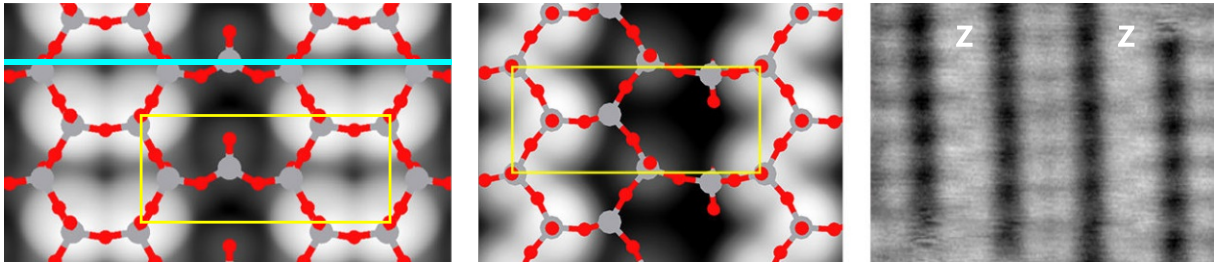
Fig. 3.31: Calculated rectangular (left) and zig-zag pattern (middle) using the superstructures obtained from optimization of random structures. The rectangular pattern recover structures 3.27b,c,f, whereas the latter evince structures 3.27d,e. The right panel contains the experimental STM image showing the zig-zag pattern observed at the domain boundaries (the rows marked with 'Z'). Right panel reprinted from [32].

(a) V_4O_{13}

(b) V_4O_{13} (shifted)

(c) V_5O_{13}

(d) V_5O_{12}
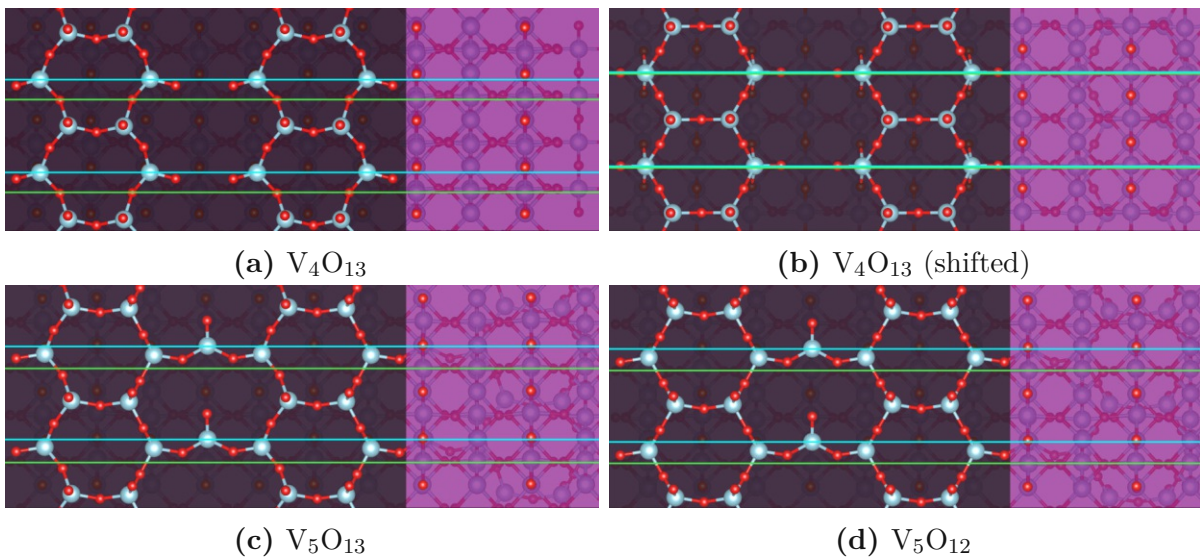
Fig. 3.32: Alignments of the obtained ring structures with respect to the (110) surface beneath (purple area). The blue and green lines denote the positions of the dark rows in the [1$\bar{1}$0] direction of the reconstructed and unreconstructed surface, respectively. The experimental STM images (Figure 3.3) revealed that the dark rows are aligned with respect to each other, *i.e.*, the blue and the green lines overlap.

molecule. Hence, one should consider the errors that can be expected in DFT calculations on these systems and look first at three separate regions in the slabs. The inner part of slabs remains bulk-like and therefore one may expect cancellation of errors therein. The second part of the slab is the surface layer with the polyhedral coordination geometry. The present results indicate that the correct description of total energies of the surface layer might be related to the good performance on the vanadium pentoxide system due to their similar electronic structure. However, structural differences between the ring termination and a vanadium pentoxide monolayer are quite large, i.e. the change of coordination geometry of vanadium atoms from distorted pyramids to tetrahedra. It is therefore still questionable whether the good performance on the stability of both vanadium oxide phases ensures a good description of ring terminations. The third region is the interface between the ring termination and the inner part of the slabs – the subsurface layer. Here one might expect correlation effects that proceed from the d electrons that form the V $3d$ band. Since the number of electrons localized at vanadium atoms is dependent on the adsorbed species, one might also expect that DFT would lead to errors that would not be cancelled by the bulk reference. To quantify this expectation one may consider the dependence of the number of V $3d$ electrons in the subsurface layer on the type of the surface layer as calculated by an integration of the projected density of states onto vanadium atoms in the subsurface layer over the occupied states that form the V-$3d$ band. The pristine $VO_2(110)$ surface contains the largest amount of d electrons and this number decreases with increasing concentration of oxygen adatoms, which can be explained by the formation of vanadyl V=O bonds. Furthermore, the buckling also leads to a decrease of the occupation numbers. The ring terminations show a similar trend: higher concentration of oxygen leads to lower occupation numbers. It has been shown that V_4O_{13} and V_5O_{15} rings yield a comparable value for the occupation number as the buckled surface covered with 2 additional oxygen ($2O@110_B$). Furthermore, the reduced ring terminations yield a comparable value to the pristine (110) surface. Therefore, this implies that DFT must describe the energetics of this systems also at reduced occupation numbers of correlated $3d$ electrons.

3.5.3.4 Summary

In this section the off-stoichiometric surface phases obtained from an optimization of random structures were studied. First of all, the previously described ring terminations produced by a modification of the vanadium pentoxide monolayer by other structurally-related ring layers exhibiting the zig-zg pattern in STM images have been complemented. The performance of PBE, PBE+U, SCAN and SCAN+rVV functionals for spin polarized and non spin-polarized configurations have been studied, showing that the absolute values of surface free energies depend on the choice of DFT functional and spin configuration. Three important parameters that influence the calculated stability of the VO_2 (110) superstructures were identified. First, the PBE and PBE+U functionals prefer open tetrahedral terminations. Such a behavior has already been seen in the structural parameters of the vanadium pentoxide phase where the separation between the V_2O_5 layers is overestimated while SCAN and SCAN+rVV functionals underestimate the distances (see Table 3.4). Therefore, one may expect the existence of a large number of polyhedral superstructures that are stable at the PBE level but unstable for the SCAN functional. Second, a correlation

	(NM)			(FM)			
	PBE	PBE+U	SCAN	PBE	PBE+U	SCAN	structure
$VO_2(110)$	5.48	5.24	5.44	5.76	6.36	6.12	3.16a
$VO_2(110)_B$	4.62	4.92	5.16	–	4.76	–	3.15
2O@110	3.54	3.44	3.6	4.14	3.68	4.26	3.16b
$2O@110_B$	3.05	3.00	3.38	3.26	3.2	3.38	–
4O@110[a]	1.80	1.60	1.80	2.36	1.80	2.32	3.16c
$4O@110^a{}_B$	1.46	1.50	1.78	1.16	1.30	1.16	–
V_4O_{13}	2.76	2.79	2.94	2.92	3.01	3.15	3.27b
V_4O_{13} shift	2.63	2.75	2.76	2.92	2.55	2.78	3.27c
V_5O_{15} (zig-zag)	3.19	3.26	3.21	3.15	2.49	3.56	3.27d
V_5O_{14} (zig-zag)	4.35	4.39	4.46	3.95	3.96	4.05	3.27e
V_5O_{13}	5.27	4.16	5.46	4.71	5.17	5.52	3.27f
V_5O_{12}	5.37	4.78	4.93	6.12	6.21	6.16	3.27f

[a] calculated on (2×1) slabs.

Tab. 3.7: Occupation numbers of the V $3d$ band per (2×2) slab, localized in the subsurface layer. The right column shows the reference to the respective structure. The subscript ('B') denotes the buckled surface.

between the calculated reaction enthalpy for the vanadium pentoxide and the V_5O_{15} ring termination has been established, which indicates that a correct description of the stabilities of the rutile VO_2 and V_2O_5 phases is necessary for reliable results concerning the calculated surface free energies. In this context the spin-polarized calculations are superior to the non-spin polarized calculations, yielding in all cases (except the SCAN+U) values closer to the oxidation enthalpy determined from experimental heats of formation[140, 156] for both phases. It could also be shown that the occupation numbers of V $3d$ band in the subsurface layer changes with respect to the structure of the ring termination above. Unfortunately, no reference data are available to either prove or disprove the importance of potential correlation effects that might emanate from changing the occupation number in the surface V $3d$ band. The third effect that influences the resulting surface free energy is the surface buckling which plays the most significant role in case of the (FM) PBE+U functional. The buckling reduces the occupation number of the V t_{2g} electrons in the buckled row which is mainly preferred for functionals including Hubbard-like on-site Coulomb interactions. In case of the fully-covered (110) surface, the buckling effect raises the additional adsorption energy by $\sim 0.3\,\mathrm{eV}$. However, the remaining functionals find the buckling effect to be much weaker. All DFT functionals independent of the spin treatment also predict that the ring structures are either more preferred or as stable as the adsorption phase at high oxygen chemical potential. Judging from this rather extensive use of different computational setups, one must conclude that the reaction enthalpy for the vanadium pentoxide with respect to vanadium dioxide is an important property for a correct description of the off-stoichiometric surface terminations because of its correlation with the effective adsorption energies.

Regarding the experimental STM images, the main features that have been identified in the experiment[32], namely the rectangular and zig-zag patterns have been recovered.

However, additional protrusions that form the flower-like pattern have not been sufficiently clarified yet.

3.6 Conclusion

The electronic and structural properties of the VO_2 bulk phases (rutile, monoclinic), low-index rutile VO_2 surface orientations and off-stoichiometric rutile $VO_2(110)$ (2×2) superstructures have been investigated with Density Functional Theory using different functionals, namely PBE, PBE+U, SCAN and SCAN+rVV. It could be shown that he non-magnetic (NM) SCAN and SCAN+rVV functionals offer the best performance in the bulk system, and describes the basic properties of the monoclinic and rutile phases in a qualitative agreement with experimental findings, such as an electronic band gap, occupation numbers of orbitals that comprise the V-t_{2g} band, lattice vectors and positions of atoms in the unit cell and relative stability between these phases. In contrast to the (NM) SCAN and SCAN+rVV functionals, other functionals exhibit a qualitatively wrong description of either the rutile or the monoclinic phase. For example, the PBE functional finds the monoclinic VO_2 phase to be metallic instead of opening a $\sim 0.6\,eV$ band gap, while the (FM) PBE+U functional opens a $0.42\,eV$ electronic band gap for the metallic rutile phase.

Considering the low-index surfaces, the (110) termination exhibits the lowest surface energy independent of the DFT functional and spin configuration and also matches best with LEED and STM experiments. The (111) surface turned out to be least stable and is even missing in calculated shapes of equilibrium rutile VO_2 particles. Surface energies for the remaining low-index orientations are independent of whether the spin-polarized or non-spin polarized calculations are used, except for the (001) orientation where (NM) calculations yield lower surface energies than ferromagnetic (FM) ones. Moreover, the PBE functional yields on average $50\,\%$ lower surface energies than the SCAN functional. However, one may assume that the (NM) PBE surface energy of the (110) orientation $24\,meV/Å^2$ is rather too small and also in this case the results from the SCAN functional are more applicable.

The off-stoichiometric rutile $VO_2(110)$ (2×2) superstructures have been investigated by three methods, namely by simulated annealing, proper adjustment of a V_2O_5 monolayer and optimization of random structures for different surface stoichiometries. The PBE and PBE+U functionals evidently favor tetrahedral terminations for the adsorption phases, whereas the SCAN and SCAN+rVV functionals show that adsorption phases are stable at very low oxygen chemical potentials ($< -1.4\,eV$, depending on the functional and spin configuration). Furthermore, the absolute values of the surface free energies of the resulting ring terminations are correlated with the calculated oxidation enthalpy of vanadium pentoxide with respect vanadium dioxide. In contrast to (NM) calculations, this phase boundary is always captured by (FM) calculations in better agreement with the experimental value of $-1.28\,eV$[140, 156]. The adsorption energies of the (2×2) reconstructions might be also influenced by two other effects. First, a surface buckling which stabilizes the surface by up to $150 - 550\,meV$ per the (2×1) slab. Second, oxygen adatoms as well as polyhedral terminations induce changes in the occupation number of the V *3d* band localized at the subsurface layer. This might also invoke correlation effects

that could influence the resulting stability of superstructures. However, due to the lack of benchmark calculations or experimental results, one cannot decide which DFT functional gives the best performance for the absolute values of surface free energies.

The suggested ring terminations were also assessed by a comparison with experimental STM images. As easily seen, the proposed ring models that are based on corner-sharing tetrahedra and square pyramids show an agreement with experiment[32] data superior to simple adsorption phases. Even though the proposed models do not provide a full explanation of all experimental STM details, they can be seen as a structural basis that explains the most prominent features, namely the rectangular and zig-zag patterns on top of the $VO_2(110)$ surface.

Chapter 4

Zirconium dioxide (ZrO$_2$)

In recent years, zirconium dioxide (ZrO$_2$, zirconia) has been intensively studied because of its large technological interest. For example, zirconia ceramics is a promising alternative for the gate insulator in Metal Oxide Semiconductor Field Effect Transistors (MOSFET) [160, 161] and High Electron Mobility Transistors (HEMT)[162] because of its high dielectric constant ($\epsilon_r \sim 23$ [163]), large electronic band gap ($E_g = 5 - 6$ eV[164, 165]) and thermal stability on Si or GaN substrates. The large value of E_g also allows to use this material as an insulator in electronic devices [166, 167]. High thermal stability among other refractory ceramics makes zirconia usable as a thermal insulator in high temperature and high pressure experiments [168]. Since oxygen vacancies can diffuse through this (perfectly insulating) material, zirconium dioxide is also used as an ionic conductor. The formation of oxygen vacancies is further improved by doping, *e.g.* with yttria[169], making this material usable as an electrolyte in Solid Oxide Fuel Cells (SOFC)[170–172] and gas sensors[173]. Zirconia is also well known as a biocompatible material and it has therefore found use *e.g.* in orthopedics as femoral heads for total hip replacement [174] and in medicine as dental fixed prostheses [175], even though an ageing effect in the human body has been reported [176]. Moreover, zirconia is being studied for its catalytic properties, *e.g.* for methanol synthesis via CO$_2$ hydrogenation [177].

Depending on pressure and temperature, zirconium dioxide exists in many different phases [178]. At low temperatures and low pressures, zirconia crystallizes in a monoclinic phase (space group $P2_1/c$)[179], also known as baddeleyte which is stable up to 1270 °C. Thereafter, it undergoes a phase transition to the tetragonal phase (space group $P4_2/nmc$)[180, 181]. At about 2650 °C the tetragonal phase is transformed into the cubic phase (space group $f\mathrm{m}\bar{3}\mathrm{m}$)[180]. Application of a compressive stress at room temperature leads to a phase transition from the monoclinic ground state to two orthorhombic phases, first at transition pressures of $\sim$10 GPa forming the orthorombic I phase (space group $Pbca$)[182], second at elevated pressure >25 GPa[182] which transforms the zirconia into the orthorhombic II phase (space group $Pnma$)[183]. Müller et al.[184] reported a discovery of the field-driven ferroelectric phase transition in ultrathin ZrO$_2$ thin films (space group $Pca2_1$). In agreement with experimental data, the applied electric field necessary to cause the phase transformation was calculated to be in order of 1 MV/cm[185].

Surfaces of zirconium dioxide have also received an increased attention in the last years from both theoretical and experimental sides. One obvious difficulty that hinders the use of surface science techniques in the investigation of this interesting system is its insulating nature. Therefore, measurements that use charged particles for analysis, *e.g.* Scanning Tunnelling Microscopy (STM) or Low-Energy Electron Diffraction (LEED) are limited

87

to ultra-thin zirconia films on a metal support to avoid a charging effect. Nevertheless, several important findings have been reported over the past ten years.

First, thin zirconia films on the Pt(111) substrate were prepared by Physical Vapour Deposition (PVD) of zirconium in an O_2 atmosphere and by a subsequent annealing by Meinel et al. [186–188]. It was shown that the quality of thin films depends on deposition annealing temperature. Depending on preparation conditions, namely number of monolayers and annealing temperature, various superstructures have been identified with LEED and STM. For example, The ZrO_2(111)-(1×1) film exhibits a rotation by $\pm 6°$ regarding the Pt(111) substrate. In addition, Maurice et al.[189] have observed a (2×2) superstructure, which had been attributed to the $(\sqrt{7} \times \sqrt{7})$ reconstruction of the Pt(111) support by the DFT calculations performed by Eichler et al.[190]. Sub-monolayer films show a (4×4) and $(2\sqrt{3} \times 2\sqrt{3})$ superstructure after annealing which fits to the (5×5) and $(\sqrt{19} \times \sqrt{19})R \pm 36.6°$ superstructure of the Pt(111) substrate, respectively. Another important finding revealed by Meinel is the fact that thin zirconia films break up at high annealing temperatures, *i.e.* $>1000\,\text{K}$, which shows their meta-stable character[188]. A similar finding had been reported by Lou et al.[191], who reported that thin zirconia films grown on Au(111) and annealed at temperatures $>1025\,\text{K}$ lead to a decrease in the Auger signals of both Zr and O, and an increase for Au.

Ultrathin zirconia films have also been prepared by oxidation of zirconium alloys – Pt_3Zr and Pd_3Zr[192–194], leading to the formation of a single zirconia monolayer. As pointed out, the diffusion of zirconium atoms in Pt_3Zr is slow so that a zirconia trilayer (O-Zr-O) is interfacing a pure Pt(111) layer. The formed ZrO_2 trilayer shows a $(\sqrt{19} \times \sqrt{19})R23.4°$ superstructure with respect to the substrate, identical to one reported by Meinel[186]. On the other hand, on a Pd_3Zr substrate a large superstructure $(\sqrt{217} \times \sqrt{217})R10.16°$ is formed.

Finally, thin zirconia films were grown with the help of a UHV-compatible sputter source which allows the growth of films layer by layer. The films with a thickness of 2-10 monolayers (ML) were deposited and analyzed by LEED and STM by Lackner et al.[34, 35] using the Rh(111) as substrate. It was shown that the structure of the film depends on thickness and annealing temperature. A film with a thickness of 2 ML shows a 'rosette' pattern with a $(\sqrt{21} \times \sqrt{21})R10.9°$ superstructure. The lattice constant related to the zirconia film was measured to be 3.41 Å, shrunken by $\sim 6\,\%$ with respect to the cubic ZrO_2 lattice. This was attributed to the fact that ZrO_2 films might be oxygen-deficient, which would reduce the O-O repulsion and therefore lead to the more compressed film. Thicker films evince a (2×1) or a distorted (2×2) superstructure corresponding to tetragonal and monoclinic zirconia, respectively, depending on the annealing temperature. Annealing at high temperatures result in a monoclinic phase, breaking up the zirconia film as pointed out before. A subsequent study revealed[34] that the tetragonal and monoclinic films exhibit a 1.8 eV difference in core level binding energy, which was explained by the presence of positively charged oxygen vacancies in tetragonal films which cause a band bending because of the large electronic gap of zirconia. This agrees with DFT calculations [195], which showed a reduction of the oxygen vacancy formation energy at the metal-oxide interface by $3 - 5$ eV compared to the bulk or unsupported surface. A similar effect has been reported for positively charged oxygen vacancies which show increased stability when lowering the Fermi level with respect to Valence Band Maximum (VBM)[196], which are more preferred

than Zr^{3+} species. Moreover, it has been concluded[34] that oxygen vacancies stabilize the tetragonal film and if they are filled via oxygen spillover, the monoclinic film is formed.

In the first part of this chapter we present a thorough examination of the performance of DFT for the description of pure zirconium phases relevant to aforementioned experiments – namely monoclinic, tetragonal and cubic ZrO_2. During our investigation, we have also found two meta-stable phases that have not been reported in experiments. The first one is denoted meta-monoclinic due to observed transitions to the monoclinic phase on supported thin films (see Appendix B), and the second one anatase as its crystal structure is structurally related to the TiO_2 phase with the same name. Both phases are included in this comparison. The present DFT results are compared to results of beyond-DFT methods, such as RPA calculations – performed by W. Mayr-Schmölzer[197], and MP2 and CCSD calculations by A. Grüneis[197]. The second part of this chapter is focused on a characterization of oxygen vacancies: (i) in bulk systems, (ii) in unsupported slabs and (iii) at the interface of a metal support.

Computational details

All calculations presented in this chapter were performed with the Vienna *Ab-initio* Simulation Package (VASP). For oxygen 6 valence electrons ($2s^2 2p^4$) and for zirconium 12 valence electrons ($4s^2 4p^6 5s^2 4d^2$) were expanded in a plane basis set with an energy cut-off 600 eV to 800 eV, depending on the calculated structure to ensure the convergence of total energies to 1 meV/atom. The Brillouin zone was sampled with a Γ-centered Monkhorst-Pack grid using the $3 \times 3 \times 3$ k-points for the monoclinic phase and adjusted grids that ensure a similar sampling for remaining phases. Bulk equilibrium volumes were obtained from a parabolic fit of calculated bulk energies at several volumes around the equilibrium value.

4.1 Pristine ZrO_2 bulk systems

In this work ZrO_2 phases are studied that are relevant for experiments regarding supported thin zirconia films. Therefore, the focus is on low-pressure phases, namely monoclinic, tetragonal and cubic ZrO_2. Apart from that, meta-stable meta-monoclinic and anatase ZrO_2 are also considered. All these phases are depicted in Figures 4.1a-e. The most simple structure has the cubic phase depicted in Figure 4.1a in the body-centered tetragonal lattice with the lattice parameter $a = 3.60$ Å. The unit cell is composed of two ZrO_2 formula units, which form O-Zr-O layered structure. All zirconium atoms are eight-fold and oxygen atoms four-fold with the Zr-O bond length of 2.20 Å and O-O distances of 2.55 Å[198]. The cubic phase undergoes a phase transition to the tetragonal phase when cooled down below 2650 °C. The main structural change is shown in Figure 4.1b as a buckling of oxygen atoms, which are situated in case of the cubic phase in a single plane. The buckling in the tetragonal phase is measured to be 0.51 Å[199]. Consequently, the [001] lattice vector is increased as well as the volume of the tetragonal unit cell. Furthermore, the buckling also changes the bond lengths to zirconium atoms, forming shorter and longer bonds with lengths 2.39 Å and 2.09 Å, respectively. Moreover, oxygen-oxygen distances are changed to 2.60 Å. The structure of the monoclinic phase that is thermodynamically stable
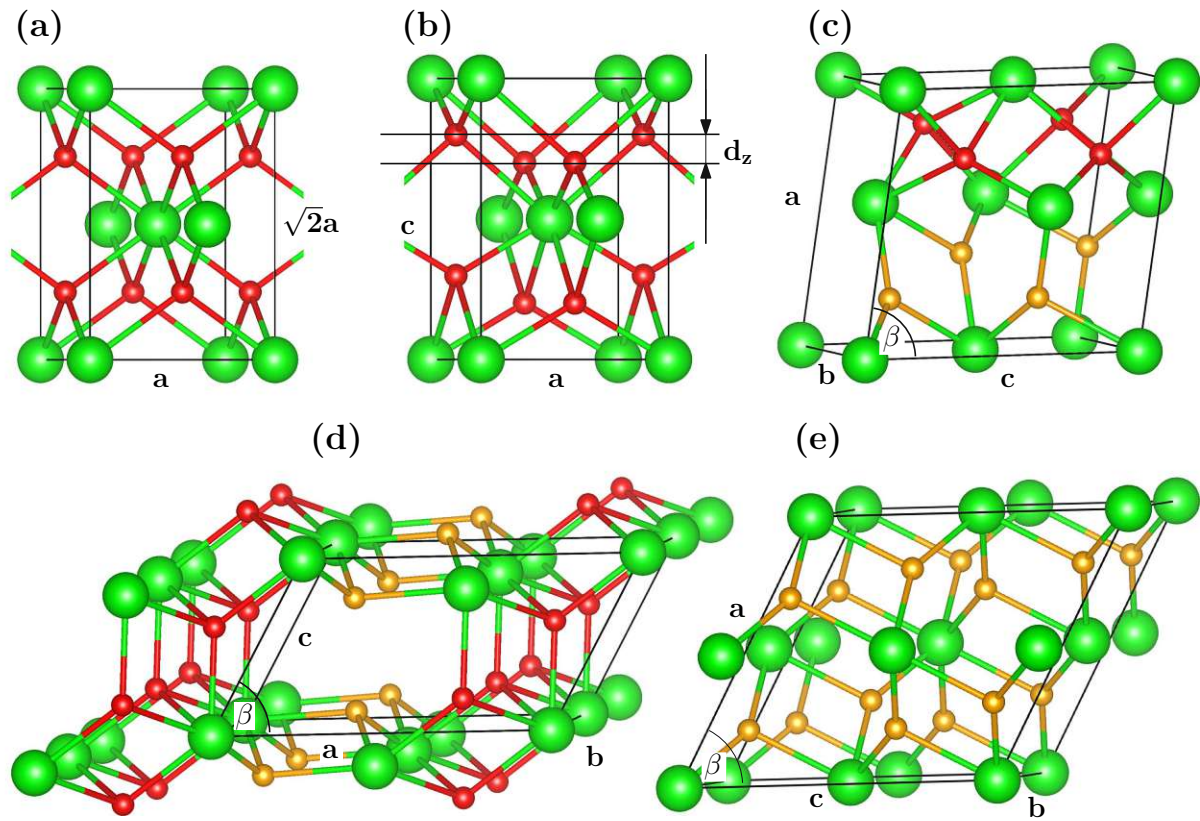
Fig. 4.1: (a) Cubic, (b) tetragonal, (c) monoclinic, (d) metamonoclinic and (e) anatase ZrO_2 phases that were considered in this work. Zirconium atoms are colored in green, three-fold oxygen in yellow and four-fold oxygen in red.

below $1270\,°C$ is illustrated in Figure 4.1c, which shows two significant changes compared to the tetragonal bulk: first, the volume of the unit cell is expanded by $\sim 6.7\,\%$ with respect to the tetragonal phase, which is accompanied by bond breaking. All zirconium atoms are coordinated seven-fold while the coordination of half of oxygen atoms changes from four-fold tetragonal (colored in red) to three-fold planar (in yellow). Second, the unit cell undergoes a distortion, which leads together with an increased volume of the unit cell to a change of the average O-O distance to $2.86\,Å$ while Zr-O distances remain short, on average $2.16\,Å$ – shortest among these phases. This also explains why the monoclinic phase is the most stable at the room temperature: oxygen atoms are negatively charged and repel each other while the shorter bonds in the monoclinic phase indicate larger stability.

The meta-stable meta-monoclinic phase has been introduced by Thomas et al. [200] as an intermediate structure between the tetragonal-to-monoclinic phase transition. In our calculations we have identified this phase after the relaxation of tetragonal $ZrO_2(101)$ multilayer slabs which is discussed more in detail in Appendix B. The relations to the monoclinic phase are the following: the meta-monoclinic structure is composed of the same amount of three-fold and four-fold oxygen atoms as well as the presence of seven-fold coordinated Zr atoms, see Figure 4.1d. Moreover, the monoclinic distortion is present which yields the similar volume of the unit cell per formula unit compared to the monoclinic phase. However, the coordination of three-fold oxygen atoms is not planar and the unit cell

is formed only by two ZrO_2 formula units. The second meta-stable phase called anatase is characterized by an uniform expansion of the monoclinic phase, which results into an additional breaking of bonds. Hence, all Zr atoms are six-fold coordinated and all oxygen atoms exhibit a planar three-fold coordination, see Figure 4.1e. More information about the identification of anatase ZrO_2 is presented in Appendix B.

In the following the performance of various DFT functionals will be studied for these ZrO_2 polymorphs, including PBE, PBE+U, SCAN and SCAN+rVV that were also used in the previous chapter. Additional functionals included were the optB88[201] and optB86b[202] van der Waals density functionals, the hybrid HSE06[76, 77] functional and the (GGA) PBEsol[63] functional. Considering the DFT+U functional, the same value for the on-site interaction parameter in Dudarev's implementation ($U-J = 4\,\mathrm{eV}$) was used as in [195, 203]. This computational setup will be marked as PBE+U. Moreover, the U parameters for O$2p$ and Zr$4d$ states were calculated by Wolloch[204] from constrained RPA calculations, which yielded $U(\mathrm{O}2p) = 4.86\,\mathrm{eV}$ and $U(\mathrm{Zr}4d) = 3.53\,\mathrm{eV}$. Calculations using these parameters for the on-site coulomb interaction for Zr$4d$ and O$2p$ states will be denoted as PBE+U*.

Calculated structural properties of the ZrO_2 phases are shown in Table 4.1. Considering the cubic phase, errors in the calculated a lattice parameter are below $1\,\%$ for all functionals except PBE, PBE+U and PBE+U*, which overestimate both lattice parameters and volume of the unit cell. An overestimation of lattice constants for the PBE functional is a known phenomenon that was also observed in other systems, see *e.g.* [206]. Regarding the tetragonal phase, a poor description of the buckling in the oxygen layer (d_z parameter) for PBE+U, PBE+U* and optB86b functionals was found which underestimates the reference value by $33\,\%$, $24\,\%$ and $16\,\%$, respectively. Furthermore, the PBE+U and PBE+U* functionals also underestimate the c/a ratio from 1.443 to 1.427 and 1.431 respectively. Note that these values are similar to the cubic $c/a = \sqrt{2} = 1.414$. Structural properties of the monoclinic ground state are described well with all functionals. The largest deviations show PBE, PBE+U and PBE+U* functionals which again overestimate the volume of the unit cell, namely by $3\,\%$, $7\,\%$ and $5\,\%$, respectively. The meta-stable meta-monoclinic phase yields almost identical volume of the unit cell compared to the monoclinic phase with differences up to $0.2\,\mathrm{\AA}^3/\mathrm{f.u.}$, except the PBE+U and PBE+U* functionals which show a different trend: the distortion angle β is reduced to $\sim 60°$ and the volume of the unit cell is similar to the tetragonal phase. A detailed analysis has also revealed that the three-fold coordinated oxygen atoms were transformed to four-fold. Thus, the PBE+U and the PBE+U* functionals have transformed the meta-monoclinic phase to tetragonal during the relaxation process. The remaining functionals show no significant differences in average Zr-O bond lengths, but O-O distances differ. For example, the SCAN+rVV functional predicts an increase of the average value for the Zr-O bond from $2.155\,\mathrm{\AA}$ to $2.165\,\mathrm{\AA}$ and average O-O distance changes from $2.784\,\mathrm{\AA}$ (monoclinic) to $2.760\,\mathrm{\AA}$. The last phase treated in this study is anatase ZrO_2, where the volume of the ground state is $\sim 20\,\%$ larger. The SCAN+rVV functional predicts average bond length to be $2.09\,\mathrm{\AA}$ and O-O distance $2.87\,\mathrm{\AA}$. Note that all Zr atoms are six-fold coordinated and thus additional bonds are broken with respect to the monoclinic ground state.

Regarding the calculated stability of these ZrO_2 phases, all DFT functionals find the monoclinic phase to be the energetic ground state. Figure 4.2 shows the calculated energy penalties with respect to the monoclinic phase for the remaining ZrO_2 structures

	PBE	PBE+U	PBE+U*	SCAN	PBESol	optB86b	optB88	HSE	SCAN+rVV	Exp.
					cubic					
a	3.64	3.66	3.64	3.60	3.58	3.57	3.61	3.59	3.59	3.60[198]
V	34.1	34.7	34.1	32.9	32.5	32.2	33.3	32.6	32.6	33.0[198]
					tetragonal					
a	3.65	3.67	3.65	3.60	3.59	3.57	3.62	3.59	3.59	3.61[199]
c	5.28	5.23	5.22	5.22	5.18	5.13	5.24	5.21	5.19	5.21[199]
d_z	0.55	0.34	0.39	0.54	0.49	0.43	0.54	0.55	0.51	0.51[199]
V	35.2	35.2	34.6	33.8	33.3	32.7	34.2	33.5	33.4	34.0[199]
					monoclinic					
a	5.19	5.28	5.25	5.15	5.13	5.15	5.16	5.15	5.13	5.15[205]
b	5.24	5.29	5.26	5.22	5.21	5.25	5.26	5.20	5.22	5.21[205]
c	5.38	5.44	5.41	5.33	5.30	5.31	5.33	5.32	5.30	5.32[205]
β	99.62°	99.51°	99.50°	99.41°	99.64°	99.26°	99.18°	99.53°	99.18°	99.23°[205]
V	36.1	37.5	36.8	35.3	35.0	35.4	35.7	35.1	35.0	35.2[205]
					metamonoclinic					
a	6.87	7.36	7.33	6.85	6.78	6.82	6.90	6.80	6.83	
b	3.52	3.66	3.64	3.50	3.47	3.49	3.51	3.48	3.48	
c	3.87	3.66	3.64	3.83	3.85	3.85	3.84	3.84	3.81	
β	68.26°	60.15°	60.19°	67.81°	68.22°	68.16°	67.50°	68.25°	67.40°	
V	36.2	35.0	34.5	35.4	35.1	35.5	35.9	35.2	34.9	
					anatase					
a	5.70	5.80	5.76	5.67	5.66	5.69	5.70	5.66	5.66	
c	6.08	6.13	6.10	6.05	6.02	6.05	6.05	6.03	6.02	
β	62.49°	61.88°	62.06°	62.12°	62.26°	62.06°	62.21°	62.38°	62.30°	
V	43.8	45.5	44.7	43.0	42.7	43.2	43.5	42.7	42.6	

Tab. 4.1: Structural parameters of stable and meta-stable ZrO_2 phases calculated with various DFT functionals. Lengths of lattice vectors are given in [Å], volumes in [Å³/f.u.].
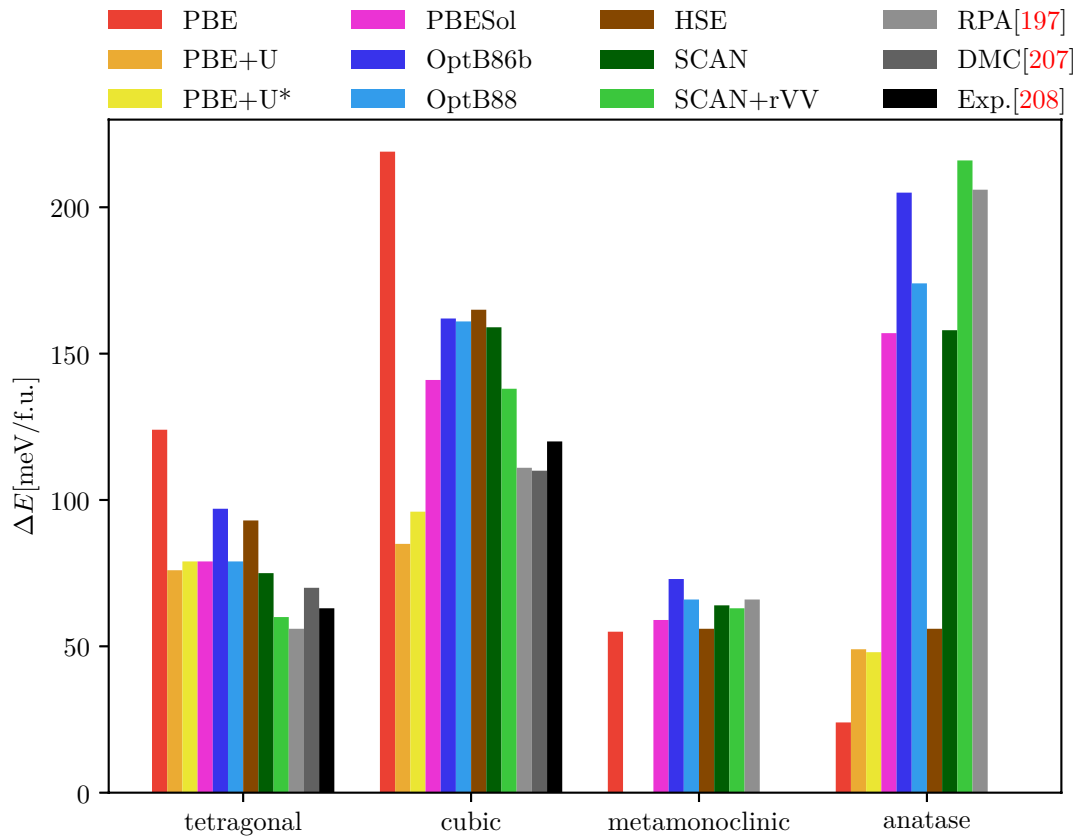
Fig. 4.2: Calculated stabilities of the tetragonal, cubic, meta-monoclinic and anatase ZrO_2, with respect to the monoclinic ground state.

including the beyond-DFT results (RPA, DMC) and experimental findings. Regarding the high-temperature phases (tetragonal, cubic), all functionals describe, in agreement with experimental findings, the tetragonal phase to be more stable than the cubic ZrO_2. The PBE functional overestimates the stability of the monoclinic ground state by 61 meV/f.u. and by 38 meV/f.u. with respect to the experimental values for high temperature tetragonal and cubic phases[208]. Underestimated stability of the tetragonal phase is fixed with all remaining functionals giving a closer value to the experimental reference. Regarding the PBE+U and PBE+U* functionals, the stability of the tetragonal phase (76 meV and 79 meV) is in a good agreement with the experimental value, but the cubic phase is calculated to be too stable. The small difference in the calculated stability between the tetragonal and the cubic phase can be attributed to the structural changes in the tetragonal phase after the relaxation, namely underestimation of the c/a ratio and size of the buckling that represent the main differences between the tetragonal and the cubic phase. On the other side, the best performance regarding the stability of the high temperature phases is found for the SCAN+rVV functional, which differs only by 3 meV and 18 meV per f.u. from the reference values for the tetragonal and the cubic phase, respectively. Also the SCAN
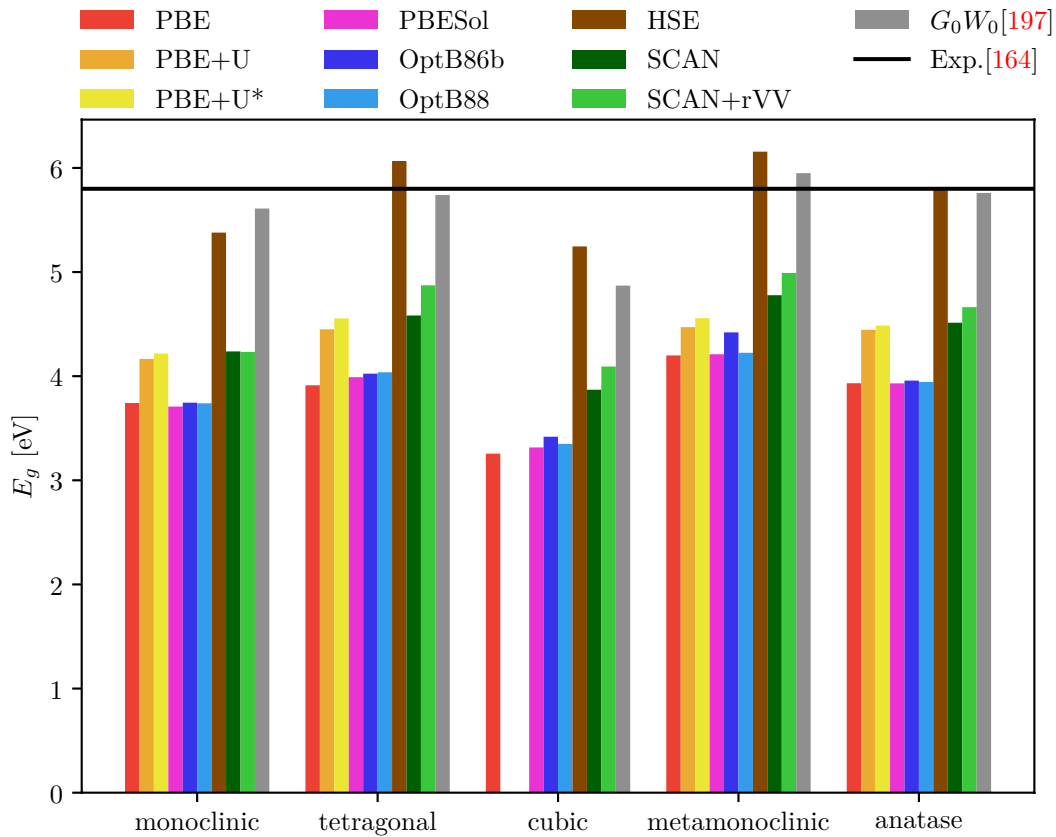
Fig. 4.3: Calculated band gaps of the ZrO_2 polymorphs using various DFT functionals. The horizontal line represents the lowest value of the experimental band gap related to the tetragonal phase.

and the PBESol functionals show a good performance. However, they underestimate the stability of the cubic phase by 40 meV/f.u. and 20 meV/f.u. respectively.

Considering the stability of the meta-monoclinic phase, the RPA benchmark calculations describe it to be 10 meV/f.u. less stable than the tetragonal phase. A qualitative agreement with the RPA benchmark is recovered only by the SCAN+rVV functional, which yields the tetragonal phase to be more stable by 3 meV/f.u. However, this can be improved by including zero-point vibrational energies, which yield a decreased stability of the meta-monoclinic phase by additional 19 meV/f.u.[197]. The second metastable phase, anatase ZrO_2, is calculated with RPA to be the least stable. However, our results show a strong dependency of the calculated stability on the DFT functional used. PBE, PBE+U, PBE+U* and HSE erroneously favour this phase and is determined to be as stable as the meta-monoclinic (HSE), or even more stable. On the other side, all the other functionals describe this phase to be similarly stable or less stable than the cubic phase. This finding indicates that the preference of the anatase phase is a PBE artefact which is compensated neither by considering the on-site interactions in PBE+U and PBE+U* nor by the HF exchange in HSE. Note that the HSE functional is based on PBE exchange and correlation.

The SCAN and SCAN+rVV functionals significantly improve the stability of all phases with respect to standard GGA and GGA+U functionals. Moreover, the electronic structure, in particular the size of the electronic band gap, is described better compared to GGA and is on the level of DFT+U. Figure 4.3 shows calculated electronic band gaps in comparison with reference G_0W_0 calculations[197] and the experimental value for the (yttria-stabilized) tetragonal phase of $\sim 5.8\,\text{eV}$, which was reported to have the smallest band gap[164]. Even though the SCAN functional systematically enlarges the electronic gap compared to PBE, the resulting values are still too small. The experimental value can only be reproduced by G_0W_0 or by HSE while the remaining functionals underestimate this value by $1 - 2\,\text{eV}$. It should also be noted that van der Waals corrected DFT functionals (OptB88, OptB86b) do not yield better results than the PBE functional.

4.2 Neutral oxygen vacancies in the ZrO$_2$ bulk

As already pointed out, oxygen vacancies play an important role in zirconia for applications such as an electrolyte in solid oxide fuel cells. Furthermore, they influence properties of thin zirconia films on a metal support. For example, they stabilize the tetragonal phase with respect to the monoclinic phase[34, 35]. In this section, the stability of oxygen vacancies in the stable and metastable zirconia polymorphs is discussed. The oxygen vacancy formation energy E^f – the energy that is necessary to create the oxygen vacancy, can be calculated as

$$E^f = E_{\text{bulk}} - E_{\text{bulk}}^{\text{vac}} - \frac{1}{2}E_{\text{O}_2}, \tag{4.1}$$

where E_{bulk} and $E_{\text{bulk}}^{\text{vac}}$ are total energies of the system without and with an oxygen vacancy, respectively. E_{O_2} denotes the total energy for an oxygen molecule in the triplet state. All calculations were performed with supercells to avoid interaction between oxygen vacancies due to the periodic boundary conditions. $4 \times 4 \times 4$ supercells were used for the cubic ZrO$_2$ phase and adjusted supercells for the remaining phases to achieve a similar separation of the oxygen vacancies. These supercells ensure the convergence of the oxygen vacancy formation energies up to 50 meV. The stability of oxygen vacancies has been studied with the subgroup of DFT functionals that were already used for the pristine bulk systems. Most of the DFT functionals used in the study of the bulk systems, namely the PBE, PBE+U, PBE+U*, OptB86b and SCAN have been considered. HSE and SCAN+rVV calculations were omitted due to a higher computational cost and remain as tasks for the near future.

The resulting oxygen vacancy formation energies are depicted in Figure 4.4. All functionals describe the formation energy to be very high – between 5.5 eV and 6.9 eV, revealing that the formation of oxygen vacancies in all ZrO$_2$ bulk phases is strongly unfavourable. However, Figure 4.4 shows that the absolute values of calculated formation energies depend on both the crystal structure and the chosen functional. In the following lines, the dependence of the vacancy formation energy with respect to the crystal structure will be discussed.

All functionals show the same trend: Oxygen vacancies are easiest to form in the cubic phase, followed by the tetragonal phase with an energy penalty $12 - 120$ meV and meta-monoclinic phase ($\Delta E^f = 12 - 120$ meV). On the other side, monoclinic and anatase polymorphs disfavour the formation of oxygen vacancies by $\sim 0.2 - 0.7$ eV compared to the cubic phase. Formation energies in the monoclinic and meta-monoclinic phases depend on the coordination geometry of the oxygen that is removed from the unit cell. These phases show a reverse behaviour: All DFT functionals prefer a removal of the four-fold coordinated oxygen atom from the monoclinic phase, whereas in the meta-monoclinic phase an oxygen vacancy at a three-fold coordinated oxygen site is preferred.

Regarding the dependence of the formation energies on a particular DFT functional, the results are qualitatively similar for all phases. The highest formation energies are predicted by the SCAN functional ($6.3 - 6.9$ eV), followed by the OptB86b ($6.3 - 6.7$ eV). Compared to the PBE functional, the SCAN and the OptB86b functionals yield $\sim 0.5 - 0.7$ eV and $\sim 0.3 - 0.5$ eV higher values for the oxygen vacancy formation energy. The increase of the vacancy formation energy is related to the calculated binding energy (E_B) of the O$_2$ molecule used as the reference system in calculations, see formula 4.1. The SCAN
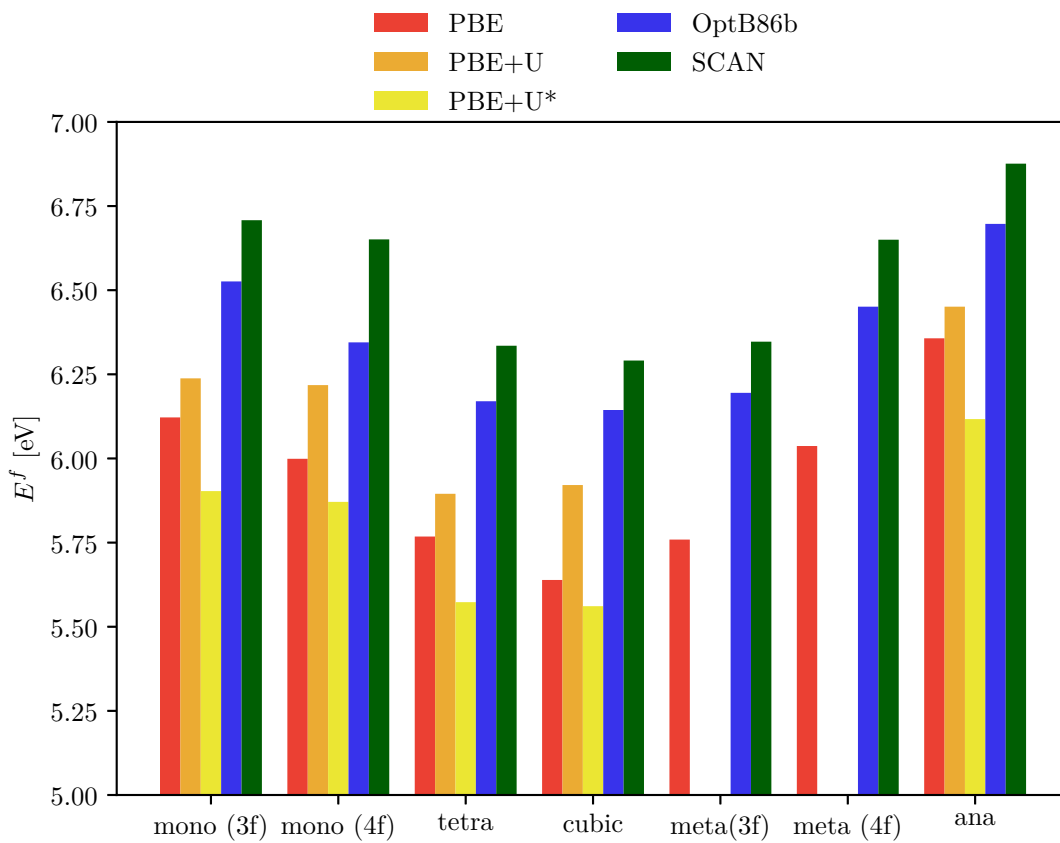
Fig. 4.4: Calculated oxygen vacancy formation energies in stable and meta-stable ZrO_2 polymorphs using various DFT functionals. Monoclinic and meta-monoclinic phases comprise three-fold and four-fold coordinated oxygen atoms which yield different vacancy formation energies. In the graph they are marked as '3f' and '4f', respectively.

functional yields the lowest $E_B(O_2)$ ($E_B = 5.15\,\text{eV}$[69]), which is closest to the experimental value $E_B = 5.12 - 5.23\,\text{eV}$[69]. The values for OptB86b and PBE are E_B $5.69\,\text{eV}$ and $6.23\,\text{eV}$, respectively[209]. Considering the differences in calculated binding energy of the oxygen molecule with respect to the PBE functional one finds $\sim 0.3\,\text{eV}$ and $\sim 0.5\,\text{eV}$ for the OptB86b and the SCAN functionals, respectively. These values are comparable to lower limits for the calculated differences in the oxygen vacancy formation energies. Thus, the correct binding energy of the oxygen molecule is an important parameter for the oxygen vacancy formation energy. Seen from this perspective, the SCAN functional yields the most reliable results.

Interestingly, compared to PBE, PBE+U and PBE+U* show a reversed trend in the calculated formation energies: PBE+U (including only Zr$4d$ on-site interactions) leads to higher vacancy formation energies by $\sim 0.1 - 0.3\,\text{eV}$, but PBE+U* (including Zr$4d$ and O$2p$ on-site corrections) lowers them approximately by the same value. The increase of formation energies with the PBE+U functional could be caused by an increased polarization of Zr-O bonds in the vicinity of an oxygen vacancy. On the other side, lower values of the oxygen vacancy formation energies for the combined corrections at both Zr and O sites (PBE+U*) are presumably caused by a different oxidation state of oxygen in the ZrO$_2$ bulk and in an oxygen molecule. Hence, the oxygen atom in the ZrO$_2$ bulk with an oxidation state of -2 is penalized by DFT+U* with respect to an oxygen atom in a O$_2$ molecule with an oxidation state of zero.

The influence of the oxygen vacancy on the electronic structure has been studied with the SCAN functional. Formation of a neutral oxygen vacancy in the bulk ZrO$_2$ leaves two electrons behind. Thus, the most prominent change in the electronic structure is the formation of occupied vacancy states localized between the valence and the conduction band, as shown in Figure 4.5a by a black solid vertical line, which represents the calculated Fermi level. Independent of the ZrO$_2$ phase, the gap state is always found in the upper half of the electronic band gap, *i.e.* closer to the conduction band minimum, as shown in Table 4.2. As a result, the calculated valence band maximum is pushed from the edge of the O$2p$ band much closer to the Zr$4d$ band. This finding corresponds to rather high values for the formation energies because of the necessity to fill rather unfavourable gap states.

The influence of the size of the supercell on the calculated formation energy has been studied with the PBE+U functional in cubic $1 \times 1 \times 1$ to $4 \times 4 \times 4$ supercells. While the energy cut-off was kept same, the k-points grid was correspondingly adjusted to the size of the supercell, starting from the $4 \times 4 \times 4$ grid for the smallest cell to $1 \times 1 \times 1$ grid for the largest. The result is depicted in Figure 4.5b as a function of the reciprocal value of the shortest distance between oxygen vacancies. Extrapolation to zero (*i.e.* infinite distance between oxygen vacancies) shows that $4 \times 4 \times 4$ supercells yield formation energies with an error of $50\,\text{meV}$.

Lastly, the charge distribution of the vacancy states inside the electronic gap is shown in Figure 4.5c for the tetragonal phase, but a similar behaviour has also been observed in the other phases. As shown, most of the left behind electrons are localized inside the oxygen vacancy and also to a much lesser degree at surrounding Zr atoms. Some charge is also visible at the surrounding nearest and next-nearest neighbour oxygen atoms.
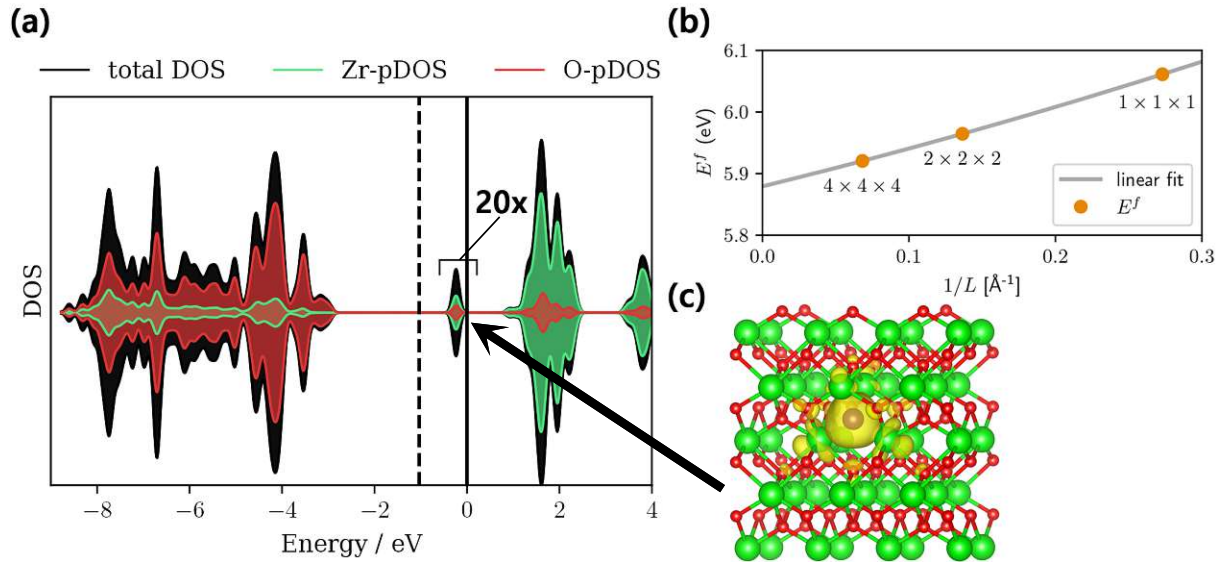
Fig. 4.5: Panel (a), calculated SCAN electronic structure of the cubic ZrO_2 $4 \times 4 \times 4$ supercell in presence of the oxygen vacancy, which induces states inside the electronic gap marked by a black solid vertical line. Vacancy states are magnified by a factor of 20 for a better visualization. The convergence of the oxygen vacancy formation energy with respect to the size of the supercell using the PBE+U is shown in panel (b). The gray line marks a linear fit of calculated values using different sizes of supercells. Errors in calculated vacancy formation energies are below 50 meV. Panel (c) displays the charge density corresponding to vacancy states marked by the black arrow.

	mono (3f)	mono (4f)	tetra	cubic	meta (3f)	meta (4f)	ana
E_{vac} [eV]	2.99	2.55	3.04	2.73	3.14	2.95	3.12
Rel. [%]	72	62	66	70	66	62	79

Tab. 4.2: Calculated positions of the induced oxygen vacancy states in ZrO_2 polymorphs with respect to the upper edge of the $O2p$ band (upper line) and relative position in the band gap (lower line). 0% correspond to the valence band maximum and 100% to the conduction band minimum.

4.3 Charged oxygen vacancies

In real systems the formation of oxygen vacancies can be accompanied by a charging of the vacancy, which would make the oxygen vacancy either negatively charged when an oxygen vacancy behaves like an electron acceptor, or positively charged – an oxygen vacancy is an electron donor. In this section, the stability of charged oxygen vacancies and their influence on the electronic structure in the tetragonal and in the cubic ZrO_2 phases will be discussed.

The stability of the charged oxygen vacancy is usually considered as a function of the Fermi energy that varies over the range of the electronic band gap[210]. Thus, one needs to modify Eq. 4.1 into the following form[196]:

$$E_{chg}^f(E_F) = E_{bulk}^{vac} - E_{bulk}^{nd} + \mu_O + q(E_V + E_F) + E_{corr.}, \qquad (4.2)$$

where E_{bulk}^{vac} and E_{bulk}^{nd} are total energies of the supercell with and without a charged vacancy, respectively. The formation of oxygen vacancies was calculated for an oxygen chemical potential $\mu_O = 1/2E_{O_2}$ fixed at the energy of the oxygen molecule in the triplet state. The next two terms – E_V and E_F, mark the energy of the valence band maximum in the unperturbed supercell and the Fermi energy, respectively. In this notation, the Fermi energy E_F is taken with respect to valence band maximum, *i.e.* it ranges from zero (valence band maximum) to the size of the band gap (conduction band minimum). The last term – $E_{corr.}$ denotes the correction energy that considers the finiteness of the calculated supercell containing the charged defect, when using periodic boundary conditions. Since the present supercells are converged to 50 meV with respect to oxygen vacancy formation energy as demonstrated above, this correction term is assumed to be rather small and is neglected. In the following calculations for cubic and tetragonal $3 \times 3 \times 3$ supercells using PBE and the SCAN functionals will be discussed. Five different charge states have been considered: positively charged ($-2e^-$ and $-1e^-$), neutral and negatively charged ($+1e^-$ and $+2e^-$) oxygen vacancies for each phase and functional.

Considering the tetragonal phase, the influence of defects with different charge state on the surrounding atoms and on the electronic structure is depicted in Figure 4.6. Panel 4.6a shows that the negatively charged oxygen vacancy with two excess electrons (the black dot) attracts the surrounding zirconium atoms and oxygen atoms are repelled. The average distance between the center of the oxygen vacancy and the nearest-neighbour oxygen atoms changes from 2.51 Å (neutral supercell) to 2.55 Å in the charged supercell while the average distance between the oxygen vacancy and surrounding zirconium atoms is shortened from 2.21 Å to 2.07 Å. On the other side, the positively charged oxygen vacancies with two electrons lost attract oxygen atoms and repel zirconium atoms, see panel 4.6b. In this case the average distances of the oxygen – oxygen vacancy and zirconium – oxygen vacancy change to 2.34 Å and 2.41 Å, respectively. This finding indicates that the extra charge induced by a point defect is localized in vicinity of an oxygen vacancy so that the positively charged defect attracts negatively charged oxygen atoms and repels positively charged zirconium atoms and vice versa.

Panels 4.6c-h show the electronic structure of the (c) unperturbed supercell, and (d-h) supercell with an oxygen vacancy with different charge state, ranging from +2 ($-2e^-$) to -2 ($+2e^-$). As shown, the most prominent changes in the electronic structure are extra states
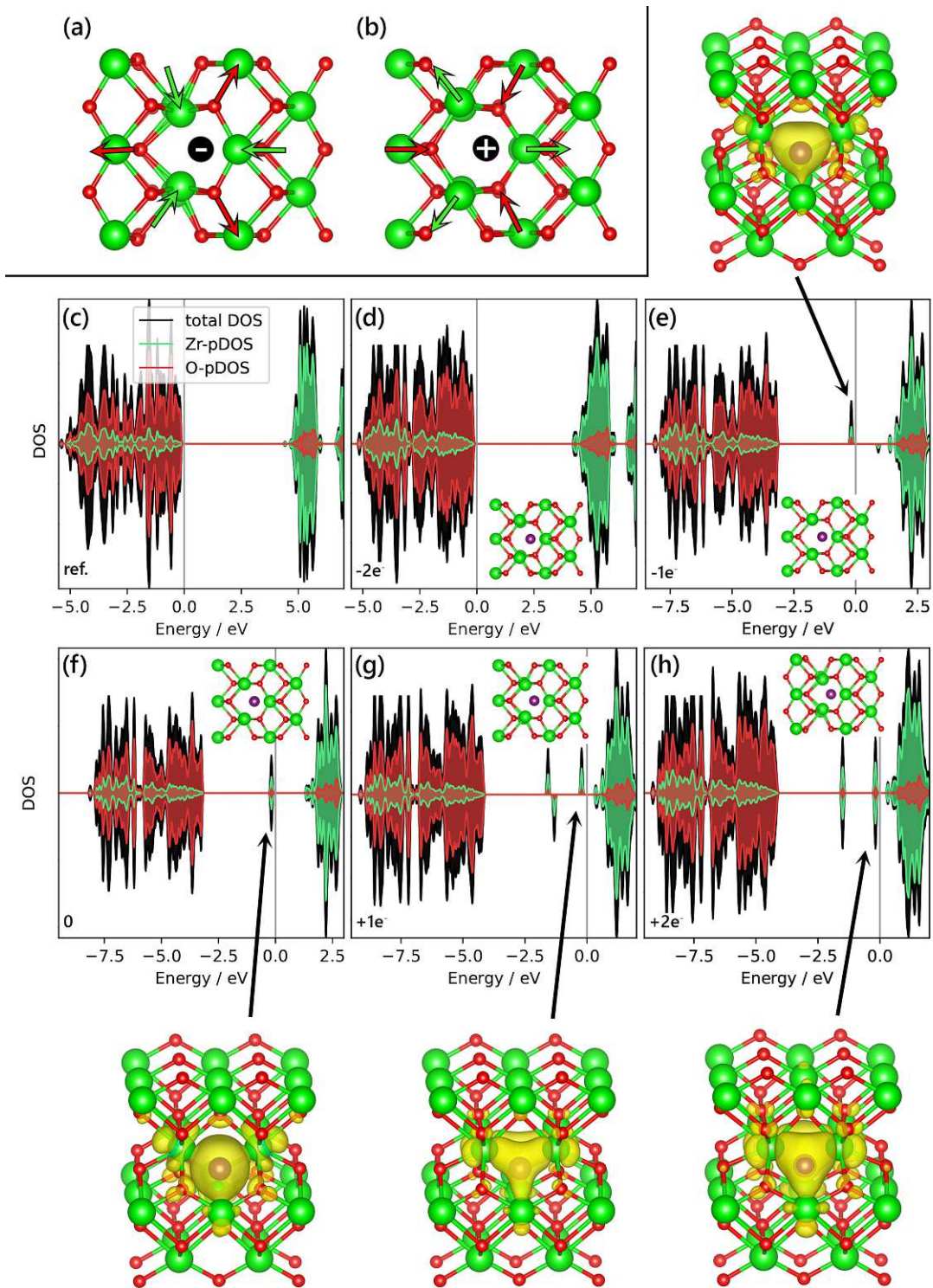
Fig. 4.6: Calculated electronic structure (SCAN) of the tetragonal ZrO_2 $3 \times 3 \times 3$ supercell. Panels (a-b) show the displacement of the nearest Zr and O atoms neighbouring negatively and positively charged oxygen vacancies. Panels (c-h) show the electronic structure of: (c) unperturbed unit cell and the unit cell containing: (d-e) positively charged ($-2e^-$, $-1e^-$), (f) neutral, and (g-h) negatively charged ($+1e^-$,$+2e-$) oxygen vacancy. Inset figures show the relaxed structure in vicinity of the oxygen vacancy, offset figures represent the charge distribution of vacancy states marked with black arrows. Vacancy states are magnified for a better visualization.
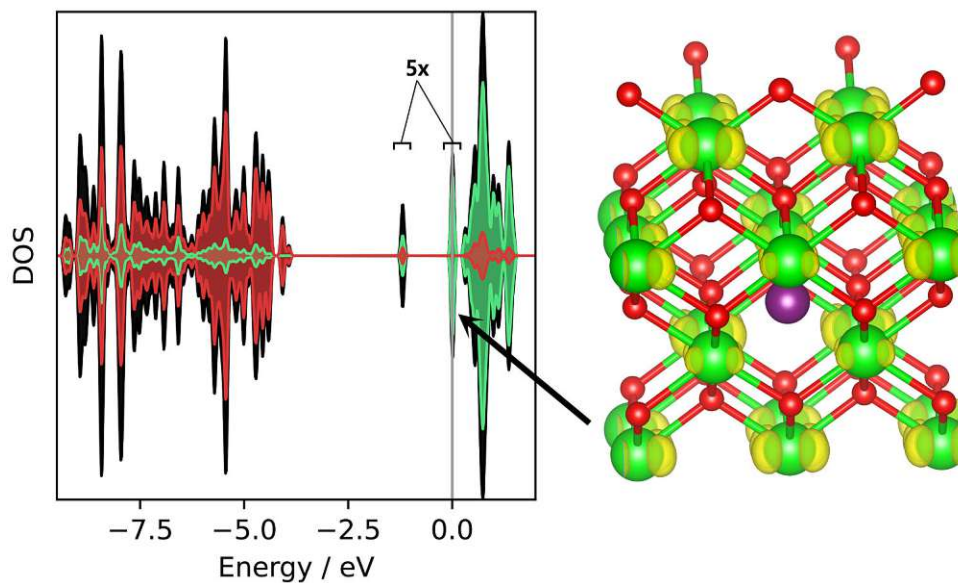
Fig. 4.7: Electronic structure of the negatively charged cubic cell with two excess electrons and the charge distribution of the gap states. The states in the electronic band gap are magnified (5×) for a better visualization.

within the electronic band gap. Starting from a supercell with two electrons lost (charge +2, panel 4.6d), the gap states are removed and the original band gap is recovered. When the charge state is changed and more electrons are put into the supercell, the gap states appear inside the electronic band gap, again in its upper half closer to the conduction band minimum, as shown in the previous section. The presence of the gap states is accompanied by a shift of the calculated valence band maximum (see gray lines) into the electronic band gap. In this respect, the major difference between the positively and negatively charged defects is the formation of an additional vacancy level in the band gap and the shift of the calculated Fermi energy almost into the conduction band minimum. The offset panels show its charge distribution to be always localized in the vicinity of the oxygen vacancy.

Regarding the cubic ZrO_2 phase, the neutral and positively charged oxygen vacancies show a similar trend for the electronic structure and the surrounding atoms. However, excess electrons (charge states $+1e^-$ and $+2e^-$) are not localized near an oxygen vacancy. As shown in Figure 4.7, the excess charge related to the second peak in the band gap is delocalized over all zirconium sites in the supercell. This finding indicates that the localization of excess charge in the tetragonal cell is possible because of the broken symmetry.

Figure 4.8 displays the evaluated stability of the charged and neutral oxygen vacancies as a function of the Fermi energy, which ranges from 0 (valence band maximum) to $5.8\,\text{eV}$ corresponding to the experimental value of the band gap[164]. The black vertical line marks the calculated conduction band minimum. In these calculations tetragonal and cubic phases have been treated with PBE and SCAN. For the tetragonal phase, both DFT functionals show that the negatively charged oxygen vacancies are only stable for a state very close to the conduction band minimum. This agrees with the electronic structure, which shows that additional gap states are located approximately at the same position.

(a) Tetragonal ZrO_2

(b) Cubic ZrO_2
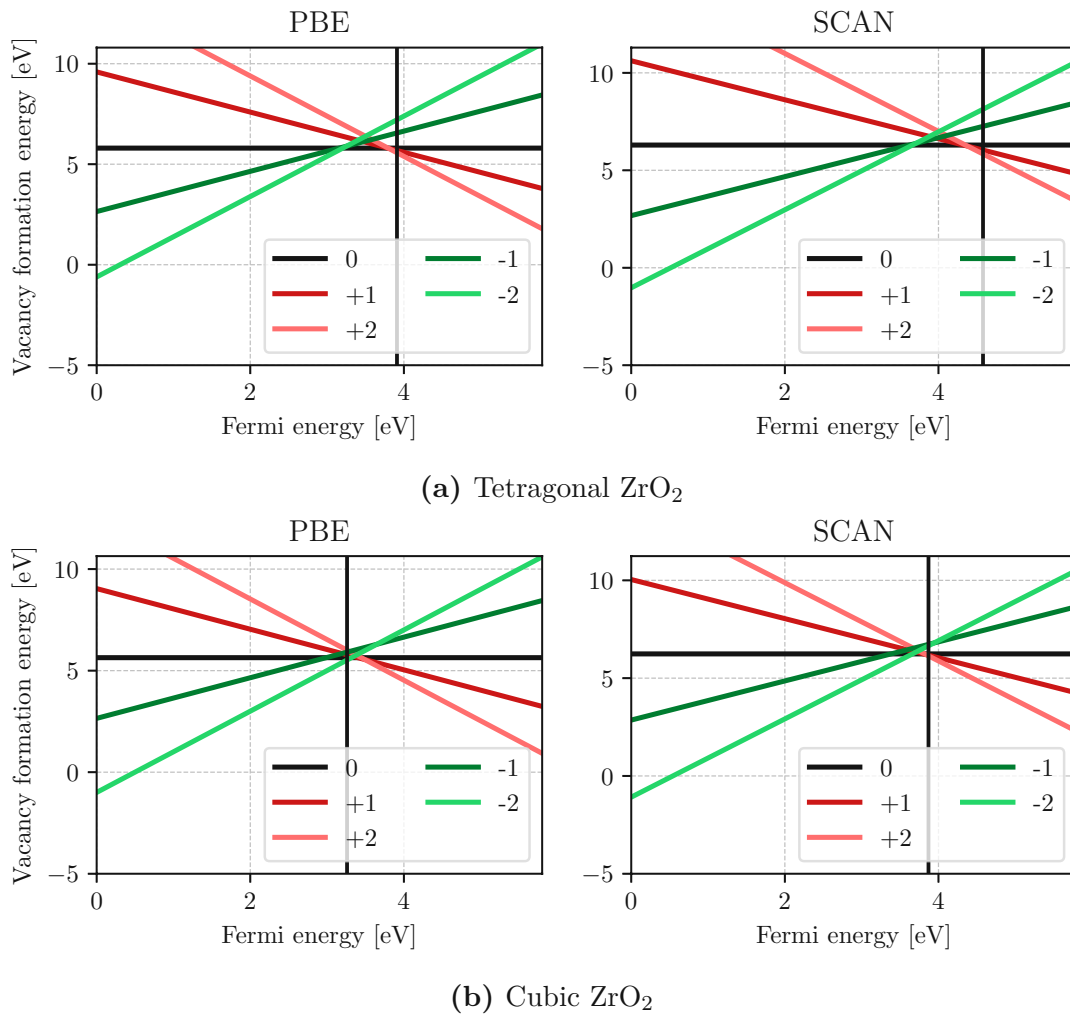
Fig. 4.8: Calculated stability of a charged oxygen vacancy using the PBE and SCAN functionals as a function of the Fermi energy relative to the valence band maximum. The horizontal line marks the formation energy of a neutral oxygen vacancy and the black vertical line the position of the conduction band minimum. Numbers in a legend denote the charge state of an oxygen vacancy.

The stability of the negatively charged oxygen vacancies is even more suppressed in the cubic phase: PBE and SCAN functionals predict a stable vacancy only for a Fermi energy above the calculated conduction band minimum (CBM). The slightly better stability of a negatively charged oxygen vacancy in the tetragonal phase can be attributed to the localization of its charge and additional structural relaxations as pointed out above. Both functionals show that over the wide range of Fermi energies, positive oxygen vacancies with a charge state $+2$ $(-2e^-)$ are the most stable species. The high stability of the positively charged defect also shows that the large formation energy of neutral oxygen vacancies is due to the formation of rather unstable gap states localized in the vicinity of an oxygen vacancy.

(a)
(b)
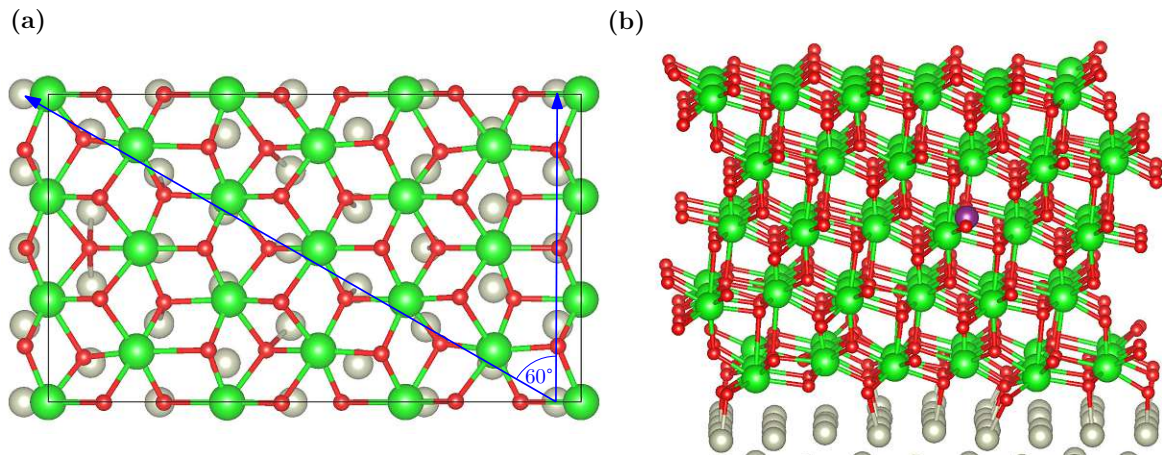
Fig. 4.9: Top view (panel a) of the interface between a t-ZrO$_2$ (101) slab and the Rh(111) substrate. Only one monolayer of both materials is shown. Blue vectors denote the original surface vectors of the Rh(111) (4×8) superstructure and the adjusted t-ZrO$_2$ (3 × 3) unit cell. The black rectangle marks the unit cell considered in calculations, created by the transformation of the original lattice. Panel (b) marks the side view of the supported t-ZrO$_2$ (101) slab after the structural relaxation. Rhodium, zirconium and oxygen atoms are colored in gray, green and red, respectively. The violet sphere represents the oxygen atom that was subsequently removed for studying the properties of defects in the supported slabs.

4.4 Vacancies in (un)supported t-ZrO$_2$(101) films

In this section the influence of a metallic support as used in experimental measurements[35] on the formation of oxygen vacancies in thin t-ZrO$_2$ films is studied. For these purposes the most stable termination of tetragonal ZrO$_2$, namely the (101) surface in a (2 × 1) superstructure on the Rh(111) substrate[35] has been investigated. The experiments [35] also show that depending on annealing temperatures and slab thickness different superstructures are obtained. Therefore, the calculations were restricted to five-layered slabs with a tetragonal structure that occurs when the thin film is annealed at temperatures below 730 °C.

A Rh unit cell with a lattice parameter $a_{\mathrm{Rh}} = 3.8$ Å[211] creates a Rh(111) surface with a surface unit cell with the size $\sqrt{2}/2 a_{\mathrm{Rh}} = 2.7$ Å. The tetragonal ZrO$_2$ (t-) (101) surface with in-plane vectors with lengths 3.61 Å and 7.30 Å can be matched to the Rh(111) substrate by considering t-(101) (3 × 3) and Rh(111) (4 × 8) supercells with a lattice mismatch of 0.8 % and 1.8 %, respectively. In the present calculations the lattice parameters of the t-ZrO$_2$(101) film were adjusted to fit the Rh(111) (4 × 8) supercell which created an interface as depicted in Figure 4.9a. The Rh(111) lattice vectors are denoted by the blue arrows and the rectangular unit cell used in the calculations is shown in black. Figure 4.9b shows a side view of the resulting interface between the Rh(111) substrate and the t-ZrO$_2$ (101) slab after the relaxation, the most prominent changes are apparent at the interface layers which are strongly buckled due to the interaction between t-ZrO$_2$ and the Rh substrate.
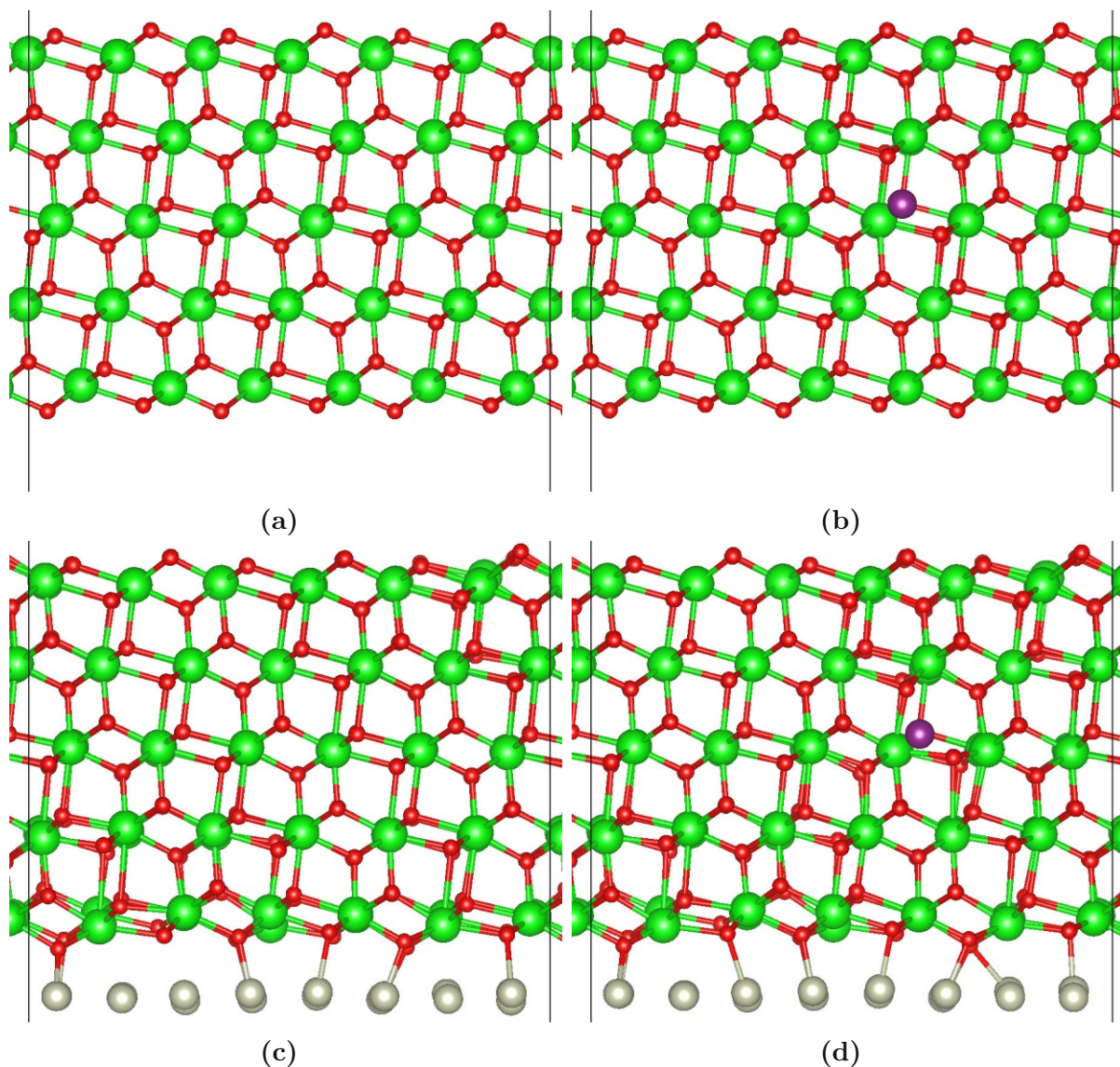
Fig. 4.10: Relaxed structures of (a-b) the unsupported t-ZrO$_2$ slab without and with an oxygen vacancy (violet sphere), and (c-d) supported t-ZrO$_2$ slab without and with an oxygen vacancy, calculated with the SCAN functional.

The influence of the metal support on the formation of an oxygen vacancy has been considered just for a single case. An oxygen vacancy both in supported and unsupported t-ZrO$_2$ (101) films has been calculated so that changes in the geometry of the system, electronic structure and oxygen vacancy formation energies can be directly compared. In order to minimize the influence of the surface and the interface on the formation energy of an oxygen vacancy, an oxygen atom was removed from the middle of the slab as shown by a violet sphere in panel 4.9b.

Figure 4.10 shows relaxed structures of the supported and unsupported thin zirconia films with and without an oxygen vacancy. As shown, the main structural differences caused by an oxygen vacancy are an attraction of surrounding oxygen atoms and repulsion of zirconium atoms, as has been observed for neutral and positively charged oxygen vacancies

	Bulk	Unsupported	Supported
PBE	5.77	5.70	3.56
SCAN	6.34	6.41	4.39
PBESol[195]	6.16	-	0.95 - 3.28[a]

[a] calculated with the 1ML t-ZrO_2 (101) film on Pt(111) support.

Tab. 4.3: Calculated oxygen vacancy formation energies (neutral) in the tetragonal ZrO_2 bulk, and in the thin t-ZrO_2 (101) film with and without a metallic support.

above. However, this effect is much more prominent in the supported slab: while the average distance between neighboring oxygen atoms and the oxygen vacancy is calculated to be $d(O - O_{vac}) = 2.50\,\text{Å}$ in unsupported slabs, the supported slabs lower this value to $2.32\,\text{Å}$. Similarly the average distance between the surrounding zirconium atoms and the oxygen vacancy is $d(Zr - O_{vac}) = 2.21\,\text{Å}$ and $2.42\,\text{Å}$ for unsupported and supported slabs, respectively. Note that the distances in the supported film are in a perfect agreement with the previously discussed average distances for positively charged bulk supercell with two loss electrons: $d(O - O_{vac}) = 2.34\,\text{Å}$, $d(Zr - O_{vac}) = 2.41\,\text{Å}$. These findings indicate a change in the charge distribution of the gap states in case of the supported zirconia films.

To investigate the influence of the surface and the metallic support on the electronic structure, the density of states for the (un)supported films with(out) an oxygen vacancy is shown, see Figure 4.11. Starting from the electronic structure of the unsupported slab without a defect – panel 4.11a, the presence of the surface causes an additional peak at the valence band maximum. A partial charge decomposition confirms that these states are localized at the surface, predominantly at the uppermost oxygen sites. If the (neutral) oxygen vacancy is formed – panel 4.11b, the electronic structure shows vacancy states inside the electronic band gap, closer to the conduction band minimum as in case of the neutral oxygen vacancy in the bulk. Regarding the metal supported slabs, the Fermi energy is now defined by the metallic substrate, located approximately in the middle of the electronic band gap. In contrast to the unsupported thin films, the presence of an oxygen vacancy does not show any significant change in the electronic structure. In both cases, neither the surface states nor the gap states are apparent. Thus, charge related to the surface states and to the localized vacancy states are transferred to the metallic substrate and the oxygen vacancy is in the charge state (+2). This is also in agreement with stronger structural relaxations in supported films compared to the floating films, where the oxygen vacancy is neutral.

Since the positively charged vacancies were calculated to be more stable, one can expect a decrease of the vacancy formation energy in presence of the metallic support. Indeed, as shown in Table 4.3, the oxygen vacancy formation energies are decreased by $\sim 2.1\,\text{eV}$ and $\sim 2.0\,\text{eV}$ as calculated with the PBE and the SCAN functionals, respectively. The absolute values can also be compared with the formation energy of the charged defect, as calculated in the previous section, see Figure 4.8. In the case of supported slabs the Fermi energy is calculated to be $2.2\,\text{eV}$ and $2.5\,\text{eV}$ above the valence band maximum with PBE and SCAN. If one uses these values to evaluate the stability of the oxygen vacancy in the bulk with the charge state (+2), one gets $3.79\,\text{eV}$ and $3.97\,\text{eV}$ for PBE and SCAN,

(a) unsupported, without a defect

(b) unsupported, with a defect; gap states at the Fermi level are magnified

(c) supported, without a defect

(d) supported, with a defect
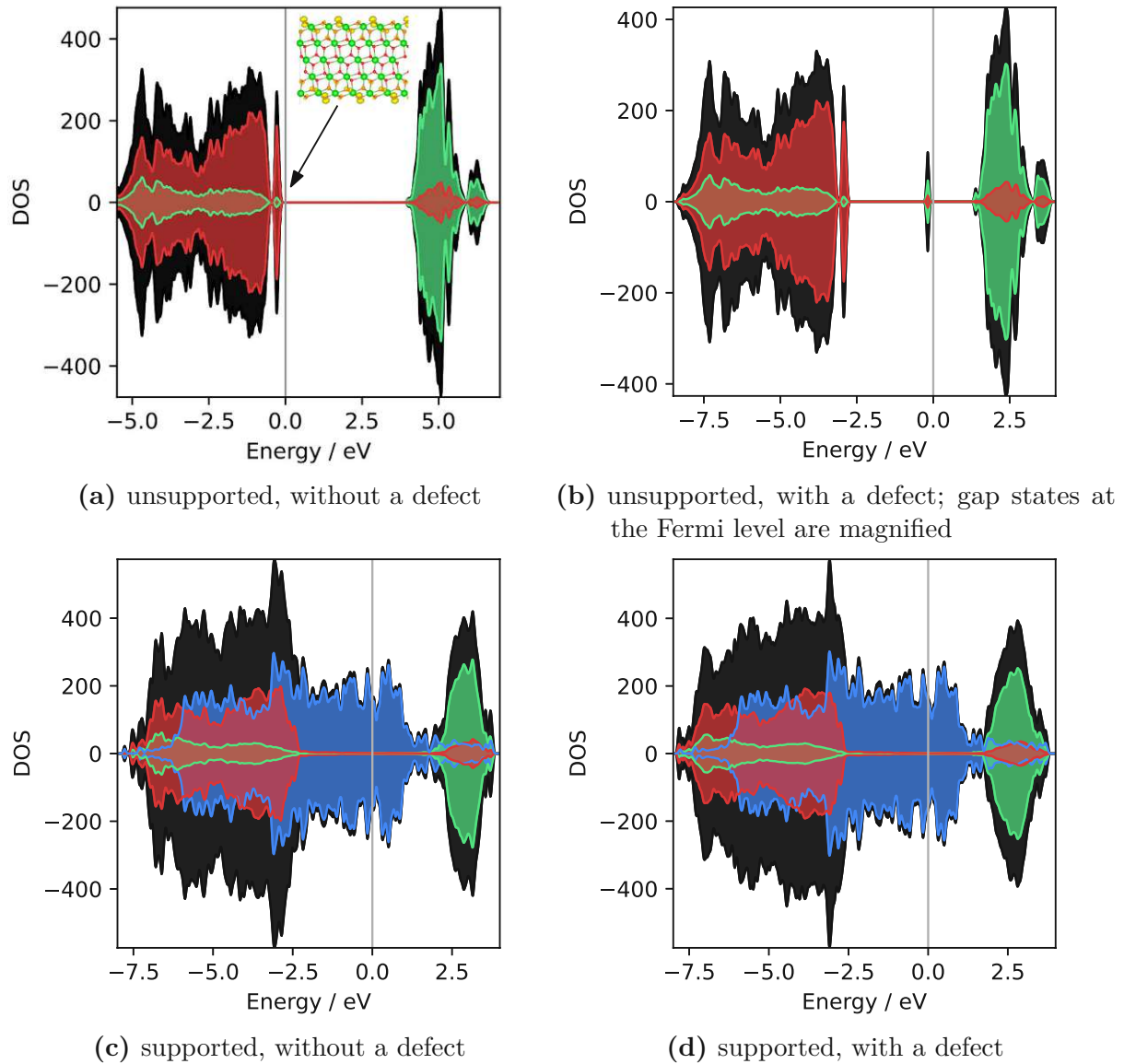
Fig. 4.11: Density of states (SCAN functional) of the (un)supported t-ZrO$_2$ films with(out) an oxygen vacancy as depicted in Panels 4.9a-d, respectively. Total density of states is colored in black, projections onto oxygen, zirconium and rhodium sites are colored in red, green and blue, respectively. The gray vertical line represents the Fermi energy.

respectively. These values are in good agreement with the calculated formation energies of an oxygen vacancy in the supported thin film, namely 3.56 eV and 4.39 eV.

4.5 Conclusion

In this chapter, the performance of various DFT functionals on the stable and meta-stable ZrO_2 polymorphs is presented first. Regarding the known phases, the monoclinic ground state, high-temperature tetragonal and cubic phases have been considered. In addition, meta-stable meta-monoclinic and anatase ZrO_2 predicted by DFT have been investigated as well. Together with accurate beyond-DFT benchmark calculations these systems form an excellent environment for a critical assessment of the performance of the various state-of-the-art functionals. Standard functionals such as PBE, PBE+U and HSE overestimate the stability of the meta-stable phases. Thus, if these functionals are used in investigations like phase transitions, one should expect a potential occurrence of DFT artifacts. First, the formation of three-fold coordinated oxygen atoms present in meta-stable phases is overestimated. Second, the buckling of the oxygen layer in the tetragonal phase (PBE+U, PBE+U*) is too small. Third, calculated band gaps are only comparable with benchmark results when using the hybrid HSE functional. On the other side, the meta-GGA SCAN and SCAN+rVV functionals have been found as an excellent compromise between the accuracy and computational cost. They resolve all aforementioned issues except the underestimated band gap.

Thereafter, the oxygen vacancy formation process is studied. This includes the influence of different charge states of an oxygen vacancy on the geometry around the vacancy, on the electronic structure and its stability in bulk polymorphs, as well as in thin films with and without a metallic support. The calculated formation energies of neutral oxygen vacancies were always higher than 5.5 eV. However, the absolute value depends on the bulk phase and DFT functional used. These parameters cause differences in the calculated formation energies by up to 1.4 eV. Concerning the electronic structure, oxygen vacancies induce extra states in the upper half of the band gap. In the tetragonal phase, these states are always localized in the vicinity of an oxygen vacancy. However, the gap states in the cubic phase are only localized for a neutral or for a positively charged (+1) defect. Regarding the geometrical changes, oxygen vacancies with a negative and positive charge attract zirconium and oxygen atoms, respectively. Regarding the stability of these defects, neutral and negative oxygen vacancies yield high values for the formation energies, which are much lower for positively charged vacancies. Specifically, this has been investigated in two ways. First, positive oxygen vacancies in the cubic and tetragonal bulk have been formed. Second, a Rh(111) support has acted as an acceptor of extra electrons that were transferred into the substrate. In both cases, a large decrease in the formation energy of an oxygen vacancy was observed. In addition, the stability of oxygen vacancies in the unsupported slabs agreed with those in the bulk, and remain rather unstable.

The present results agree with experimental studies[34, 35], which reported a presence of oxygen vacancies in thin tetragonal films that are stabilized by a charge transfer of the gap states to the metallic substrate. If these defects are removed by an oxygen spillover from Rh to zirconia films[34], the thin film is transformed into the monoclinic structure.

Therefore, the next step in the investigation of this interesting system should include the properties of point defects in the supported monoclinic films.

Appendix A

Computational setup (VO$_2$)

All calculations were performed with the Vienna *Ab initio* Simulation Package (VASP) [212, 213]. The projector augmented wave (PAW) method [214, 215] for treating the core electrons has been used. The orbitals for 6 and 13 valence electrons, $(2s^2 2p^4)$ for oxygen and $(3s^2 3p^6 3d^4 4s^1)$ for vanadium, were expanded in a plane wave basis set. Calculations using a smaller dataset for vanadium atoms that contained only five valence electrons $(3d^4 4s^1)$ showed differences of the projected density of states in the O *2p* band. The projected densities of states obtained from these datasets are depicted and compared in Figure A.1, showing that the smaller PAW dataset yields identical results in the V *3d* band, but the vanadium contributions in the O *2p* band are more localized on the vanadium sites as compared to the larger PAW dataset.

A.1 Bulk Calculations

The energy cut-off for the plane waves basis set and the density of the k-points grid was determined separately for the Rutile and Monoclinic VO$_2$ phases to ensure a convergence within the accuracy 1 meV per atom. A Γ-centered Monkhorst-Pack scheme [216] was used for all calculations and k-point grids. Spin-polarized and non spin-polarized PBE and SCAN functionals have been tested and as an outcome neither the spin configuration nor the functional has a significant effect on the final values for the energy cut-off and k-points grid. The energy cut-off that reaches the convergence criterion was determined as 750 eV for both rutile and monoclinic VO$_2$ phases and the k-point grids were estimated as $6 \times 6 \times 9$ and $4 \times 4 \times 4$ for the rutile and the monoclinic VO$_2$ phases, respectively. Hence, these parameters have been used for all bulk calculations. The electronic optimization self-consistent loop was converged to 10^{-5} eV and the ionic relaxation was stopped when residual forces were smaller than 10^{-2} eV/Å. In this work, several DFT functionals were considered to describe the exchange-correlation energy, namely the PBE, the PBE+U, the SCAN[67] and the SCAN+rVV10 [89]. The influence of the Hubbard U_{eff} within Dudarev's implementation [92] on the properties of VO$_2$ phases has been studied in the work of Stahl et al [120], showing that the values of U_{eff} between 1.4 eV to 2.6 eV open a band gap in the monoclinic phase, but not in the rutile phase when using experimental structures, i.e. experimentally determined lattice constants. A value of $U_{eff} = 2$ eV was employed in the present work, a value also used in point defect calculations [217]. All together non spin-polarized calculations (NM), spin-polarized calculations with a ferromagnetic spin order (FM) and spin-polarized calculations with antiferromagnetic (AFM) spin order have been performed for both rutile and monoclinic VO$_2$ phases.
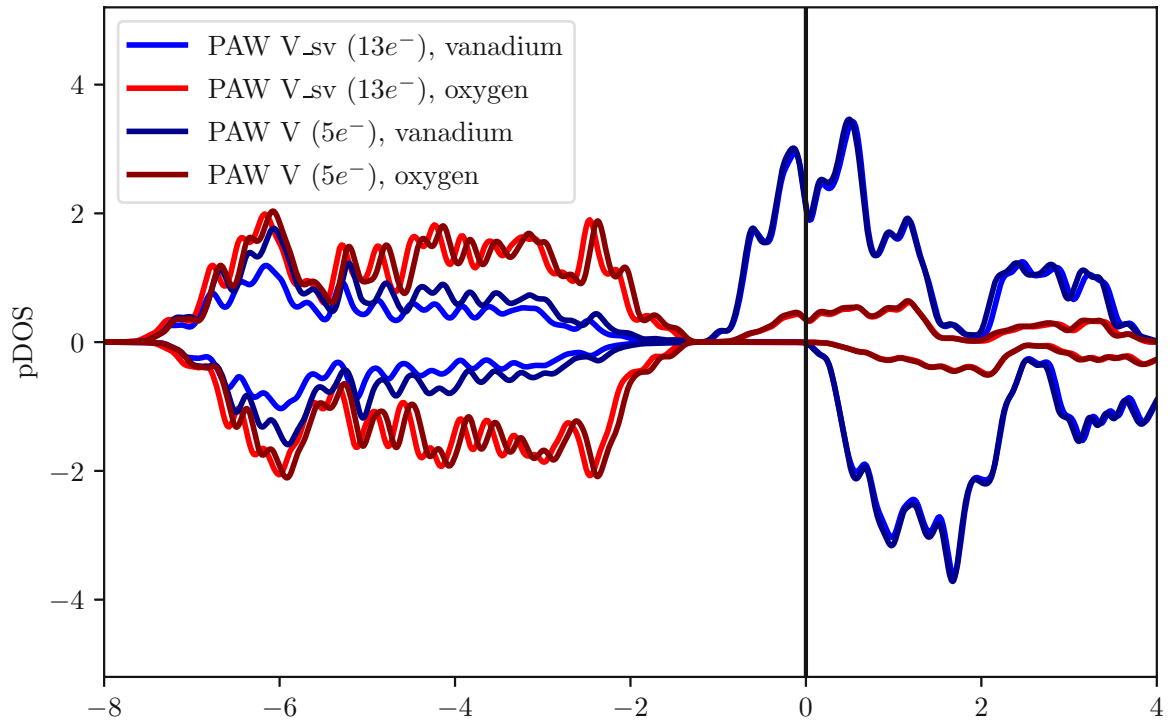
Fig. A.1: Projected density of states on oxygen and vanadium sites in the bulk Rutile VO_2 phase using two different PAW datasets for vanadium. The oxygen *2p* and vanadium *3d* bands are shown in ranges (-8, -1.5) eV and (-1.5, 4) eV, respectively.

Since the energy cutoff and k-point grids are absolutely converged and therefore the results should not be influenced by the Pulay stress, the bulk phases were optimized by a direct optimization of cell shape, cell volume and ionic positions as implemented in VASP. The experimental structures served as starting point and the appropriateness of such an optimization procedure was checked by a comparison of equilibrium volume obtained from a quadratic polynomial interpolation fitted to a set of total energies calculated at fixed volumes. The results are depicted for spin-polarized and non spin-polarized SCAN calculations in Figure A.2, showing that both methods yield unit cells for which the scaling factor differs by less than 0.2 % and the energy difference is always within the accuracy 1 meV per atom. Since the same trend was also found for the PBE functional, the direct optimization procedure was also used for the other DFT functionals and spin configurations.

The local electronic structure was studied with the help of the Wannier90 code [218]. All subbands that comprise O2*p* and V3*d* bands were projected onto the same number of Wannier functions. The local coordinate system of the Wannier functions localized at vanadium atoms was rotated by 45° around the $z-$axis of vanadium octahedra as proposed by Eyert [117] to ensure that y and z axes of all local coordinate systems of vanadium atoms are perpendicular to the rutile c axis. This rotation implies an interchange of d_{xy}
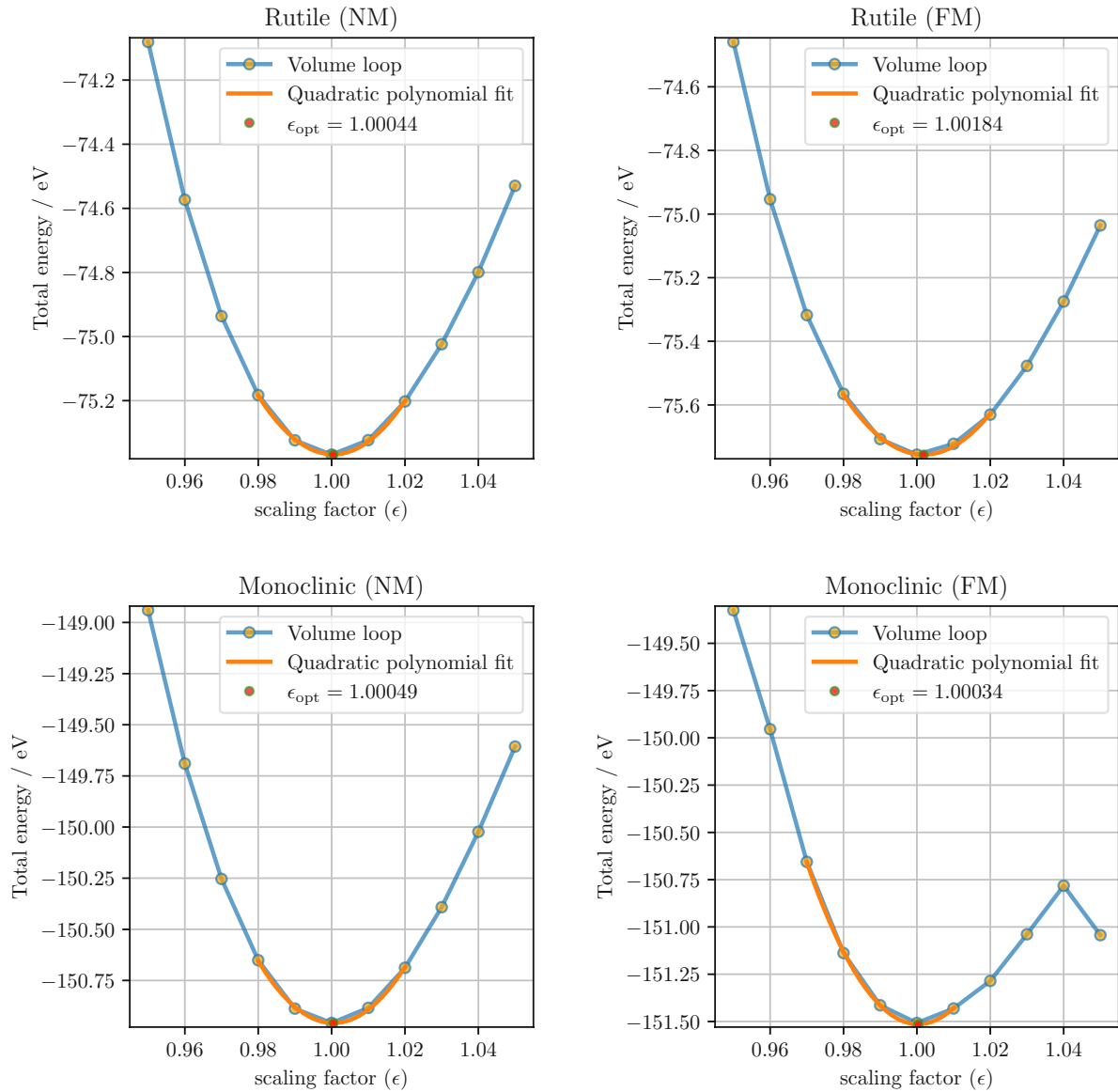
Fig. A.2: Calculated total energies of VO$_2$ phases at fixed volumes given by the scaling factor (ϵ) of the unit cell vectors (the blue lines). The scaling factors are normalized with respect to the directly optimized bulk structures and respective spin configurations for the SCAN functional. The orange line is the quadratic polynomial fitted to the respective energy values at fixed volumes and is used to evaluate ϵ_{opt}. In case of the (FM) calculations of the monoclinic phase the bulk instability at $\epsilon = 1.05$ is visible. Therefore, the compressed part was used for quadratic polynomial interpolation.
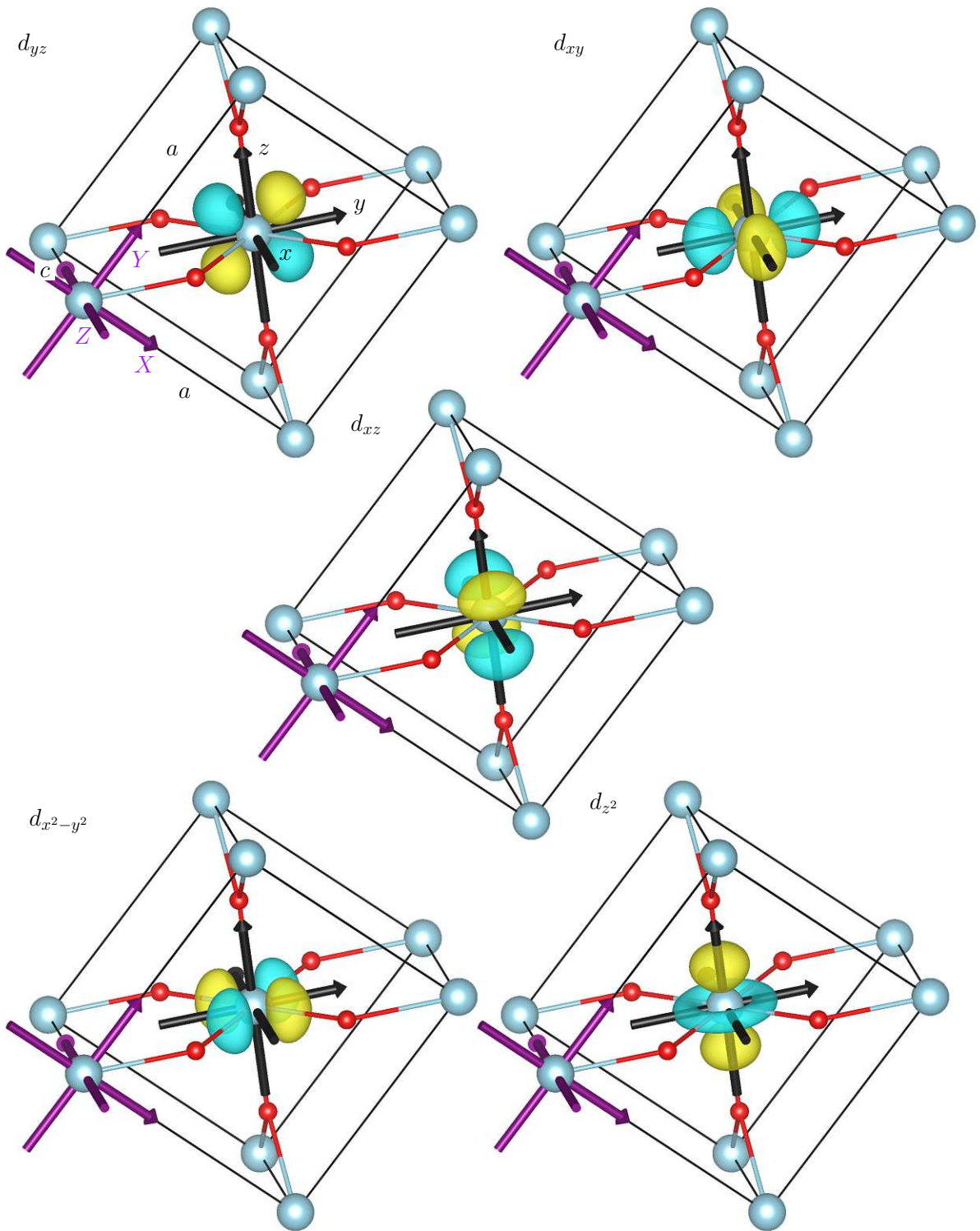
Fig. A.3: Wannier projections in the local coordinate system (x, y, z) of the rutile VO$_2$ phase as proposed by Eyert [117]. The global coordinate system is marked with (X, Y, Z). In this notation, V-t_{2g} states are formed by d_{xy}, d_{xz} and d_{yz} whereas $d_{x^2-y^2}$ and d_{z^2} comprise the V-e_g band.

and $d_{x^2-y^2}$ orbitals, but in the present work, the same notation of the orbitals as in the original basis was kept. The Wannier d-orbitals are depicted with respect to the local and the global coordinate systems in Figure A.3.

A.2 Stoichiometric surface calculations

All slab calculations were performed at bulk optimized lattice constants for the corresponding DFT functional and spin ordering. The stability of a VO_2 termination was determined via an evaluation of the surface free energy, calculated by linear regression from total energies of 5 to 8-layered slabs, as described in the following scheme. The surface energy of a slab that is composed of N bulk formula units having a surface area S is extracted from DFT calculations according to the formula:

$$\sigma = \frac{E_{\text{slab}} - N \cdot E_{\text{bulk}}}{2 \cdot S}, \tag{A.1}$$

where E_{slab} and E_{bulk} are total slab and bulk energies obtained from DFT calculations. In the calculations the energy of both unrelaxed slabs and relaxed slabs was considered. In the first case atoms in a slab are kept at bulk positions, whereas the relaxed slabs undergo subsequent relaxation of all atomic positions until all forces were smaller than $0.01\,\text{eV/Å}$. A direct evaluation of σ requires different sampling of the Brillouin zones for bulk and slab models. In order to avoid this drawback, this formula can be rewritten for a slab energy as a function of the number of layers,

$$E_{\text{slab}} = E_{\text{slab}}(N) = k \cdot N + q. \tag{A.2}$$

A comparison of these equations yields the expression for the surface energy:

$$\sigma = \frac{q}{2S}, \tag{A.3}$$

where q is a parameter that is obtained from a linear regression of slab calculations for several number of layers.

For all surface calculations the value for the cut-off energy was reduced to $500\,\text{eV}$ which yielded a good convergence with respect to the interpolated energy of the bulk and the surface energy of both unrelaxed and relaxed slabs. The dependence of these values on the chosen energy cut-off is shown in Figure A.4. As can be seen, the interpolated surface energy of the unrelaxed slabs does not show a significant dependence on the chosen energy cut-off, varying from $73.966\,\text{meV/Å}^2$ to $73.802\,\text{meV/Å}^2$. The surface energy of the relaxed slabs using the cut-off energy $500\,\text{eV}$ shows a relative error of $0.15\,\text{meV/Å}^2$ with respect to the reference cut-off energy $800\,\text{eV}$. A further decrease of the cut-off energy induces larger errors in the obtained surface energy up to $\sim 0.4\,\text{meV/Å}^2$. The convergence of the interpolated bulk energies shows a similar trend: a cut-off energy $400\,\text{eV}$ induces a $32\,\text{meV}$ difference between the reference value calculated with a cut-off energy $800\,\text{eV}$. A further comparison of the interpolated value for the bulk energy with respect to the total energy obtained from the bulk calculation is shown as a red line in panels A.4(c,d). Both interpolated bulk energies converge to values lower than the reference real-bulk value,

(a)

(b)

(c)

(d)
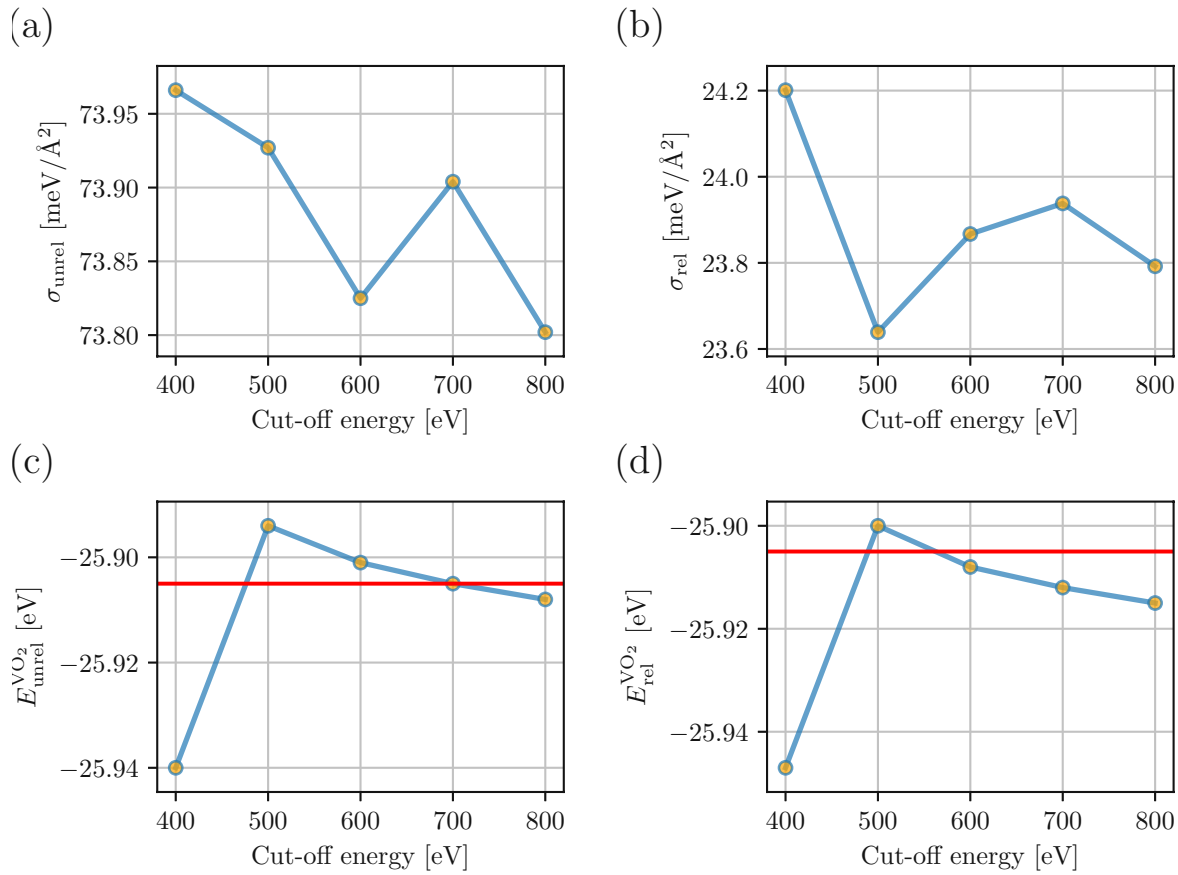
Fig. A.4: Dependence of the interpolated bulk and surface properties on the chosen cut-off energy calculated with the (NM) PBE functional. Panels (a,b) show the surface energy obtained for unrelaxed and relaxed (110) surfaces. Panels (c,d) display the dependence of the interpolated energy of the bulk obtained from the unrelaxed and relaxed slabs respectively. The red line marks the energy obtained from a rutile bulk unit cell.

more prominently visible for the interpolated bulk energy from relaxed slabs. This energy difference can be blamed on the slab thicknesses considered in the interpolation. Even when the computational cost limits the usage of thicker slabs for surface calculations, this can be partially improved by using the interpolated energies from the slabs rather than those calculated directly from the bulk, which leads to a cancellation of errors due to a finite slab thickness.

A.3 Off-stoichiometric calculations on VO$_2$ (110) surfaces

A.3.1 Finding an appropriate computational setup

To find an appropriate computational setup for a calculation of the surface free energies, the impact of several parameters on the oxygen adsorption energies were considered that are in the main focus of the Chapter 3. This study sticks with the rutile VO$_2$(110) (2×1) surface covered with oxygen atoms by $50\,\%$ and $100\,\%$ as depicted in Figure 3.16. The following parameters of the computational setup impacting adsorption energies were considered:

Type of the slab

Since off-stoichiometic (2×2) surface reconstructions will be studied, a computational setup as simple as possible is searched which captures the adsorption energies within a reasonable range of accuracy. In the present study two types of slabs have been employed and used for the extraction of adsorption energies and surface free energies. Both of them are depicted in Figure A.5. First, partially fixed asymmetric slabs were used and in a second step, their fully symmetric varieties. In the first case atoms forming the bottom layer are fixed at their bulk-like positions, the middle of the slab was fixed laterally to avoid the observed bulk instabilities (see Section 3.4.2) . Finally, the surface layer was relaxed in all coordinates. This is depicted in Figure A.5 (left panel). The second type – symmetric slabs, contain a mirror plane in the middle of the slab. In this case, all atoms were fully relaxed.
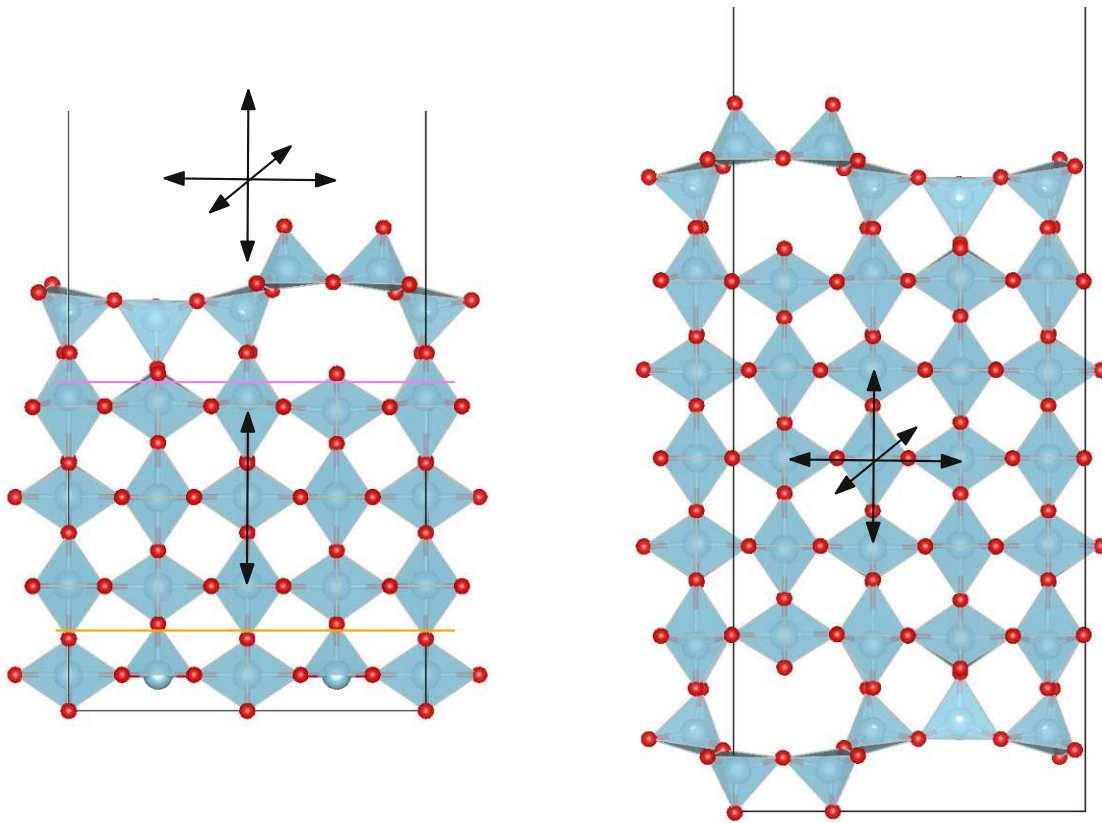
Fig. A.5: Structures of fixed slabs (left panel) and symmetric slabs (right panel). The horizontal lines in the fixed slab separate the bottom layer that was kept in bulk-like positions and the middle layer which was relaxed only in direction perpendicular to the surface plane. The arrows show directions along which the atoms were relaxed.
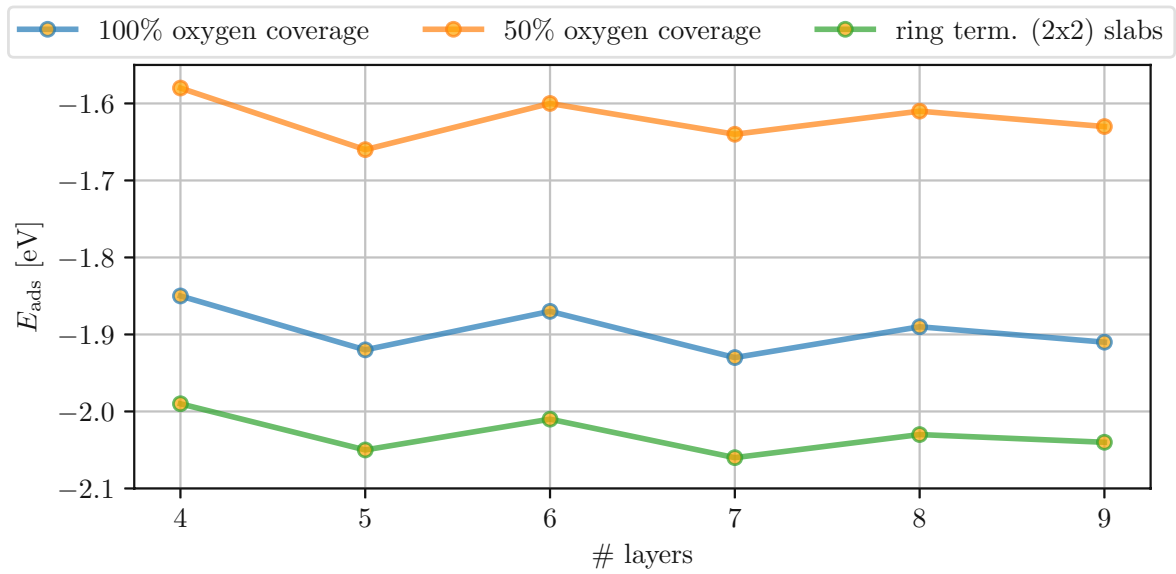
Fig. A.6: Dependence of the adsorption energies on the thickness of a symmetric slab, calculated with the (NM) PBE functional. Here we considered 50 %, 100 % oxygen coverage and a tetrahedral (2×2) superstructure.
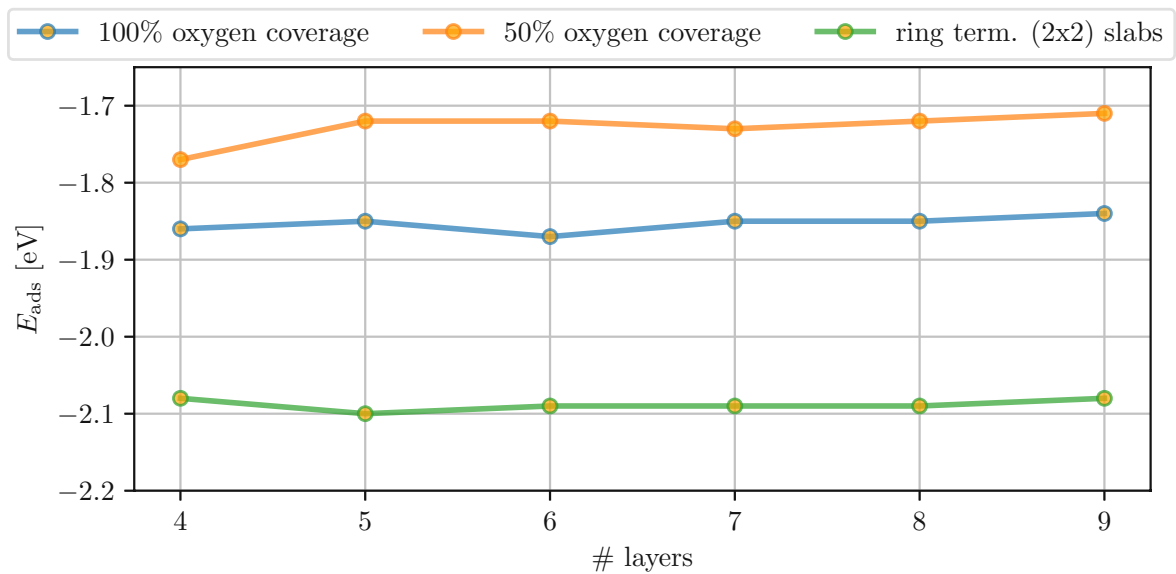
Fig. A.7: Dependence of the adsorption energies on the thickness of a fixed slab, calculated with the (NM) PBE functional. Here we considered 50 %, 100 % oxygen coverage and a tetrahedral (2×2) superstructure.

Thickness of the slab

The dependence of adsorption energies on the thickness of the slab was studied with the non-magnetic PBE functional. Considering the symmetric slabs, the values for the adsorption energies obtained from the four-layered slabs deviate by 0.06 eV as shown in Figure A.6. However, the five-layered slabs lower this value to 0.02 eV and 0.01 eV in the 50 % and 100 % covered slabs, respectively. Therefore the latter computational setup was used in the final calculations. Figure A.6 also shows the convergence of the effective adsorption energy of a tetrahedral termination, showing the same trend as adsorption phases. Another important finding is the fact that the adsorption energies do not show a strong dependency on a choice of even- or odd-layered slabs.

The convergence of adsorption energies in the fixed slabs displayed in Figure A.7 shows a dependency on the surface system. While the fully-covered (110) surface and the ring termination is already converged to 0.02 eV for four-layered slabs, 50 %-covered slabs yield the error of 0.06 eV in the adsorption energy. However, converged adsorption energies with respect to the thickness of slabs, resulting from fixed and symmetric slabs are different: while the 50 % covered (110) surface show 0.05 eV lower adsorption energies for symmetric slabs, the fully-covered (110) surface is lower by 0.09 eV. Therefore, the differences in adsorption energies are much lower in calculations using fixed slabs. This difference can be associated with the constraints of the middle part of the fixed slabs. On the other side, ring terminations yield similar adsorption energies in both systems, differing only by 0.04 eV. A further analysis revealed that this holds only true when the subsurface layer misses no oxygen atoms. Superstructures with a reduced subsurface layer show significantly different adsorption energies when calculated with fixed and symmetric slabs.

These results show that the comparison of surface free energies of polyhedral superstructures with adsorption phases requires the use of more complex symmetric slabs while for a comparison between polyhedral superstructures the fixed four-layered slabs are in most cases sufficient, yielding an error of 0.04 eV. In the thesis either five-layered symmetric slabs or four-layered fixed slabs are used for a comparison of adsorption energies and surface free energies.

Energy cut-off and the k-points grid

The decreased energy cut-off was also checked with respect to the oxygen adsorption energy. The results are shown in Figure A.8 for energy cut-off values that range from 500 eV to 800 eV. Figure A.8 displays two lines for the adsorption energies referring to 50 % and 100 % oxygen-covered (2×1) slabs, and showing that in both cases the resulting adsorption energy is well-converged even for the lowest 500 eV energy cut-off, which yields only 0.01 eV difference with respect to the reference 800 eV energy cut-off calculations. Therefore, the energy cut-off was kept to 500 eV in all final calculations. These results are shown for the symmetric slabs. However, the fixed slabs show the same dependence on the cut-off energy.

To keep a similar sampling of the first Brillouin zone as in the bulk calculations, a $4 \times 4 \times 1$ k-points grid was chosen for the rutile VO_2 (110) (2×1) slabs. This sampling was checked by considering denser grids which, however, gave changes in adsorption energies lower than 0.01 eV.
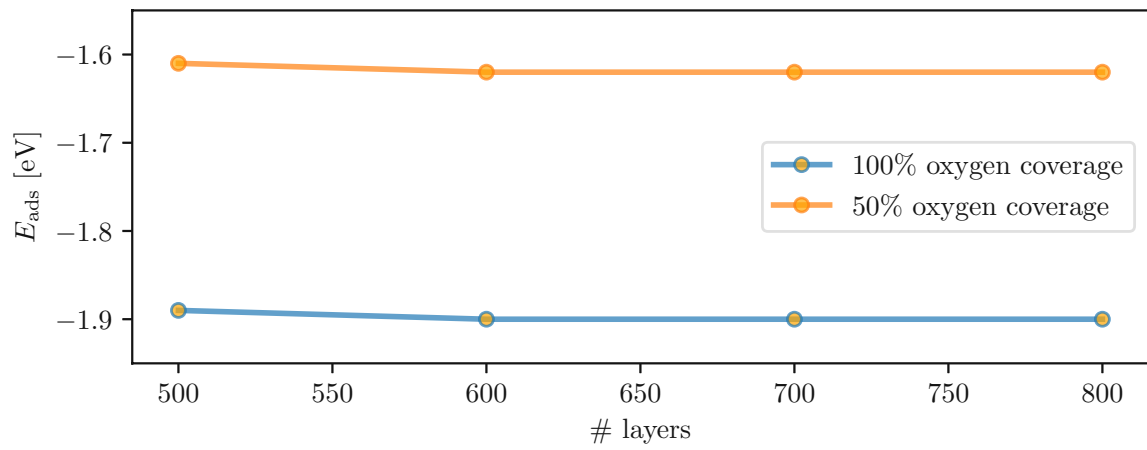
Fig. A.8: Dependence of the adsorption energies on the thickness of the slab, calculated with the (NM) PBE functional. 50 % and 100 % oxygen coverages were considered.

A.3.2 Surface free energy calcuations

To calculate the surface free energy of the most stable off-stoichiometric terminations the procedure described in the work of Reuter [94] is followoed. The Gibbs free energy is approximated by the total DFT energies of the slabs and reference systems in the oxygen-rich limit so that all vibrational contributions are neglected. The formula used to extract the surface free energy from a slab that consists of N_V vanadium atoms and N_O oxygen atoms as a function of oxygen chemical potential μ_O reads

$$\gamma(\mu_O) = \frac{E_{\text{slab}} - N_V \cdot E_{\text{VO}_2} - (N_O - 2N_V) \cdot \left(\frac{1}{2} E_{\text{O}_2} + \mu_O\right)}{2S}, \tag{A.4}$$

where E_{VO_2} and E_{O_2} are reference energies for the total energy of the rutile VO_2 bulk and oxygen molecule respectively, E_{slab} marks the total energy of the slab with the surface area S.

In several calculations, mainly in those presented in simulated annealing results (section 3.5.1) one needs to extract the surface free energy from the fixed slabs which are not symmetric. In this model atoms in the bottom layer were fixed to bulk positions and therefore one may approximate the surface energy of the bottom part of fixed slabs by a surface energy of unrelaxed slabs ($\sigma_{\text{unrel.}}$), obtained from a linear regression of five to eight-layered slabs. The formula for the surface free energy therefore changes to:

$$\gamma(\mu_O) = \frac{E_{\text{slab}} - N_V \cdot E_{\text{VO}_2} - (N_O - 2N_V) \cdot \left(\frac{1}{2} E_{\text{O}_2} + \mu_O\right)}{S} - \sigma_{\text{unrel}}. \tag{A.5}$$

The oxygen chemical potential is considered in the range of energies where the VO_2 phase is thermodynamically stable. Its oxygen-rich limit is approximately given by the reaction enthalpy of the oxidation reaction of the VO_2 phase:

$$2VO_2 + 1/2O_2 \rightarrow V_2O_5. \tag{A.6}$$

The experimental value $-1.28\,\text{eV}$ is given by the formation enthalpies of the VO_2[156] and V_2O_5[140] while the calculated value is considered in the $0\,\text{K}$ temperature limit. Neglecting vibrational and entropic contributions yields an $1.3\,\%$ error in the experimental heat of formation of vanadium pentoxide as compared to the value obtained at room temperature[140]. The enthalpy of reaction is therefore calculated using the total energies of bulk systems and oxygen molecule as

$$H_{\text{f}}^{\text{DFT}}(V_2O_5) = E_{\text{V}_2\text{O}_5}^{\text{bulk}} - (2E_{\text{VO}_2}^{\text{bulk}} + 1/2E_{\text{O}_2}). \tag{A.7}$$

A.4 Optimization of random structures

The steps that make up the optimization procedure for the generated random structures have been described in Section 3.5.3. Here, the performance of this procedure and its limitations is assessed. The first finding is that increasing the number of layers of the slab influences the reactivity of the surface. This is illustrated in Figure A.9 that shows the dependence of oxygen adsorption energy on the thickness of slabs, compared to the values obtained from the last step of the optimization procedure, marked as red lines. As shown, the adsorption energy is lower when using thinner slabs, indicating that the $VO_2(110)$ surface is too reactive in the first two steps of the optimization procedure running on two-layered slabs, while four-layered slabs yield adsorption energies close to the reference value. Since the number of substrate layers is changed stepwise after the relaxation, the final superstructures tend to be compressed despite the fact that more stable open structures might exist. This is illustrated by two examples, both having a V_5O_{12} surface stoichiometry, already presented in Figures 3.27a and 3.27f and shown in this section in Figure A.10. A comparison of these structures reveals that the more open ring (Figure A.10a) is composed of vanadium tetrahedra while the more compact structure depicted in Figure A.10b has a surface layer composed of corner-sharing tetrahedra and polyhedra.

Now the stability of these structures is compared. Since both of them have the same surface stoichiometry, the difference in the total energy per the calculated slab that is composed of two layers and four layers is directly shown, see Table A.1. While the compressed ring termination is calculated to be more stable for all DFT functionals when using a two-layered substrate, the difference in total energies calculated for four-layered slabs is either flipped (PBE and PBE+U) or dramatically decreased (SCAN). As a consequence, the more open structures might not be found with the present optimization procedure due to optimization of all structures on the more reactive two-layered substrate.

Another natural limitation lies in an incomplete sampling of the configuration space. First of all, this procedure deals with the surface terminations with a fixed stoichiometry. Moreover, even at the chosen stoichiometry one cannot guarantee that the most stable surface termination would be found. The range of this limitation can be demonstrated in one specific example, namely for superstructures with a V_8O_{18} surface stoichiometry related to a one VO_2 (2×2) monolayer with two additional oxygen ad-atoms. In this specific case one might expect six different combinations of adsorption phases, created by the adsorption of two oxygen atoms on four different vanadium sites present in (2×2) slabs. Out of these six combinations three of them have been found. Therefore the conclusion is that structures obtained by this procedure might not recover the ground state, but the most stable structures found will be related to the real ground-state structure at the given surface stoichometry.
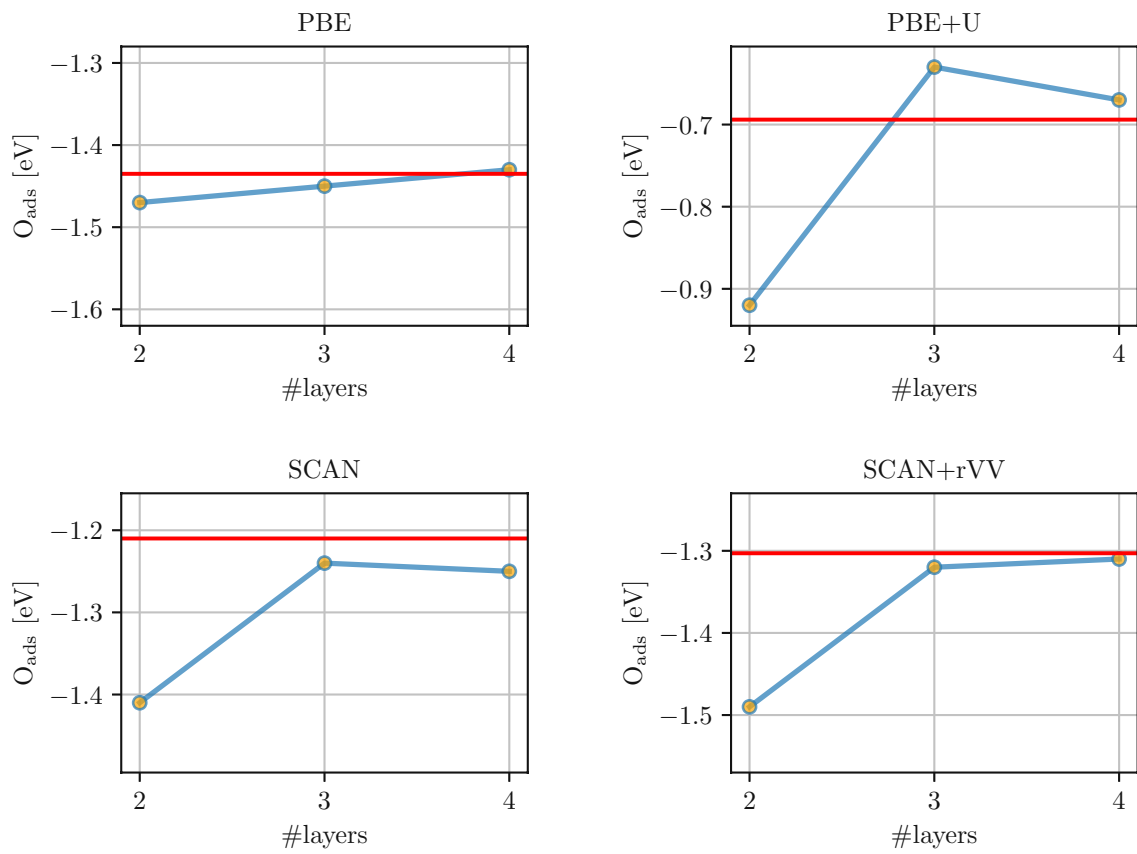
Fig. A.9: Dependence of the calculated oxygen adsorption energies in the fully covered $VO_2(110)$ surface on the thickness of slabs used for the stepwise optimization of the random structures. Spin-polarized PBE, PBE+U, SCAN and SCAN+rVV calculations are shown. Red lines mark the reference value from the last optimization step, where symmetric five-layered slabs were used.

(a)   **(b)**
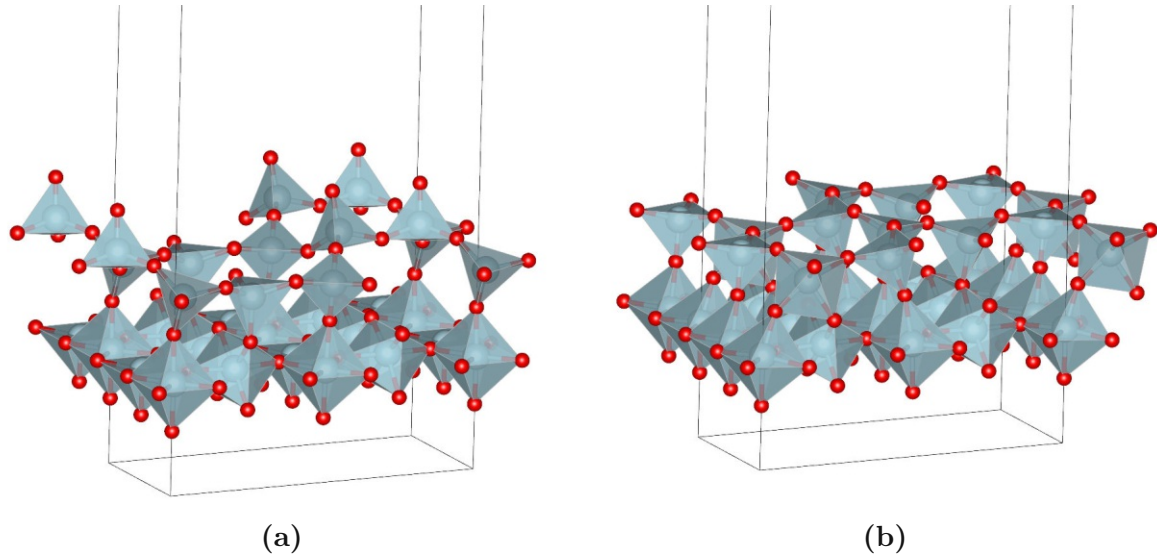
Fig. A.10: Side views of two ring terminations with the V_5O_{12} surface stoichiometry. The left panel shows more open structure with the partially reduced subsurface layer while the latter structure (right panel) is composed of the fully-covered subsurface layer while the surface layer is more compressed.

# layers	PBE	PBE+U	SCAN
2	-267	-426	-1319
4	484	714	-221

Tab. A.1: Differences in the total energy (in meV per slab) between the ring terminations shown in Figures A.10a and A.10b. Negative values mean that the open ring termination (Figure A.10a) is less stable.

Appendix B

Meta-stable ZrO$_2$ phases

It is certainly instructive to see how the meta-stable zirconia phases may bias calculated results in bulk systems, unsupported slabs and supported slabs when the PBE functional is used. Actually, the meta-stable meta-monoclinic and anatase ZrO$_2$ phases discussed in Chapter 4 have been identified by such calculations.
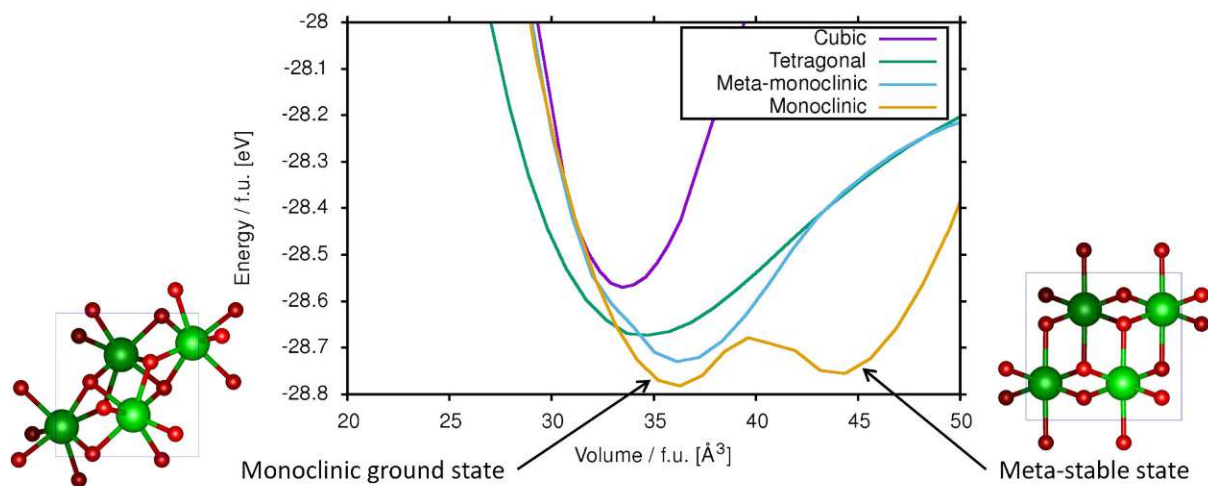
Fig. B.1: Total energy of the zirconia polymorphs as a function of the unit cell volume. The monoclinic phase is transformed to the anatase phase when the unit cell is expanded by $\sim 20\,\%$.
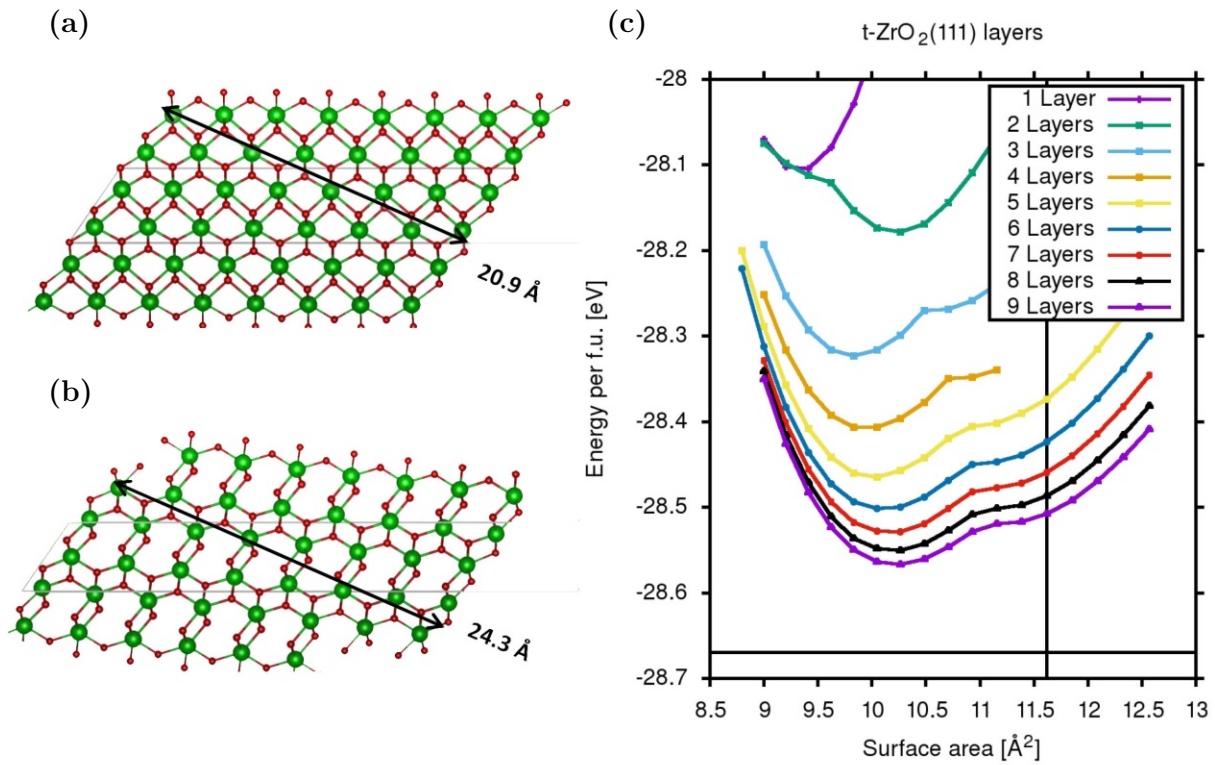
Fig. B.2: Calculated transition of a thin tetragonal $ZrO_2(101)$ slab (panel a) to the meta-monoclinic structure (panel b). The structural transition is accompanied by bond breaking and expansion of the slab, see both black arrows and the grey lines marking the unit cell of the slabs. Panel (c) presents the energy of the slab/f.u. as a function of surface area. Black line denotes the surface area (vertical) and energy/f.u. (horizontal) as calculated for a tetragonal bulk unit cell. One immediately seen that even thicker slabs converge to a $\sim 10\%$ lower value.
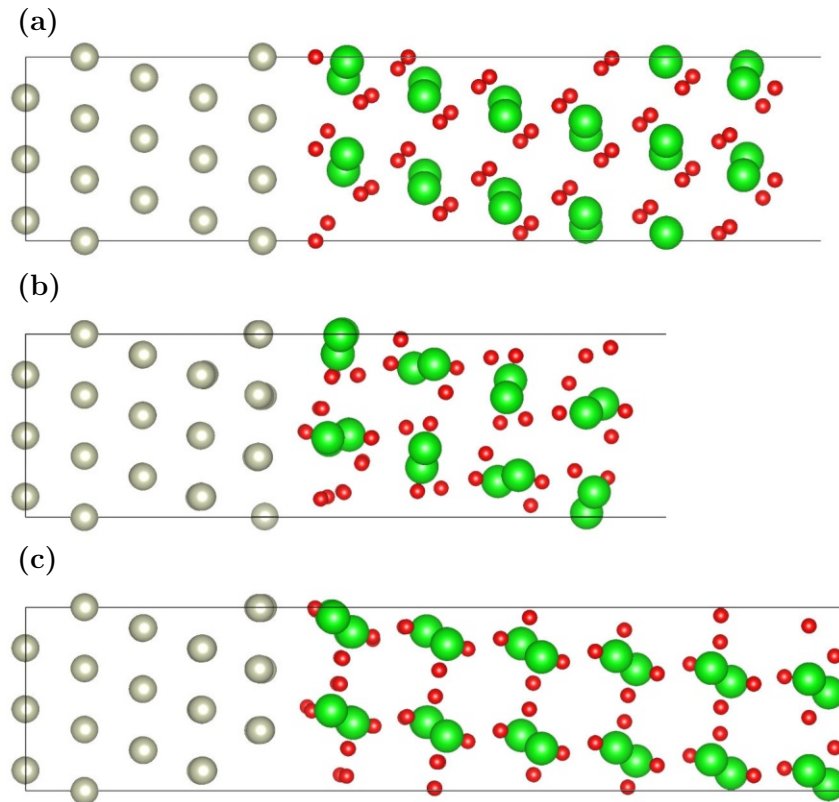
Fig. B.3: Calculated phase transition in supported slabs. Panel (a) shows the initial structure of a meta-monoclnic (-111) slab. As seen in panel (b), a four-layered meta-monoclinic film undergoes a structural transition to the monoclinic (-111) film. When relaxing thicker slabs (panel c), all four-fold coordinated oxygen atoms are changed to three-fold, which indicates a transformation to the anatase phase. These findings indicate that the barrier for a phase transformation from the meta-monoclinic phase to either monoclinic or anatase phases is rather small.

Bibliography

[1] C. W. Bauschlicher, C. J. Nelin, and P. S. Bagus. "Transition metal oxides: CrO, MoO, NiO, PdO, AgO". *The Journal of Chemical Physics* 82.7 (1985), pp. 3265–3276. DOI: 10.1063/1.448224.

[2] G. Sproul. "Electronegativity and Bond Type: Predicting Bond Type". *Journal of Chemical Education* 78.3 (2001), p. 387. DOI: 10.1021/ed078p387.

[3] J. Duffy. "Chemical bonding in the oxides of the elements: A new appraisal". *Journal of Solid State Chemistry* 62.2 (1986), pp. 145–157. DOI: 10.1016/0022-4596(86)90225-2.

[4] A. Filippetti and V. Fiorentini. "Coexistence of ionic and metallic bonding in noble-metal oxides". *Phys. Rev. B* 72 (2005), p. 035128. DOI: 10.1103/PhysRevB.72.035128.

[5] A. Emeline, G. V. Kataeva, et al. "Spectroscopic and Photoluminescence Studies of a Wide Band Gap Insulating Material: Powdered and Colloidal ZrO_2 Sols". *Langmuir* 14.18 (1998), pp. 5011–5022. DOI: 10.1021/la980083l.

[6] S. Lany. "Semiconducting transition metal oxides". *Journal of Physics Condensed Matter* 27.28 (2015). DOI: 10.1088/0953-8984/27/28/283203.

[7] T. P. Pearsall and C. A. Lee. "Electronic transport in ReO_3: dc conductivity and Hall effect". *Phys. Rev. B* 10 (1974), pp. 2190–2194. DOI: 10.1103/PhysRevB.10.2190.

[8] S. Hackwood, A. H. Dayem, and G. Beni. "Amorphous-nonmetal-to-crystalline-metal transition in electrochromic iridium oxide films". *Phys. Rev. B* 26 (1982), pp. 471–478. DOI: 10.1103/PhysRevB.26.471.

[9] B. Raveau. "Transition metal oxides: Promising functional materials". *Journal of the European Ceramic Society* 25.12 (2005). Elecroceramics IX, pp. 1965–1969. DOI: 10.1016/j.jeurceramsoc.2005.03.220.

[10] Z. Ren Xiao, G. Yu Guo, et al. "Oxygen Vacancy Induced Ferromagnetism in V_2O_{5-x}". *Journal of the Physical Society of Japan* 77.2 (2008), p. 023706. DOI: 10.1143/JPSJ.77.023706.

[11] A. A. Valeeva, S. Z. Nazarova, and A. A. Rempel. "Nanosize effect on phase transformations of titanium oxide Ti_2O_3". *Journal of Alloys and Compounds* 817 (2020), p. 153215. DOI: 10.1016/j.jallcom.2019.153215.

[12] K. Nakahigashi, N. Fukuoka, and Y. Shimomura. "Crystal Structure of Antiferromagnetic NiO Determined by X-Ray Topography". *Journal of the Physical Society of Japan* 38.6 (1975), pp. 1634–1640. DOI: 10.1143/JPSJ.38.1634.

[13] R. Masrour, E. Hlil, et al. "Electronic and magnetic structures of Fe_3O_4 ferrimagnetic investigated by first principle, mean field and series expansions calculations". *Journal of Magnetism and Magnetic Materials* 378 (2015), pp. 37–40. DOI: `10.1016/j.jmmm.2014.10.135`.

[14] R. S. Keizer, S. T. Goennenwein, et al. "A spin triplet supercurrent through the half-metallic ferromagnet CrO_2". *Nature* 439.7078 (2006), pp. 825–827. DOI: `10.1038/nature04499`.

[15] N. Bahlawane and D. Lenoble. "Vanadium Oxide Compounds: Structure, Properties, and Growth from the Gas Phase". *Chemical Vapor Deposition* 20.7-8-9 (2014), pp. 299–311.

[16] K. Cao, T. Jin, et al. "Recent progress in conversion reaction metal oxide anodes for Li-ion batteries". *Mater. Chem. Front.* 1 (2017), pp. 2213–2242. DOI: `10.1039/C7QM00175D`.

[17] M. A. Aizat, N. H. N. Azman, et al. "Review of the use of transition-metal-oxide and conducting polymer-based fibres for high-performance supercapacitors". *Materials & Design* 186 (2020), p. 108199. DOI: `10.1016/j.matdes.2019.108199`.

[18] C. Wang, L. Yin, et al. "Metal oxide gas sensors: Sensitivity and influencing factors". *Sensors* 10.3 (2010), pp. 2088–2106. DOI: `10.3390/s100302088`.

[19] S. Hussain and L. Yangping. "Review of solid oxide fuel cell materials: cathode, anode, and electrolyte". *Energy Transitions* 4.2 (2020), pp. 113–126. DOI: `10.1007/s41825-020-00029-8`.

[20] F. Lechermann. "Late transition metal oxides with infinite-layer structure: Nickelates versus cuprates". *Phys. Rev. B* 101 (2020), p. 081110. DOI: `10.1103/PhysRevB.101.081110`.

[21] A. Clark. "Oxides of the Transition Metals as Catalysts". *Industrial & Engineering Chemistry* 45.7 (1953), pp. 1476–1480. DOI: `10.1021/ie50523a034`.

[22] S. Biswas, A. Pal, and T. Pal. "Supported metal and metal oxide particles with proximity effect for catalysis". *RSC Adv.* 10 (2020), pp. 35449–35472. DOI: `10.1039/D0RA06168A`.

[23] J. B. Goodenough. "Perspective on Engineering Transition-Metal Oxides". *Chemistry of Materials* 26.1 (2014), pp. 820–829. DOI: `10.1021/cm402063u`.

[24] J. A. Duffy. "Ionic–Covalent Character of Metal and Nonmetal Oxides". *The Journal of Physical Chemistry A* 110.49 (2006), pp. 13245–13248. DOI: `10.1021/jp063846j`.

[25] M. Lenglet. "Iono-Covalent Character of the Metal–Oxygen Bonds in Oxides: A Comparison of Experimental and Theoretical Data". *Active and Passive Electronic Components* 27.1 (2004), pp. 1–60. DOI: `10.1080/0882751031000116142`.

[26] E. Larsen and G. N. La Mar. "The angular overlap model. How to use it and why". *Journal of Chemical Education* 51.10 (1974), p. 633. DOI: `10.1021/ed051p633`.

[27] H. A. Jahn, E. Teller, and F. G. Donnan. "Stability of polyatomic molecules in degenerate electronic states - I–Orbital degeneracy". *Proceedings of the Royal Society of London. Series A - Mathematical and Physical Sciences* 161.905 (1937), pp. 220–235. DOI: `10.1098/rspa.1937.0142`.

[28] N. F. Mott. "The Basis of the Electron Theory of Metals, with Special Reference to the Transition Metals". *Proceedings of the Physical Society. Section A* 62.7 (1949), pp. 416–422. DOI: 10.1088/0370-1298/62/7/303.

[29] R. E. Peierls. *Quantum Theory of Solids.* Oxford University Press, 2001. ISBN: 9780198507819. DOI: 10.1093/acprof:oso/9780198507819.001.0001.

[30] M. J. Wahila, N. F. Quackenbush, et al. *The Breakdown of Mott Physics at VO$_2$ Surfaces.* 2020. arXiv: 2012.05306 [cond-mat.str-el].

[31] S. Fischer, J. O. Krisponeit, et al. "Massively Strained VO$_2$ Thin Film Growth on RuO$_2$". *Crystal Growth and Design* 20.4 (2020), pp. 2734–2741. DOI: 10.1021/acs.cgd.0c00120.

[32] M. Wagner, J. Planer, et al. "An oxygen-rich, tetrahedral surface phase on high-temperature rutile VO$_2$(110)$_T$ single crystals". *Physical Review Materials* submitted (2021). arXiv: 2107.00350 [cond-mat.mtrl-sci]. URL: https://arxiv.org/abs/2107.00350.

[33] P. Lackner, A. J. Brandt, et al. "Few-monolayer yttria-doped zirconia films: Segregation and phase stabilization". *The Journal of Chemical Physics* 152.6 (2020), p. 064709. DOI: 10.1063/1.5140266.

[34] P. Lackner, Z. Zou, et al. "Using photoelectron spectroscopy to observe oxygen spillover to zirconia". *Physical Chemistry Chemical Physics* 21.32 (2019), pp. 17613–17620. DOI: 10.1039/C9CP03322J.

[35] P. Lackner, Z. Zou, et al. "Surface structures of ZrO$_2$ films on Rh(111): From two layers to bulk termination". *Surface Science* 679 (2019), pp. 180–187. DOI: 10.1016/j.susc.2018.09.004.

[36] P. Lackner, J. I. J. Choi, et al. "Substoichiometric ultrathin zirconia films cause strong metal–support interaction". *Journal of Materials Chemistry A* 7.43 (2019), pp. 24837–24846. DOI: 10.1039/C9TA08438J.

[37] L. J. Butler. "Chemical reaction dynamics beyond the Born-Oppenheimer approximation". *Annual Review of Physical Chemistry* 49.1 (1998), pp. 125–171. DOI: 10.1146/annurev.physchem.49.1.125.

[38] S. Pisana, M. Lazzeri, et al. "Breakdown of the adiabatic Born-Oppenheimer approximation in graphene". *Nature Materials* 6.3 (2007), pp. 198–201. DOI: 10.1038/nmat1846.

[39] R. K. Nesbet. "Theory of Superconductivity. I. Electron-Lattice Interaction". *Phys. Rev.* 126 (1962), pp. 2014–2020. DOI: 10.1103/PhysRev.126.2014.

[40] V. Fock. "Näherungsmethode zur Lösung des quantenmechanischen Mehrkörper-problems". *Zeitschrift für Physik* 61.1-2 (1930), pp. 126–148. DOI: 10.1007/BF01340294.

[41] R. O. Jones. "Density functional theory: Its origins, rise to prominence, and future". *Reviews of Modern Physics* 87.3 (2015). DOI: 10.1103/RevModPhys.87.897.

[42] R. Van Noorden, B. Maher, and R. Nuzzo. "The top 100 papers". *Nature* 514 (2014), pp. 550–3. DOI: 10.1038/514550a.

[43] C. Lee, W. Yang, and R. G. Parr. "Development of the Colle-Salvetti correlation-energy formula into a functional of the electron density". *Phys. Rev. B* 37 (1988), pp. 785–789. DOI: 10.1103/PhysRevB.37.785.

[44] A. D. Becke. "Density-functional thermochemistry. III. The role of exact exchange". *The Journal of Chemical Physics* 98.7 (1993), pp. 5648–5652. DOI: 10.1063/1.464913.

[45] W. Kohn and L. J. Sham. "Self-Consistent Equations Including Exchange and Correlation Effects". *Phys. Rev.* 140 (1965), A1133–A1138. DOI: 10.1103/PhysRev.140.A1133.

[46] P. Hohenberg and W. Kohn. "Inhomogeneous Electron Gas". *Phys. Rev.* 136 (1964), B864–B871. DOI: 10.1103/PhysRev.136.B864.

[47] E. Engel and R. M. Dreizler. *Density Functional Theory An Advanced Course*. Springer Berlin Heidelberg, 2011.

[48] J. Lehtomäki, I. Makkonen, et al. "Orbital-free density functional theory implementation with the projector augmented-wave method". *Journal of Chemical Physics* 141.23 (2014). DOI: 10.1063/1.4903450.

[49] W. C. Witt, B. G. Del Rio, et al. "Orbital-free density functional theory for materials research". *Journal of Materials Research* 33.7 (2018), pp. 777–795. DOI: 10.1557/jmr.2017.462.

[50] R. P. Feynman. "Forces in Molecules". *Phys. Rev.* 56 (1939), pp. 340–343. DOI: 10.1103/PhysRev.56.340.

[51] J. Thijssen. *Computational Physics*. 2nd ed. Cambridge University Press, 2007. DOI: 10.1017/CBO9781139171397.

[52] D. M. Ceperley and B. J. Alder. "Ground State of the Electron Gas by a Stochastic Method". *Phys. Rev. Lett.* 45 (1980), pp. 566–569. DOI: 10.1103/PhysRevLett.45.566.

[53] S. H. Vosko, L. Wilk, and M. Nusair. "Accurate spin-dependent electron liquid correlation energies for local spin density calculations: a critical analysis". *Canadian Journal of Physics* 58.8 (1980), pp. 1200–1211. DOI: 10.1139/p80-159.

[54] J. P. Perdew and A. Zunger. "Self-interaction correction to density-functional approximations for many-electron systems". *Phys. Rev. B* 23 (1981), pp. 5048–5079. DOI: 10.1103/PhysRevB.23.5048.

[55] J. P. Perdew and Y. Wang. "Accurate and simple analytic representation of the electron-gas correlation energy". *Phys. Rev. B* 45 (1992), pp. 13244–13249. DOI: 10.1103/PhysRevB.45.13244.

[56] N. Mardirossian and M. Head-Gordon. "Thirty years of density functional theory in computational chemistry: an overview and extensive assessment of 200 density functionals". *Molecular Physics* 115.19 (2017), pp. 2315–2372. DOI: 10.1080/00268976.2017.1333644.

[57] J. P. Perdew and W. Yue. "Accurate and simple density functional for the electronic exchange energy: Generalized gradient approximation". *Phys. Rev. B* 33 (1986), pp. 8800–8802. DOI: 10.1103/PhysRevB.33.8800.

[58] J. P. Perdew. "Density-functional approximation for the correlation energy of the inhomogeneous electron gas". *Phys. Rev. B* 33 (1986), pp. 8822–8824. DOI: 10.1103/PhysRevB.33.8822.

[59] Y. Wang and J. P. Perdew. "Correlation hole of the spin-polarized electron gas, with exact small-wave-vector and high-density scaling". *Phys. Rev. B* 44 (1991), pp. 13298–13307. DOI: 10.1103/PhysRevB.44.13298.

[60] J. P. Perdew, K. Burke, and M. Ernzerhof. "Generalized Gradient Approximation Made Simple". *Phys. Rev. Lett.* 77 (1996), pp. 3865–3868. DOI: 10.1103/PhysRevLett.77.3865.

[61] B. Hammer, L. B. Hansen, and J. K. Nørskov. "Improved adsorption energetics within density-functional theory using revised Perdew-Burke-Ernzerhof functionals". *Phys. Rev. B* 59 (1999), pp. 7413–7421. DOI: 10.1103/PhysRevB.59.7413.

[62] Y. Zhang and W. Yang. "Comment on "Generalized Gradient Approximation Made Simple"". *Phys. Rev. Lett.* 80 (1998), pp. 890–890. DOI: 10.1103/PhysRevLett.80.890.

[63] G. I. Csonka, J. P. Perdew, et al. "Assessing the performance of recent density functionals for bulk solids". *Phys. Rev. B* 79 (2009), p. 155107. DOI: 10.1103/PhysRevB.79.155107.

[64] J. P. Perdew, J. A. Chevary, et al. "Atoms, molecules, solids, and surfaces: Applications of the generalized gradient approximation for exchange and correlation". *Phys. Rev. B* 46 (1992), pp. 6671–6687. DOI: 10.1103/PhysRevB.46.6671.

[65] A. D. Becke. "Density-functional thermochemistry. II. The effect of the Perdew–Wang generalized-gradient correlation correction". *The Journal of Chemical Physics* 97.12 (1992), pp. 9173–9177. DOI: 10.1063/1.463343.

[66] A. D. Becke. "Density-functional thermochemistry. I. The effect of the exchange-only gradient correction". *The Journal of Chemical Physics* 96.3 (1992), pp. 2155–2160. DOI: 10.1063/1.462066.

[67] J. Sun, A. Ruzsinszky, and J. P. Perdew. "Strongly Constrained and Appropriately Normed Semilocal Density Functional". *Phys. Rev. Lett.* 115 (2015), p. 036402. DOI: 10.1103/PhysRevLett.115.036402.

[68] Y. Yao and Y. Kanai. "Plane-wave pseudopotential implementation and performance of SCAN meta-GGA exchange-correlation functional for extended systems". *The Journal of Chemical Physics* 146.22 (2017), p. 224105. DOI: 10.1063/1.4984939.

[69] G. Sai Gautam and E. A. Carter. "Evaluating transition metal oxides within DFT-SCAN and SCAN + U frameworks for solar thermochemical applications". *Phys. Rev. Materials* 2 (2018), p. 095401. DOI: 10.1103/PhysRevMaterials.2.095401.

[70] Y. Zhang, W. Zhang, and D. J. Singh. "Localization in the SCAN meta-generalized gradient approximation functional leading to broken symmetry ground states for graphene and benzene". *Phys. Chem. Chem. Phys.* 22 (2020), pp. 19585–19591. DOI: 10.1039/D0CP03567J.

[71] Y. Fu and D. J. Singh. "Applicability of the Strongly Constrained and Appropriately Normed Density Functional to Transition-Metal Magnetism". *Phys. Rev. Lett.* 121 (2018), p. 207201. DOI: 10.1103/PhysRevLett.121.207201.

[72] R. T. Sharp and G. K. Horton. "A Variational Approach to the Unipotential Many-Electron Problem". *Phys. Rev.* 90 (1953), pp. 317–317. DOI: 10.1103/PhysRev.90.317.

[73] J. D. Talman and W. F. Shadwick. "Optimized effective atomic central potential". *Phys. Rev. A* 14 (1976), pp. 36–40. DOI: 10.1103/PhysRevA.14.36.

[74] A. D. Becke. "Density-functional thermochemistry. IV. A new dynamical correlation functional and implications for exact-exchange mixing". *The Journal of Chemical Physics* 104.3 (1996), pp. 1040–1046. DOI: 10.1063/1.470829.

[75] J. P. Perdew, M. Ernzerhof, and K. Burke. "Rationale for mixing exact exchange with density functional approximations". *The Journal of Chemical Physics* 105.22 (1996), pp. 9982–9985. DOI: 10.1063/1.472933.

[76] J. Heyd, G. E. Scuseria, and M. Ernzerhof. "Hybrid functionals based on a screened Coulomb potential". *The Journal of Chemical Physics* 118.18 (2003), pp. 8207–8215. DOI: 10.1063/1.1564060.

[77] A. V. Krukau, O. A. Vydrov, et al. "Influence of the exchange screening parameter on the performance of screened hybrid functionals". *The Journal of Chemical Physics* 125.22 (2006), p. 224106. DOI: 10.1063/1.2404663.

[78] B. G. Janesko, T. M. Henderson, and G. E. Scuseria. "Screened hybrid density functionals for solid-state chemistry and physics". *Phys. Chem. Chem. Phys.* 11 (2009), pp. 443–454. DOI: 10.1039/B812838C.

[79] S. Z. Butler, S. M. Hollen, et al. "Progress, Challenges, and Opportunities in Two-Dimensional Materials Beyond Graphene". *ACS Nano* 7.4 (2013), pp. 2898–2926. DOI: 10.1021/nn400280c.

[80] M. Xu, T. Liang, et al. "Graphene-Like Two-Dimensional Materials". *Chemical Reviews* 113.5 (2013), pp. 3766–3798. DOI: 10.1021/cr300263a.

[81] M. Chhowalla, H. S. Shin, et al. "The chemistry of two-dimensional layered transition metal dichalcogenide nanosheets". *Nature Chemistry* 5.4 (2013), pp. 263–275. DOI: 10.1038/nchem.1589.

[82] Q. H. Wang, K. Kalantar-Zadeh, et al. "Electronics and optoelectronics of two-dimensional transition metal dichalcogenides". *Nature Nanotechnology* 7.11 (2012), pp. 699–712. DOI: 10.1038/nnano.2012.193.

[83] R. Peköz and D. Donadio. "Effect of van der Waals interactions on the chemisorption and physisorption of phenol and phenoxy on metal surfaces". *The Journal of Chemical Physics* 145.10 (2016), p. 104701. DOI: 10.1063/1.4962236.

[84] F. Muttaqien, Y. Hamamoto, et al. "CO_2 adsorption on the copper surfaces: van der Waals density functional and TPD studies". *The Journal of Chemical Physics* 147.9 (2017), p. 094702. DOI: 10.1063/1.4994149.

[85] S. Grimme, J. Antony, et al. "A consistent and accurate *ab initio* parametrization of density functional dispersion correction (DFT-D) for the 94 elements H-Pu". *The Journal of Chemical Physics* 132.15 (2010), p. 154104. DOI: 10.1063/1.3382344.

[86] M. Dion, H. Rydberg, et al. "Van der Waals Density Functional for General Geometries". *Physical Review Letters* 92.24 (2004), p. 246401. DOI: 10.1103/PhysRevLett.92.246401.

[87] O. A. Vydrov and T. Van Voorhis. "Nonlocal van der Waals density functional: The simpler the better". *The Journal of Chemical Physics* 133.24 (2010), p. 244103. DOI: 10.1063/1.3521275.

[88] R. Sabatini, T. Gorni, and S. de Gironcoli. "Nonlocal van der Waals density functional made simple and efficient". *Physical Review B* 87.4 (2013), p. 041108. DOI: 10.1103/PhysRevB.87.041108.

[89] H. Peng, Z.-H. Yang, et al. "Versatile van der Waals Density Functional Based on a Meta-Generalized Gradient Approximation". *Physical Review X* 6.4 (2016), p. 041005. DOI: 10.1103/PhysRevX.6.041005.

[90] K. Terakura, T. Oguchi, et al. "Band theory of insulating transition-metal monoxides: Band-structure calculations". *Phys. Rev. B* 30 (1984), pp. 4734–4747. DOI: 10.1103/PhysRevB.30.4734.

[91] J. Hubbard and B. H. Flowers. "Electron correlations in narrow energy bands". *Proceedings of the Royal Society of London. Series A. Mathematical and Physical Sciences* 276.1365 (1963), pp. 238–257. DOI: 10.1098/rspa.1963.0204.

[92] S. L. Dudarev, G. A. Botton, et al. "Electron-energy-loss spectra and the structural stability of nickel oxide: An LSDA+U study". *Phys. Rev. B* 57 (1998), pp. 1505–1509. DOI: 10.1103/PhysRevB.57.1505.

[93] K. Reuter and M. Scheffler. "First-Principles Atomistic Thermodynamics for Oxidation Catalysis: Surface Phase Diagrams and Catalytically Interesting Regions". *Phys. Rev. Lett.* 90 (2003), p. 046103. DOI: 10.1103/PhysRevLett.90.046103.

[94] K. Reuter and M. Scheffler. "Composition, structure, and stability of $RuO_2(110)$ as a function of oxygen pressure". *Phys. Rev. B* 65 (2001), p. 035406. DOI: 10.1103/PhysRevB.65.035406.

[95] F. Bloch. "Über die Quantenmechanik der Elektronen in Kristallgittern". *Zeitschrift für Physik* 52.7-8 (1929), pp. 555–600. DOI: 10.1007/BF01339455.

[96] G. H. Wannier. "The Structure of Electronic Excitation Levels in Insulating Crystals". *Physical Review* 52.3 (1937), pp. 191–197. DOI: 10.1103/PhysRev.52.191.

[97] A. A. Mostofi, J. R. Yates, et al. "wannier90: A tool for obtaining maximally-localised Wannier functions". *Computer Physics Communications* 178.9 (2008), pp. 685–699. DOI: 10.1016/j.cpc.2007.11.016.

[98] N. Marzari and D. Vanderbilt. "Maximally localized generalized Wannier functions for composite energy bands". *Physical Review B* 56.20 (1997), pp. 12847–12865. DOI: 10.1103/PhysRevB.56.12847.

[99]   N. Wang, M. Duchamp, et al. "Terbium-Doped VO$_2$ Thin Films: Reduced Phase Transition Temperature and Largely Enhanced Luminous Transmittance". *Langmuir* 32.3 (2016), pp. 759–764. DOI: 10.1021/acs.langmuir.5b04212.

[100] M. Netsianda, P. E. Ngoepe, et al. "The displacive phase transition of vanadium dioxide and the effect of doping with tungsten". *Chemistry of Materials* 20.5 (2008), pp. 1764–1772. DOI: 10.1021/cm701861z.

[101] C. Piccirillo, R. Binions, and I. P. Parkin. "Synthesis and characterisation of W-doped VO2 by Aerosol Assisted Chemical Vapour Deposition". *Thin Solid Films* 516.8 (2008), pp. 1992–1997. DOI: 10.1016/j.tsf.2007.06.009.

[102] G. Khan, K. Asokan, and B. Ahmad. "Room temperature tunability of Mo-doped VO 2 nanofilms across semiconductor to metal phase transition". *Thin Solid Films* 625 (2017), pp. 155–162. DOI: 10.1016/j.tsf.2017.02.006.

[103] C. Piccirillo, R. Binions, and I. P. Parkin. "Nb-Doped VO$_2$ Thin Films Prepared by Aerosol-Assisted Chemical Vapour Deposition". *European Journal of Inorganic Chemistry* 2007.25 (2007), pp. 4050–4055. DOI: 10.1002/ejic.200700284.

[104] M. Ghedira, H. Vincent, et al. "Structural aspects of the metal-insulator transitions in $V_{0.985}Al_{0.015}O_2$". *Journal of Solid State Chemistry* 22.4 (1977), pp. 423–438. DOI: 10.1016/0022-4596(77)90020-2.

[105] G. Villeneuve, A. Bordet, et al. "Proprietes physiques et structurales de la phase $Cr_xV_{1-x}O_2$". *Materials Research Bulletin* 6.2 (1971), pp. 119–130. DOI: 10.1016/0025-5408(71)90096-1.

[106] A. Krammer, A. Magrez, et al. "Elevated transition temperature in Ge doped VO$_2$ thin films". *Journal of Applied Physics* 122.4 (2017), p. 045304. DOI: 10.1063/1.4995965.

[107] M. F. Becker, A. B. Buckman, et al. "Femtosecond laser excitation of the semiconductor-metal phase transition in VO 2". *Applied Physics Letters* 65.12 (1994), pp. 1507–1509. DOI: 10.1063/1.112974.

[108] S. Lysenko, N. Kumar, et al. "Ultrafast structural dynamics of VO$_2$". *Physical Review B* 96.7 (2017), p. 075128. DOI: 10.1103/PhysRevB.96.075128.

[109] M. F. Jager, C. Ott, et al. "Tracking the insulator-to-metal phase transition in VO 2 with few-femtosecond extreme UV transient absorption spectroscopy". *Proceedings of the National Academy of Sciences* 114.36 (2017), pp. 9558–9563. DOI: 10.1073/pnas.1707602114.

[110] G Stefanovich, a Pergament, and D Stefanovich. "Electrical switching and Mott transition in VO$_2$". *Journal of Physics: Condensed Matter* 12.41 (2000), pp. 8837–8845. DOI: 10.1088/0953-8984/12/41/310.

[111] E Strelcov, Y Lilach, and A Kolmakov. "Gas Sensor Based on Metal-Insulator Transition in VO$_2$ Nanowire Thermistor". *Nano Letters* 9.6 (2009), pp. 2322–2326. DOI: 10.1021/Nl900676n.

[112] S. Sengupta, K. Wang, et al. "Field-effect modulation of conductance in VO$_2$ nanobeam transistors with HfO$_2$ as the gate dielectric". *Applied Physics Letters* 99.6 (2011), p. 062114. DOI: 10.1063/1.3624896.

[113] M.-J. Lee, Y. Park, et al. "Two Series Oxide Resistors Applicable to High Speed and High Density Nonvolatile Memory". *Advanced Materials* 19.22 (2007), pp. 3919–3923. DOI: 10.1002/adma.200700251.

[114] N. Wang, Y. K. Peh, et al. "Surface engineering on continuous VO$_2$ thin films to improve thermochromic properties: Top-down acid etching and bottom-up self-patterning". *Journal of Colloid and Interface Science* 512 (2018), pp. 529–535. DOI: 10.1016/j.jcis.2017.10.096.

[115] Z. Qu, L. Yao, et al. "Surface and interface engineering for VO$_2$ coatings with excellent optical performance: From theory to practice". *Materials Research Bulletin* 109 (2019), pp. 195–212. DOI: 10.1016/j.materresbull.2018.09.043.

[116] Z. Zhu and U. Schwingenschlögl. "Comprehensive picture of VO$_2$ from band theory". *Physical Review B - Condensed Matter and Materials Physics* 86.7 (2012), pp. 2–5. DOI: 10.1103/PhysRevB.86.075149.

[117] V. Eyert. "The metal-insulator transitions of VO$_2$: A band theoretical approach". *Annalen der Physik (Leipzig)* 11.9 (2002), pp. 650–702. DOI: 10.1002/1521-3889(200210)11:9<650::AID-ANDP650>3.0.CO;2-K.

[118] R. M. Wentzcovitch, W. W. Schulz, and P. B. Allen. "VO$_2$: Peierls or Mott-Hubbard? A view from band theory". *Physical Review Letters* 72.21 (1994), pp. 3389–3392. DOI: 10.1103/PhysRevLett.72.3389.

[119] G. H. Liu, X. Y. Deng, and R. Wen. "Electronic and optical properties of monoclinic and rutile vanadium dioxide". *Journal of Materials Science* 45.12 (2010), pp. 3270–3275. DOI: 10.1007/s10853-010-4338-2.

[120] B. Stahl and T. Bredow. "Critical Assessment of the DFT+U Approach for the Prediction of Vanadium Dioxide Properties". *Journal of Computational Chemistry* 41.3 (2020), pp. 258–265. DOI: 10.1002/jcc.26096.

[121] T. Bredow and B. Stahl. "Systematic variation of Fock exchange in hybrid functionals: Effect on the structural, electronic and energetic properties of VO$_2$". *Chemical Physics Letters* 695 (2018), pp. 28–33. DOI: 10.1016/j.cplett.2018.01.048.

[122] S. Xu, X. Shen, et al. "Unified band-theoretic description of structural, electronic, and magnetic properties of vanadium dioxide phases". *Phys. Rev. B* 95 (2017), p. 125105.

[123] W. H. Brito, M. C. Aguiar, et al. "Metal-Insulator Transition in VO$_2$: A DFT+DMFT Perspective". *Physical Review Letters* 117.5 (2016), pp. 1–6. DOI: 10.1103/PhysRevLett.117.056402.

[124] G. Kotliar, S. Y. Savrasov, et al. "Electronic structure calculations with dynamical mean-field theory". *Rev. Mod. Phys.* 78.3 (2006), pp. 865–951. DOI: 10.1103/RevModPhys.78.865.

[125] T. A. Mellan and R. Grau-Crespo. "Density functional theory study of rutile VO$_2$ surfaces". *The Journal of Chemical Physics* 137.15 (2012), p. 154706. DOI: 10.1063/1.4758319.

[126] B. Stahl and T. Bredow. "Surfaces of VO₂ Polymorphs: Structure, Stability and the Effect of Doping". *ChemPhysChem* (2021), cphc.202000969. DOI: `10.1002/cphc.202000969`.

[127] D. Kucharczyk and T. Niklewski. "Accurate X-ray determination of the lattice parameters and the thermal expansion coefficients of VO₂ near the transition temperature". *Journal of Applied Crystallography* 12.4 (1979), pp. 370–373. DOI: `10.1107/S0021889879012711`.

[128] W. Brückner. "Structural relations between the VO₂ phases". *Kristall und Technik* 16.3 (1981), K28–K31. DOI: `10.1002/crat.19810160320`.

[129] E. Arcangeletti, L. Baldassarre, et al. "Evidence of a Pressure-Induced Metallization Process in Monoclinic VO₂". *Physical Review Letters* 98.19 (2007), p. 196406. DOI: `10.1103/PhysRevLett.98.196406`.

[130] J. H. Park, J. M. Coy, et al. "Measurement of a solid-state triple point at the metal–insulator transition in VO2". *Nature* 500.7463 (2013), pp. 431–434. DOI: `10.1038/nature12425`.

[131] V. Eyert. "The metal-insulator transitions of VO2: A band theoretical approach". *Annalen der Physik* 11.9 (2002), pp. 650–704. DOI: `https://doi.org/10.1002/1521-3889(200210)11:9<650::AID-ANDP650>3.0.CO;2-K`.

[132] A. Zylbersztejn and N. F. Mott. "Metal-insulator transition in vanadium dioxide". *Phys. Rev. B* 11 (1975), pp. 4383–4395. DOI: `10.1103/PhysRevB.11.4383`.

[133] K. D. Rogers. "An X-ray diffraction study of semiconductor and metallic vanadium dioxide". *Powder Diffraction* 8.4 (1993), pp. 240–244. DOI: `10.1017/S0885715600019448`.

[134] H. W. Verleur, A. S. Barker, and C. N. Berglund. "Optical Properties of V O 2 between 0.25 and 5 eV". *Reviews of Modern Physics* 40.4 (1968), pp. 737–737. DOI: `10.1103/RevModPhys.40.737`.

[135] F. Pintchovski, W. Glaunsinger, and A. Navrotsky. "Experimental study of the electronic and lattice contributions to the VO2 transition". *Journal of Physics and Chemistry of Solids* 39.9 (1978), pp. 941–949. DOI: `10.1016/0022-3697(78)90108-7`.

[136] S. Kim, K. Kim, et al. "Correlation-assisted phonon softening and the orbital-selective Peierls transition in VO₂". *Phys. Rev. B* 87 (2013), p. 195106. DOI: `10.1103/PhysRevB.87.195106`.

[137] R. Enjalbert and J. Galy. "A refinement of the structure of V2O5". *Acta Crystallographica Section C Crystal Structure Communications* 42.11 (1986), pp. 1467–1469. DOI: `10.1107/S0108270186091825`.

[138] J. Goclon, R. Grybos, et al. "Oxygen vacancy formation on clean and hydroxylated low-index V₂O₅ surfaces: A density functional investigation". *Phys. Rev. B* 79 (2009), p. 075439. DOI: `10.1103/PhysRevB.79.075439`.

[139] G. Kresse, S. Surnev, et al. "First-principles calculations for VₓOᵧ grown on Pd(111)". *Surface Science* 492.3 (2001), pp. 329–344. DOI: `https://doi.org/10.1016/S0039-6028(01)01454-6`.

[140]   Collaboration: Scientific Group Thermodata Europe (SGTE). "Thermodynamic Properties of Compounds, V_2O_5 to ThP". *Pure Substances. Part 4, Compounds from HgH_g to $ZnTe_g$*. Ed. by Lehrstuhl für Theoretische Hüttenkunde and Rheinisch-Westfälische Technische Hochschule Aachen. Vol. 19A4. Berlin/Heidelberg: Springer-Verlag, 2001, pp. 351–374. ISBN: 9783540410256. DOI: 10.1007/10688868_17.

[141]   J. E. Wainwright and J. Starkey. "A refinement of the structure of anorthite* ,[1]". *Zeitschrift für Kristallographie* 133.133 (1971), pp. 75–84. DOI: 10.1524/zkri.1971.133.133.75.

[142]   A. Moshfegh and A. Ignatiev. "Formation and characterization of thin film vanadium oxides: Auger electron spectroscopy, X-ray photoelectron spectroscopy, X-ray diffraction, scanning electron microscopy, and optical reflectance studies". *Thin Solid Films* 198.1-2 (1991), pp. 251–268. DOI: 10.1016/0040-6090(91)90344-W.

[143]   S. F. Cogan, N. M. Nguyen, et al. "Optical properties of electrochromic vanadium pentoxide". *Journal of Applied Physics* 66.3 (1989), pp. 1333–1337. DOI: 10.1063/1.344432.

[144]   N. V. Hieu and D. Lichtman. "Bandgap radiation induced photodesorption from V_2O_5 powder and vanadium oxide surfaces". *Journal of Vacuum Science and Technology* 18.1 (1981), pp. 49–53. DOI: 10.1116/1.570698.

[145]   S. Bates, G. Kresse, and M. Gillan. "A systematic study of the surface energetics and structure of TiO_2(110) by first-principles calculations". *Surface Science* 385.2-3 (1997), pp. 386–394. DOI: 10.1016/S0039-6028(97)00265-3.

[146]   J. Rahm and P. Erhart. "WulffPack: A Python package for Wulff constructions". *Journal of Open Source Software* 5.45 (2020), p. 1944. DOI: 10.21105/joss.01944.

[147]   J. Tersoff and D. R. Hamann. "Theory of the scanning tunneling microscope". *Phys. Rev. B* 31 (1985), pp. 805–813. DOI: 10.1103/PhysRevB.31.805.

[148]   U. Diebold, J. F. Anderson, et al. "Evidence for the Tunneling Site on Transition-Metal Oxides: TiO_2(110)". *Physical Review Letters* 77.7 (1996), pp. 1322–1325. DOI: 10.1103/PhysRevLett.77.1322.

[149]   H. Over, A. Seitsonen, et al. "Experimental and simulated STM images of stoichiometric and partially reduced RuO_2(110) surfaces including adsorbates". *Surface Science* 515.1 (2002), pp. 143–156. DOI: 10.1016/S0039-6028(02)01853-8.

[150]   E. Goering, M. Schramme, et al. "LEED and photoemission study of the stability of VO 2 ssurfaces". *Physical Review B* 55.7 (1997), pp. 4225–4230. DOI: 10.1103/PhysRevB.55.4225.

[151]   S. Nosé. "A unified formulation of the constant temperature molecular dynamics methods". *The Journal of Chemical Physics* 81.1 (1984), pp. 511–519. DOI: 10.1063/1.447334.

[152]   W. G. Hoover. "Canonical dynamics: Equilibrium phase-space distributions". *Phys. Rev. A* 31 (1985), pp. 1695–1697. DOI: 10.1103/PhysRevA.31.1695.

[153]   R.-P Blum, H. Niehus, et al. "Surface Metal-Insulator Transition on a Vanadium Pentoxide(001) Single Crystal". *Physical Review Letters* 99.22 (2007), p. 226103. DOI: 10.1103/PhysRevLett.99.226103.

[154] C. Klein, G. Kresse, et al. "Vanadium surface oxides on Pd(111): A structural analysis". *Physical Review B* 68.23 (2003), p. 235416. DOI: 10.1103/PhysRevB.68.235416.

[155] J. A. Enterkin, A. K. Subramanian, et al. "A homologous series of structures on the surface of $SrTiO_3$(110)". *Nature Materials* 9.3 (2010), pp. 245–248. DOI: 10.1038/nmat2636.

[156] Collaboration: Scientific Group Thermodata Europe (SGTE). "Thermodynamic Properties of Compounds, SbO_2 to Rh_2O_3". *Pure Substances. Part 4, Compounds from HgH_g to $ZnTe_g$*. Ed. by Lehrstuhl für Theoretische Hüttenkunde and Rheinisch-Westfälische Technische Hochschule Aachen. Vol. 19A4. Berlin/Heidelberg: Springer-Verlag, 2001, pp. 301–324. ISBN: 9783540410256. DOI: 10.1007/10688868_15.

[157] A. R. Oganov and C. W. Glass. "Crystal structure prediction using *ab initio* evolutionary techniques: Principles and applications". *The Journal of Chemical Physics* 124.24 (2006), p. 244704. DOI: 10.1063/1.2210932.

[158] A. O. Lyakhov, A. R. Oganov, et al. "New developments in evolutionary structure prediction algorithm USPEX". *Computer Physics Communications* 184.4 (2013), pp. 1172–1182. DOI: 10.1016/j.cpc.2012.12.009.

[159] A. R. Oganov, A. O. Lyakhov, and M. Valle. "How Evolutionary Crystal Structure Prediction Works and Why". *Accounts of Chemical Research* 44.3 (2011), pp. 227–237. DOI: 10.1021/ar1001318.

[160] Z. Shomali, J. Ghazanfarian, and A. Abbassi. "Effect of film properties for non-linear DPL model in a nanoscale MOSFET with high-k material: ZrO_2/HfO_2/La_2O_3". *Superlattices and Microstructures* 83 (2015), pp. 699–718. DOI: 10.1016/j.spmi.2015.03.060.

[161] J. P. Chang, Y.-S. Lin, and K. Chu. "Rapid thermal chemical vapor deposition of zirconium oxide for metal-oxide-semiconductor field effect transistor application". *Journal of Vacuum Science & Technology B: Microelectronics and Nanometer Structures Processing, Measurement, and Phenomena* 19.5 (2001), pp. 1782–1787. DOI: 10.1116/1.1396639.

[162] C.-C. Hu, C.-A. Chiu, et al. "Liquid-phase-deposited high dielectric zirconium oxide for metal-oxide-semiconductor high electron mobility transistors". *Vacuum* 118 (2015). 3rd IEEE International Symposium on Next-Generation Electronics (ISNE2014), pp. 142–146. DOI: 10.1016/j.vacuum.2015.01.012.

[163] P. J. Harrop and J. N. Wanklyn. "The dielectric constant of zirconia". *British Journal of Applied Physics* 18.6 (1967), pp. 739–742. DOI: 10.1088/0508-3443/18/6/305.

[164] R. H. French, S. J. Glass, et al. "Experimental and theoretical determination of the electronic structure and optical properties of three phases of ZrO_2". *Phys. Rev. B* 49 (1994), pp. 5133–5142. DOI: 10.1103/PhysRevB.49.5133.

[165] H. Jiang, R. I. Gomez-Abal, et al. "Electronic band structure of zirconia and hafnia polymorphs from the G W perspective". *Physical Review B* 81.8 (2010), p. 085119. DOI: 10.1103/PhysRevB.81.085119.

[166] S. J. Kim, D. H. Yoon, et al. "Low-Temperature Solution-Processed ZrO_2 Gate Insulators for Thin-Film Transistors Using High-Pressure Annealing". *Electrochemical and Solid-State Letters* 14.11 (2011), E35. DOI: 10.1149/2.006111esl.

[167] O. N. Gorshkov, I. N. Antonov, et al. "Resistive switching in metal-insulator-metal structures based on germanium oxide and stabilized zirconia". *Technical Physics Letters* 40.2 (2014), pp. 101–103. DOI: 10.1134/S1063785014020084.

[168] T. Hiratoko, A. Yoneda, and M. Osako. "Thermal properties of Ca-doped stabilized zirconia under high pressure and high temperature". *Ceramics International* 40.8 (2014), pp. 12471–12475. DOI: 10.1016/j.ceramint.2014.04.101.

[169] M Filal. "Ionic conductivity of yttrium-doped zirconia and the 'composite effect'". *Solid State Ionics* 80.1-2 (1995), pp. 27–35. DOI: 10.1016/0167-2738(95)00137-U.

[170] J. H. Shim, C.-C. Chao, et al. "Atomic Layer Deposition of Yttria-Stabilized Zirconia for Solid Oxide Fuel Cells". *Chemistry of Materials* 19.15 (2007), pp. 3850–3854. DOI: 10.1021/cm070913t.

[171] A. Buyukaksoy and V. I. Birss. "Highly active nanoscale Ni - Yttria stabilized zirconia anodes for micro-solid oxide fuel cell applications". *Journal of Power Sources* 307 (2016), pp. 449–453. DOI: 10.1016/j.jpowsour.2015.12.022.

[172] S. McIntosh and R. J. Gorte. "Direct Hydrocarbon Solid Oxide Fuel Cells". *Chemical Reviews* 104.10 (2004), pp. 4845–4866. DOI: 10.1021/cr020725g.

[173] Y. Liu, J. Parisi, et al. "Solid-state gas sensors for high temperature applications – a review". *J. Mater. Chem. A* 2.26 (2014), pp. 9919–9943. DOI: 10.1039/C3TA15008A.

[174] T. von Schewelov, L. Sanzen, et al. "Total hip replacement with a zirconium oxide ceramic femoral head: A Randomised Roentgen Stereophotogrammetric Study". *The Journal of Bone and Joint Surgery. British volume* 87-B.12 (2005), pp. 1631–1635. DOI: 10.1302/0301-620X.87B12.16873.

[175] G. M. Tartaglia, E. Sidoti, and C. Sforza. "Seven-year prospective clinical study on zirconia-based single crowns and fixed dental prostheses". *Clinical Oral Investigations* 19.5 (2015), pp. 1137–1145. DOI: 10.1007/s00784-014-1330-2.

[176] J Chevalier. "Critical effect of cubic phase on aging in 3mol% yttria-stabilized zirconia ceramics for hip replacement prosthesis". *Biomaterials* 25.24 (2004), pp. 5539–5545. DOI: 10.1016/j.biomaterials.2004.01.002.

[177] T. Witoon, J. Chalorngtham, et al. "CO_2 hydrogenation to methanol over Cu/ZrO_2 catalysts: Effects of zirconia phases". *Chemical Engineering Journal* 293 (2016), pp. 327–336. DOI: 10.1016/j.cej.2016.02.069.

[178] P. Bouvier, E. Djurado, et al. "High-pressure structural evolution of undoped tetragonal nanocrystalline zirconia". *Physical Review B* 62.13 (2000), pp. 8731–8737. DOI: 10.1103/PhysRevB.62.8731.

[179] J. D. McCullough and K. N. Trueblood. "The crystal structure of baddeleyite (monoclinic ZrO_2)". *Acta Crystallographica* 12.7 (1959), pp. 507–511. DOI: 10.1107/S0365110X59001530.

[180] J. Wang, H. P. Li, and R. Stevens. "Hafnia and hafnia-toughened ceramics". *Journal of Materials Science* 27.20 (1992), pp. 5397–5430. DOI: 10.1007/BF00541601.

[181] X. Luo, W. Zhou, et al. "Monoclinic to tetragonal transformations in hafnia and zirconia: A combined calorimetric and density functional study". *Physical Review B* 80.13 (2009), p. 134119. DOI: 10.1103/PhysRevB.80.134119.

[182] J. M. Leger, P. E. Tomaszewski, et al. "Pressure-induced structural phase transitions in zirconia under high pressure". *Physical Review B* 47.21 (1993), pp. 14075–14083. DOI: 10.1103/PhysRevB.47.14075.

[183] Y. Al-Khatatbeh, K. K. M. Lee, and B. Kiefer. "Phase relations and hardness trends of ZrO_2 phases at high pressure". *Physical Review B* 81.21 (2010), p. 214102. DOI: 10.1103/PhysRevB.81.214102.

[184] J. Müller, T. S. Böscke, et al. "Ferroelectricity in Simple Binary ZrO_2 and HfO_2". *Nano Letters* 12.8 (2012), pp. 4318–4323. DOI: 10.1021/nl302049k.

[185] R. Materlik, C. Künneth, and A. Kersch. "The origin of ferroelectricity in $Hf_{1-x}Zr_xO_2$: A computational investigation and a surface energy model". *Journal of Applied Physics* 117.13 (2015), p. 134109. DOI: 10.1063/1.4916707.

[186] K. Meinel, A. Eichler, et al. "Surface and interface structures of epitaxial ZrO_2 films on Pt(111): Experiment and density-functional theory calculations". *Physical Review B* 74.23 (2006), p. 235444. DOI: 10.1103/PhysRevB.74.235444.

[187] K Meinel, A Eichler, et al. "STM, LEED, and DFT characterization of epitaxial ZrO_2 films on Pt(111)". *Surface Science* 562.1-3 (2004), pp. 204–218. DOI: 10.1016/j.susc.2004.06.035.

[188] K. Meinel, K.-M. Schindler, and H. Neddermeyer. "Growth, structure and annealing behaviour of epitaxial ZrO_2 films on Pt(111)". *Surface Science* 532-535 (2003), pp. 420–424. DOI: 10.1016/S0039-6028(03)00187-0.

[189] V. Maurice, M. Salmeron, and G. Somorjai. "The epitaxial growth of zirconium oxide thin films on Pt(111) single crystal surfaces". *Surface Science* 237.1-3 (1990), pp. 116–126. DOI: 10.1016/0039-6028(90)90524-C.

[190] A. Eichler. "Modeling oxide-metal interfaces from density functional theory: Platinum adsorption on tetragonal zirconia". *Phys. Rev. B* 68 (2003), p. 205408. DOI: 10.1103/PhysRevB.68.205408.

[191] J. Lou, U. Hess, and K. Mitchell. "The growth of zirconium oxide thin films on Au(111) single-crystal surfaces". *Applied Surface Science* 62.3 (1992), pp. 175–180. DOI: 10.1016/0169-4332(92)90143-L.

[192] M. Antlanger, W. Mayr-Schmölzer, et al. "$Pt_3Zr(0001)$: A substrate for growing well-ordered ultrathin zirconia films by oxidation". *Physical Review B* 86.3 (2012), p. 035451. DOI: 10.1103/PhysRevB.86.035451.

[193] J. I. J. Choi, W Mayr-Schmölzer, et al. "The growth of ultra-thin zirconia films on $Pd_3Zr(0001)$". *Journal of Physics: Condensed Matter* 26.22 (2014), p. 225003. DOI: 10.1088/0953-8984/26/22/225003.

[194] H. Li, J.-I. J. Choi, et al. "Growth of an Ultrathin Zirconia Film on Pt₃Zr Examined by High-Resolution X-ray Photoelectron Spectroscopy, Temperature-Programmed Desorption, Scanning Tunneling Microscopy, and Density Functional Theory". *The Journal of Physical Chemistry C* (2015), p. 150127093244008. DOI: 10.1021/jp5100846.

[195] A. Ruiz Puigdollers and G. Pacchioni. "Reducibility of ZrO_2/Pt_3Zr and ZrO_2/Pt 2D films compared to bulk zirconia: a DFT+U study of oxygen removal and H_2 adsorption". *Nanoscale* 9.20 (2017), pp. 6866–6876. DOI: 10.1039/C7NR01904A.

[196] C. Imparato, M. Fantauzzi, et al. "Unraveling the Charge State of Oxygen Vacancies in ZrO_{2-x} on the Basis of Synergistic Computational and Experimental Evidence". *The Journal of Physical Chemistry C* 123.18 (2019), pp. 11581–11590. DOI: 10.1021/acs.jpcc.9b00411.

[197] W. Mayr-Schmölzer, J. Planer, et al. "Many-electron calculations of the phase stability of ZrO_2 polymorphs". *Phys. Rev. Research* 2 (2020), p. 043361. DOI: 10.1103/PhysRevResearch.2.043361.

[198] G. Katz. "X-Ray Diffraction Powder Pattern of Metastable Cubic ZrO_2". *Journal of the American Ceramic Society* 54.10 (1971), pp. 531–531. DOI: 10.1111/j.1151-2916.1971.tb12197.x.

[199] N. Igawa and Y. Ishii. "Crystal Structure of Metastable Tetragonal Zirconia up to 1473 K". *Journal of the American Ceramic Society* 84.5 (2001), pp. 1169–1171. DOI: 10.1111/j.1151-2916.2001.tb00808.x.

[200] J. C. Thomas and A. Van der Ven. "Order parameters for symmetry-breaking structural transitions: The tetragonal-monoclinic transition in ZrO_2". *Physical Review B* 96.13 (2017), p. 134121. DOI: 10.1103/PhysRevB.96.134121.

[201] J. Klimeš, D. R. Bowler, and A. Michaelides. "Chemical accuracy for the van der Waals density functional". *Journal of Physics: Condensed Matter* 22.2 (2010), p. 022201. DOI: 10.1088/0953-8984/22/2/022201.

[202] J. Klimeš, D. R. Bowler, and A. Michaelides. "Van der Waals density functionals applied to solids". *Physical Review B* 83.19 (2011), p. 195131. DOI: 10.1103/PhysRevB.83.195131.

[203] S. Tosoni and G. Pacchioni. "Acetic acid ketonization on tetragonal zirconia: Role of surface reduction". *Journal of Catalysis* 344 (2016), pp. 465–473. DOI: 10.1016/j.jcat.2016.10.002.

[204] M. Wolloch. *Report on the application of DFT+U for bulk ZrO_2. Personal communications, unpublished.* 2020.

[205] C. J. Howard, R. J. Hill, and B. E. Reichert. "Structures of ZrO_2 polymorphs at room temperature by high-resolution neutron powder diffraction". *Acta Crystallographica Section B Structural Science* 44.2 (1988), pp. 116–120. DOI: 10.1107/S0108768187010279.

[206] J. Harl and G. Kresse. "Accurate Bulk Properties from Approximate Many-Body Techniques". *Physical Review Letters* 103.5 (2009), p. 056401. DOI: 10.1103/PhysRevLett.103.056401.

[207] H. Shin, A. Benali, et al. "Zirconia and hafnia polymorphs: Ground-state structural properties from diffusion Monte Carlo". *Phys. Rev. Materials* 2 (2018), p. 075001. DOI: 10.1103/PhysRevMaterials.2.075001.

[208] E. V. Stefanovich, A. L. Shluger, and C. R. A. Catlow. "Theoretical study of the stabilization of cubic-phase ZrO_2 by impurities". *Phys. Rev. B* 49 (1994), pp. 11560–11571. DOI: 10.1103/PhysRevB.49.11560.

[209] J. Martincová, M. Otyepka, and P. Lazar. "Is Single Layer MoS_2 Stable in the Air?" *Chemistry - A European Journal* 23.53 (2017), pp. 13233–13239. DOI: 10.1002/chem.201702860.

[210] C. Freysoldt, B. Grabowski, et al. "First-principles calculations for point defects in solids". *Reviews of Modern Physics* 86.1 (2014), pp. 253–305. DOI: 10.1103/RevModPhys.86.253.

[211] L. Huey-Lin and P. Duwez. "Solid solutions of rhodium with copper and nickel". *Journal of the Less Common Metals* 6.3 (1964), pp. 248–249. DOI: 10.1016/0022-5088(64)90108-0.

[212] G. Kresse and J. Furthmüller. "Efficiency of ab-initio total energy calculations for metals and semiconductors using a plane-wave basis set". *Computational Materials Science* 6.1 (1996), pp. 15–50. DOI: 10.1016/0927-0256(96)00008-0.

[213] G.-M. Zhang and A. C. Hewson. "Non-Fermi-liquid theory of a compactified Anderson single-impurity model". *Physical Review B* 54.2 (1996), pp. 1169–1186. DOI: 10.1103/PhysRevB.54.1169.

[214] P. E. Blöchl. "Projector augmented-wave method". *Physical Review B* 50.24 (1994), pp. 17953–17979. DOI: 10.1103/PhysRevB.50.17953.

[215] G. Kresse and D. Joubert. "From ultrasoft pseudopotentials to the projector augmented-wave method". *Physical Review B* 59.3 (1999), pp. 1758–1775. DOI: 10.1103/PhysRevB.59.1758.

[216] J. D. Pack and H. J. Monkhorst. ""Special points for Brillouin-zone integrations"—a reply". *Physical Review B* 16.4 (1977), pp. 1748–1749. DOI: 10.1103/PhysRevB.16.1748.

[217] D. Wickramaratne, N. Bernstein, and I. I. Mazin. "Role of defects in the metal-insulator transition in VO 2 and V 2 O 3". *Physical Review B* 99.21 (2019), p. 214103. DOI: 10.1103/PhysRevB.99.214103.

[218] G. Pizzi, V. Vitale, et al. "Wannier90 as a community code: new features and applications". *Journal of Physics: Condensed Matter* 32.16 (2020), p. 165902. DOI: 10.1088/1361-648X/ab51ff.

Acknowledgement

Jakub Planer | Curriculum Vitae

Nationality: Czech

Date of birth: 03.09.1992

Phone: +420 773 295 152

E-mail: jakub.planer@tuwien.ac.at

Address: Hamiltongasse 4/5/12, 1140 Wien, Austria

Education

PhD in Computational Materials Science   09/2017 - present

Vienna University of Technology, Austria
Supervisors: Josef Redinger, Florian Mittendorfer
Title of the PhD Thesis: *Surface and Bulk Characterization of Transition Metal Oxides: A Density Functional Theory Study of ZrO_2 and VO_2*

ERASMUS stay   02/2016 – 07/2016

Vienna University of Technology, Austria
Field of study: Ab initio calculations of ultrathin zirconia films and zirconia — rhodium (111) interfaces

Master's Degree in Physical Engineering

Brno University of Technology, Czech Republic   09/2015 – 06/2017
Title of the Master Thesis: *First-principles studies of the electronic and structural properties of Lead Zirconate Titanate (PZT)*

Bachelor's Degree in Physical Engineering

Brno University of Technology, Czech Republic   09/2012 – 08/2015
Title of the Bachelor Thesis: *Photocontrolled biomolecules*

Outreach

VASP Lecturer   12/2018

Organization of the two-day VASP tutorial at the Faculty of Science, University of South Bohemia

List of Publications

W. Mayr-Schmölzer, J. Planer, J. Redinger, A. Grüneis, and F. Mittendorfer, "Many-electron calculations of the phase stability of ZrO_2 polymorphs", Physical Review Research, vol. 2, no. 4, 2020.

M. Wagner, J. Planer, B. Heller, J. Langer, A. Limbeck, L. A. Boatner, H. Steinrück, J. Redinger, F. Maier, F. Mittendorfer, M. Schmid and U. Diebold, "*A Novel Surface Phase on High-Temperature Rutile VO2(110)T Single Crystals*", **submitted**, Preprint (2107.00350) https://arxiv.org/abs/2107.00350

J. Planer, F. Mittendorfer, J. Redinger, "*First principles studies of the electronic and structural properties of the rutile VO₂(110) surface and its oxygen-rich terminations*", **submitted**, Preprint (2107.07899) https://arxiv.org/abs/2107.07899

Conference Contributions

Ab-initio studies of the (110) surface terminations of rutile VO_2
DPG Spring Meeting, Dresden/Germany, 2019 (oral)

Ab-initio studies of the (011) and (110) surfaces of rutile VO_2
European Conference on Surface Science, Aarhus/Denmark, 2018 (oral)

First-principles studies of the electronic and structural properties of vanadium dioxide and characterization of VO₂(011) surfaces
APS March Meeting, Los Angeles/California, 2018 (oral)

DFT study of the stability of thin zirconia films and meta-stable bulk phases
DPG Spring Meeting, Dresden/Germany, 2017 (oral)